uS

FACULTY OF SCIENCE AND TECHNOLOGY

MASTER THESIS

Study programme / specialisation:

Marine and Offshore Technology   The spring semester, 2022

Open

Author: **Milad Hassani (No. 261821)**

....
(signature author)

Course coordinator: **Prof. Yihan Xing**

Supervisor(s): **Associate Prof. Lin Li, Filippos Kalofotias**

Thesis title: **Hydrodynamic performance optimization of semi-submersible floaters for offshore wind turbines**

Credits (ECTS): 30

Keywords: Hydrodynamic response; optimization; semi-submersible; offshore wind turbine; hull geometry

Pages: 106

+ appendix: 3

Stavanger, 06/22

Hydrodynamic performance optimization of semi-submersible floaters for offshore wind turbines

Author   : Milad Hassani
Supervisor   : Associate Prof. Lin Li
Co-Supervisor   : Filippos Kalofotias

University of Stavanger

Faculty of Science and Technology

Department of Mechanical and Structural Engineering and Material Science

Master Thesis, June 2022

Abstract

Floating structures have become viable alternatives for supporting wind turbines as offshore wind projects move deeper into the water. The wind is prevalent in deep water (depths > 60 m) all around the world. Because of the amount of potential at these depths, wind turbines will require the design of a floating platform, as current wind turbines are usually fixed at the bottom and rely on ordinary concrete with a gravity base, which is not practical at these depths. Floating offshore wind offers a huge potential for green energy production offshore and the overall energy transition to zero carbon emission in general. With the development of even larger wind turbines in the range beyond 15 MW, the floating concepts become more attractive and competitive from a cost perspective. However, larger turbines and cost optimization also require a re-thinking of established solutions and concepts. New ideas and innovations are required to optimize floating offshore wind farms further.

An approach for the optimization of semi-submersible floaters using different surrogate models has been developed in this thesis. A semi-submersible floater is selected and designed to support a 15-MW wind turbine in the North Sea. The optimization framework consists of automatic modeling and numerical simulations in open-source tools as well as obtaining the Pareto fronts using surrogate models and the Genetic Algorithm in CEASES software. A Python-SALOME-NEMOH interface is used to obtain the hydrodynamic properties for geometries defined by various variables. The geometries are subjected to three performance constraints: the static platform pitch, metacentric height, nacelle acceleration, and wind. Loads in operating and parked conditions are considered. Finally, the geometries are optimized using two objective functions related to material cost and nacelle acceleration, and the results are discussed. This work contributes to developing efficient design optimization methods for floating structures.

Acknowledgements

Contents

List of Figures

List of Tables

1. Introduction

1.1   Background

Wind energy is an important source of natural renewable energy. In recent years, efforts have increased to create offshore wind farms to exploit this precious resource in many countries. Norway has ambitious climate targets that involve reducing emissions by 55% by 2030 compared with 1990 levels, with a further reduction down to net-zero by 2050. Norway's energy use already has low carbon intensity owing to its hydropower-dominated electricity system. This sets up a challenge because most of the remaining emissions are in hard-to-abate sectors, such as oil and gas production, heavy transport, and agriculture — and it is those sectors that will need to be targeted if Norway is to reach its ambitious climate targets. On the other hand, we see comparatively successful decarburization of the road transport sector, especially for passenger vehicles. By 2030, Battery Electric Vehicles (BEVs) will make up half of the Norwegian passenger vehicle fleet, resulting in a CO2 emission reduction of 25% of the total road sector emissions compared with 1990 levels [1].

The development of floating offshore wind turbines (FOWTs) to capture the stronger and more reliable offshore wind resources in deeper oceans is gaining popularity. In the last decade, several FOWT designs supporting an offshore reference wind turbine have been developed and researched [2-6], such as the NREL 5MW wind turbine model [2]. Floating foundations have the potential to be a "game-changer" in terms of effectively harnessing abundant wind potential in deeper waters, paving the way for rapid future growth in the offshore wind power market and, as a result, the decarburization of the energy sector in many countries where traditional bottom-fixed offshore wind turbines are not permitted.

Floating Offshore Wind Energy (FOWE) costs will continue to be reduced as economies of scale, more competitive supply chains, and technical advancements increase. For example, in European seas, 80 percent of the offshore wind resource is found in waters 60 meters and deeper, where typical bottom-fixed offshore wind is not technically nor commercially viable. As the only region in the world having pre-commercial projects, the European Union is already at the forefront of this technology [7].

Spar buoys, semisubmersibles, and TLPs are some of the more mature concepts borrowed from the oil and gas industry, whereas barges, hybrids, and 'game changers' are more novel concepts. Some features of these floaters are listed below:

- A cylinder is ballasted to keep the center of gravity below the center of buoyancy in spar buoy technology. A catenary or taut spread mooring lines with drag or suction anchors keep the floating structure in place.
- Semi-submersible floaters are made up of a series of massive columns that give hydrostatic stability and are connected by connecting submerged pontoons that contribute to buoyancy. The buoyancy on these platforms is distributed broadly at the water plane, resulting in static stability.

- Barge-type structures have a huge pontoon structure and achieve stability through a distributed pontoon system.
- Hybrids are made up of elements and properties from several different groups.
- Game changers are defined as those with the most novel and disruptive concepts.

Semi-submersible structures receive the most positive feedback from marine professionals, followed by the barge and the spar. However, this is not a conclusive conclusion because the suitability of technology is highly reliant on the individual conditions of each project; for example, a spar-buoy floater will be the most appropriate for a project site with adverse sea conditions. A fair assessment of hybrid concepts and game-changers is impossible due to significant disparities between the many technology concepts within each group. Due to its modest waterline, the semi-submersible platform has comparatively low environmental loads, and its movement performance is better in extreme sea conditions. At the same time, it has steadily become one of the most popular floating structures for deep-sea oil research and development due to its enormous deck area and benefits of big variable load [1, 2]. Due to the complicated maritime environment, the platform is subjected to wind, waves, currents, and even earthquakes, necessitating stricter standards for the supporting platform's safety and stability. The semi-submersible support platform's overall performance is constantly being improved through platform optimization research.

The Levelized cost of energy (LCOE) is a calculation of an energy plant's average lifetime net present cost of electricity generation. It's used to calculate the present value of a power plant's total cost of construction (CAPEX) and operation (OPEX) over a given period. When operating in competitive marketplaces, this metric helps you to compare alternative power generation systems.

Because the concepts within each group share comparable characteristics, the LCOE for FOWE has only been estimated for spars, semi-submersibles, TLPs, and Barges. Calculating the LCOE of hybrids and game-changers would necessitate a far more in-depth examination of each notion among these many technological groupings. The outcome of the LCOE calculation for the four technology groups is shown in Fig. 1-1.

These findings suggest that semi-submersible and spar-buoy technologies will have lower LCOE values than TLP and barge technologies. The estimated variance of the LCOE for each technology has also been provided with a range, as the LCOE is highly reliant on the unique characteristics of a project's site. A steel TLP achieves the highest value, while a concrete semisubmersible unit achieves the lowest. These studies also suggest that, regardless of technology, concrete structures have a lower LCOE than steel structures [3].

Because no full-scale commercial projects have yet been completed, the current LCOE for FOWE is still unknown. Although current LCOE estimates are much higher than those for other renewable energy sources (RES), the analysis presented in [3] suggests that the LCOE of a 500 MW farm might be comparable to that of other RES like BFOW or solar PV. Furthermore, in some remote places that are

largely reliant on fuel imports, such as small archipelagos, FOWE could already be competitive with diesel power generation.

Based on the information now available, spar-buoy and semi-submersible technologies have been identified as the most promising technologies for future FOWE development. Semi-submersible technology ranks highest in terms of applicability due to its favorable low draft requirements and self-stability qualities, which allow onshore turbine installation, resulting in the lowest overall costs (CAPEX and OPEX) of all technologies. However, spar buoys' key advantages are their simple structural design and remarkable seakeeping performance in rough seas, resulting in an LCOE that is comparable to semi-submersibles despite higher total expenditures. During its first year of operation, the Hywind Scotland 30 MW farm, for example, attained an average capacity factor of around 65 percent. According to this theory, semi-submersible floating structures will be the most prevalent technology for FOWE applications, except for sites with harsh sea conditions that could limit the capacity factor, necessitating the use of a spar buoy floater.

The LCOE of FOWE must be greatly decreased for it to compete with other renewable generation sources in grid-scale power generation. Even though the future LCOE of FOWE is unclear because of its technological and market immaturity, all projections predict significant decreases.
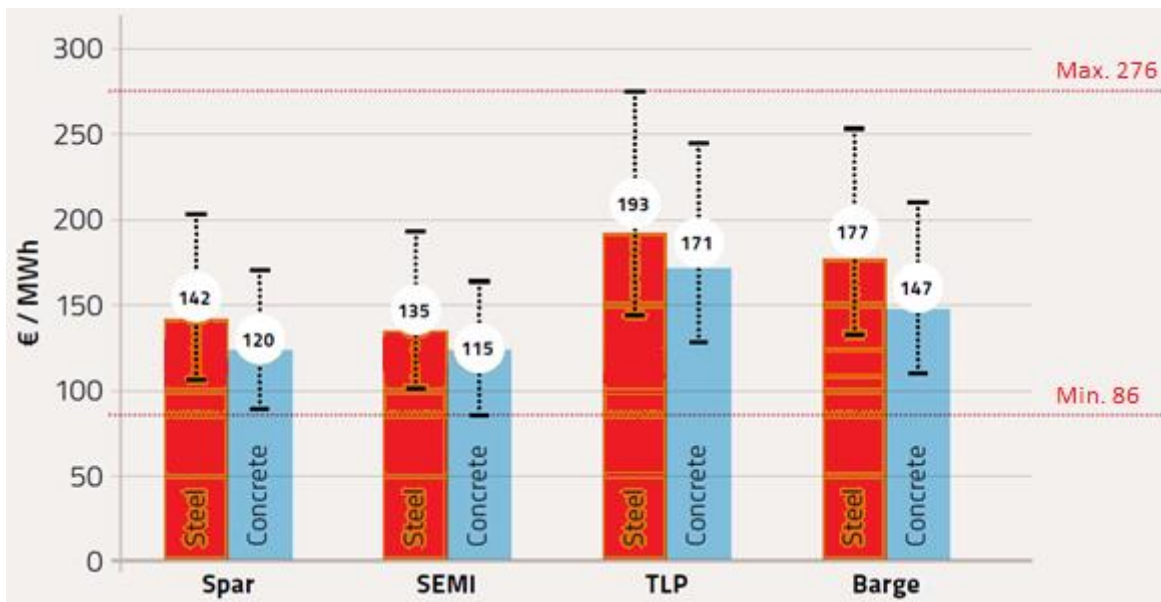
Fig. 1-1: LCOE comparison for FOWT technologies [3]

1.2 Motivation

As it is mentioned in 1.1, when compared to other options, semi-submersible floaters provide numerous benefits. They are weather-resistant, have a big deck space, and are simple to build and install [8, 9]. Natural frequencies of semisubmersibles are inversely proportional to the platform's draft and length [9,

10]. As a result, geometric shape selection is an important consideration in semi-submersible design. Existing semi-submersible wind turbine designs typically employ three columns with one wind turbine on each side, or four columns with one wind turbine in the center [11]. Fig. 1-2 shows various innovative semi-submersible wind turbine concepts.

Offshore substructure design is a complicated process that considers stability, tower tilt, and mooring loads, all of which are influenced by wind, waves, and controller activities [12]. One issue for the Floating Offshore Wind Turbine (FOWT) is to eliminate tower-top vibrations. FOWTs are susceptible to large platform vibrations, which can shorten turbine life and reduce energy output. Waves and wave-induced platform motions cause the top of the tower to oscillate. Optimizing the design of the substructure can improve performance by enhancing hydrodynamic characteristics and reducing motion. FOWTs are also faced with the difficulty of cost reduction.

The cost of the substructures makes a considerable contribution to the entire cost of a FOWT. Using optimization techniques to create hull shape designs for floating wind turbines has proven to be a successful strategy to minimize the cost of these machines [13].

When compared to many common design procedures from commercial software, using open-source tools can provide you greater control over the settings, and more freedom with data processing, however, possibly more man-hours. The open-source tools used in this project are NEMOH, SALOME, and Python.

Fig. 1-2: Innovative concepts of FOWT (left to right), 5-MW-CSC, Nautilus, Olav Olsen OO-Star, UMaine VolturnUS-S [11, 14]

1.3   Scope and objective

The thesis is a continuation of a project assignment completed in the fall of 2021 as part of the master's thesis preparation. The project task was to conduct complete research utilizing open-source technologies to analyze the hydrodynamic performance of a semi-submersible floater (5-MW-CSC) in two different seas states. The goal of this research is to use open-source/commercial programs to optimize the design of a semi-submersible floater (the UMaine VolturnUS-S Reference Platform, see Sec. 3.2) over a grid of

different geometries. The study will examine how changes in geometry affect various performance measures and motion responses in different sea states.

The UMaine VolturnUS-S and the NREL 15 MW Reference Offshore Wind Turbine will be used as baseline designs. The four variables that determine the geometries are the submerged height and diameter of the side columns, side column spacing, and pontoon height. To create the model, simulate the hydrodynamics, and perform post-processing on a semi-submersible floater, open-source tools are employed. The following is the thesis's main goal:

- Using open-source/commercial software, automate the simulation and analysis process
- Investigate the geometries' hydrostatic properties
- Examine the geometries' hydrodynamic performance
- Determine the best design using objective functions and restrictions

The purpose of this thesis is to provide an open-source framework for performance optimization, with a semisubmersible floater serving as a typical support structure for FOWTs. Frequency-domain analysis of the platform response is employed with pre-calculated hydrodynamic parameters, and the performances of numerous geometries are evaluated in terms of material cost and nacelle acceleration. The analysis using the proposed framework might be seen as preliminary research before a comprehensive design optimization.

1.4   Structure of the thesis

A brief description of the chapters in this thesis is presented below:

Chapter 1 An introduction to offshore wind's potential, the current state of floating offshore wind, as well as the thesis's goal, scope, and structure are provided.

Chapter 2 Offers the relevant theory for hydrostatics, hydrodynamics, and wave statistics that are used to arrive at the conclusions in this thesis.

Chapter 3 The baseline design and environmental conditions are presented. It also explains which open-source tools are employed and how they're used to construct an automated optimization process.

Chapter 4 Displays the results of the hydrodynamic evaluation.

Chapter 5 Provides explanations for the optimization framework and methodologies.

Chapter 6 Displays the results of the optimization study.

Chapter 7 Includes a summary of the work as well as suggestions for future research.

2. Theory

This chapter contains the theories and assumptions that the author believes are necessary for a clear understanding of the thesis's work.

2.1 Hydrostatic stability

The starting point of the naval design is stability, which is one of the most important features of offshore engineering. Its goal is to ensure that a vessel will stay afloat in balance and will not heel to the point of breaching water tightness. Stability analysis for commercially manufactured vessels follows widely recognized guidelines. Rules are based on classical rigid body mechanics and rely on the computation of a set of variables that are common to the stability analysis of any floating body. Offshore platforms come in a variety of shapes and sizes: semisubmersible, TLP, Spar... The most prevalent offshore platforms are semisubmersibles. The submerged pontoons and columns beneath the water's surface give buoyancy. As a result, the wave forces acting on the platform are lower than they would be otherwise, resulting in smaller platform motions, which is a desirable outcome.

2.1.1 Gravitational and buoyancy force

The weight of the system and the buoyancy force are balanced to establish floating equilibrium. The buoyancy force is derived from Archimedes' principle, which states that any item partially or completely immersed in a fluid is buoyed up by a force equal to the weight of the fluid displaced by the body. The weight of the displaced volume is calculated by multiplying the volume, the fluid density, and the gravitational acceleration. At this time, mooring forces were not taken into account. The relationship between the buoyancy force FB and the weight of the system FG at equilibrium, which works in opposite directions, is seen in Eq. 2-1:

$$F_B - W = \rho \, g \, \forall \, -mg \, = 0$$

Eq. 2-1

The system's weight is made up of the substructure, which includes steel and ballast materials like water or concrete, as well as the turbine (blades, hub, nacelle, rotor, and tower). Once the total weight is known, it is possible to estimate the submerged volume, knowing that ρ_w is the seawater density is 1025 kg/m3 and g is the gravity acceleration, assumed 9.81 m/s^2.

Mass properties

Ballast water is always evenly distributed at the bottom of the pontoon and side columns to enhance the structure's righting moment. The mass characteristics of the substructure can be computed using the following relationships once these relationships have been defined.

$$m_{total} = m_{steel} + m_{ballast} \qquad \text{Eq. 2-2}$$

2.1.2 Metacentric height

The ability of a system to manage disturbances like waves, currents, and the wind is defined as stability. The metacentric height, abbreviated as GM, is the distance between the center of gravity and the metacenter and is the most important parameter of static stability. A metacentric height of a floating body is depicted in Fig. 2-1. G stands for the center of gravity, B for the center of buoyancy, K for the structure's keel, and M for the metacenter. The metacenter is a made-up point that exists at the junction of the structure's center line with a vertical line drawn from the center of buoyancy.
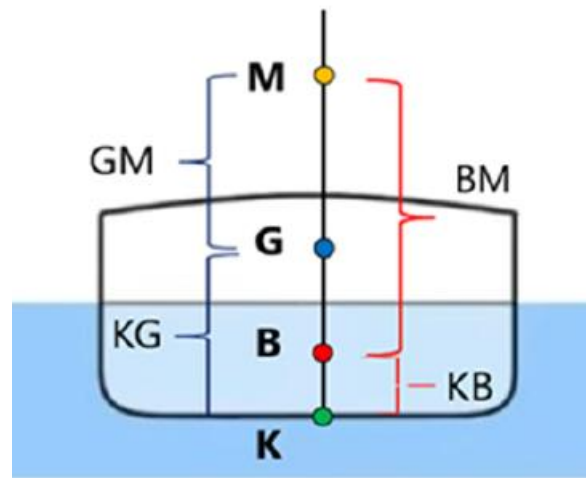
Fig. 2-1: Metacentric height

If the metacentric height is positive, the floating body is characterized by initial static stability and in the presence of disturbing forces, it returns to the original position. On the other hand, if the metacentric height is negative, the structure is not able to return to the original position and continues to turn over. Consequently, the structure is unstable and must be modified. For small heel angles, less than 6 degrees, GM is assumed to be constant and is given by Eq. 2-3:

$$GM = KB + BM - KG \qquad \text{Eq. 2-3}$$

The distance from the metacenter to the COB, also known as the metacentric radius, is given by Eq. 2-4; the distance from the keel to the COB is supplied by KB, and the distance from the keel to the COG is given by KG. The metacentric radius can be computed using the formula:

$$BM = \frac{I}{V} \qquad \text{Eq. 2-4}$$

where I is the second moment of area of the water plane area and V is the structure's displaced volume. Eq. 2-5 gives the second moment of area, also known as the moment of inertia:

$$I = \int_A x^2 \, dA = I_0 + d^2 A \qquad \text{Eq. 2-5}$$

The first term, I, refers to an element's moment of inertia when the reference axis is at its centroid; the second term, Steiner's contribution, refers to the offset between the actual center point and the part under consideration.

2.1.3 Restoring matrix

The restoring matrix includes hydrostatic stiffness C_{hst}:

$$C = C_{hst} \qquad \text{Eq. 2-6}$$

The hydrostatic stiffness matrix describes how the vessel's net weight and buoyancy load (force and moment) change with a heave, roll, and pitch about the vessel's datum configuration. The change in load caused by movement of the vessel's center of gravity and center of buoyancy as it rolls and pitches (often referred to as water plane area effects) and the change in moment caused by movement of the vessel's center of gravity and center of buoyancy as it rolls and pitches both contribute to C_{hst} (moment arm effects).

Only the contributions from the center of buoyancy (CB) and the water plane area should be included in the hydrostatic matrix.

The elements of the hydrostatic restoration forces and moments are such that

$$F_{S_i} = \left(-C_{ij} \cdot X_j(\omega) \right) \quad i,j = 1,2,\cdots,6 \qquad \text{Eq. 2-7}$$

Because the hydrostatic restoring coefficients for horizontal movements are negative,

$$C_{ij} = 0, \; i,j = 1,2,\cdots,6 \qquad \text{Eq. 2-8}$$

Also, C_{ij} can be shown to be the elements of a symmetric matrix, that is, $C_{ij} = C_{ji}$.
The heave restoring force is written as

$$F_{S_3} = -(C_{33}x_3 + C_{34}x_4 + C_{35}x_5) \qquad \text{Eq. 2-9}$$

Where the heave restoring coefficient is given by

$$C_{33} = \rho g A_{wp}, \quad A_{wp} = \sum_{m=1}^{M} A_{wp_m} \quad \left[\frac{N}{m} = \frac{kg}{s^2}\right] \qquad \text{Eq. 2-10}$$

If there is no water plane area, there is no hydrostatic vertical restoration, assuming the body is in equilibrium. The index $m = 1,2, \cdots ,M$ refers to the surface-piercing members only. In other words, if a member is not surface piercing, then it is not included in Eq. 2-10 since a motion in the x3 direction is not going to result in a change in volume (as this would be the case for a completely submerged structure).

The heave-roll restoring coefficient is given by

$$C_{34} = C_{43} = \rho g \iint_{A_{wp}} y \, dS = \rho g \sum_{m=1}^{M} y_m A_{wp_m} \qquad \text{Eq. 2-11}$$

Note that $C_{34} = C_{43} = 0$ if there is symmetry concerning the x–z plane of the platform, and this is common.

On the other hand, the heave-pitch restoring coefficient is given by

$$C_{53} = C_{35} = -\rho g \iint_{A_{wp}} x \, dS = -\rho g \sum_{m=1}^{M} x_m A_{wp_m} \qquad \text{Eq. 2-12}$$

Note that $C_{53} = C_{35} = 0$ if there is symmetry concerning the y–z plane of the platform.

The roll restoring force is written as

$$F_{S_4} = -(C_{43}x_3 + C_{44}x_4 + C_{45}x_5) \qquad \text{Eq. 2-13}$$

where the roll-restoring coefficient C_{44} is given by

$$C_{44} = \rho g \nabla (z_B - z_G) + \rho g \iint_{A_{wp}} y^2 \, dS = -\rho g \nabla \overline{BG} + \rho g \nabla \overline{BM}_T$$

$$= \rho g \nabla \overline{GM}_T = \Delta \overline{GM}_T \quad [Nm/rad] \qquad \text{Eq. 2-14}$$

The roll-pitch restoring coefficient, on the other hand, is given by

$$C_{45} = C_{54} = -\rho g \iint\limits_{A_{wp}} xy \, dS = -\rho g \sum_{m=1}^{M} x_m y_m A_{wp_m} \qquad \text{Eq. 2-15}$$

Note that $C_{45} = C_{54} = 0$ if there is symmetry concerning both the x–z and y–z planes of symmetry.

The pitch-restoring moment is written as

$$F_{S_5} = -(C_{53}x_3 + C_{54}x_4 + C_{55}x_5) \qquad \text{Eq. 2-16}$$

where the pitch-restoring coefficient is given by

$$C_{55} = \rho g \nabla (z_B - z_G) + \rho g \iint\limits_{A_{wp}} x^2 \, dS = -\rho g \nabla \overline{BG} + \rho g \nabla \overline{BM}_L$$

$$= \rho g \nabla \overline{GM}_L = \Delta \overline{GM}_L \ [Nm/rad]$$

$$\text{Eq. 2-17}$$

$$C = \begin{bmatrix} 0 & 0 & 0 & 0 & 0 & 0 \\ 0 & 0 & 0 & 0 & 0 & 0 \\ 0 & 0 & C_{33} & 0 & C_{35} & 0 \\ 0 & 0 & 0 & C_{44} & 0 & 0 \\ 0 & 0 & C_{53} & 0 & C_{55} & 0 \\ 0 & 0 & 0 & 0 & 0 & 0 \end{bmatrix} \qquad \text{Eq. 2-18}$$

The heave, roll, and pitch components of the matrix are the only ones that are stated; the surge, sway, and yaw components are all zero.

In this work due to the simplicity and objective of the thesis, the mooring stiffness is neglected.

2.1.4 Mass matrix

The mass matrix M for 6 DOF can be written as:

$$M = \begin{bmatrix} m & 0 & 0 & 0 & 0 & 0 \\ 0 & m & 0 & 0 & 0 & 0 \\ 0 & 0 & m & 0 & 0 & 0 \\ 0 & 0 & 0 & I_{44} & 0 & -I_{46} \\ 0 & 0 & 0 & 0 & I_{55} & 0 \\ 0 & 0 & 0 & -I_{46} & 0 & I_{66} \end{bmatrix} \qquad \text{Eq. 2-19}$$

The I-terms are the mass moments of inertia, and m is the dry mass of the body.

2.2 Motion response in waves

The sum of the wave excitation forces, added mass force, and damping forces applied on the floating structure (Eq. 2-20) determines the hydrodynamic forces acting on it.

$$F_{float} = F_{fk} + F_{diff} + F_{add} + F_{damp}$$

Eq. 2-20

F_{float} equals the sum of the hydrodynamic forces acting on the floating collar, F_{fk} equals Froude-Krylov force, F_{diff} equals diffraction force, F_{add} equals increased mass force, and F_{damp} equals damping force. Froude-Krylov and diffraction forces are the pressure forces exerted on the body by the oscillating flow. The Froude-Krylov force is the pressure force produced by an undisturbed oscillating flow caused by a wave passing over the wetted surface of the floater, and the diffraction is the correction of the Froude-Krylov force because the flow is disturbed by the presence of the body.

2.2.1 Motions and degrees of freedom

Motions

These motions are estimated around the system's Center of Gravity (COG). The following are the responses in regular waves, according to Linear Wave Theory (LWT):

$$z = z_a \cos(\omega t + \varepsilon_{z\zeta})$$

Eq. 2-21

Where z_a is the heave response amplitude and $\varepsilon_{z\zeta}$ is the phase shift between wave elevation and heave displacement of the vessel's COG. This degree of freedom's related velocity and acceleration are as follows:

$$\dot{z} = -\omega z_a \sin(\omega t + \varepsilon_{z\zeta})$$

Eq. 2-22

$$\ddot{z} = -\omega^2 z_a \cos(\omega t + \varepsilon_{z\zeta})$$

Eq. 2-23

The equation of motion of the system can be written as:

$$(m + a)\ddot{z} + b\dot{z} + cz = F(t)$$

Eq. 2-24

Eq. 2-24 is then used to find the response amplitude operator (RAO).

Degree of freedom

The motions of the floating structure are defined as follows:

- Three translations of the ship's center of gravity (CoG) in the direction of the x-, y-, and z-axes:

– the surge in the longitudinal x-direction, positive forwards
– sway in the lateral y-direction, positive to the port side
– heave in the vertical z-direction, positive upwards

- Three rotations about these axes:

– roll about the x-axis, positive right turning
– pitch about the y-axis, positive right turning
– yaw about the z-axis, positive right turning

Fig. 2-2 shows the degrees of freedom of the UMaine VolturnUS-S Reference Platform.
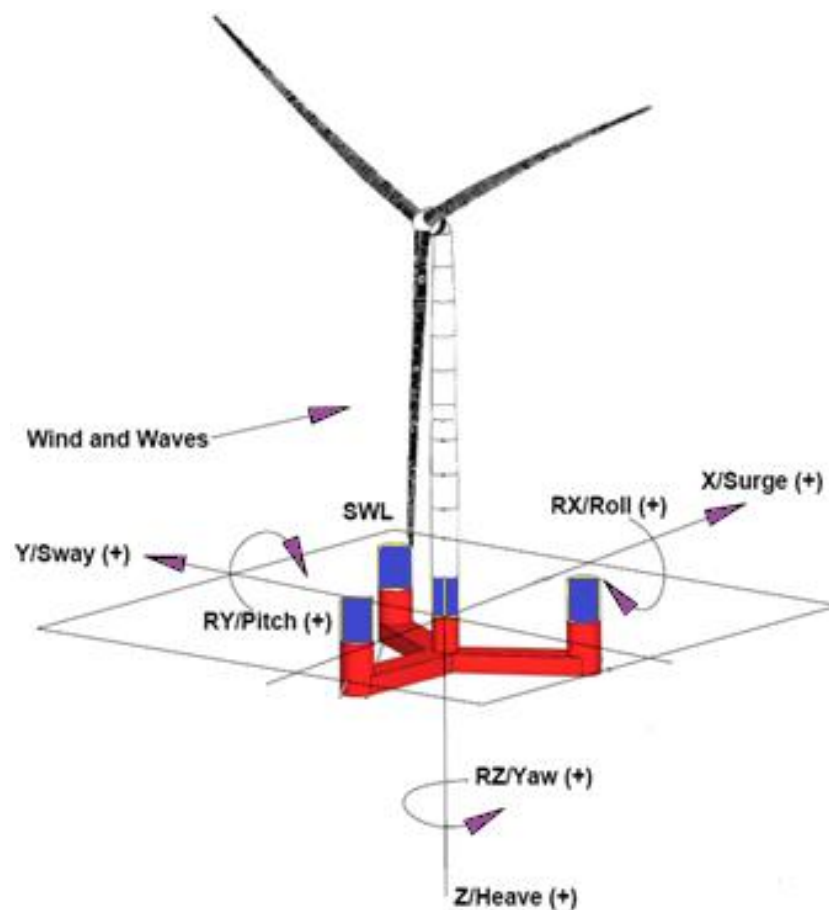
Fig. 2-2: Floating offshore wind turbine degrees of freedom [14]

2.2.2 Response Amplitude Operators (RAO)

Floating substructure motions are typically calculated initially in the Frequency Domain (FD), which gives a decent first estimate of motion behavior (see 2.2.8). Wave forces, added mass, and potential damping coefficients are all wave frequency-dependent terms that are defined in (2.2.4). The motion amplitude, such as heave z_a and phase shift $\xi_{z\zeta}$ can then be written in proportion to the wave amplitude ζ_a. Response Amplitude Operators (RAOs) are transfer functions that define the first-order motion of a vessel in response to waves of a specific period and amplitude. The potential theory is used to locate them. The phase determines the phase lag from the time the wave crest crosses the RAO origin until the maximum positive excursion is reached ($\mathcal{E}_{z\zeta_a}$), and the amplitude links the amplitude of the vessel motion to the amplitude of the wave ($^{z_a}/_{\zeta_a}$).

The quantity and phase of the force (surge, sway, heave) or moment (roll, pitch, yaw) ($^{F_a}/_{\zeta_a}$) RAOs are determined by evaluating the dynamic behavior of a vessel as a result of an incoming harmonic wave. The displacement RAOs for the six DOF can be obtained by solving the following relation for X_j:

$$\left\{ -\omega^2 \cdot \left(M_{ij} + A_{ij}(\omega) \right) + i\omega \cdot B_{ij}(\omega) + C_{ij} \right\} \cdot X_j(\omega) = F_i(\omega) \quad for\ i$$
$$= 1 \cdots 6$$

Eq. 2-25

$$RAO(\omega) = \frac{\hat{F}(\omega)}{\left\{ -\omega^2 \cdot \left(M + A(\omega) \right) + i\omega \cdot \left(B(\omega) \right) + C \right\}}$$

Eq. 2-26

where,

M – is a matrix of the structure's mass and inertia around the COG of the system

A – is a matrix of hydrodynamic added mass

B – is a matrix of radiation damping

$\hat{F}$ – is a complex amplitude of the wave excitation force acting on the structure per unit wave amplitude

C – is a matrix stiffness

The right-hand side of the Equation of Motion (EOM) is made up of a wave of exciting forces and moments that come in on the confined body around the COG. After the RAOs have been calculated, the motion response spectra are derived. Using a particular wave spectrum and RAO of a floating structure, the following motion responses can be calculated:

$$S_i(\omega) = \int_{-\pi}^{\pi} S_\zeta(\omega) \cdot RAO_i(\omega)^2 \, d\omega$$

Eq. 2-27

The DOF is denoted by the subscript i the response spectrum by S_i, and the wave spectrum by S_ζ. The parameters of the RAO can have a considerable impact on whether or not the floating structures can operate in particular sea states. As they approach shallower water, incoming waves may change

direction (concerning the above deep water equations). The hydrodynamic coefficients in A_{ij} and B_{ij} may alter due to shallow water.

These hydrodynamic coefficients and their sensitivity to shallow water circumstances are discussed in the following sections. Initially, the wave stimulating forces are described as an external component that creates motions.

2.2.3 Natural Frequencies

Eq. 2-28, which considers the system's restoring and inertial qualities, can be used to derive the natural frequency of the combined wind turbine and floating platform system.

$$\omega_i = \sqrt{\frac{C_{ii}}{M_{ii} + A_{ii}(0)}} \qquad \text{Eq. 2-28}$$

Where the subscript i indicates the mode of motion, and $A_{ii}(0)$ indicates the zero-frequency limit of the added mass in that mode.

In weakly recovered modes of motion, the natural frequency will be considered to be zero. Cross-coupling, on the other hand, permits other kinds of motion to pick up a natural frequency. The natural frequencies can be graphically determined in this circumstance by looking at the frequency at which the RAO peaks.

2.2.4 Forces and moments

Wave exciting forces are those that are imposed on a body as a result of water waves' unequal fluid pressure, preventing it from moving. The integration of pressure on the submerged section of the body S_H generates the Froude-Krylov (FK) and diffraction forces. The first-order velocity potential $\Phi^{(1)}$ of a structure subjected to linear waves can be expressed as the sum of the velocity potentials at each ω:

$$\Phi^{(1)}(x,y,z,t) = Re\left[\sum_{j=1}^{6} \phi_j\, e^{\omega_j t}\right] \qquad \text{Eq. 2-29}$$

The lower case velocity potential's space-dependent component ϕ_j belongs to a single frequency ω_j. The potential is divided into three pieces under the LWT assumption: the undisturbed incoming wave potential Φ_I, the radiation potential Φ_R, and the diffraction potential Φ_D [15]:

$$\Phi = \Phi_I + \Phi_D + \Phi_R \qquad \text{Eq. 2-30}$$

Substituting it to the equation

Eq. 2-31

$$\Phi(X,Y,Z)\, e^{-i\omega t} = \left[(\Phi_I + \Phi_D) + \sum_{i=1}^{6} \Phi_j x_j \right] e^{-i\omega t}$$

The incident wave potential Φ_I, which is used to represent the flow of the undisturbed arriving waves, characterized the FK forces. The diffraction potential, written as Φ_D, is used to illustrate how a body in the flow might produce flow disturbances. It describes the incoming waves' overall potential, Φ_W, when added to the undisturbed wave potential. The radiation potential Φ_R, which is computed for oscillation in still water [16] and exists for each of a body's six degrees of freedom in waves, is calculated for each of a body's six degrees of freedom in waves.

The diffraction problem

The body's kinematic boundary condition must be zero when considering a watertight body. The potentials Φ_I and Φ_D for undisturbed wave and diffraction potentials can be written in space and time-dependent parts:

$$\Phi_I = Re\{\emptyset_W \cdot i\omega\zeta_a e^{i\omega t}\} \qquad\qquad \text{Eq. 2-32}$$

$$\Phi_D = Re\{\emptyset_D \cdot i\omega\zeta_a e^{i\omega t}\} \qquad\qquad \text{Eq. 2-33}$$

With the space-dependent part:

$$\Phi_W = \frac{\zeta_a g}{\omega^2}\, e^{kz}\, e^{i(kx\,\cos\mu\, +\, k\mu\sin\mu)} \qquad\qquad \text{Eq. 2-34}$$

where x is the space-dependent part.

The diffraction potential is determined via NEMOH diffraction analysis. The incoming wave potential Φ_I and the radiation potential $\emptyset_R$ are the only two factors that influence the diffraction potential. The pressures due to incoming and diffracted waves are then calculated using Φ_I, which ultimately describes total wave forces by Eq. 2-32. The forces and moments on the body include radiation forces F_R.

$$F_D + F_W = -\iint_{S_H} (p \cdot \vec{n}_k)\, dS = \rho\omega^2\, \zeta_a e^{i\omega t} \int_S (\Phi_W + \Phi_D)\, dS_H \qquad \text{Eq. 2-35}$$

$$\vec{M} = -\iint_{S_H} p \cdot (\vec{r} \times \vec{n})\, dS_H \qquad\qquad \text{Eq. 2-36}$$

In which $\vec{n}$ is the surface's outward normal vector and $\vec{r}$ is the coordinate system's position vector for surface dS_H. The second-order elements in the above equation are neglected in the Linear Wave Theory (LWT) since the wave's steepness is considered minimal. The pressure created by water waves is then:

$$p = -\rho \frac{\partial \Phi}{\partial t} - \rho g z = -\rho \left(\frac{\partial \Phi_I}{\partial t} + \frac{\partial \Phi_R}{\partial t} + \frac{\partial \Phi_D}{\partial t} \right) - \rho g z \qquad \text{Eq. 2-37}$$

$$p = -\rho g z + \rho g \zeta_a \cdot \frac{\cosh k(d+z)}{\cosh kd} \cdot \cos(kx - \omega t) \qquad \text{Eq. 2-38}$$

The hydrodynamic loads must be taken into account when calculating body forces and moments in waves. As seen in the diagram, pressure is separated into four components (Eq. 2-24). As a result, the forces and moments $\vec{F}$ and $\vec{M}$ are split into four sections:

$$F_{total} = F_I + F_D + F_S + F_R \qquad \text{Eq. 2-39}$$

- F_I : hydrodynamic forces and moments on the body due to undisturbed incoming wave
- F_D: hydrodynamic forces and moments due to the diffracted waves
- F_S: hydrodynamic forces and moments due to hydrostatic buoyancy and loads due to
- changes in water plane area
- F_R: hydrodynamic forces and moments due to radiating waves from the oscillating body

Diffraction analysis is used to calculate the displacement and load RAOs of incoming wave loads. This load RAO describes the wave exciting force on the vessel:

$$F_W = F_{A,\zeta_a} \cdot \zeta_a \cos(\omega t - \varepsilon_{F,\zeta}) \qquad \text{Eq. 2-40}$$

Where F_{A,ζ_a} is the load RAO amplitude at ω and ζ_a is the incoming wave amplitude.

The radiation problem

As a result of the incoming wave forces, the floating structures will oscillate, causing waves to radiate from the body. The associated force in six degrees of freedom can be expressed using the radiation force F_R. These radiation forces contain the coefficients of added mass and potential damping, A_{ij} and B_{ij}. Added mass is the increased force necessary to accelerate the fluid particles around the vessel when compared to oscillation in air, and potential damping is the damping caused by the production of waves by the vessel's oscillation, which drains energy from the vessel's motions [16]. These terms are shown in the A_{ij} and B_{ij} as functions of oscillation frequency, as shown in Eq. 2-43.

Additional mass and potential damping are greatly influenced by the vicinity of the seabed and the more intense free surface oscillations in shallow water [15]. In vertical modes of motion, the impacts are very obvious. A considerable increase in extra mass, according to research, produces a fundamental shift in motion behavior [17]. Several of the mechanisms discussed in Chapter 2 can make an accurate prediction of these coefficients problematic, limiting the scope of a thorough analysis of floating bodies in waves [15].

In the case of damping, potential damping may not be enough, and an additional damping term may be necessary. This is especially true near resonance because, at these frequencies, the damping factor dominates the equation of motion [16].

The determination of the hydrodynamic coefficients is explained in the following section.

Added Mass and Potential Damping

The precision of A_{ij} and B_{ij} affects numerical models of vessel motions directly. Hydrodynamic pressure can be computed using the linearized Bernoulli equation, and the pressure distribution on the hull can then be utilized to derive the additional mass and potential damping terms. The radiation potential Φ_R can be written in the potential for each DOF:

$$\frac{\partial \Phi}{\partial n} = \sum_{j=1}^{6} v_j \, f_j(x,y,z) \quad with \quad f_j = \frac{\partial \emptyset_j}{\partial n} \qquad \text{Eq. 2-41}$$

The mean wetted component S_H of the hull, which reflects a distribution of source singularities, is approximated using panel elements. These sources have an impact on the velocity potential, which describes the flow at every point in the domain. The total radiation force F_R on S_H is obtained by integrating the pressure:

$$F_R = \iint_{S_H} (p \, n_k) \, dS = \rho \iint_{S_H} \left(\frac{\partial \Phi_R}{\partial t}\right) \vec{n} \, dS_H \qquad \text{Eq. 2-42}$$

The partial surface elements' direction cosines are included in the $\vec{n}$ matrix. It should be noted that the EOM can characterize the forces and moments that make up the Φ_R the solution in terms of added mass and potential damping:

$$M_{ij} \cdot \ddot{X}_j(\omega) = F_{W_i} + F_{D_i} + \left(-C_{ij} \cdot X_j(\omega)\right)$$
$$+ \left(-A_{ij}(\omega) \cdot \ddot{X}_j(\omega) - B_{ij}(\omega) \cdot \dot{X}_j(\omega)\right) \qquad \text{Eq. 2-43}$$

In which the following can be recognized:

$$F_{S_i} = \left(-C_{ij} \cdot X_j(\omega) \right) \qquad \text{Eq. 2-44}$$

$$F_{R_i} = \left(-A_{ij}(\omega) \cdot \ddot{X} \right) j(\omega) - B_{ij}(\omega) \cdot \dot{X}_j(\omega) \qquad \text{Eq. 2-45}$$

The only unknown is the radiation potential's space-dependent term $\emptyset_j$. The panel method can be used to figure out potential $\emptyset$. To use for calculations in this way, S_H is approximated by a large number of panel elements. A_{ij} and B_{ij} should be estimated after finding Φ_R for each of the six DOF:

$$\iint_{S_H} \left(\rho \, \frac{\partial \Phi_j}{\partial t} \cdot n_i \right) dS_H = -A_{ij} \ddot{X}_j - B_{ij} \dot{X}_j \qquad \text{Eq. 2-46}$$

$$A_{ij} = Re \left\{ -\rho \iint (\emptyset_j \cdot n_i) \, dS_H \right\} \qquad \text{Eq. 2-47}$$

$$B_{ij} = -\omega \, Im \left\{ -\rho \iint (\emptyset_j \cdot n_i) \, dS_H \right\} \qquad \text{Eq. 2-48}$$

These coefficients A_{ij} and B_{ij} are sensitive to water depth in shallow water. As the bottom gets closer, the most severe changes in hydrodynamics will influence the vertical DOF [18]. The heave added mass and pitch added mass is underestimated by linear radiation-diffraction estimates when viscosity is ignored.

The mass displacement of the body in issue determines the additional mass. The added mass is proportional to the displacement. Though it is easy to confuse it with buoyancy forces, it is vital to understand that buoyant forces are constant characteristics of a floating body that are solely determined by the shape and fluid density of the body. In other words, it is a hydrostatic effect. This is not related to increased mass, which is a hydrodynamic process involving finite-sized floating bodies surging at a given speed in the water. The added mass is determined for symmetric bodies like cylinders and cubes by multiplying the displaced volume by the fluid density. Due to the intricate geometric design of a floating object, the new mass is computed using the displaced water plus some extra fluid in its wake.

2.2.5 Wave Spectrum

There are a lot of wave crests and troughs on the ocean surface, and it appears to be a completely random process. Wave spectra are used to characterize the sea as a series of regular waves to formalize this. The shape of regular waves is determined by their time, which assures that each cycle is identical [3]. Regular waves of varying amplitudes, wavelengths, and phase angles represent the sea surface. To establish the wave spectrum, it is necessary to first evaluate a wave record. That is, the elevation of the surface $\zeta(t)$ at a particular location as a function of time during a certain time interval t_d. It is feasible to perfectly recreate that record as the sum of a large number of harmonic wave components:

$$\zeta(t) = \sum_{i=1}^{N} \zeta_{a_i} \cdot \cos(2\pi f_i t + \alpha_i)$$ <div style="text-align:right">Eq. 2-49</div>

where,

ζ_{a_i} = amplitude of the i − th component

α_i = phase of the i − th component

$f_i = \dfrac{i}{t_d} \cdot$ frequency of the i − th component. The frequency interval is then $\Delta f = \dfrac{1}{t_d}$

JONSWAP spectrum

The Joint North Sea Wave Project (JONSWAP) was established towards the end of the 1960s to record oceanic waves along a line reaching over 100 miles into the North Sea. For fetch-limited (or coastal) wind-generated seas, analysis of the data yielded the following spectral formulation [16]:

$$S_\zeta(\omega) = \frac{320 \cdot H_s^2}{2} \cdot \omega^{-5} \cdot exp\left(\frac{-1950}{T_p^4} \cdot \omega^{-4}\right) \cdot \gamma^A$$ <div style="text-align:right">Eq. 2-50</div>

where

γ = peakness factor = 3.3

$$A = exp\left[-\left(\frac{\frac{\omega}{\omega_p} - 1}{\sigma\sqrt{2}}\right)^2\right]$$

T_p − peak period of the spectrum

$\omega_p = \dfrac{2\pi}{T_p}$. the circular frequency at spectral peak

σ = a step function of ω:

if $\omega < \omega_p$ then: $\sigma = 007$, if $\omega > \omega_p$ then: $\sigma = 0.09$

JONSWAP spectrums for different environmental conditions are shown in Fig. 3-3.

2.2.6 Response in irregular waves and nacelle motions

In the previous sections, different versions of the EOM in regular waves were discussed. Solving those equations yields the RAO for each DOF. In this part how the RAOs are changed to get the floating body's response in irregular waves are discussed. The heave motion spectrum can be defined as:

$$S_z(\omega) \cdot d\omega = \frac{1}{2} Z_a^2(\omega)$$ <div style="text-align:right">Eq. 2-51</div>

Second, this equation is multiplied and divided by ζ_a^2, obtaining:

$$S_z(\omega) \cdot d\omega = \left| \frac{Z_a}{\zeta_a}(\omega) \right|^2 \frac{1}{2} \zeta_a^2 \qquad \text{Eq. 2-52}$$

$$S_z(\omega) = \left| \frac{Z_a}{\zeta_a}(\omega) \right|^2 S_\zeta(\omega) \qquad \text{Eq. 2-53}$$

where,

$$\left| \frac{Z_a}{\zeta_a}(\omega) \right| = RAO_3 \qquad \text{Eq. 2-54}$$

These equations apply to all RAOs. That is, they are also employed in the current work with the RAOs in surge and pitch (RAO_1 and RAO_5), as well as the RAO for horizontal nacelle acceleration ($\text{RMS}_{a_{nac}}$).

Nacelle motions

Wave energy spectra and response amplitude operators can be used to find response spectra that characterize platform motion under various wave conditions. The response spectrum, S_R, can be computed using Eq. 2-55, where $S_\zeta(\omega)$ is the wave energy spectrum [19].

$$S_R(\omega) = \left| RAO_{a_{nac}} \right|^2 S_\zeta(\omega) \qquad \text{Eq. 2-55}$$

The moments of the response spectra can be calculated using Eq. 2-56, where $i = 0$ defines the amplitude of motion, $i = 2$ defines the velocity, and $i = 4$ defines the acceleration [20].

$$m_{R.i} = \int_0^\infty |\omega|^i \, S_R(\omega) \cdot d\omega \qquad \text{Eq. 2-56}$$

The root mean square (RMS) value is equal to the square root of the response spectrum's moment, which is equal to the variance, $\sigma_{R.i}{}^2$. As a result, Eq. 2-57 is used to get the RMS value of the nacelle pitch amplitude, and Eq. 2-58 is used to find the RMS values of the nacelle lateral and vertical acceleration.

$$Amplitude_{RMS} = \sqrt{m_{R.0}} = \sqrt{\int_0^\infty S_R(\omega) \cdot d\omega} \qquad \text{Eq. 2-57}$$

$$Acceleration_{RMS} = \sqrt{m_{R.4}} = \sqrt{\int_0^\infty |\omega|^4 \cdot S_R(\omega) \cdot d\omega} \qquad \text{Eq. 2-58}$$

2.2.7 Viscous damping

Computer programs that only use linear wave theory to estimate hydrodynamic responses fail to calculate adequate vessel responses [16]. The biggest damping source for semi-submersibles is viscous damping from flow separation. It can usually be well simulated using the Morison equation [21] if the drag coefficients are properly calibrated. In frequency-domain analysis, the viscous damping force is generally linearized by multiplying a similar linear damping coefficient, B^{vi}, by the velocity in the corresponding degree of freedom:

$$F_{vis} = B^{vi} * \dot{x}$$

Eq. 2-59

Depending on the sea conditions, the comparable damping coefficient for Morison-type drag forces is proportional to the root-mean-square (RMS) of the associated velocity. The viscous damping in pitch for each shape is studied in this study, and the RMS pitch velocity is calculated at various sea conditions using:

$$RMS_{\dot{x}_{55}} = \sqrt{\int_0^\infty \omega^2\, S_{x_{55}}(\omega)\, d\omega}$$

Eq. 2-60

where,

$S_{x_{55}}(\omega)$ is the spectral density of the pitch motion for corresponding sea states.
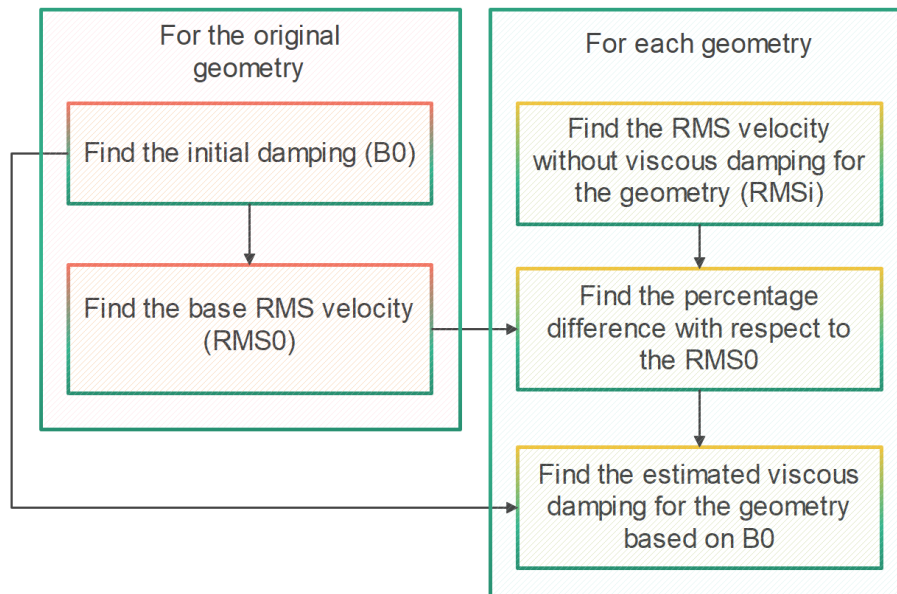

Fig. 2-3: Flowchart of the viscous damping estimation [22]

An iterative approach is used to calculate the equivalent damping coefficients for various geometries and sea states. First, for the baseline geometry, reference damping coefficients [14] from Table 2-1 are utilized to account for viscous effects by tuning the RAOs and comparing them to previous studies (see

Fig. 3-6 and 3-7). This initial damping coefficient correlates to the baseline geometry's initial RMS velocity. Then, using the same initial damping coefficient, a new RMS velocity is derived for different geometries at different sea states. As a result, the equivalent damping is changed to match the current RMS velocity. This method is repeated until the RMS velocity is equal. A flowchart of how the viscous damping is determined in this thesis is shown in Fig. 2-3.

Table 2-1: Viscous damping matrix

	Surge	Sway	Heave	Roll	Pitch	Yaw
Surge	9.225E+05	0	0	0	-8.918E+06	0
Sway	0	9.225E+05	0	8.918E+06	0	0
Heave	0	0	2.296E+06	0	0	0
Roll	0	8.918E+06	0	16.76E+10	0	0
Pitch	-8.918E+06	0	0	0	1.676E+10	0
Yaw	0	0	0	0	0	4.798E+10

In [14], the viscous damping model was estimated using OpenFOAM, an open-source computational fluid dynamics system, and notably SimpleFoam, its steady-state, incompressible solver.

Using B^{vi} for the viscous damping terms, the Eq. 2-25 can be written as:

$$RAO(\omega) = \frac{\hat{F}(\omega)}{\left\{-\omega^2 \cdot \left(M + A(\omega)\right) + i\omega \cdot \left(B(\omega) + B^{vi}\right) + C\right\}} \qquad \text{Eq. 2-61}$$

where,

M – is a matrix of the structure's mass and inertia around the COG of the system
A – is a matrix of hydrodynamic added mass
B – is a matrix of radiation damping
$\hat{F}$ – is a complex amplitude of the wave excitation force acting on the structure per unit wave amplitude
C – is a stiffness matrix

2.2.8 Frequency domain analysis

The dynamics of a floating structure may be anticipated by multiplying the sum of forces acting on the structure by the product of acceleration and inertia. All forces are assumed to vary linearly with wave height and period in the most basic version of this analysis, which is typically the case for long-period waves. The potential theory is a Frequency Domain (FD) based model of vessel motions that are based on assumptions from Linear Wave Theory (LWT). The hydrodynamic coefficients a_{ij} and b_{ij} are dependent on and have a linear relationship with wave amplitude ζ. In irregular waves, the superposition idea can be utilized to determine a body's response. All motions and pressures oscillate

at the same frequency as the incoming waves, and a system's behavior in the presence of numerous wave frequencies is the sum of its behavior at each frequency, according to linearized frequency domain analysis. Under these assumptions, differential equations of motion become algebraic equations that are easily solved. A complex amplitude, which is the amplitude and phase of a sinusoidal motion, is used to represent each variable quantity.

3. Numerical model setup

The purpose of this chapter is to discuss the aspects of the baseline design, ballasting effects, and the environmental conditions. The variables, constraints, objective functions, simplifications, and assumptions used in the thesis are also extensively explained. Finally, numerical techniques, open-source applications, and verification of the results will be discussed.

3.1 Reference Wind Turbines

Reference wind turbines are very important in the wind energy industry. They serve as openly available benchmarks for experimenting with new technologies and designs, as well as encouraging collaboration between researchers and industry [14]. The National Renewable Energy Laboratory (NREL) designed a three-bladed 15 MW reference offshore wind turbine for the braceless semi-submersible substructure investigation, which is used in this thesis. Table 3-1 shows the properties of the Reference Wind Turbine.

Table 3-1: NREL 15MW Reference Wind Turbine properties [23, 24, 25]

Property	Unit	Value
Rotor and Hub mass	kg	385000
Nacelle mass	kg	632000
Tower mass	kg	860000
Wind turbine (WT) Center of Gravity (COG) above SWL	(m,m,m)	(0,0,56.5)
The total mass of WT	kg	1877000
Total WT mass moment of inertia about X-axis (Ixx)*	$kg \cdot m^2$	6.474e9
Total WT mass moment of inertia about Y-axis (Iyy)*	$kg \cdot m^2$	6.474e9
Total WT mass moment of inertia about Z-axis (Izz)*	$kg \cdot m^2$	3.532e8
Rated wind speed	m/s	11.4
Turbine thrust	KN	1800
Tower base interface above SWL (freeboard)	m	15

* - with respect to the COG of the wind turbine

3.2 Platform structure

The UMaine VolturnUS-S reference platform [14] was chosen for this research. The reference platform in this study is a four-column steel semisubmersible, and its general parameters, such as system mass, dimensions, center of gravity and buoyancy, and inertias, are listed in Table 3-2. The hull arrangement, as shown in Fig. 3-1, consists of three 12.5-m-diameter buoyant columns radially separated with centers 51.75 m from the tower's vertical axis. The platform-tower interface is positioned atop a fourth buoyant column in the surge-sway plane at the platform's center. Three 12.5-m-wide by 7.0-m-high rectangular bottom pontoons connect this core column to the outside columns.
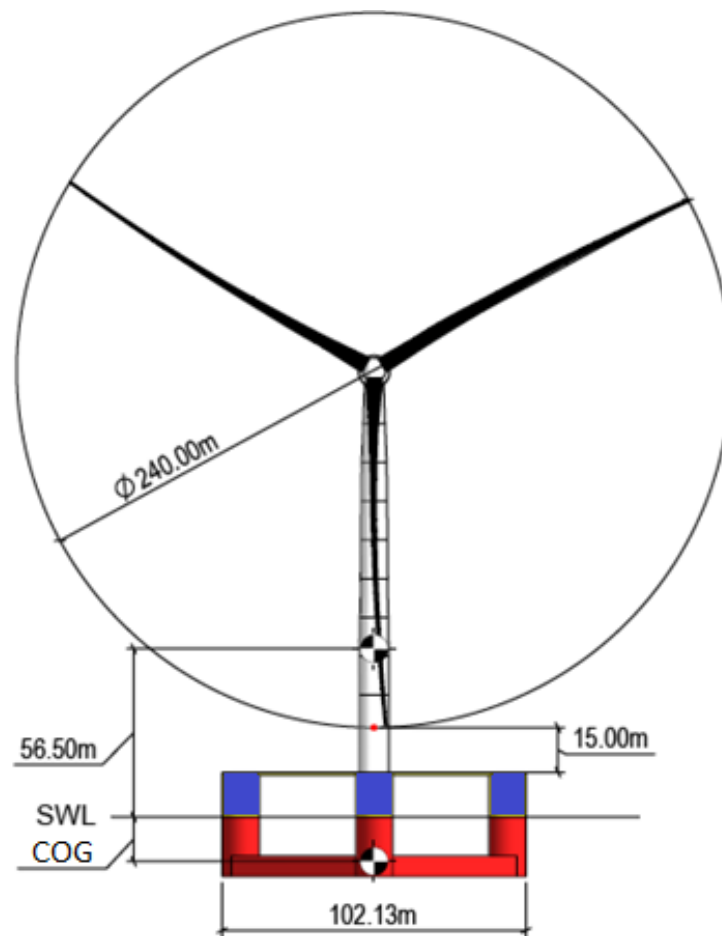

Fig. 3-1: General arrangement of the UMaine VolturnUS-S reference platform [14]

Table 3-2: The UMaine VolturnUS-S reference platform with and
without wind turbine properties [14, 25]

Parameter	Units	Value
Platform		
Hull displacement	m^3	20206
Hull steel mass	t	3914
Tower interface mass	t	100
Ballast mass (Fixed/Fluid)	t	2541/11300
Draft	m	20
Freeboard	m	15
Hub height	m	150
The vertical center of gravity from SWL	m	-14.94
The vertical center of buoyancy from SWL	m	-13.63
Roll inertia about the center of gravity	$kg \cdot m^2$	1.251E+10
Pitch inertia about the center of gravity	$kg \cdot m^2$	1.251E+10
Yaw inertia about the center of gravity	$kg \cdot m^2$	2.367E+10
The system of platform and wind turbine		
The vertical center of gravity of the system from SWL	m	-2.234
Roll inertia of the system about the center of gravity	$kg \cdot m^2$	4.457E+10
Pitch inertia of the system about the center of gravity	$kg \cdot m^2$	4.449E+10
Yaw inertia of the system about the center of gravity	$kg \cdot m^2$	2.394E+10

The platform material cost has been calculated considering a steel thickness of 3 mm on all platform
walls.

3.3 Ballasting system

The required water ballast mass is added inside the pontoons and three side columns. The SALOME-
Python interface was used to perform the stability analysis. It should be noted that the additional ballast
mass will be placed in the three side columns if the pontoons are filled with water. The additional
required ballast mass is added to the semisubmersible platform's side columns shifting both the center
of gravity (COG) and the center of buoyancy (COB) to a higher level. A flowchart for estimating
ballasting is shown in Fig. 3-2.

It should be noted that the 'DEL' parameter represents the difference between the required ballast
volume and the pontoon's internal volume. The presence of a positive 'DEL' indicates that the pontoon

is full of ballast water and that the side columns should help with ballasting. When 'DEL' is negative, the Python script considers the ballast volume to be the same as the pontoon's internal volume. The height of the ballast water in the side columns is referred to as ballast height.
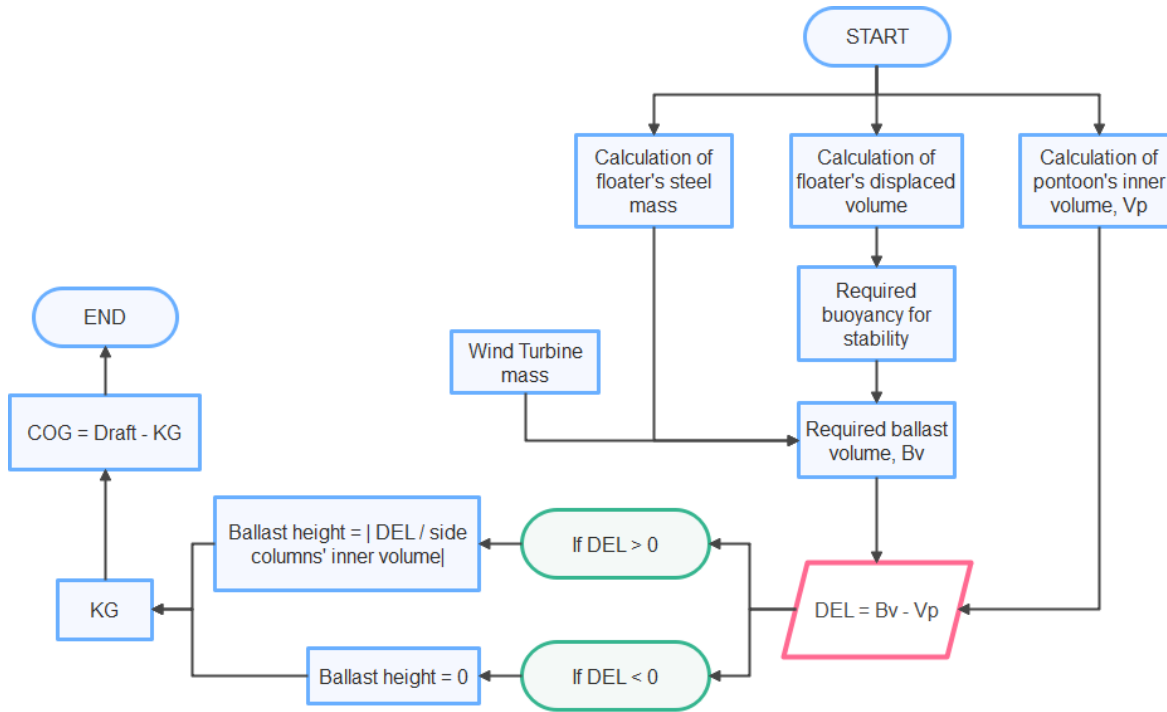
Fig. 3-2: Ballasting estimation flowchart

3.4 Environmental conditions

Appropriate environmental conditions must be used to study the floater's dynamic response. This study uses combined data from the North Sea for wind and waves [26]. For the years 2001 and 2010, the environmental data is based on hourly samples from a hindcast model. The environmental conditions in this investigation are listed in Table 3-3. The U_w varies from the cut-in wind speed (3 m/s) to the extreme wind speed at the reference site at the hub height (90 m). The analysis also takes into account the rated wind speed (11.4 m/s). The corresponding H_s for each U_w is chosen as the most probable value from the conditional distribution of H_s given U_w, while the T_p values are the most probable values from the conditional distribution of T_p given both U_w and H_s [26]. Fig. 3-3 shows JONSWAP spectrums for various environmental conditions.

Table 3-3: Environmental conditions

EC	Mean wind speed (m/s)	H_s (m)	T_p (s)
1	3	1.46	10.91
2	11.4	2.59	10.18
3	24	6.14	11.22
4	25	6.51	11.34
5	31.2	15.6	14.5

EC1 is a mild condition and the cut-in wind speed is considered.

EC2 is situated at the rated wind speed.

EC3 and EC4 have above-rated wind speeds. The maximum thrusts are less than that for EC2. U_w in EC4 corresponds to the cut-off wind speed. The wave spectrum for this spans a much larger frequency range than compared to the previous ECs.

EC5 is the extreme case, where the wind speed corresponds to 50 year return period. The rotor is parked in this condition.

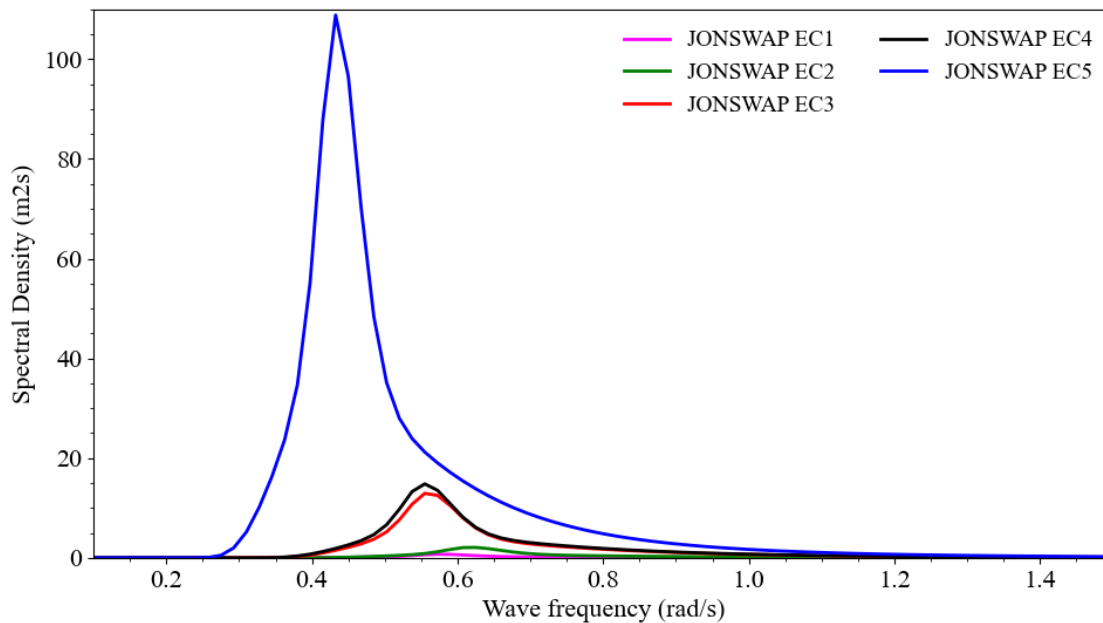Fig. 3-3: JONSWAP spectrums for environmental conditions

3.5 Open-source and commercial programs

The numerical methods used to automate, sample, and analyze the data in this thesis are explained in this section. It' should be noted that the author's Python scripts are used for all of the calculations. The hydrodynamic coefficients are calculated using NEMOH. The hydrodynamic parameters of added

mass, radiation damping, and wave excitation force are all determined using NEMOH. Python is used to calculate hydrostatic properties, hydrodynamic responses, environmental conditions, optimization techniques, and Pareto fronts. The mesh model is created with SALOME.

SALOME

SALOME [27] is a free and open-source numerical simulation program that may be used for both pre- and post-processing. It is based on an open and flexible reusable component-based architecture. SALOME can be used independently to create CAD models, prepare them for numerical calculations, and post-process the results. SALOME can also be used as a framework for integrating third-party numerical codes to construct a new application for managing CAD models during their entire life cycle.

NEMOH

NEMOH [28] is a free and open-source Boundary Element Method (BEM) solver. The BEM method, also known as the panel approach, employs Green's functions to transform a flow problem into a source distribution problem over the body surface. The radiated velocity potentials are then used to determine the wave excitation forces, added mass, and radiation damping terms. The sea depth and wave direction are both assumed to be 200 meters and zero degrees, respectively. Before calling NEMOH, the surface of each geometry is built and discretized in SALOME. SALOME meshes are converted to NEMOH format before being exported. The NEMOH input files are updated for each shape in Python. NEMOH can generate the added mass matrix A, the radiation damping matrix B, and the exciting force vector F (see Appendix B). The RAO is calculated using both the input data and the output data (Eq. 2-25).

Python

Python [29] has recently been the programming language of choice for the aforementioned research areas, not only because it is easy to use, but also because it has a big user base. Python is a high-level, cross-platform, interpreted programming language that prioritizes readability. There are a plethora of high-quality libraries as well as support for any form of scientific computation available. Python's characteristics make it an excellent choice for a wide range of academic and industrial applications needing complex research.

This thesis makes use of the open-source tool Spyder. Spyder is an open-source scientific development environment based on Python that employs several Python scientific plugins for data inspection, calculation, and analysis. Plugins like SciPy, NumPy, and Matplotlib, which offer tools for interpolation, matrix calculations, and data visualization, are available in the Spyder environment for more advanced work. Because Spyder uses the Python programming language, the mesh can be changed using scripts using the SALOME-Python interface.

Because NEMOH does not provide facilities for data post-processing or analysis, pre- and post-processing Python scripts are used to generate the results (see Appendix B). As a result, NEMOH results like added mass, radiation damping, and wave excitation force are read and built in such a way that they match the required matrix structure and correlate to the correct frequency. The same method

is used to generate stiffness matrices, mass matrices, and center of gravity (CoG). Table 3-4 shows the inputs used for NEMOH in this work.

Table 3-4: NEMOH inputs

Input	Unit	Default	Selected
Sea water density	kg/m^3	1000	1025
Gravitational acceleration	m/s^2	9.81	9.81
Water depth	m	Infinite	200
Number of DoF	-	6	6
Name of the mesh file	-	nemohMesh.dat	User-defined mesh file name .dat
Number of points and panels	-	Derived automatically from the correlated mesh file	Derived automatically from the correlated mesh file
Coordinate system	-	User-Defined	COG
Min, Max, frequency range	rad/s	0.05-2	0.1-1.5
Frequency resolution	-	0.0475	0.0175
Number of wave directions	-	1	1

ANSYS AQWA

ANSYS AQWA [30] is an engineering toolkit for studying the effects of wave, wind, and current on floating and stationary offshore and marine structures, such as spars, FPSO systems, semi-submersibles, tension leg platforms (TLPs), ships, renewable energy systems, and breakwater construction.

AQWA Hydrodynamic Diffraction is a fully integrated environment for generating the key hydrodynamic parameters required for sophisticated motion and reaction analysis. Three-dimensional linear radiation and diffraction analysis can be carried out with many bodies, taking into account all hydrodynamic interaction effects. The models, which are primarily built for floating constructions, can include fixed bodies such as breakwaters or gravity-based structures. Second-order wave forces can be computed using full quadratic transfer function matrices over a wide range of water depths.

AQWA's hydrodynamics Diffraction can also generate pressure and inertial loads, which can be employed in a structural study as part of the vessel hull design process. A diffraction analysis' results can be transferred to an ANSYS Mechanical finite element model for a more thorough structural study. Because the mapping function automatically accommodates mesh changes, the hydrodynamic and finite element models do not need to be topologically identical.

3.6 Verification of the results

To have reasonable results at the end of the optimization approach, it is important to perform sensitivity studies on the mesh size and verify the RAOs.

3.6.1 Mesh sensitivity study

The mesh is created using the SALOME-Python interface. NEMOH specifies the symmetry of the platform, allowing only half of it to be simulated, which has several vertical and circular sides. The accuracy of the hydrodynamic analysis using the panel approach is affected by the mesh size. Considering that the highest wave frequency involved in the calculations is 1.5 rad/s and using a required length of $\frac{\lambda}{8}$ [31], the geometries are meshed with a maximum panel size of 2 m. The sensitivity analysis of the mesh is also considered. The mesh model developed in SALOME, as well as the mesh sensitivity analysis, are shown in Figures 3-4 and 3-5 respectively.

$$\omega^2 = g \, d \, k^2 \qquad\qquad \text{Eq. 3-1}$$

Then,

$$\frac{\lambda}{8} = 3.375m$$

The mesh convergence study is carried out at the specified panel lengths. With an incoming wave frequency range of 0.1 to 1.5 rad/s, the wave came from a single direction (zero-degree wave). Three mesh scenarios are compared. As shown in Table 3-5, each scenario corresponds to a given panel length. There are only slight changes in the NEMOH results for the last two different mesh refinements, as can be seen in Fig. 3-5 (a, b, c, d, and e). If the MS3 mesh scenario provides the most accurate results, then the disparities between the MS2 and MS3 mesh scenarios might be regarded as errors when compared to the MS3. The greatest error values found in the examined NEMOH data are less than 1.2 percent.

Table 3-5: Mesh sensitivity study
(hull geometry d = 12.5m, s = 51.75m, hp = 7m, hc = 20m)

Mesh scenario	Type	Number of the triangles	Number of the quadrangles	Panel length [m]
MS1	Coarse	18	756	3
MS2	Medium	24	1452	2
MS3	Fine	30	2445	1.5
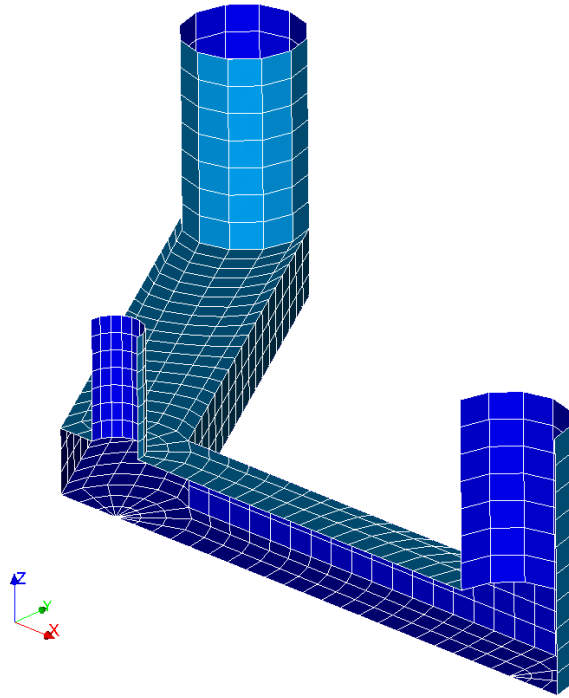
(a) MS1
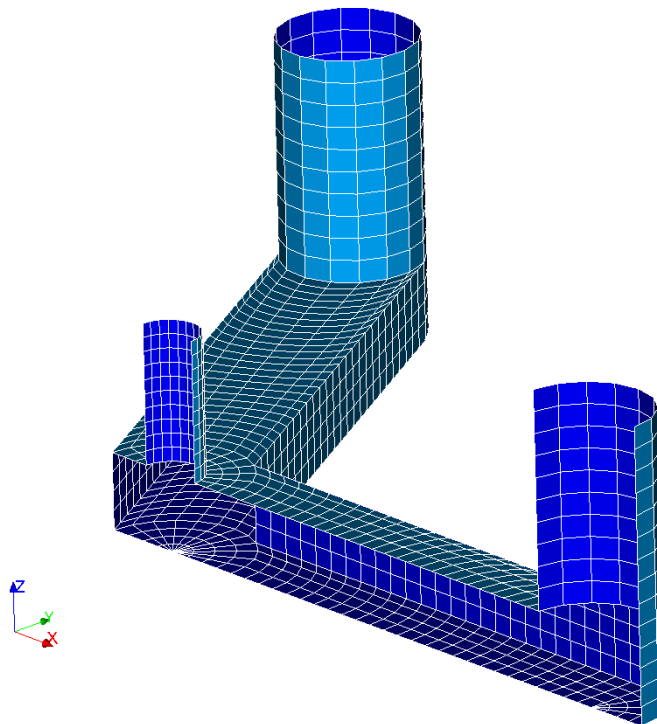
(b) MS2
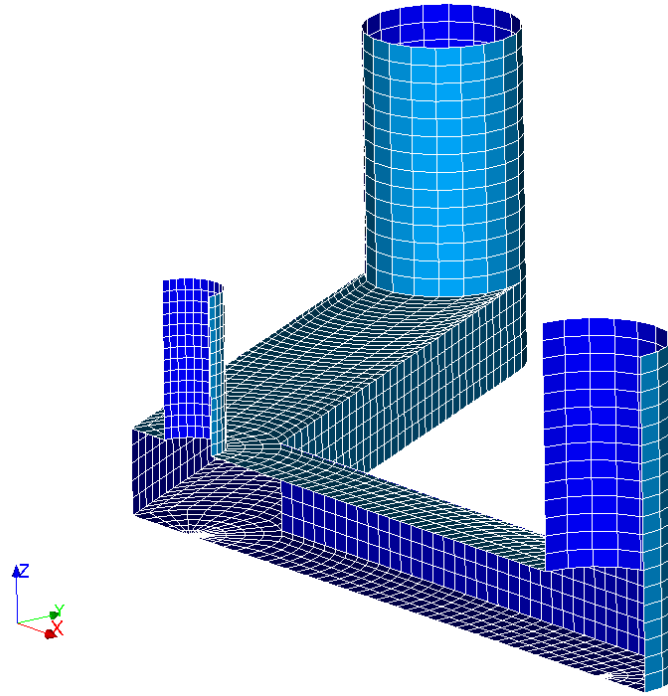
(c) MS3

Fig. 3-4: Mesh models in SALOME

(a) A_{11}

(b) B_{11}

(c) A_{55}

(d) B_{55}

(e) X_5

Fig. 3-5: Influence of the mesh on hydrodynamic coefficients in surge and pitch

where,

A_{11} − Added mass in surge
A_{33} − Added mass in heave
A_{55} − Added mass in pitch
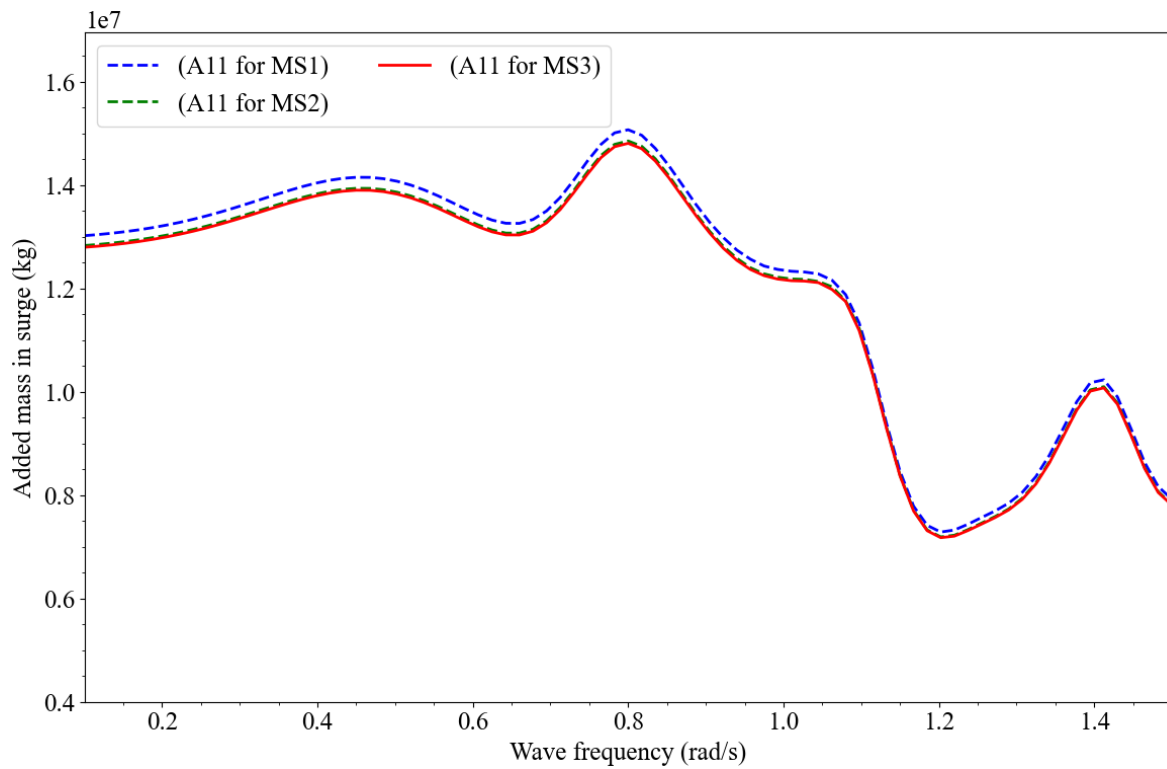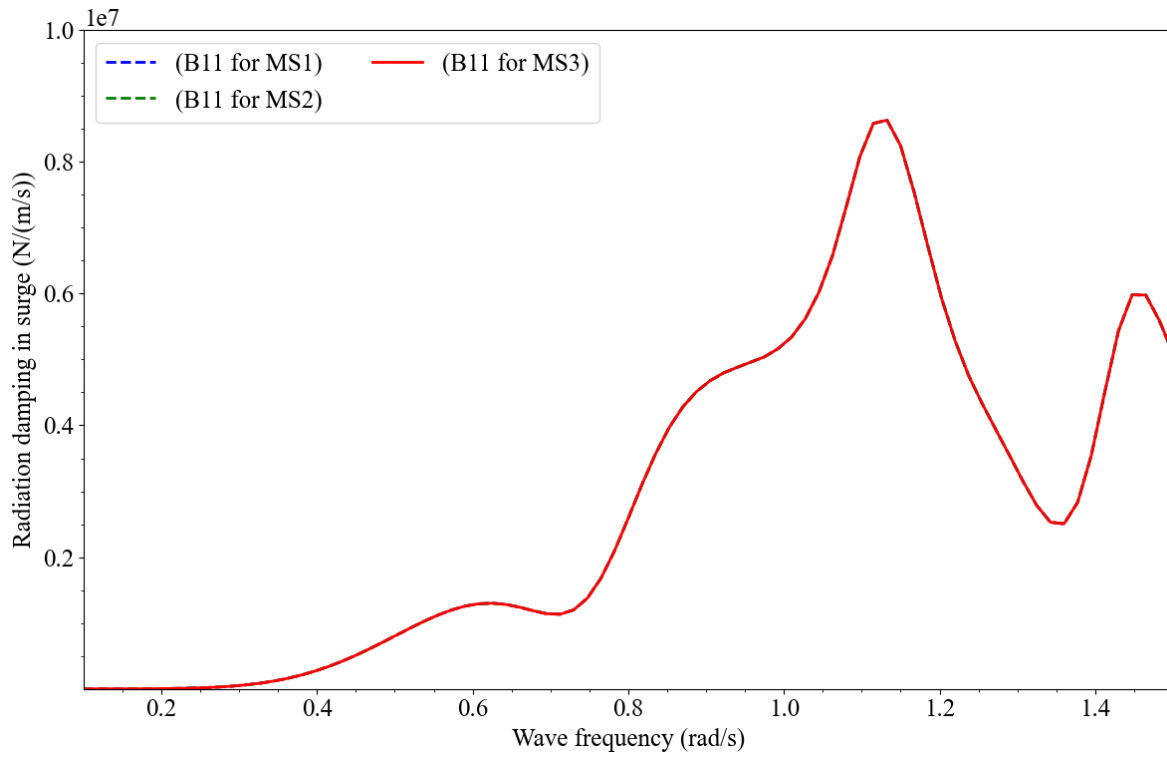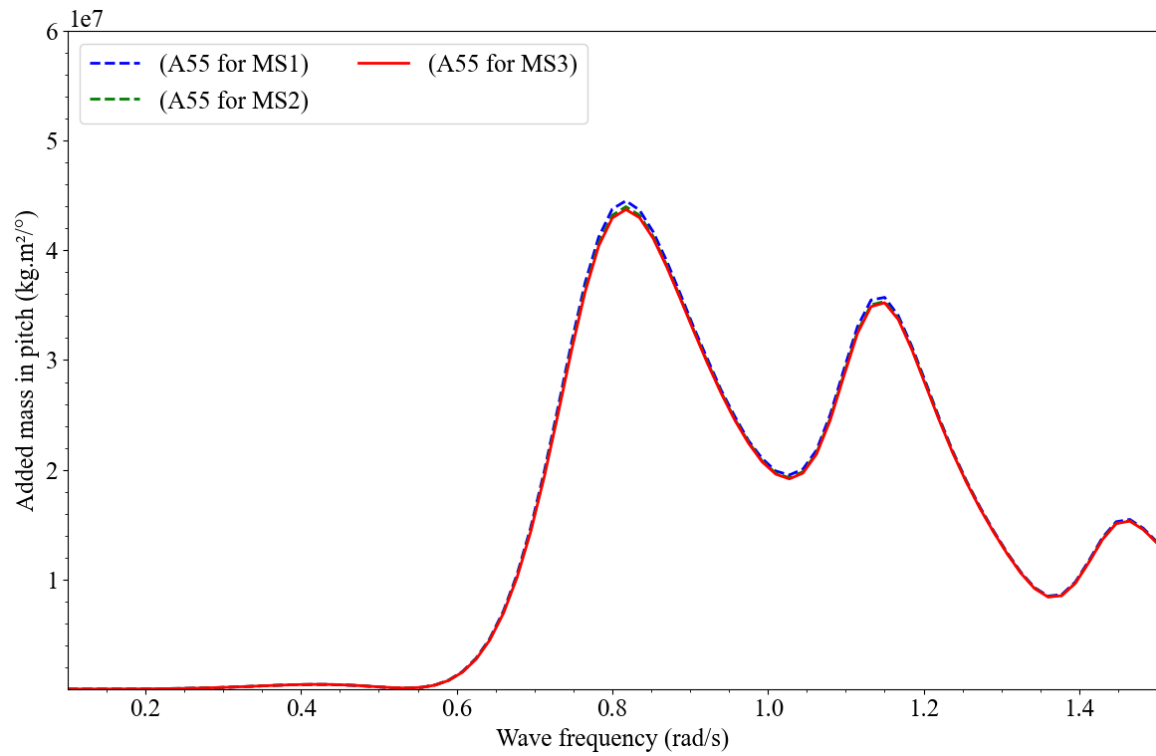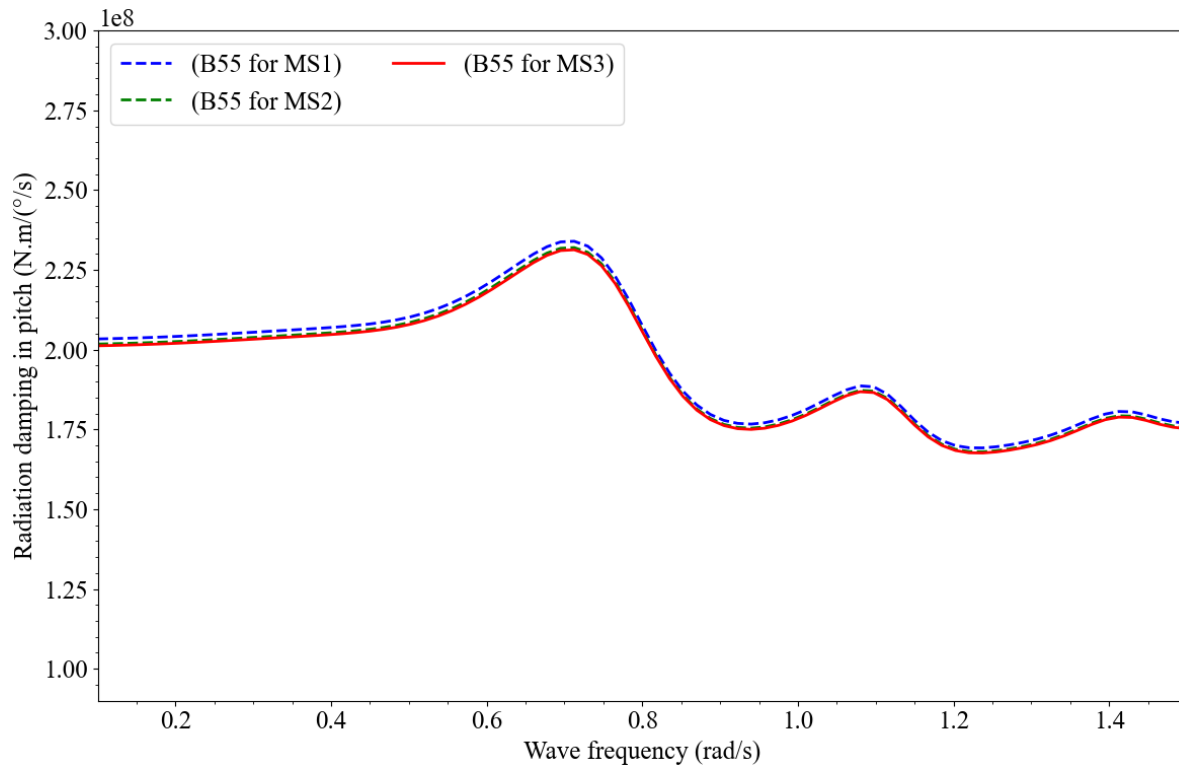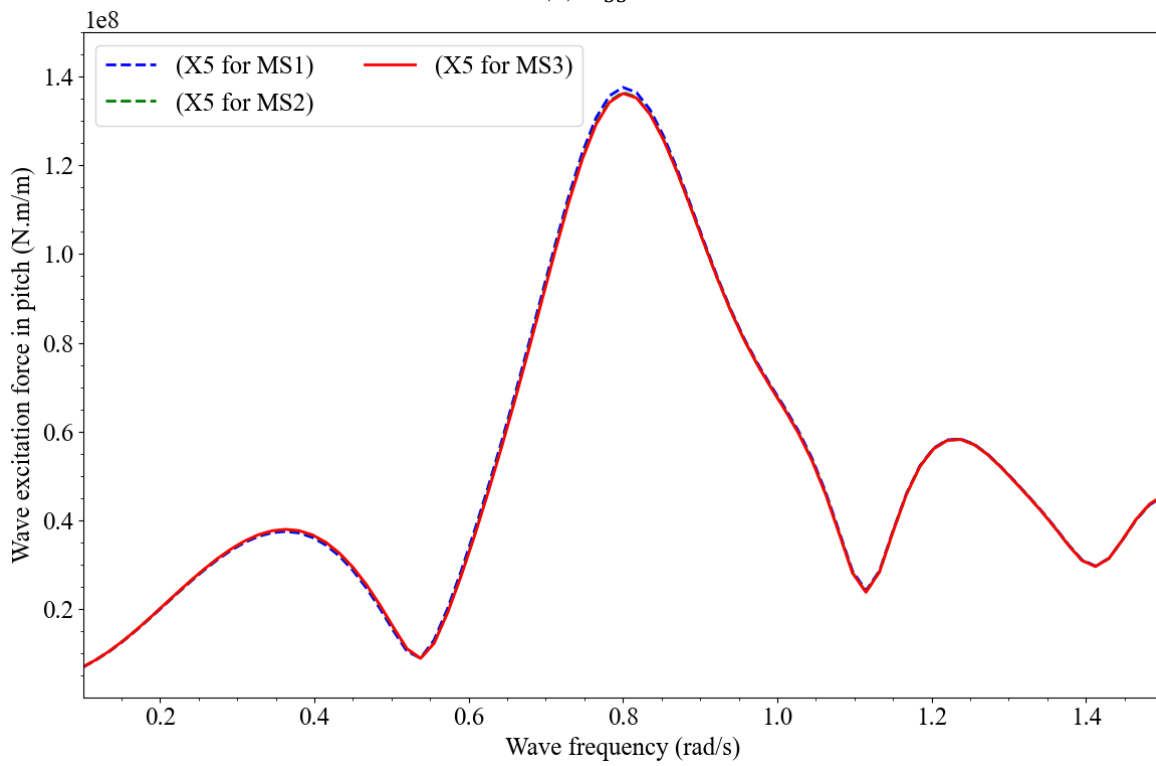B_{11} − Radiation damping in surge
B_{33} − Radiation damping in heave
B_{55} − Radiation damping in pitch
X_1 − Diffraction and Froude − Krylov force in surge
X_3 − Diffraction and Froude − Krylov force in heave
X_5 − Diffraction and Froude − Krylov force in pitch

3.6.2   Verification of motion RAOs

After the panel length has been verified and the most crucial hydrodynamic coefficients have been certified, it is important to examine if the equations of motion have been solved correctly. To do so, a search is made for RAO data for geometry similar to the one explored in this thesis. This study's geometry is identical to that of [14]. In Figures 3-6 and 3-7, the RAO from the current study is compared to RAO obtained from [14] and ANSYS AQWA. The pitch RAO value peaks at 0.205 rad/s and 0.6425 rad/s, respectively, as can be observed. As expected, the peak of the pitch RAO at its natural frequency decreases considerably with the addition of viscous damping. The Pitch RAO with viscous damping shows a good agreement with the previous study (See Fig. 3-7).
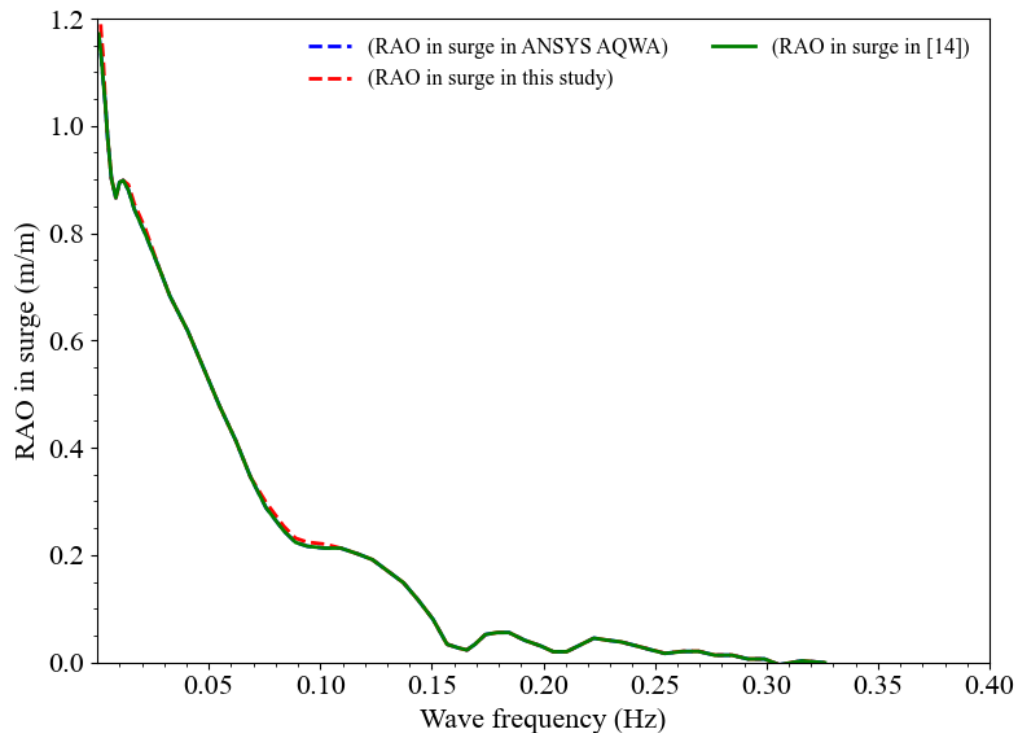
Fig. 3-6: RAO in surge verification
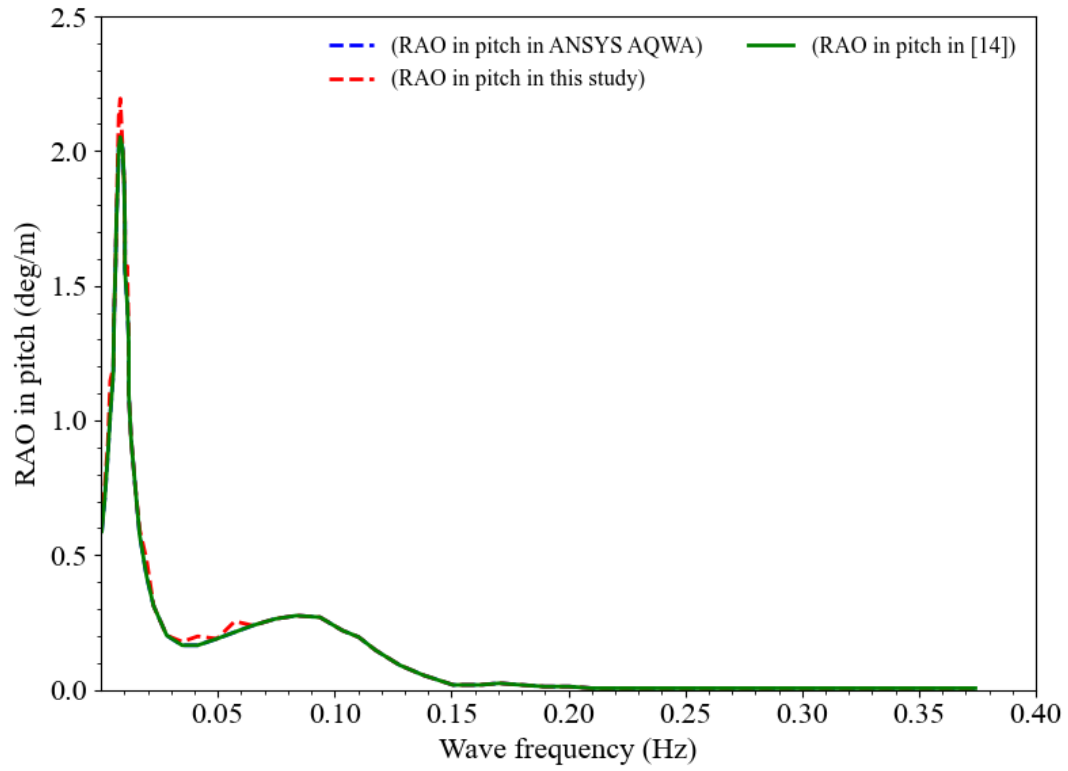
Fig. 3-7: RAO in pitch verification

4. Hydrodynamic performance evaluation

In this chapter, the results of hydrodynamic evaluations performed on the semi-submersible floaters are shown. The motion responses of different platforms under different conditions are presented separately and compared.

4.1 Sensitivity analysis of design variables

As is mentioned in 5.1.1, it is desirable to reduce the number of design variables to a manageable level and to do that we perform a sensitivity analysis. In this section, the results of the sensitivity analysis are shown and discussed. Based on the sensitivity analysis (Fig. 4-1, 4-2, 4-3, and 4-4), it is found that the column spacing has more influence on the motion response than other design variables.
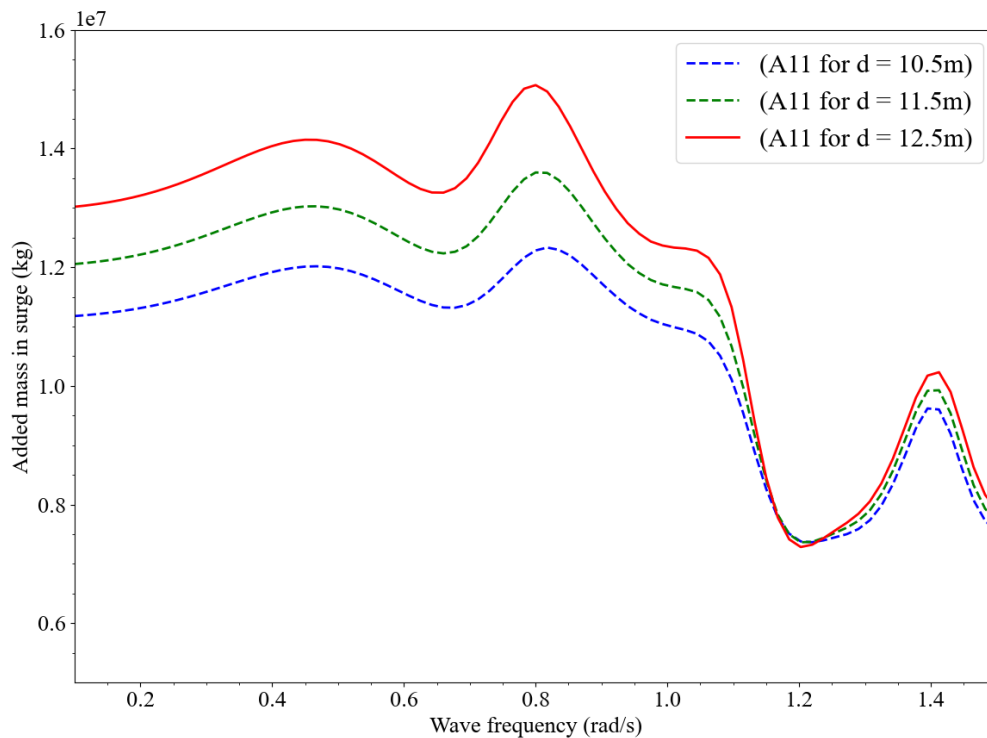
(a)
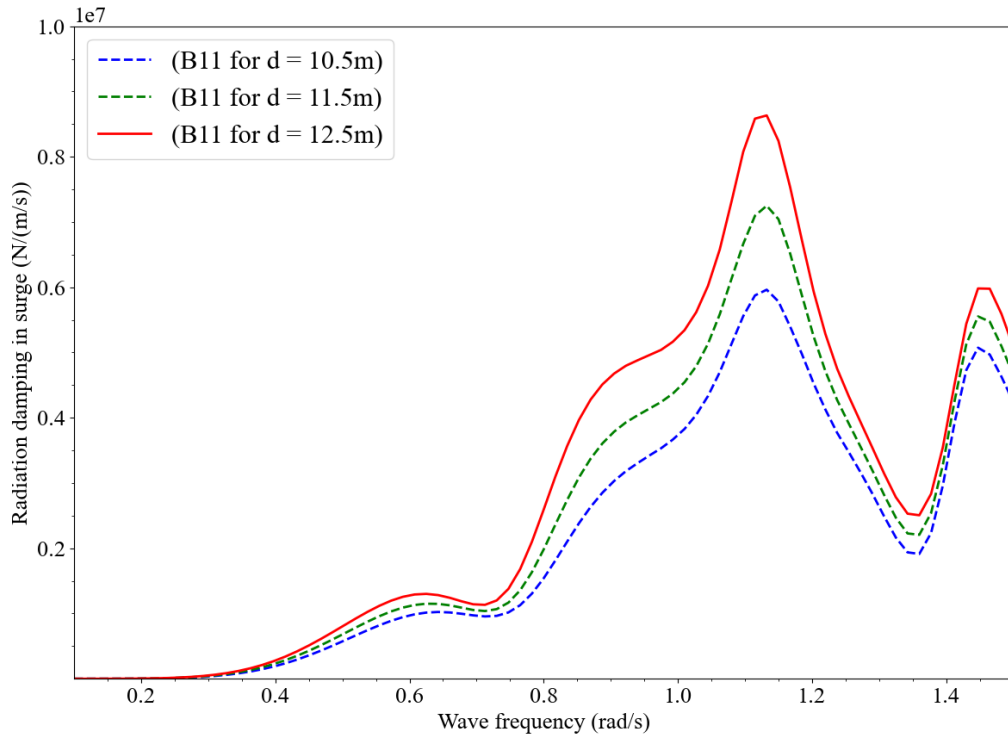
(b)
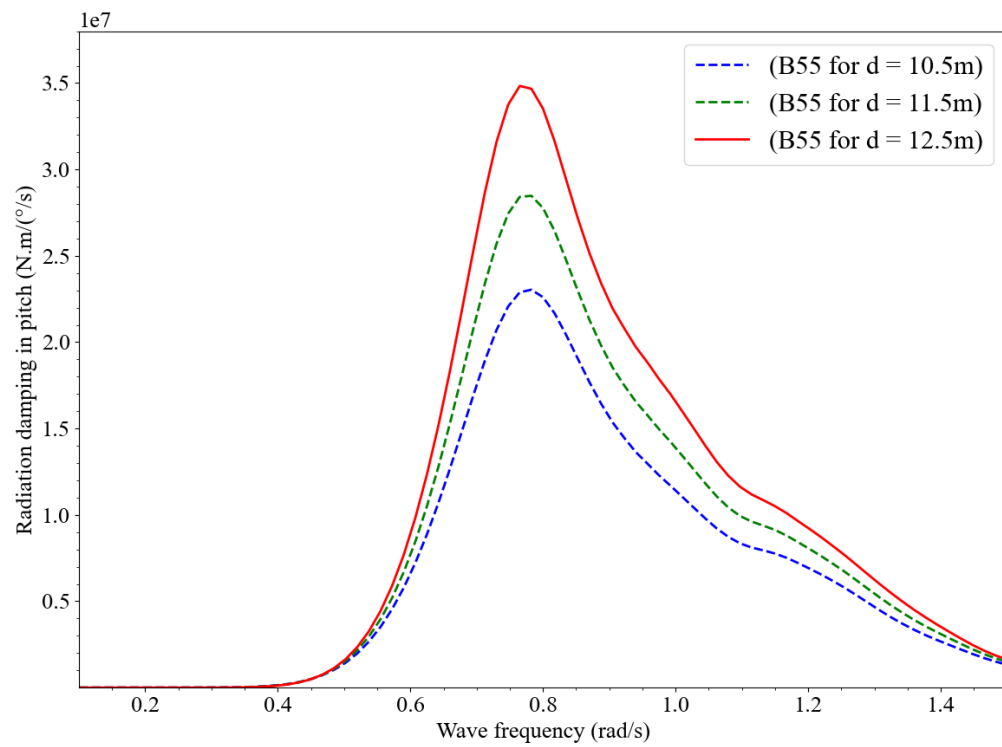
(c)
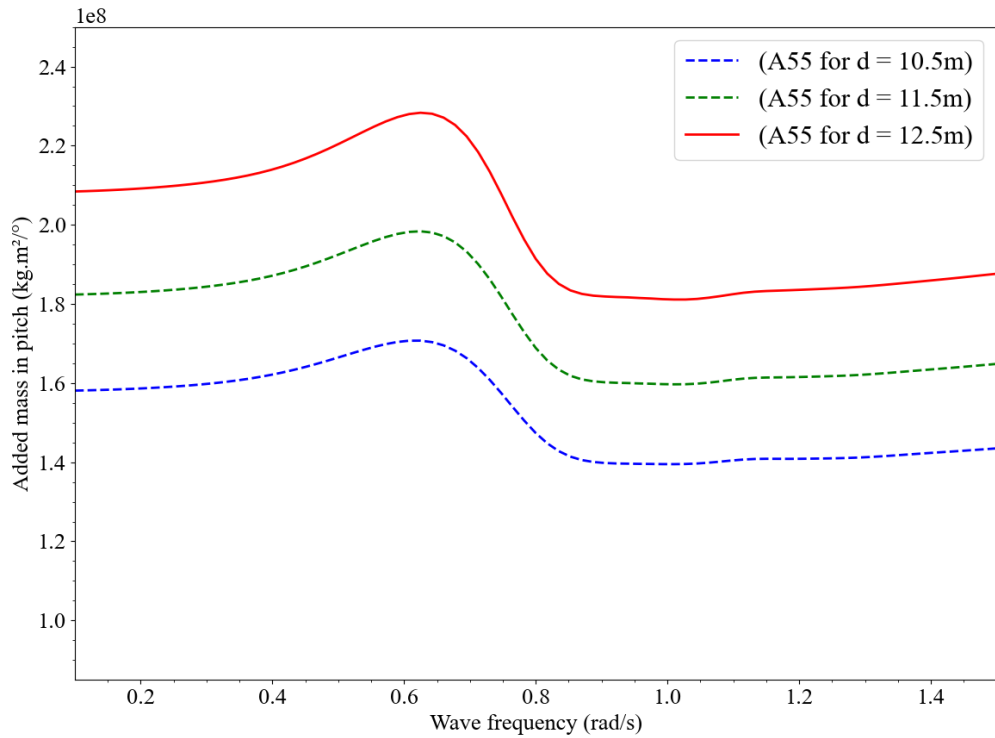
(d)
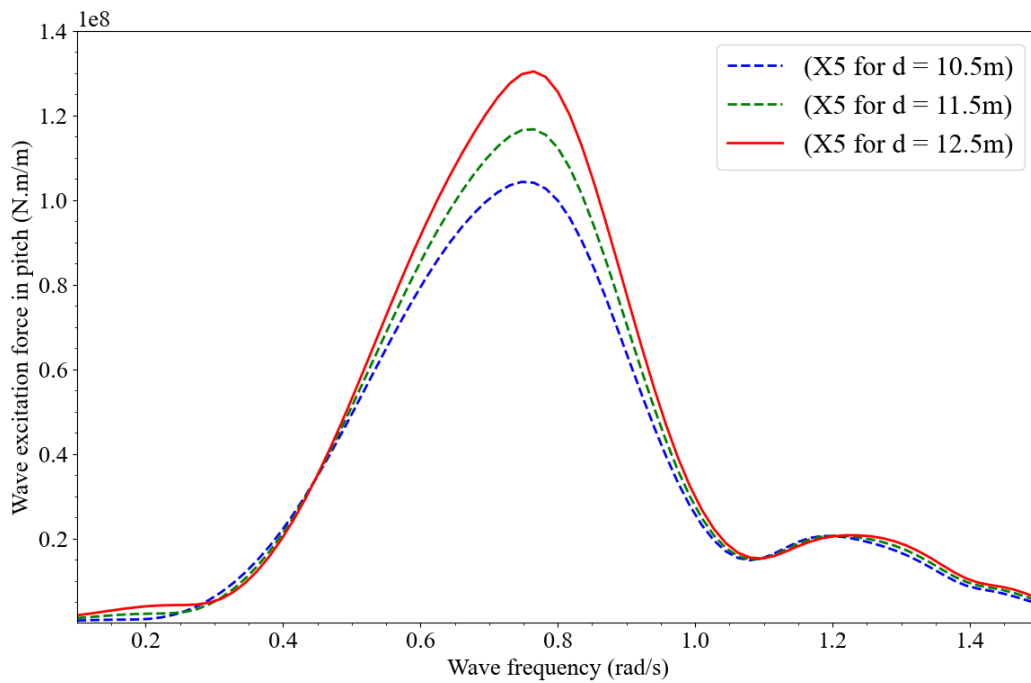
(e)

Fig. 4-1: Hydrodynamic properties of the semi-submersible floater with varying side column diameter (*d*) (hc = 24m, hp = 7m, s = 51.75m, water depth = 1000m)

As seen in Fig. 4-1 (a) and (d), increasing the diameter of the side columns increases the added mass in surge and pitch. The same trend is found for radiation damping in surge and pitch. Significant variations in added mass in surge are seen in frequencies ranging from 0.1 to 1.15 rad/s. In the frequency range of 0.1 to 0.4 rad/s, there are no changes in radiation damping in surge and pitch. A peak occurs at the frequency of 1.12 rad/s for B_{11}; however, for B_{55} is at 0.75 rad/s.
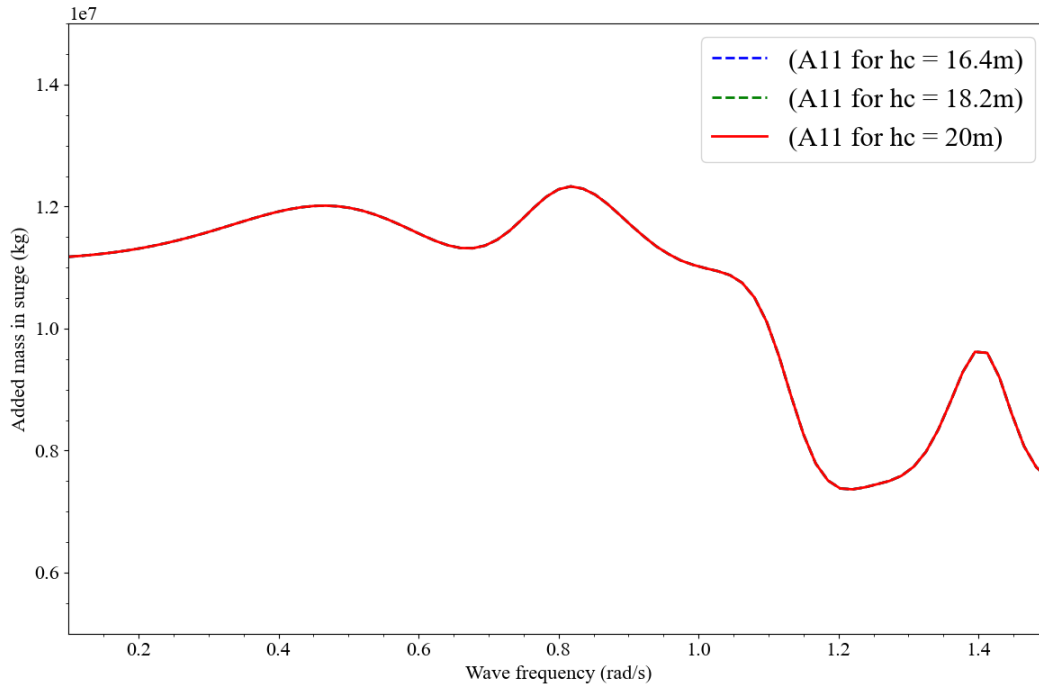
(a)
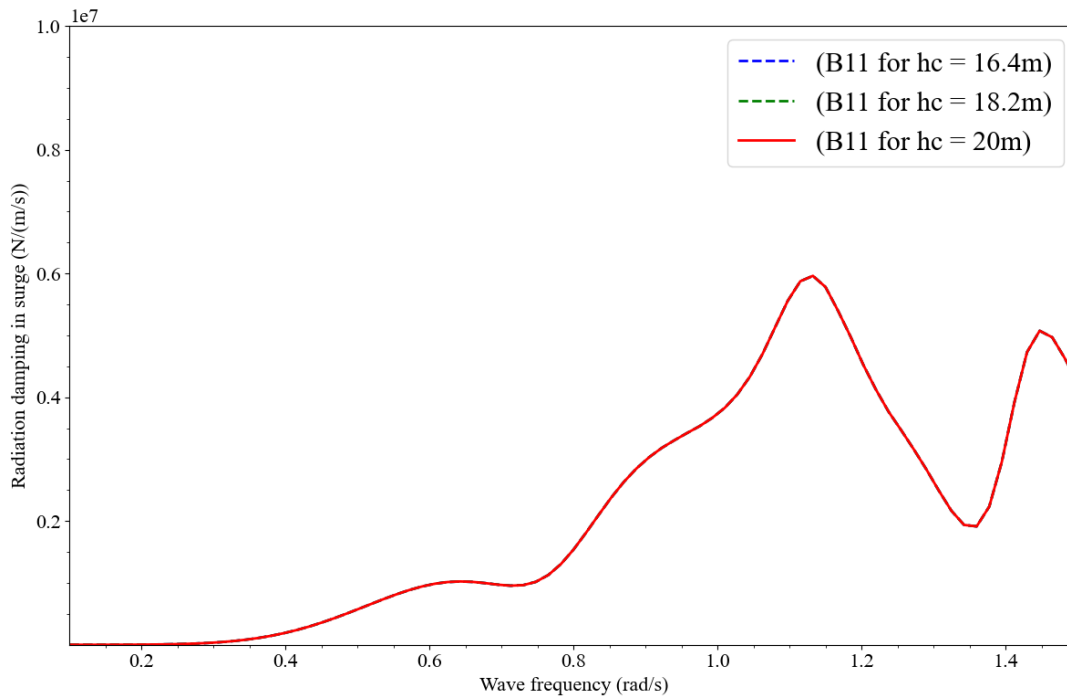
(b)
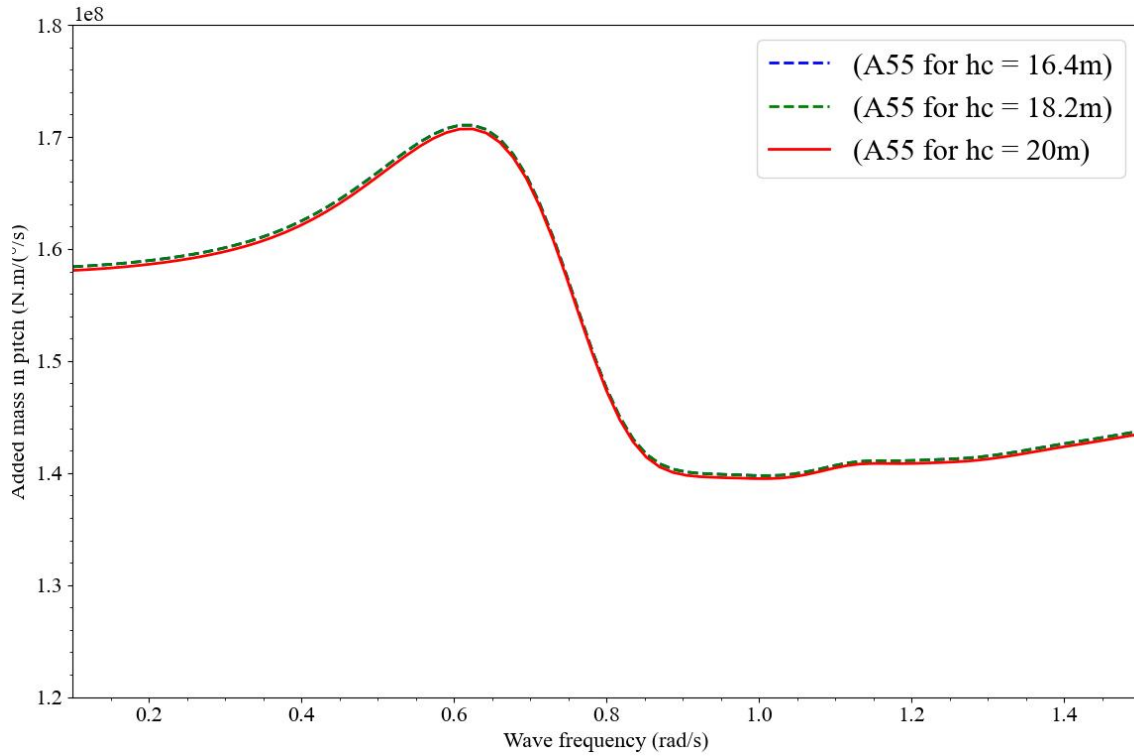
(c)

(d)
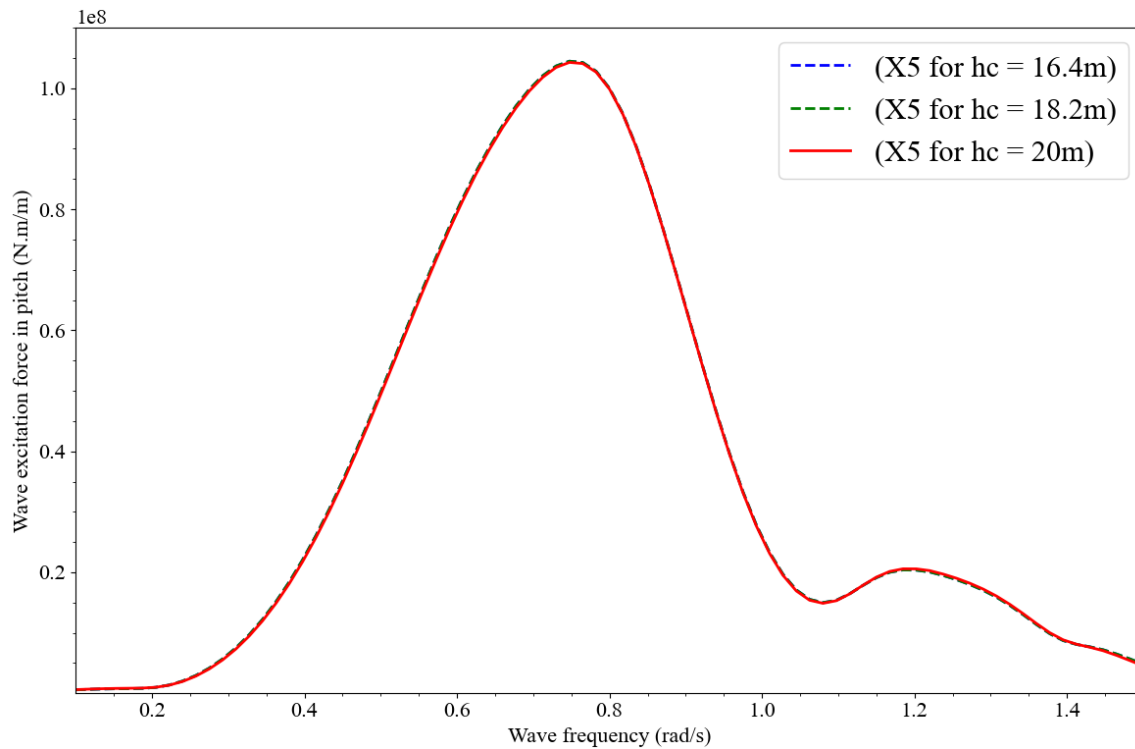
(e)

Fig. 4-2: Hydrodynamic properties of the semi-submersible floater with varying submerged column
height (hc) (d= 12.5m, hp = 7m, s = 51.75m, water depth = 1000m)

According to Fig. 4-2, changes in submerged column height (hc) do not influence hydrodynamic
coefficients; nevertheless, as shown in Fig. 4-3, changing pontoon height (hp) affects hydrodynamic
coefficients in surge and pitch but is not as significant as columns' diameter (d) and column spacing
(s).

Based on Fig. 4-4, column spacing has significant effects on all hydrodynamic coefficients. There are
some changes in the variations of radiation damping in surges above 1.15 rad/s (see Fig. 4-4 (b)).

Changes in design factors (particularly d and s, as shown in Figures 4-1 (d) and 4-4 (c)) have a
considerable impact on the added mass in pitch. The reason behind this is that as waves crash onto the
FOWT, the hull surges through the water, creating a viscous boundary layer in the surrounding fluid.
The normal surrounding flow is separated from the 'flow altered by the body motion' by a boundary
layer. As a result, the hull motion has an impact on the fluid composition of this boundary layer. Forces
are created on the hull's contact surface by this speeding fluid particle. Because the substructure motion
has already disrupted the fluid's potential flow, the fluid particles have some kinetic energy. As a result,
in addition to accelerating itself, it must also expend some extra kinetic energy on the surrounding
fluid. As a result, a change in 'd' and 's' causes a considerable disturbance in the fluid's potential flow,
resulting in more mass being added.
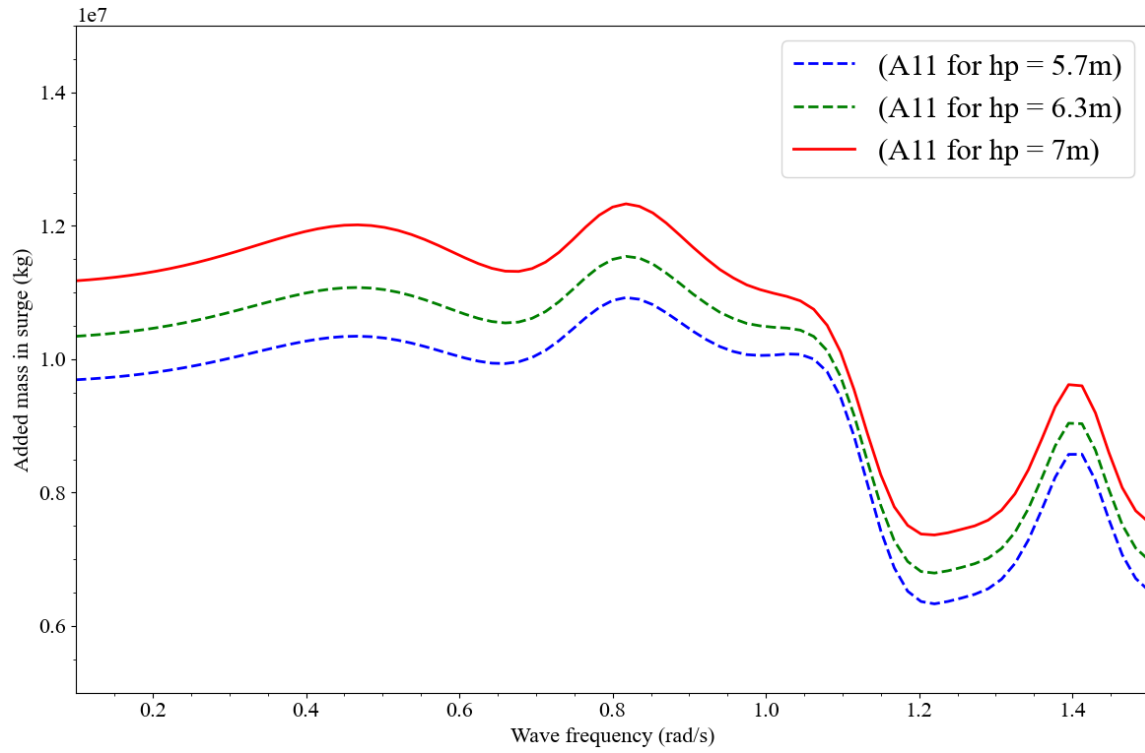
(a)
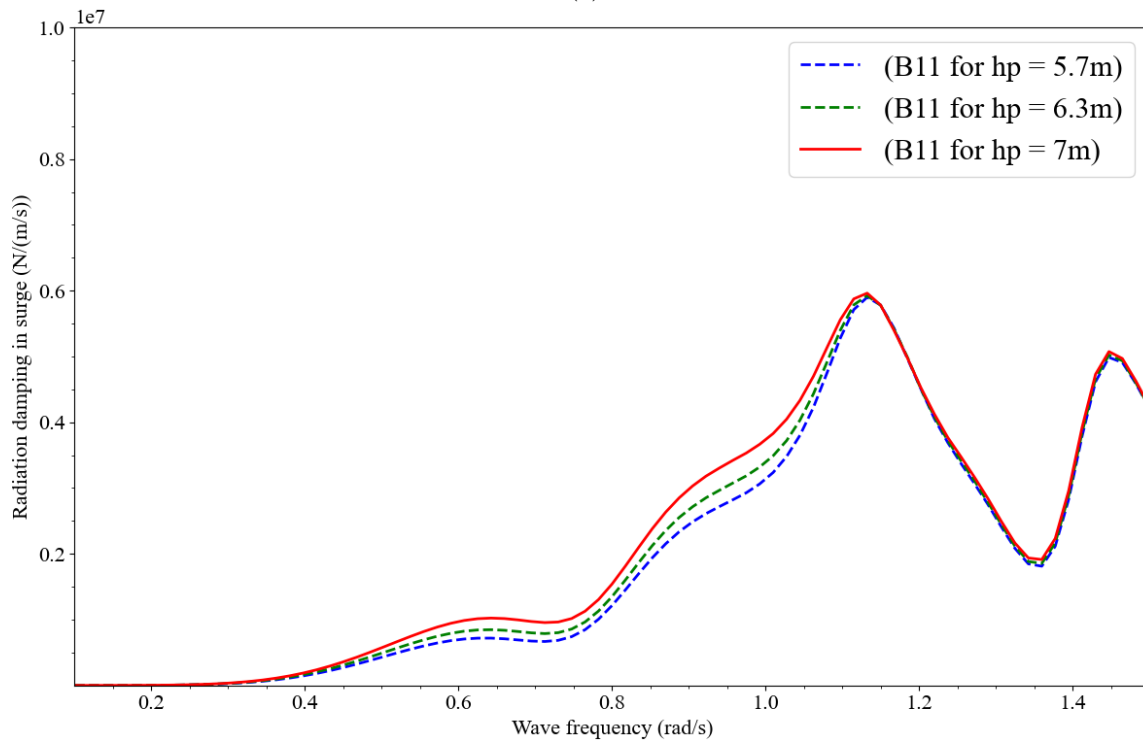
(b)
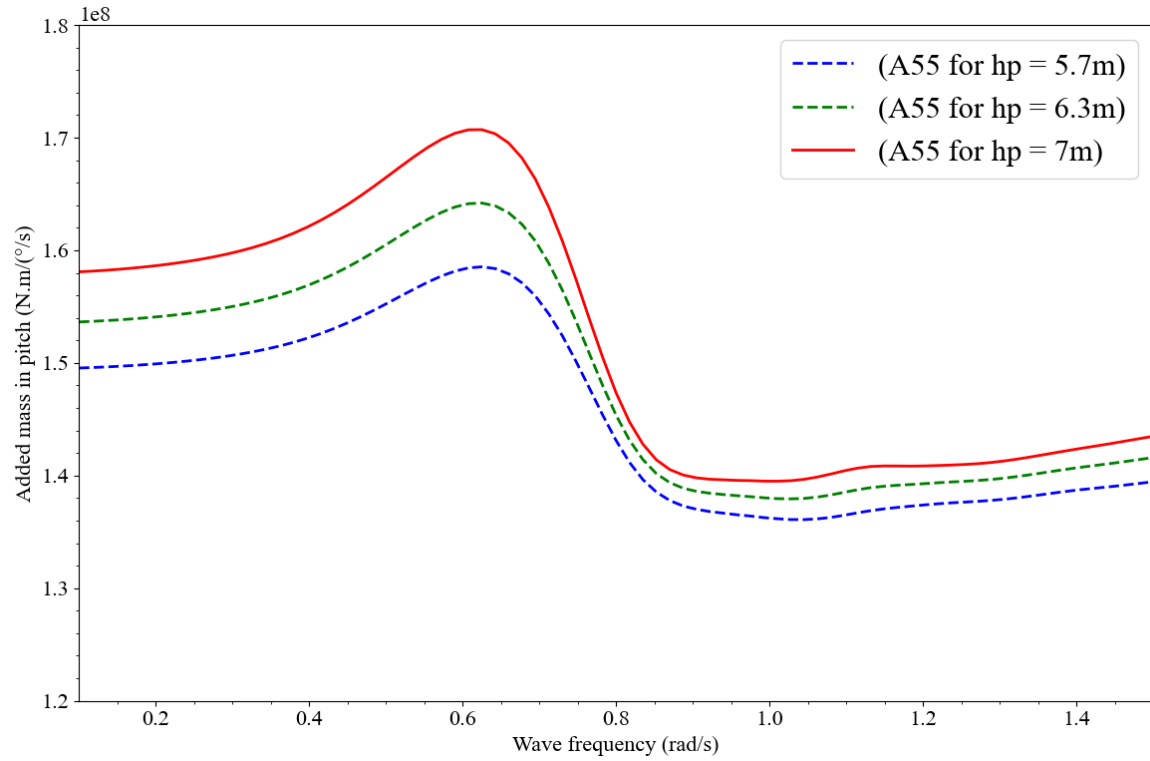
(c)
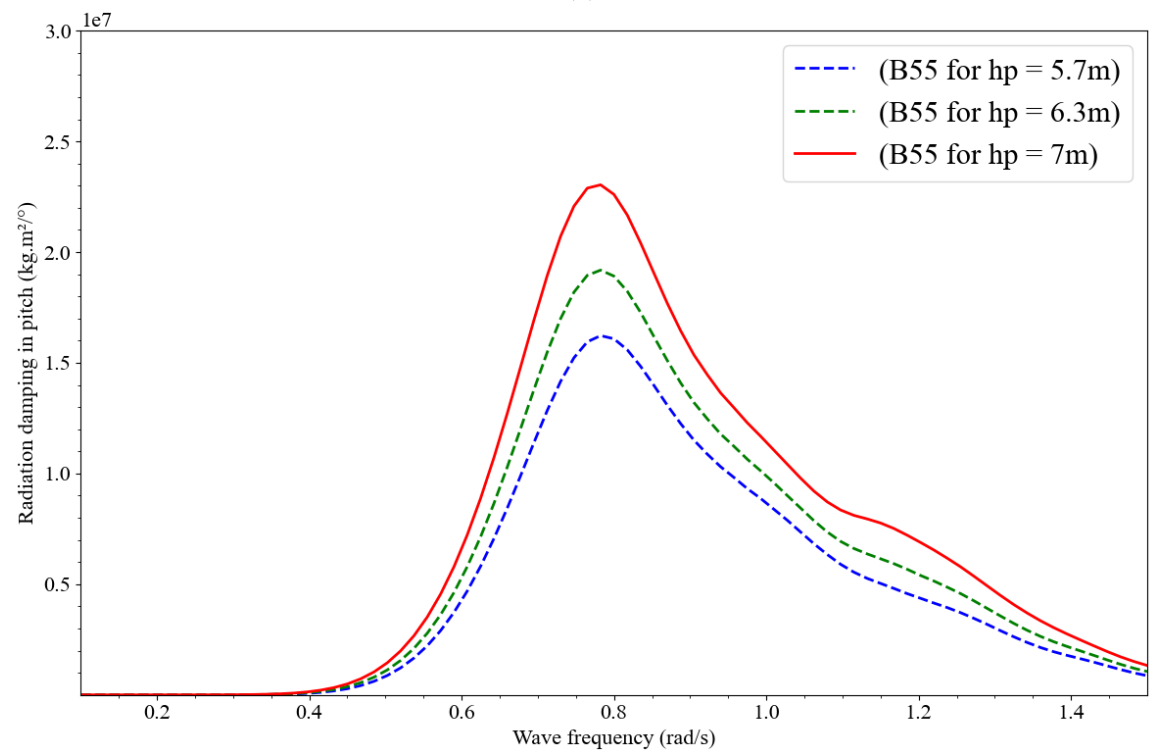
(d)
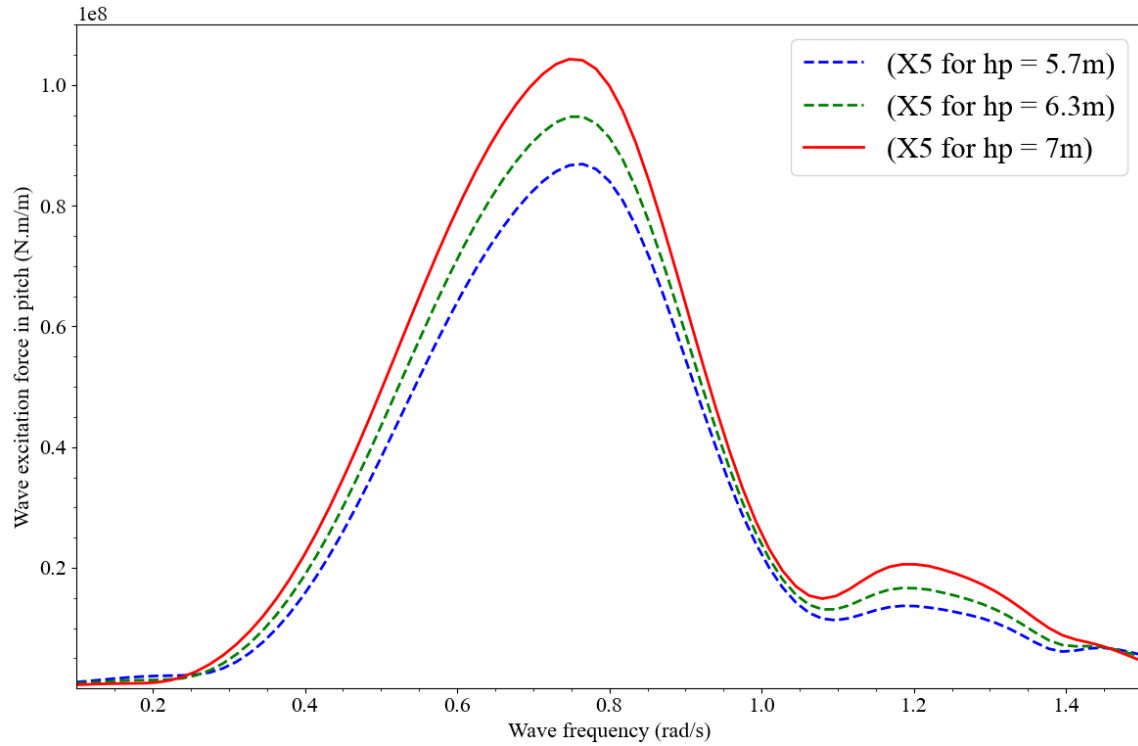
(e)

Fig. 4-3: Hydrodynamic properties of the semi-submersible floater with varying pontoon height (hp) (hc = 24m, d= 12.5m, s = 51.75m, water depth = 1000m)
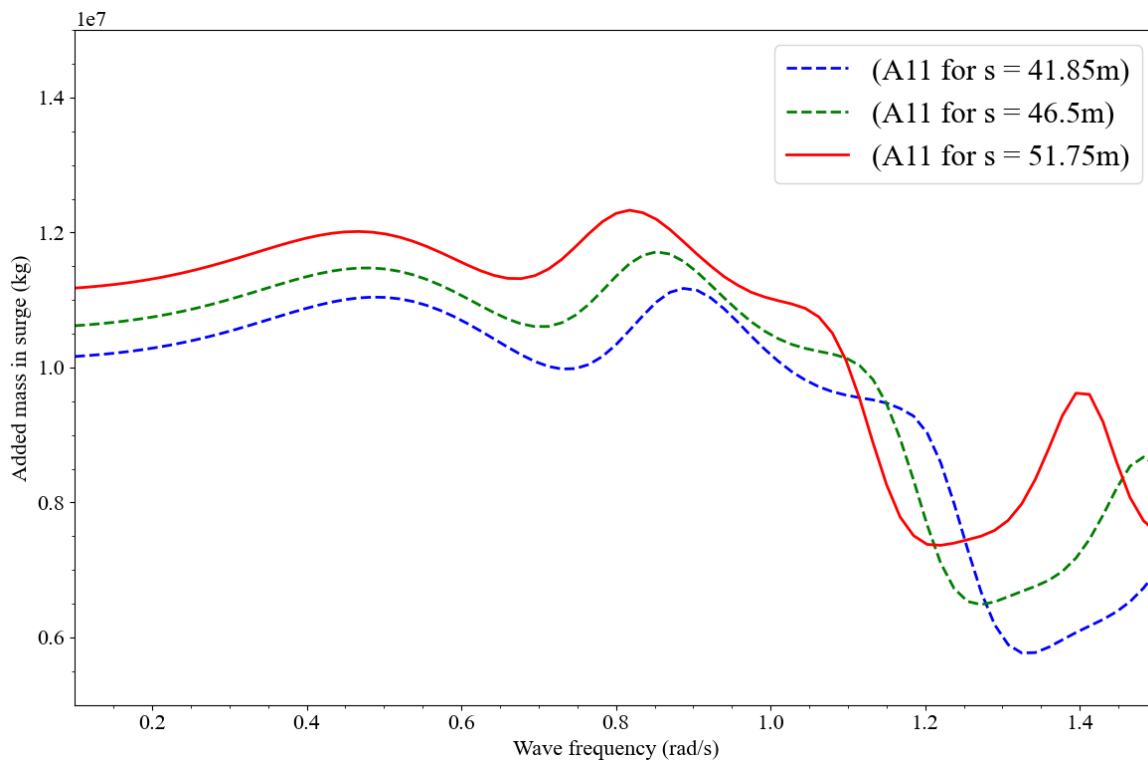
(a)
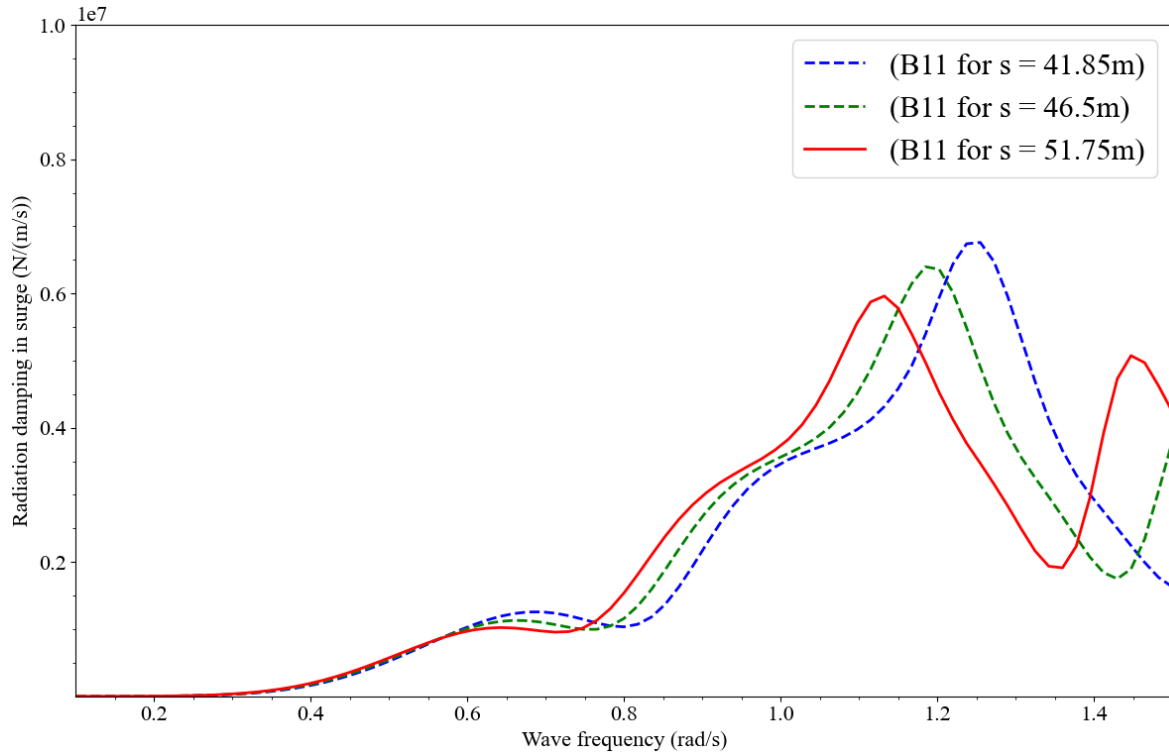
(b)
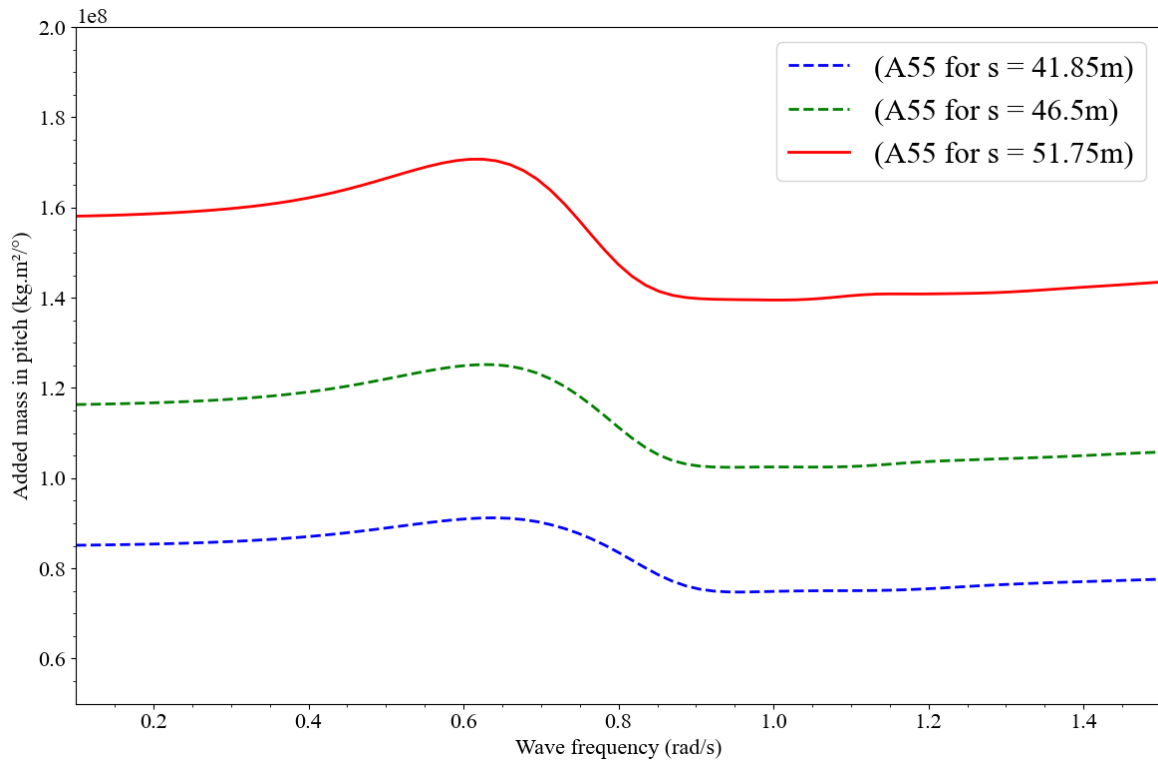
(c)
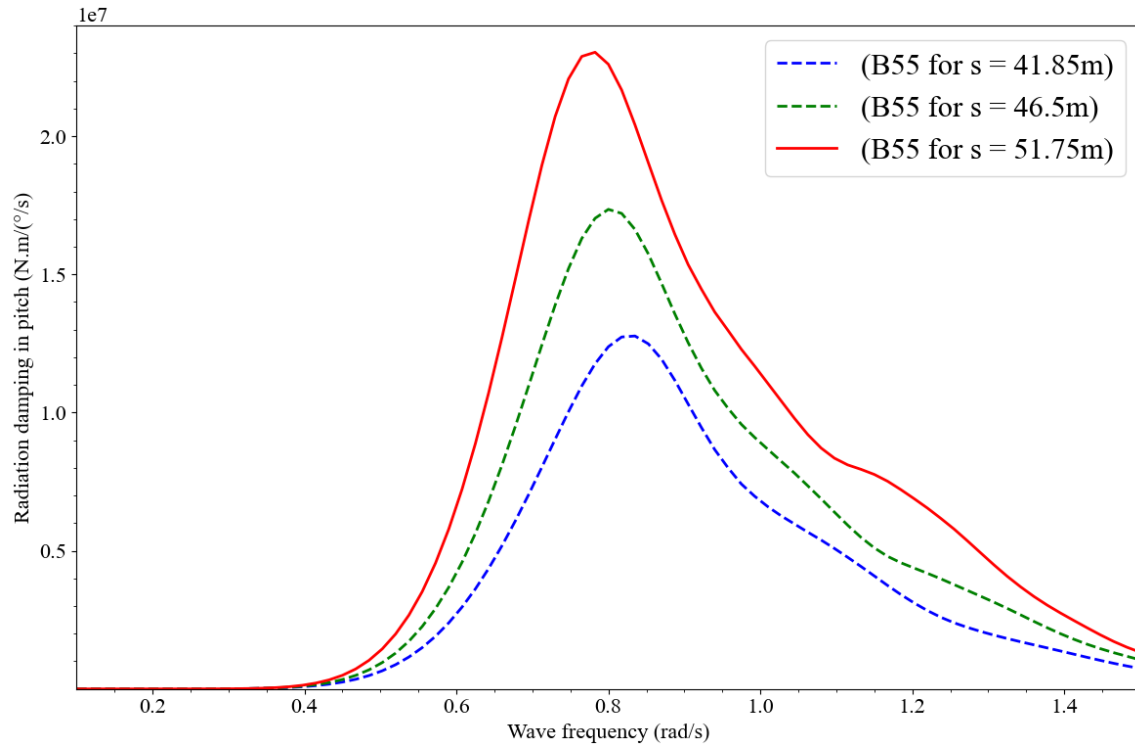
(d)
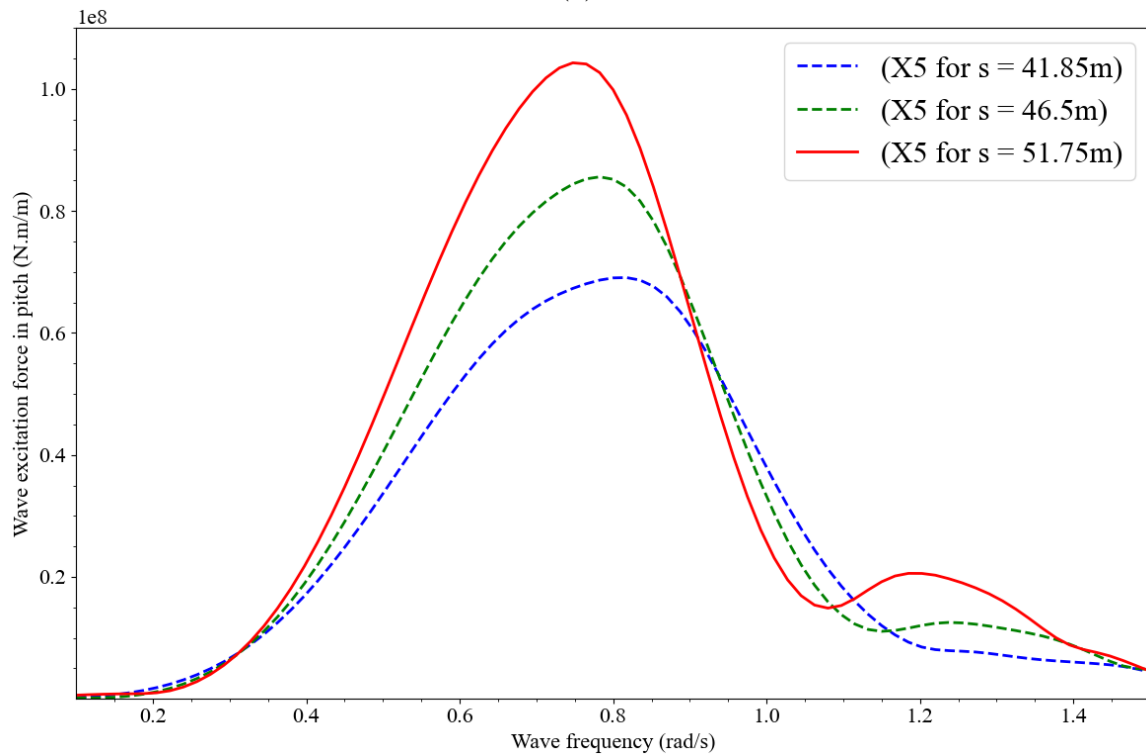
(e)

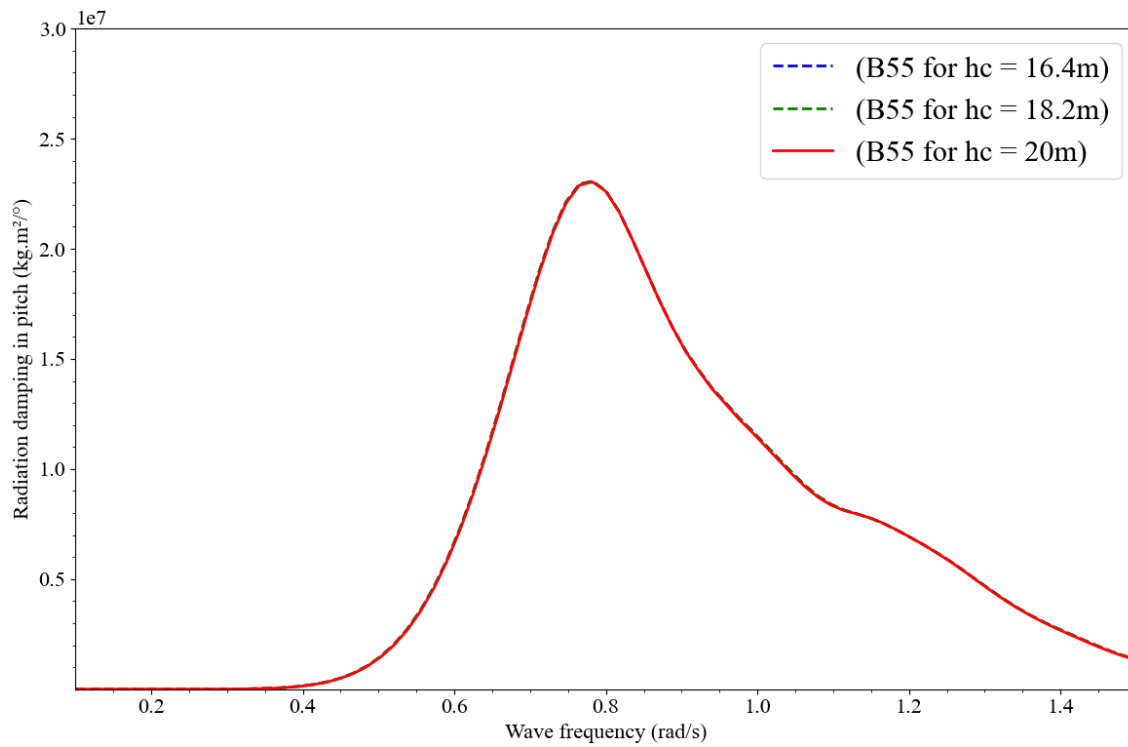Fig. 4-4: Hydrodynamic properties of the semi-submersible floater with varying column spacing (s) (hc = 24m, d= 12.5m, hp = 7m, water depth = 1000m)

4.2 Hydrostatic and ballast analysis

The COG and mass matrix of the structure is affected by the position of the ballast water inside the floater for a given geometry, which impacts both the hydrostatic performance and the nacelle acceleration. The pontoon or the side columns might both contain ballast water. When compared to the pontoon, ballasting in the side columns results in a greater COG, lower nacelle acceleration RAO, and higher GM. Two different ballasting scenarios are explored for the original geometry. In both cases, the hull draft is the same, but the mass and stiffness matrices referring to the COG are different. The required ballast height in the side columns for the second scenario is 10m, which elevates the metacentric height by 20% over scenario one.

In most geometries, it is decided to evaluate both pontoon and side columns for ballasting; however, in some geometries, it is decided to examine both pontoon and side columns for ballasting. Because of the high amplitudes of response motions, notably in pitch, this decision was chosen. As a result, most geometries would fail to satisfy the acceleration limitation PC2 specified in Section 5.1.4.
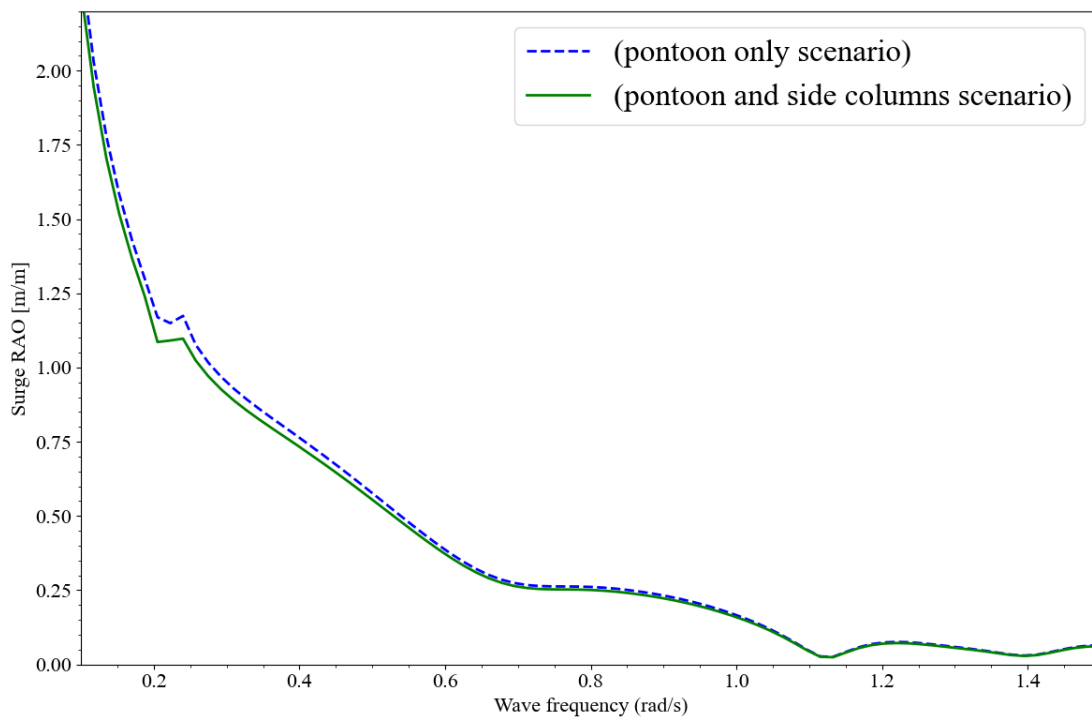
(a) Surge
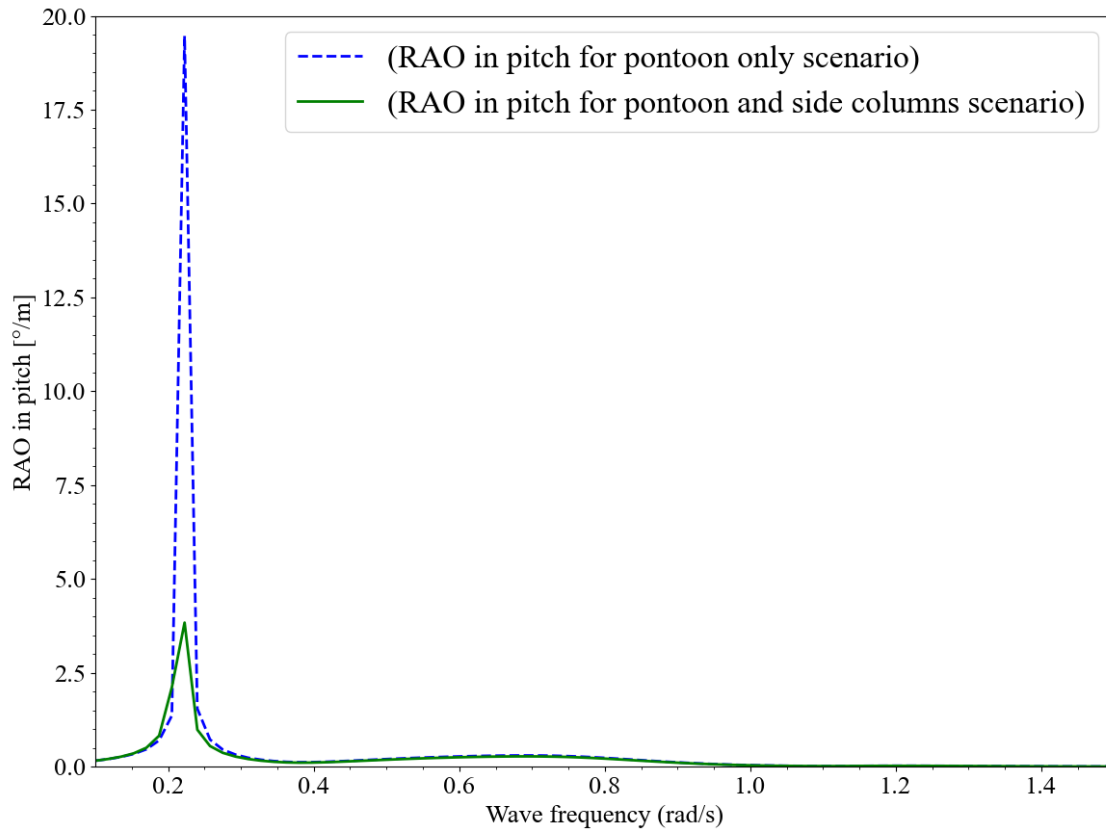
(b) Pitch

Fig. 4-5: RAO in pitch and surge using different ballasting
(hull geometry; $d = 12.5$m, $s = 51.75$m, $hp = 7$m and $hc = 13$m, EC2)

Most constructions with column diameters less than 10 meters and column spacing less than 31.75 meters are unstable, according to hydrostatic analysis, and cannot pass the GM constraint PC1. Because these structures are too small to sustain the NREL 15MW wind turbine, they cannot be considered floating while the turbine is installed on top of them. The column spacing has a significant impact on the system's stability.
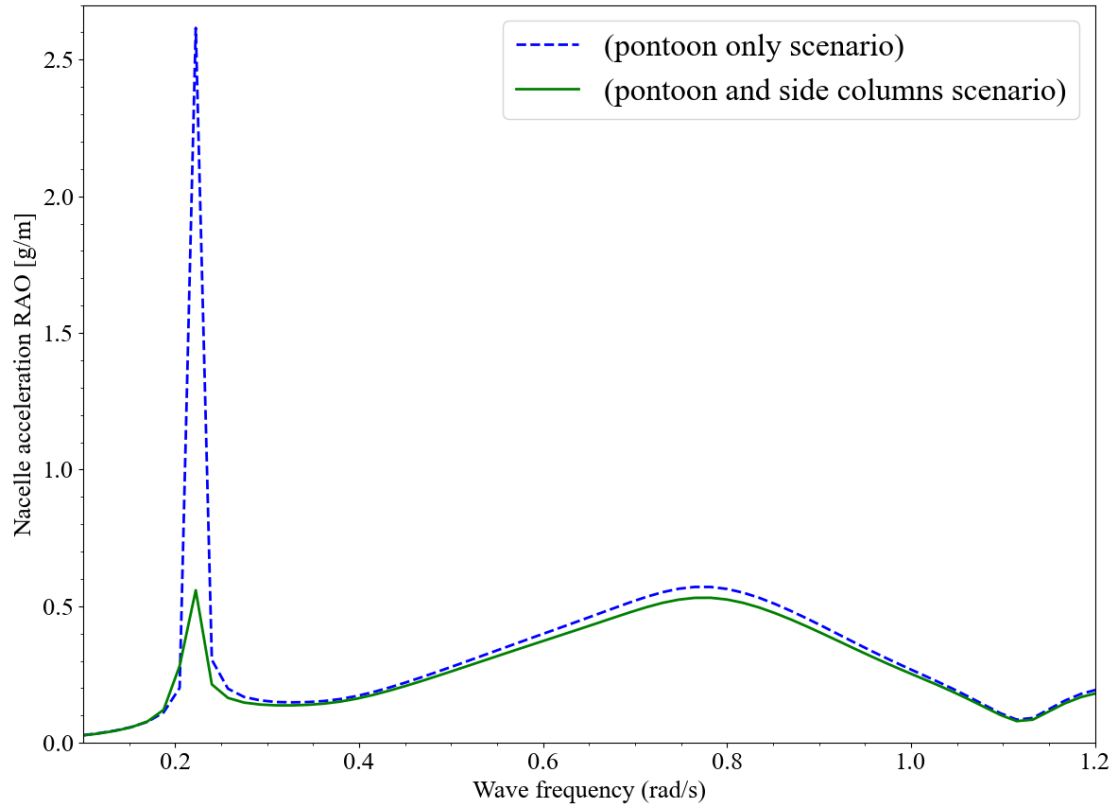
Fig. 4-6: Nacelle acceleration RAO with different ballasting
(hull geometry; d = 12.5m, s = 51.75m, hp = 7m and hc = 13m, EC2)
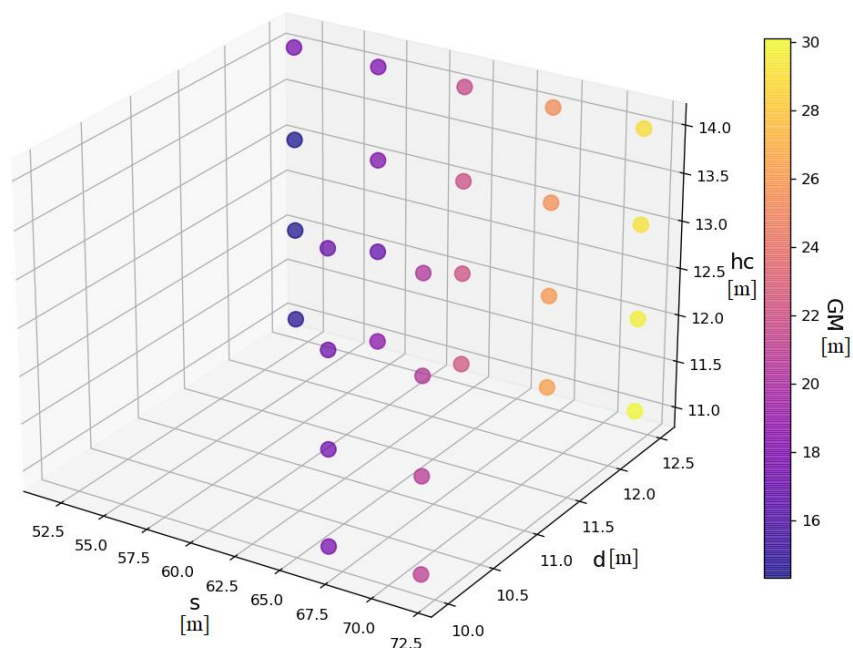
(a) for hp = 6m
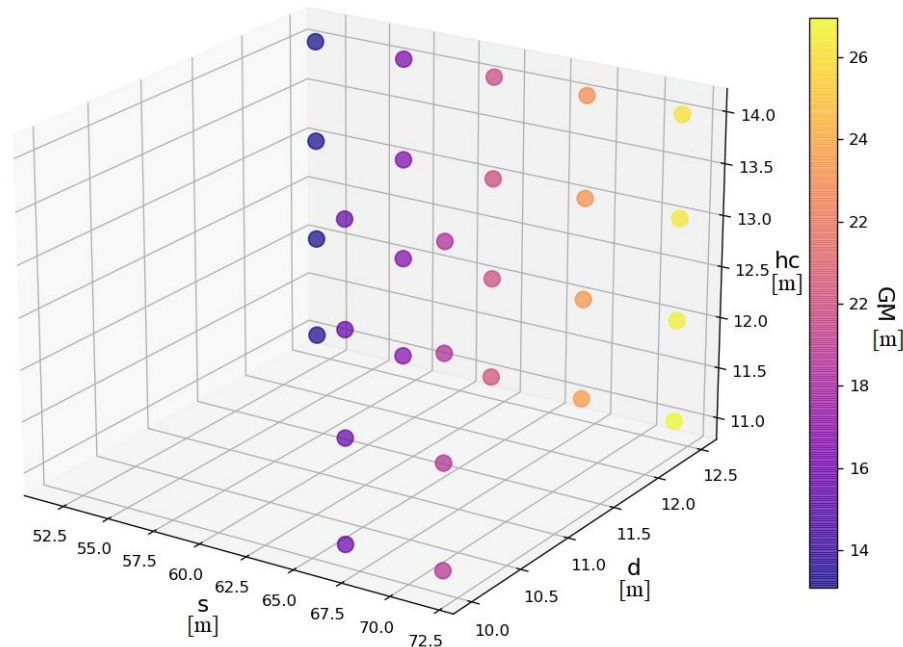
(b) for $hp = 7$m

Fig. 4-7: GM versus design variables

Figure 4-5 shows the comparison of RAOs in pitch and surge for various ballasting scenarios. The pitch and nacelle acceleration RAO have been greatly reduced by considering the pontoon and side columns for ballasting. It is self-evident that raising the overall mass of the structure in Eq. 2-61 and Eq. 5-2 reduces the structure's reaction as well as the nacelle acceleration.

It should be noted that putting ballast water into the side columns will modify the pitch inertia and hence the pitch resonance period dramatically. So why does the resonance period appear to be the same in both scenarios? To answer this question, we'll apply the Eq. 2-28 in Sec. 2.2.4. The hull draft is constant in both ballasting scenarios. Due to an increase in $\overline{GM}_L$, the C_{55} increase as the mass matrix components (in this case M_{55}) grow with the addition of more ballast water into the side columns (see Eq. 2-17). According to Eq. 2-28, the increase in numerator and denominator is more or less the same, therefore, there is a small change in the natural frequency of the system.

Fig. 4-6 depicts a comparison of nacelle acceleration RAO for various ballasting scenarios. Between the frequency of 0.1 and 0.3 rad/s, the curve follows the same pattern, with a peak at 0.7825 rad/s. The nacelle acceleration RAO is most influenced by pitch RAO.

Fig. 4-7 and 4-8 depict the variations of GM and the platform steel mass vs design factors respectively.
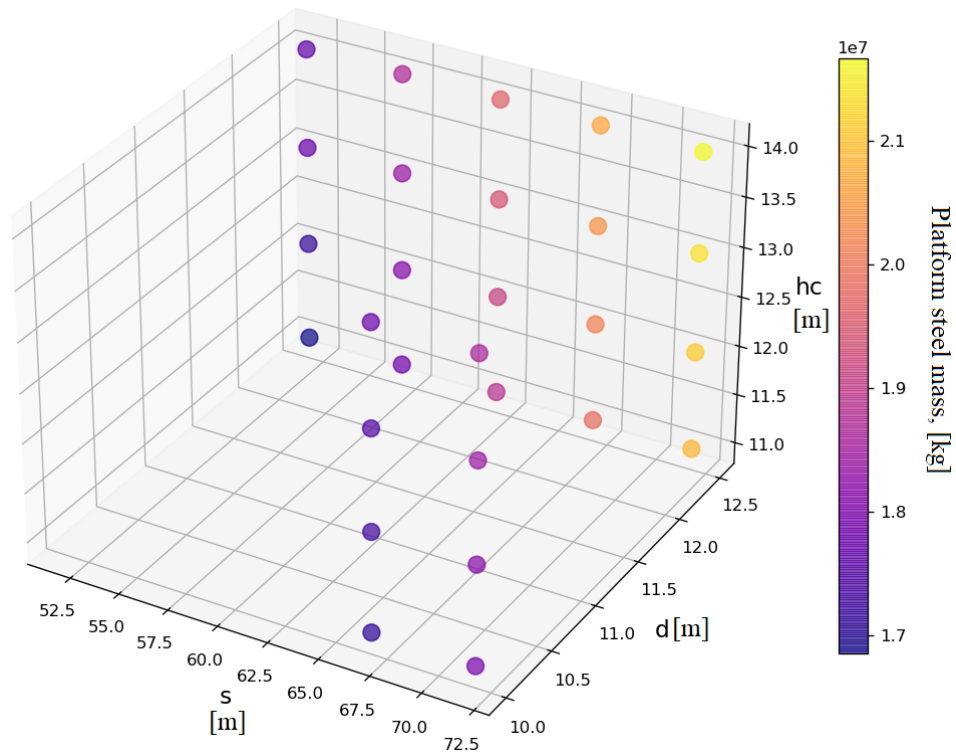
(a) for $hp = 6$m
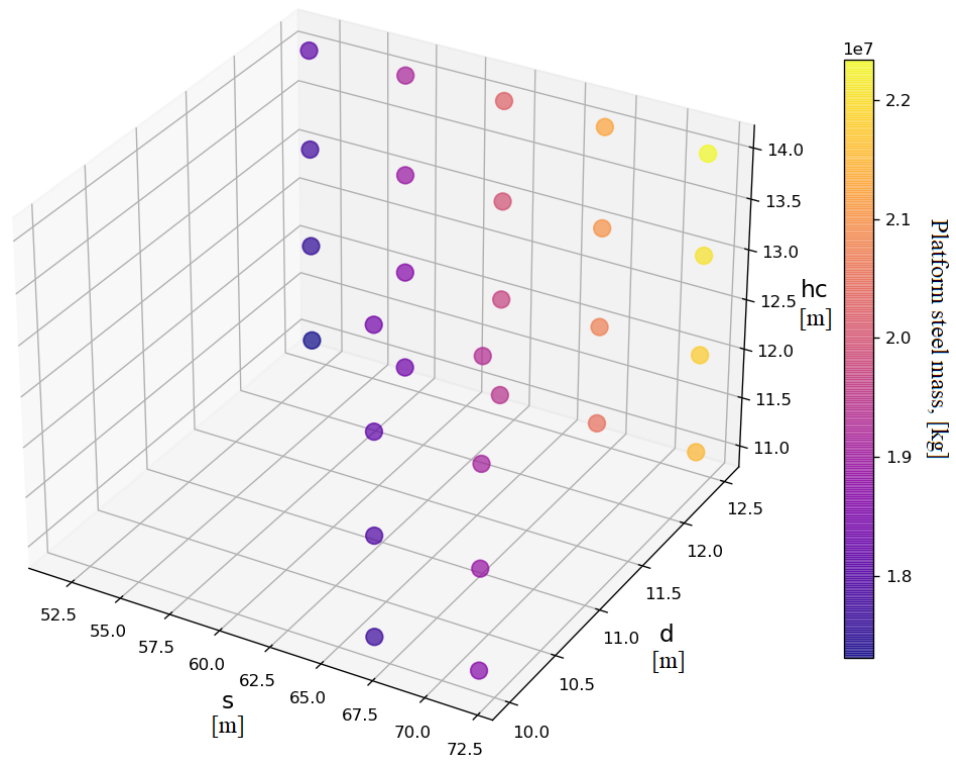
(b) for $hp = 7$m

Fig. 4-8: Platform steel mass versus design variables

(a) for *hp* = 6m

(b) for *hp* = 7m
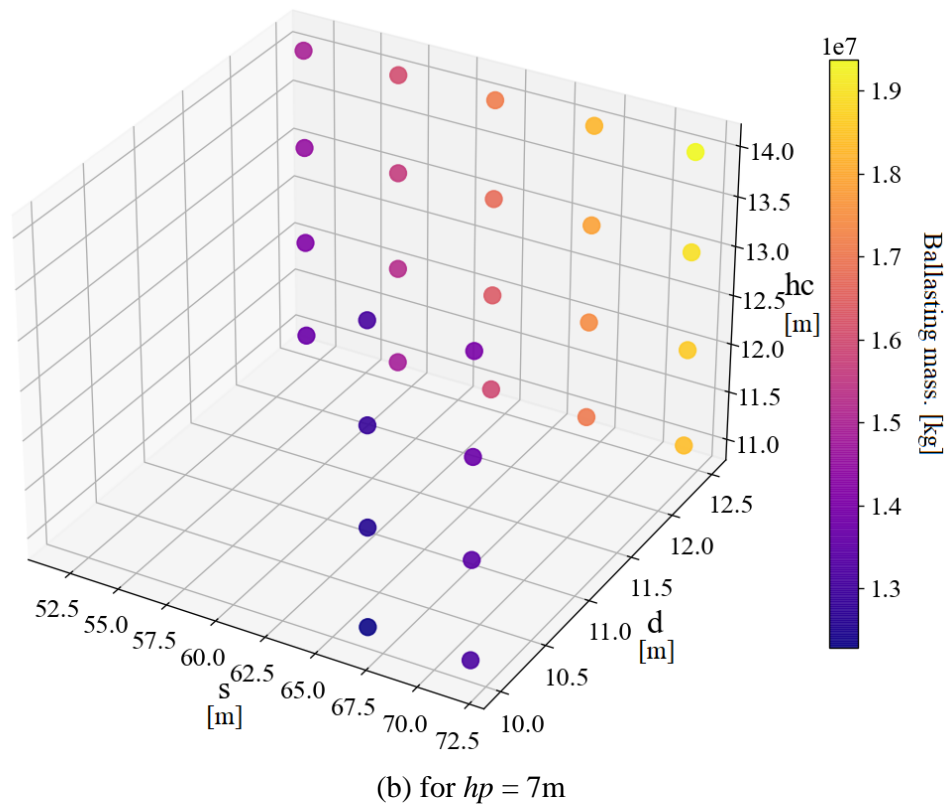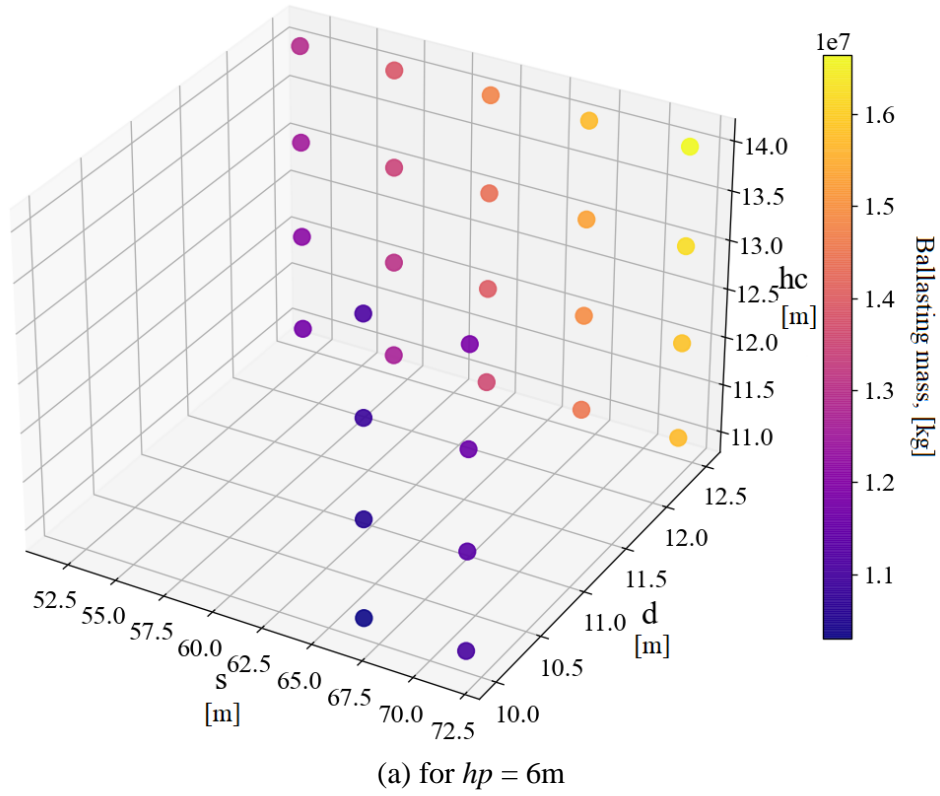
Fig. 4-9: Ballasting mass versus design variables

The following are some major outcomes from the hydrodynamic evaluations done in this chapter:

- The most influential design variables on hydrodynamic coefficients are column diameter (d) and column spacing (s).
- For a floater to be statically stable, (d) and (s) must be more than 10m and 31.75m respectively.
- The ballast mass has a significant effect on the floater's motion responses.

5. Optimization problem formulation

This chapter contains the definition of selected design variables, multi-objective optimization as well as sampling and optimization methods used in this work.

5.1   Optimization framework definition

The term optimization refers to the process of identifying one or more viable solutions that correspond to the extreme values of one or more objectives. In scientific studies, especially in engineering design, optimization procedures are critical. Many scientific fields, such as engineering, data analytics, and deep learning, rely on optimization. Single-objective optimization refers to a problem in which the goal is to identify the best solution to a single objective. There are several gradient-based and heuristic-based strategies for solving single-objective optimization issues. Aside from deterministic search approaches, stochastic search algorithms have helped to advance the science of optimization by making it easier to locate the global optimal solution. Evolutionary algorithms (EAs) are a type of algorithm that mimics nature's evolutionary principles and is becoming increasingly popular for solving hard optimization problems [32].

5.1.1   Design variables

The first stage in creating an optimization issue is to identify the underlying design variables, which are primarily changed during the optimization process. A design issue usually involves a variety of design aspects, some of which are critical to the design's success. These parameters are known as design variables in the optimization world. Other design variables usually determine whether other design parameters are fixed or fluctuate.

Structure parameterization is desirable because it minimizes the number of design variables that can be studied and conclusions formed about design possibilities to a manageable level. [33] is an example of a parametric study that takes into account a variety of platform designs. According to the sensitivity analysis done in [34], the column spacing and draft are the primary variables that are most associated with the dynamic responses. A sensitivity analysis is also carried out to determine how the pontoon height, submerged column height, and side column diameter affect the motion responses. The column spacing and diameter have significant effects on the motion response, according to the sensitivity study reported in Sec. 4.1.

In this thesis, only the hull geometry will be altered; the wind turbine will remain unchanged. The submerged height of the columns (hc), the diameter of the side columns (d), column spacing (s), and pontoon height (hp) are the four design factors addressed in this study (see Fig. 5-1). The dependent

variables that change when the design factors change are the draft, pontoon width, and ballast. The freeboard of 10m, center column diameter of 10m, and steel thickness of the pontoons and columns of 6mm are also considered. The design variables are shown in Table 5-1.

Table 5-1: Design variables

Design variables	Unit	Lower bound	Upper bound
Side columns diameter, d	m	10	12.5
Column spacing, s	m	31.75	71.75
Submerged column height, hc	m	11	14
Pontoon height, hp	m	6	7

(a)

(b)
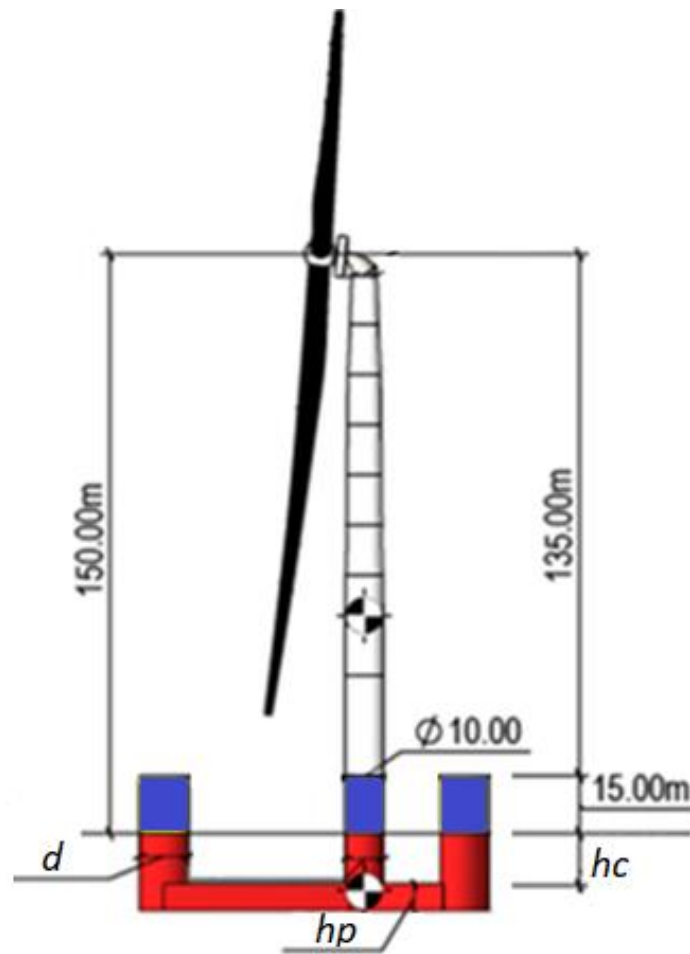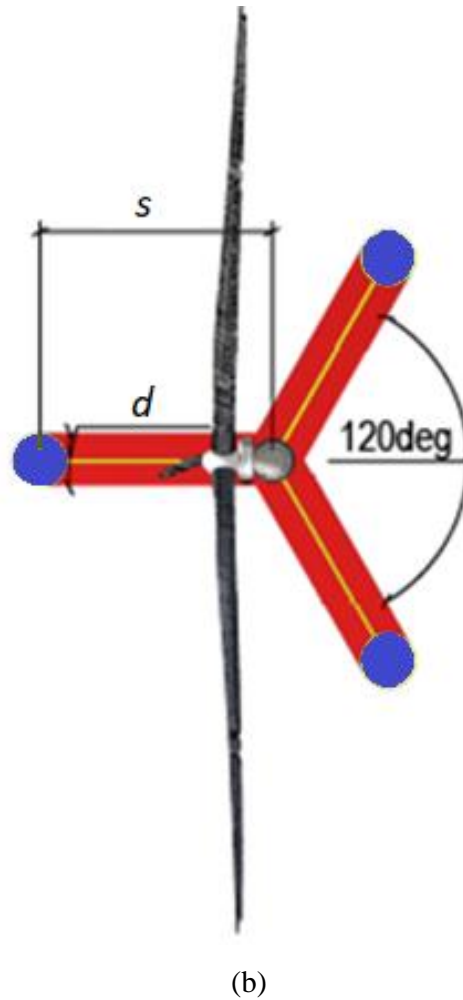
Fig. 5-1: Design variables of the UMaine VolturnUS-S reference platform [14]

5.1.2 Multi-objective optimization problems

A multi-objective optimization problem (MOOP) includes many objective functions that must be maximized or minimized. The MOOP, like single-objective problems, has a set of design constraints that must be met by an optimal solution. The general form of a multi-objective optimization problem can be stated as follows [32]:

$minimize \ f_m(\vec{x}). \ m = 1. 2 \cdots M$ objective functions

$subject \ to \ g_i(\vec{x}) \geq 0 \quad j = 1. 2 \cdots J$ nonlinear inequality constraints

$h_k(\vec{x}) = 0 \quad k = 1. 2 \cdots K$

$\vec{x}_i^L \leq \vec{x}_i \leq \vec{x}_i^U \quad i = 1. 2 \cdots N$

The solution $\vec{x}$ is an n-variable vector $\vec{x} = (x_1. x_2. \cdots x_n)^T$. The user will frequently limit the design variables to the lower and upper bounds $\vec{x}_i^L$ and $\vec{x}_i^U$, respectively. There are J inequality and K equality requirements in the problem above, which can be linear or nonlinear functions.

When all of the restrictions (J + K + 2N) are satisfied, a solution x is said to be viable. It is frequently convenient to apply the duality principle when there are M objective functions that need to be minimized and/or maximized. The latter argues that by multiplying the objective function by -1, we can change a maximizing problem into a minimization problem. Because many optimization methods are developed to handle one sort of problem, such as minimization problems, this is a viable strategy. When any of the objective or constraint functions are nonlinear, the resultant MOOP becomes a nonlinear multi-objective problem, which is a significant challenge. Until recently, there have been no proofs of convergence for the approaches used to tackle such issues. Unfortunately, most real-world MOOPs are nonlinear, posing a significant difficulty for researchers [32].

One of the most notable differences between single-objective and multi-objective optimization is that the objective functions, in addition to the typical decision variable space, form a multi-dimensional space in multi-objective optimization. The objective space is the name given to this extra space. There is a point in the objective space for each solution to x in the decision variable space. An n-dimensional solution vector and an m-dimensional objective vector are mapped together. Fig. 5-2 and 5-3 depict the decision and objective spaces, as well as the mapping between them [35].

As previously stated, the goal of multi-objective optimization issues is to find a set of solutions known as the Pareto optimal solution set, in which no two solutions can be dominated by each other. The goal is to minimize and/or maximize the objective functions of $f_1(x)$ and $f_2(x)$. Fig. 5-4 shows the non-dominated (p_1, p_2, p_3, p_4, p_5, and p_6) and dominated (p_7, p_8,..., p_{21}) solutions.

Furthermore, at least one point in the Pareto set must dominate any solution in the search space. The Pareto front is the most crucial result of multi-objective optimization, which presents the decision-maker with the most promising solutions. As a result, the ultimate goal of multi-objection optimization is to discover a set of solutions that are both close to and varied from the Pareto optimal front. Most MOOP algorithms employ the concept of dominance. Without going into too much detail, if both of the following conditions are met, a solution $\vec{x}_1$ is said to dominate $\vec{x}_2$.

1. The solution $\vec{x}_1$ is no worse than $\vec{x}_2$ in all objectives.
2. The solution $\vec{x}_1$ is strictly better than $\vec{x}_2$ in at least one objective.
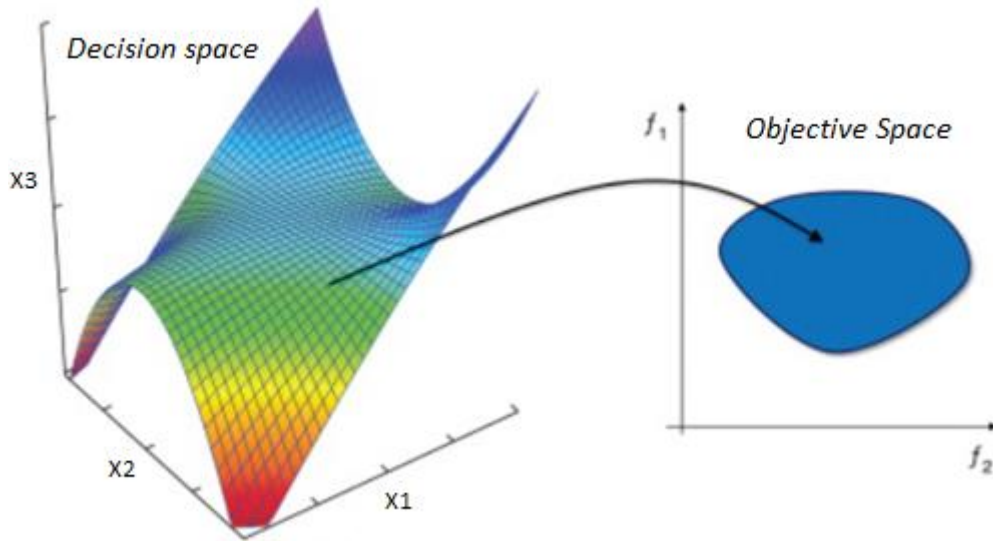
Fig. 5-2: Decision and objective spaces [35]
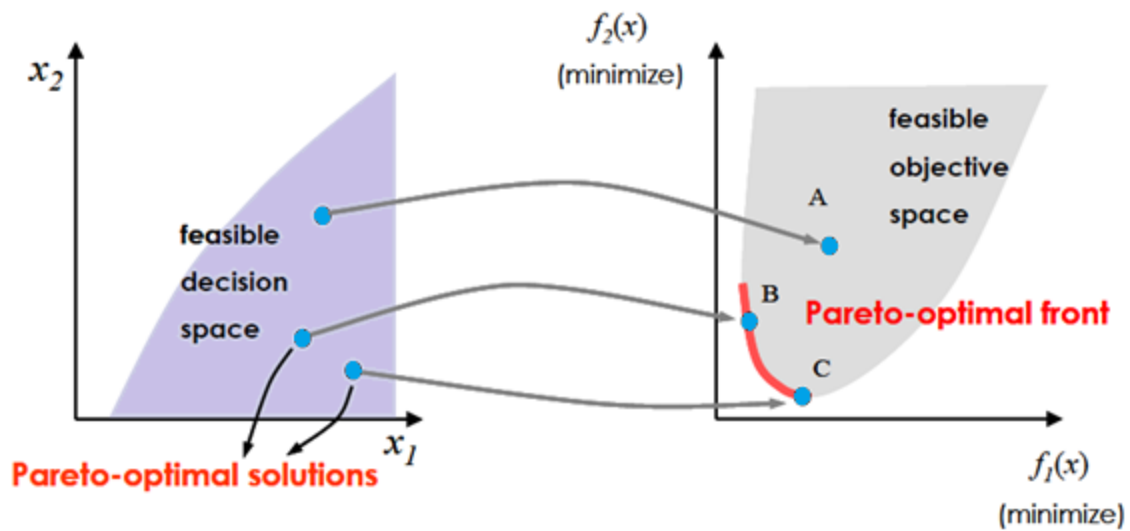
Fig. 5-3: Pareto optimal solution graph [36]
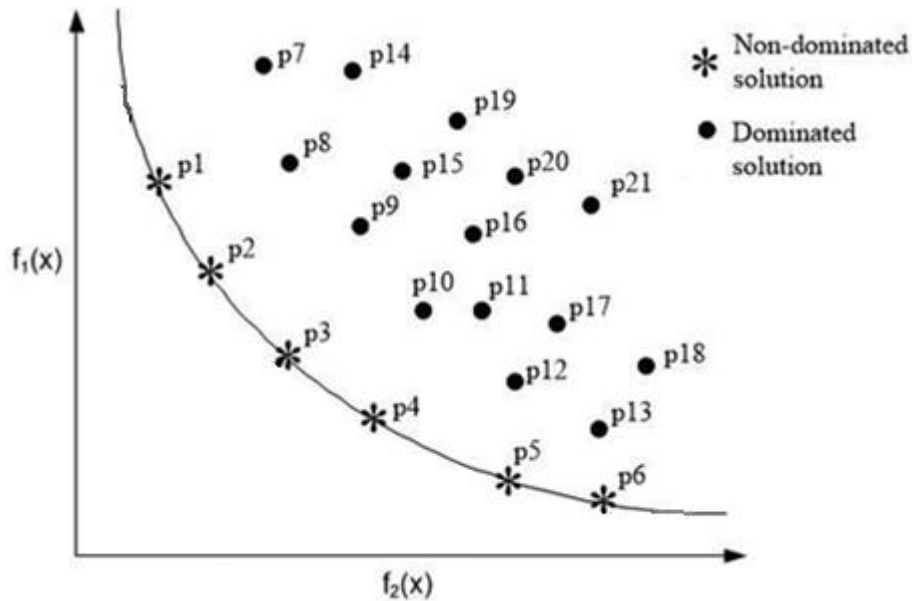
Fig. 5-4: The Pareto front for two objective functions [37]

5.1.3 Objective functions

Objective function 1 – the cost model

The stability of a floating structure improves with the size of the structure. The primary stumbling block is the cost of the structure. As a result, a meaningful representation of the design challenge requires accounting for the cost of the support structure. The first objective function is the cost of the support structure, and the purpose is to reduce the cost of the structure as much as possible; hence, minimize $f_1(x)$

$$f_1(x) = Cost = c_1$$ Eq. 5-1

c_1 – the cost of the platform structure

Because of the inexpensive materials that can be used as ballast, the cost of the ballast is not considered.

The cost of the platform structure (c_1):

The cost of the platform structure is related to the mass of the structure. In the simplest and linear method, this accounts for material, manufacture, and installation costs. Specific costs for various structural components are overlooked. The per-mass cost differences across columns, trusses, braces, and decks in a floating wind turbine platform study published with different cost values for different components differ by no more than 20% of the mean [38]. In this work, a cost of $2.50 per kg of steel is employed, based on the cost statistics, the per-mass material, and manufacturing costs reported in [39, 40]. A ballast cost is not employed due to the low cost of materials that can be used as ballast.

Objective function 2 – the RMS nacelle acceleration

Large platform vibrations in a floating wind turbine can potentially affect turbine lifetime or energy production. Another optimization aim utilized to account for this is the minimizing of platform vibrations that produce troublesome turbine loadings. The nacelle's acceleration is taken into account in this research. The significant fore-aft nacelle motion may place additional loads on the wind turbine, cause drivetrain wear, and reduce the system's lifetime [41]. The linearity of the reduced dynamic system was used to define the RAO of nacelle acceleration at each sea state condition in order to develop the second objective function. The root-mean-square (RMS) of the fore-aft nacelle acceleration [11] is the metric for platform motions that affects the wind turbines.

$$f_2(x) = RMS_{a_{nac}} = \sqrt{\int_0^\infty \left| RAO_{a_{nac}}(\omega) \right|^2 S_\zeta(\omega)\, d\omega} \qquad \text{Eq. 5-2}$$

where,

- $S_\zeta(\omega)$ (JONSWAP) is the spectral density of the waves at prescribed sea states (H_s and T_p)
- $RAO_{a_{nac}}(\omega)$ is the fore-aft nacelle acceleration response amplitude operator

$$RAO_{a_{nac}}(\omega) = -\omega^2(RAO_1 + h_{nacelle}\, RAO_5) \qquad \text{Eq. 5-3}$$

The numerical subscripts denote the platform degrees of freedom (DOFs) – 1 being surge and 5 being pitch – and $h_{nacelle}$ is the distance from the COG of the system to the nacelle.

5.1.4 Performance constraints

The majority of engineering optimization problems have a set of equality and inequality constraints, which might be linear or nonlinear. In general, addressing restricted optimization problems is more difficult than solving problems with no constraints. The following performance limits are utilized in this work to ensure that the candidate designs are realistic.

PC1) Initial metacentric height (GM0):

To preserve intact hydrostatic stability, the floater must have a GM equal to or greater than zero. Based on the DNVGL-ST-0119 Standard [42], a metacentric height larger than 1 m was adopted for the semi-submersible in this investigation. This GM is for a wind turbine that is in operation.

$$GM_0 > 1 \qquad \text{Eq. 5-4}$$

PC2) Static pitch angle due to the mean wind thrust (φ^{55}_{static}):

The effect of the wind on the turbine, which causes the tower to incline and a loss in energy production, is a significant consideration for preliminary design. The system must be stable within the conventional heel angle threshold value, as well as maintain an acceptable steady-state heel angle (less than 6°) in maximum static wind loading circumstances, or the wind turbine will lose significant efficiency [14]. The maximum static wind thrust was calculated to be 2,000,000 N, which is the steady-state push acting on the wind turbine hub at a rated wind speed of 11.4 m/s [43]. As seen here, the required restoring coefficient should be greater than the restoring coefficient required to limit the pitch to 6 degrees:

$$C_{55lim} > \frac{F_{thrust} \, h_{nacelle}}{\varphi^{55}_{static}} \qquad \text{Eq. 5-5}$$

where, F_{thrust} is the static wind thrust at rated wind speed and $h_{nacelle}$ is the hub height measured from the COG of the system. To satisfy this constraint, the geometry must have more pitch restoring coefficient than C_{55lim}. A sufficient restoring coefficient can be achieved by adjusting the dimensions of the substructure, and by adding more ballast. The hub height has been adjusted for each geometry with respect to the COG of the system.

PC3) RMS nacelle acceleration ($RMS_{a_{nac}}$):

The nacelle acceleration performance constraint is selected based on Ref. [33]. The common operational limit for the maximum allowable nacelle acceleration is 0.2g to 0.3g, where g = 9.81 $\frac{m}{s^2}$ is the gravitational acceleration. The tolerated acceleration highly depends on the specific turbine. As it is applied by Hall et al. [44], the standard deviation of the nacelle acceleration is selected as the second performance constraint used in the present research.

$$RMS_{a_{nac}} < 0.2g \qquad \text{Eq. 5-6}$$

5.1.5 Integrated design optimization

One of the most straightforward approaches is to combine multiple objective functions into one overall objective function by using weight coefficients. However, in practice, it is difficult to trade off the multiple goals and the final optimal results are highly dependent on the selected weights. To avoid these disadvantages, the widely-used surrogate-based multi-objective optimization algorithm is employed. The optimization procedure is performed by connecting the results from the hydrostatic calculations in Python as well as the results from the hydrodynamic simulations performed in NEMOH. The geometries are then subjected to the constraints (see chapter 5.1.4), whereas the geometries which not fulfill the criteria are eliminated. The optimization architecture is described in Fig. 5-5.

SALOME - NEMOH Automation

The SALOME and NEMOH interaction is usually used for only one geometry, whereas in this thesis *N* simulations are required. As described in Sec. 3.6, NEMOH allows for several modifications to be performed in the input file, however, in this thesis only the mesh file and the corresponding CoG need

to be updated in the NEMOH input file for each simulation. To simulate *N* geometries, an automated modeling script was created.

The approach requires several calculations to be performed for each simulation. The simulation architecture is shown in Fig. 5-5, and can be described in the following steps:

1. An initial design space, which contains 144 geometries, is created in the python based on Table 5-1

2. The performance constraints of PC1 and PC2 are applied to all geometries. Those geometries that pass the constraints have been sent to the meshing function to use SALOME to generate the mesh file. Simultaneously, the cost function is run to calculate the cost of the platform.

3. The .dat conversion script mentioned is then automated to convert the correct .dat file for NEMOH provided for each iteration.

4. The converted .dat file is then placed in the same folder as the nemoh.cal input file where the properties for the name of the mesh file, number of points and panels, and the location of the COG are changed accordingly for each iteration. Thus NEMOH is ready to run.

5. NEMOH is run, and the results are stored in folders with the name same as the mesh file.

6. After obtaining the hydrodynamic coefficients and wave excitation forces from NEMOH, the RAO Python function is run to get the RAOs.

7. After estimating the RAOs, the RMS function based on Eq. 5-2 is used to find the RMS nacelle acceleration for the particular geometry.

8. Once all objective functions are calculated, the surrogate function is run to find the Pareto front.

9. Using items on the Pareto front, the simulation is run again to get a converged result.
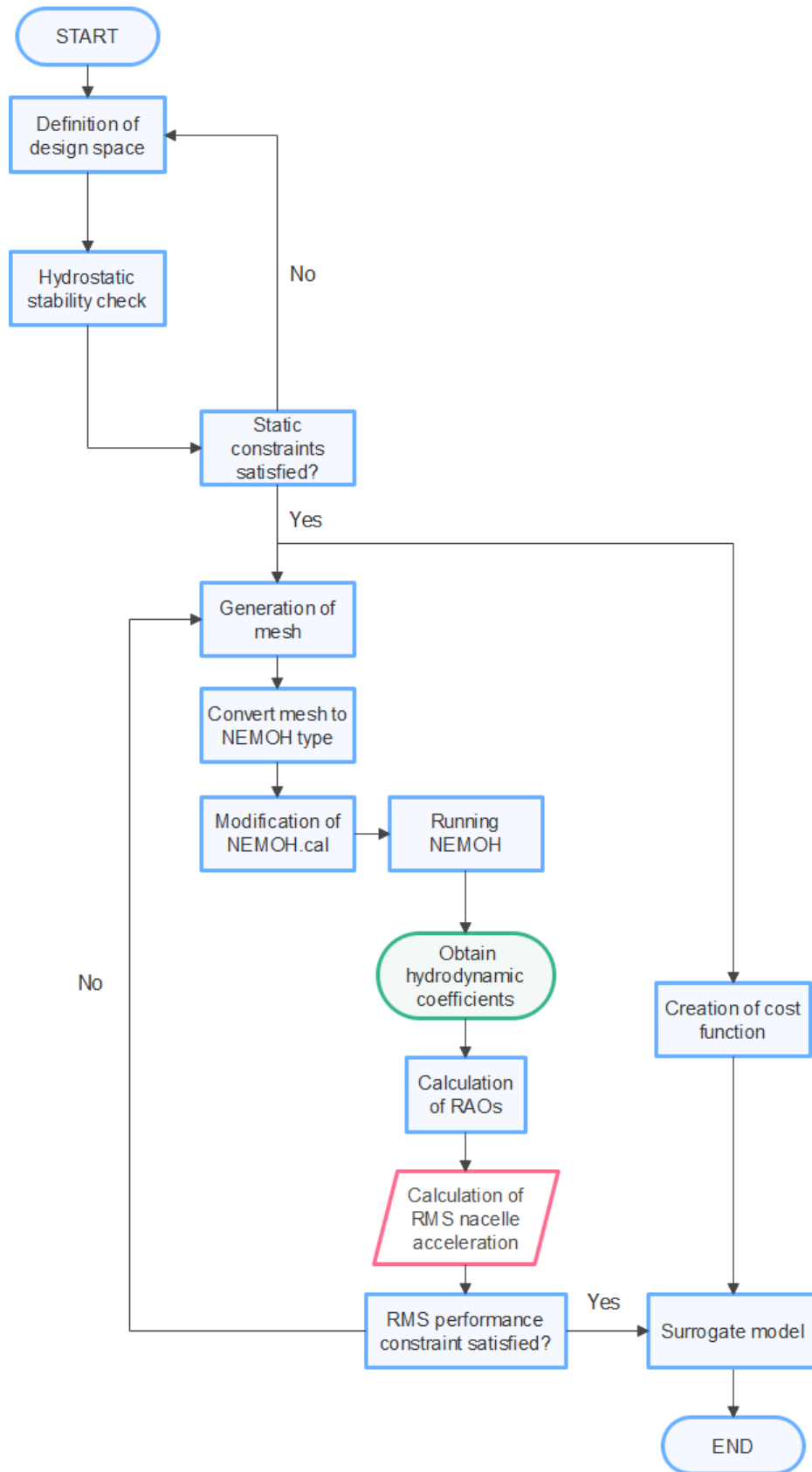
Fig. 5-5: Automated simulation flowchart

5.2 Response surface methodology

Response surfaces are commonly estimated using a second-order regression model since higher-order effects are frequently minor [45, 46]. In this work, we only use first-order regression to the response surface.

First-order response surface regression

Interpretation

Use the regression equation to describe the relationship between the response and the terms in the model. The regression equation is an algebraic representation of the response surface. The first-order regression equation with more than one term takes the following form:

$$y = b_0 + b_1 X_1 + b_2 X_2 + \cdots + b_k X_k \qquad \text{Eq. 5-7}$$

If the response surface contains curvature, then a polynomial model of a higher degree is used. The second-order model is:

$$y = \beta_0 + \sum_{i=1}^{k} \beta_i x_i + \sum_{i=1}^{k} \beta_{ii} x_i^2 + \sum_{i<j} \sum \beta_{ij} x_i x_j + \in \qquad \text{Eq. 5-8}$$

In the regression equation, the letters represent the following:

- y is the response variable
- b_0 is the constant
- b_1, b_2, ..., b_k are the coefficients
- X_1, X_2, ..., X_k are the values of the terms
- $\in$ is the error term

For a regression equation in coded units, the low level of a factor is -1 and the high level of a factor is $+1$. Because the equation is averaged over blocks, no coefficients for any blocks are in the equation.

5.3 Sampling

Sampling methods, also known as sampling plans, select the evaluation points to construct the initial surrogate. These evaluation points must be chosen carefully. A straightforward approach is full factorial sampling, where we discretize each dimension and evaluate all combinations of the resulting grid. This is not efficient because it scales exponentially with the number of input variables. For SBO, even with better sampling plans, using a large number of variables is costly. We need to identify the most important or most influential variables. Knowledge of the particular domain is helpful, as is exploring the magnitude of the entries in a gradient vector across multiple points in the domain. We can use various strategies to help us decide which variables matter most, but for our purposes, we assume that the most influential variables have already been determined so that the dimensionality is

reasonable. Having selected a set of variables, we are now interested in sampling methods that characterize the design space of interest more efficiently than full factorial sampling [47].

Latin Hypercube Sampling (LHS)

Latin hypercube sampling (LHS) is a common sampling approach based on a random process that is more effective and efficient than pure random sampling. Although random sampling scales better than complete factorial searches, it is prone to clustering and requires a large number of points to get the desired distribution (i.e., the law of large numbers). Fig. 5-6, for example, contrasts 50 randomly generated points in two dimensions over uniform distributions against Latin hypercube sampling. Each sample is independent of previous samples in random sampling, but with LHS, we choose all samples ahead of time to achieve a well-spread distribution.

Consider two random variables with boundaries, whose design space may be represented as a square, to explain the process. If we just needed eight samples, we could partition the design space into eight intervals in each dimension, resulting in the cell grid illustrated in Fig. 5-7.

A full factorial search would find a point in each cell, but this is inefficient on a large scale. A better search would be to have one sample in each row and column to be as efficient as feasible while yet covering the variety. To put it another way, the projection of points onto each dimension must be consistent. The projection of a homogeneous LHS onto each dimension, for example, is shown on the left side of Fig. 5-8. We can observe that the points form a histogram with a uniform distribution.
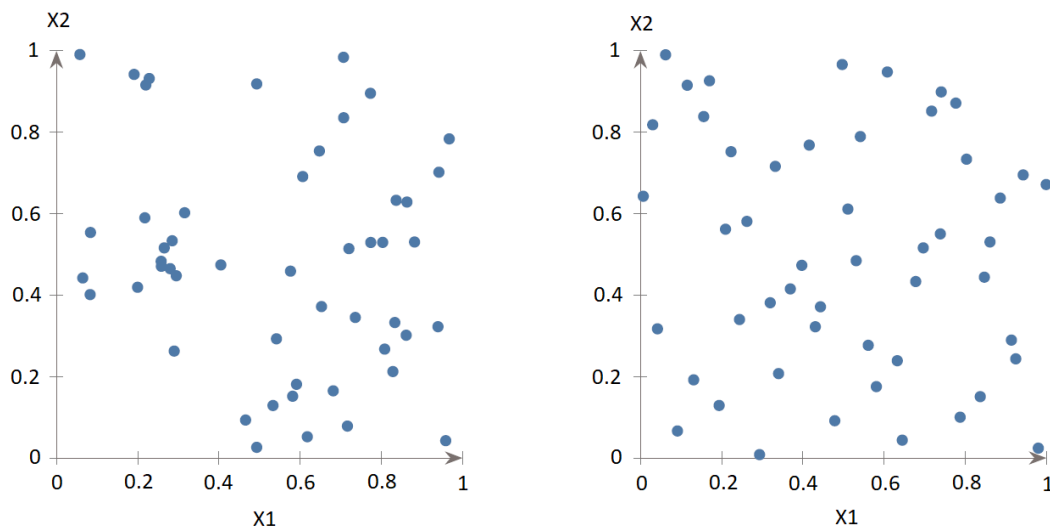
Fig. 5-6: Random and Latin hypercube sampling with 50 points using uniform distributions [47]
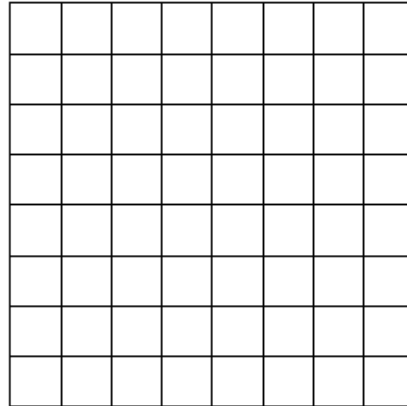
Fig. 5-7: In each dimension, a two-dimensional design space is divided into eight intervals [47]
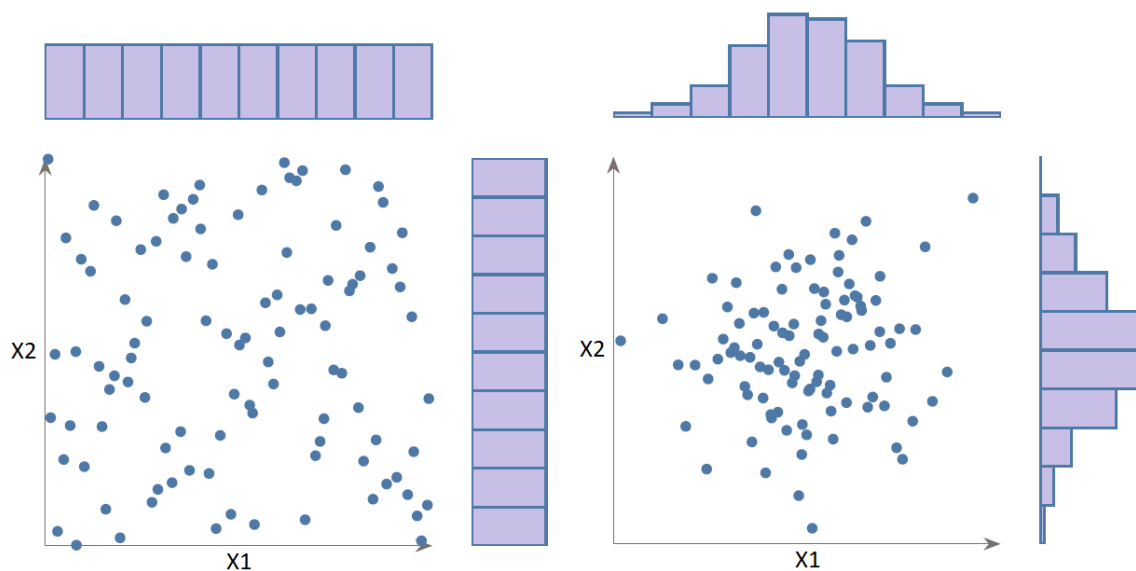
Fig. 5-8: Example LHS with projections onto the axes [47]

A Latin square is a concept in which one and only one point exists in each row or column, while a Latin hypercube is a generalization to higher dimensions. There are numerous options available, some of which are superior to others. Consider the sampling plan in Fig. 5-9 on the left. This plan fits our requirements, however, it does not cover the available area and will most certainly fail to express the relationships between design elements. The right side of Fig. 5-9, on the other hand, has a sample in each row and column while also spanning the space more effectively.

A sampling strategy with uniformly spans each dimension but does not fill the space well

A sampling strategy with uniformly spans each dimension and fills space more effectively
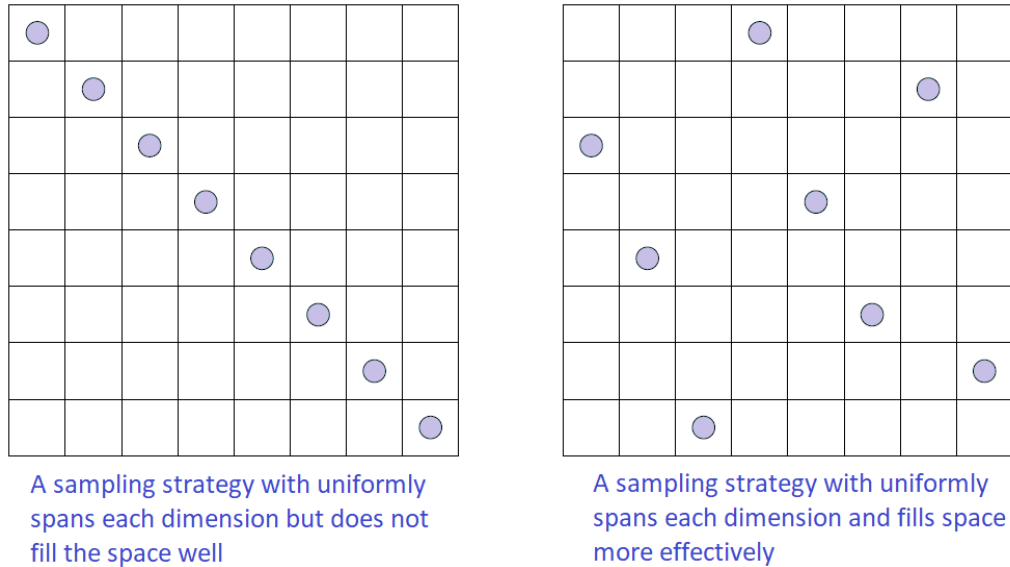
Fig. 5-9: Contrasting sampling strategies that both fulfill the uniform projection requirement [47]

LHS can be thought of as an optimization problem in which the goal is to maximize the distance between samples. The limitation is that each axis' projection must follow a specific probability distribution. The stated distribution is frequently uniform, as in the preceding examples, but it might be any distribution, such as a normal distribution. Because there is no unique solution to this optimization problem, random procedures are employed to decide the point combinations. Furthermore, points are typically not put at cell centers, but rather at random locations inside a cell to provide access to any point in the domain. The LHS technique has the advantage of enforcing the law of large numbers as a constraint rather than relying on it to fill out our selected probability distributions. Although this method may still necessitate a large number of samples to fully characterize the design space, it usually necessitates significantly less than pure random sampling.

5.4 Optimization methods

In this thesis, three methods are used for optimization and they are explained in detail in this section.

5.4.1 Surrogate model

Hydrodynamic performance calculations are often time-consuming and require additional memory and storage. Because of the hundreds or even millions of simulation evaluations required, routine activities like design optimization, design space exploration, sensitivity analysis, and what-if analysis become impossible. One strategy for alleviating this burden is to build approximation models (mathematical response surface models), also known as surrogate models, meta-models, or emulators, that mirror the behavior of the simulation model as exactly as possible while being computationally cheap(er) to evaluate. Surrogate models are created using a data-driven, bottom-up approach. As a result, it was thought that replacing full-optimization tools with surrogate models throughout the optimization process would be more efficient, as they provided a sufficiently accurate approximation of the hydrodynamic performance of each design option while consuming virtually no processing time. This strategy tries to make a connection between the input variables and the output of the goal function [48].

Surrogate models for optimization problems can be thought of as cost and state function approximation models that are built using sampled data gathered by randomly probing the design space. Following the creation of the surrogate models, an optimization technique can be used to determine which new candidate is most likely to be the best based on the surrogate models. Because prediction with a surrogate model is often substantially more efficient than prediction with a numerical analysis code, the computational cost associated with the search based on surrogate models is often trivial [49].

In this study, a commercial software called CAESES® from FRIENDSHIP SYSTEMS [50] is used. CAESES stands for "CAE System Empowering Simulation". CAESES® features several complex parameter studies and shape optimization strategies (such as response surface approaches) that are simple to use and integrate into the GUI. It has a batch mode and may be controlled by other optimization tools; it is simple to use and dependable. For optimization, the Dakota tool [51] is utilized. Improved sampling methodologies and strategies, such as surrogate models for robust design optimization, are part of this. No scripting or other programming abilities are required because CAESES® handles the full variation and data management process. The procedure of mapping to Dakota is shown in Fig. 5-10.
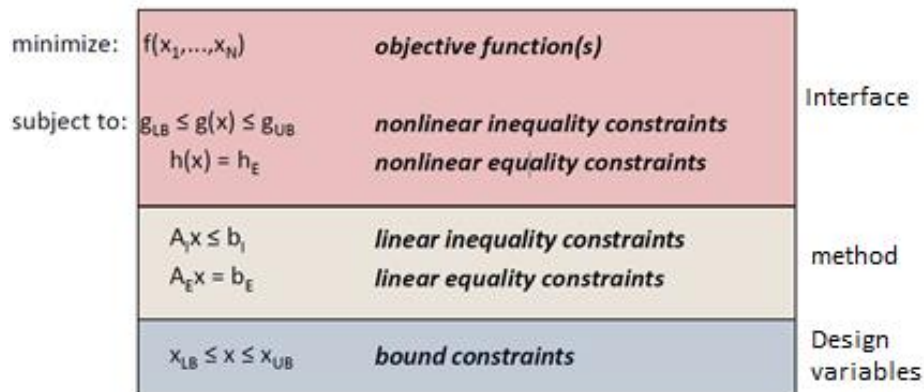
Fig. 5-10: Mapping to Dakota Input [52]

Kriging surrogate model

Generally, there are a large number of iterations for solving engineering optimization problems, making the optimization time-consuming, especially when the problem is complex. Surrogate model-based optimization provides an alternative approach for improving optimization efficiency, in which the Kriging model is one of the most used surrogate models because of its high accuracy for predicting nonlinear responses [49]. Kriging surrogate model includes two parts: polynomial function and random distribution. The approximate function expression of the Kriging surrogate model is:

$$\hat{y}(x) = f^T(x) \cdot \beta + z(x) \qquad \text{Eq. 5-9}$$

where β represents the regression coefficient vector. $f^T(x)$ is the polynomial of design variable vector x for representing the global approximation model of design space. $z(x)$ represents the random

distribution, which can be expressed as a random process with a mean of zero and a standard deviation of σ. Thus, the covariance matrix of random distribution z(x) can be expressed as:

$$Cov[z(x_i).z(x_j)] = \sigma^2 R \qquad \text{Eq. 5-10}$$

where R represents the correlation symmetric matrix with $n \times n$ order diagonal 1. $R(x_i.x_j)$ represents the spatial correlation equation of two random sample points x_i and x_j in n sample points, which plays an absolutely key role in the simulation accuracy. $R(x_i.x_j)$ can be expressed by the Gaussian correlation equation, which, featuring a good calculation effect, is widely used. It is formulated as:

$$R(x_i.x_j) = EXP\left(-\sum_{k=1}^{m} \lambda_k |x_{ik} - x_{jk}|^2\right) \qquad \text{Eq. 5-11}$$

where m represents the number of design variables. λ_k represents the correlation coefficient of the fitting surrogate model. x_{ik} and x_{jk} represent the kth value of x_i and x_j, respectively. To ensure the unbiasedness of the simulation process, after determining the correlation function, the relational expression of the estimated value $\hat{y}(x)$ of the approximate response, the regression coefficient matrix $\hat{\beta}$ and the estimated value $\hat{\sigma}^2$ of the variance can be obtained as follows:

$$\begin{cases} \hat{y}(x) = f^T(x) \cdot \hat{\beta} + r^T(X^*)R^{-1}(y - F\hat{\beta}) \\ \hat{\beta} = (F^T R^{-1} F)^{-1} F^T R^{-1} y \\ \hat{\sigma}^2 = \frac{(y-F\hat{\beta})R^{-1}(y-F\hat{\beta})}{n} \end{cases} \qquad \text{Eq. 5-12}$$

According to the above equations, the maximum natural estimation of parameter λ_k can be obtained as follows:

$$\max_{\lambda_k > 0}(\lambda_k) = -\frac{[n \ln(\hat{\sigma}^2) + \ln|R|]}{2} \qquad \text{Eq. 5-13}$$

Polynomial surrogate model

The surrogate-based optimization methods are often successful when using polynomial models, particularly quadratic models. However, a polynomial surface fit may not be the best choice for modeling data trends over the entire parameter space, unless it is known a priori that the true data trends are close to linear, quadratic, or cubic. See [49] for more information on polynomial models.

The form of the linear polynomial model is

$$\hat{f}(x) \approx c_0 + \sum_{i=1}^{n} c_i x_i \qquad \text{Eq. 5-14}$$

the form of the quadratic polynomial model is:

$$\hat{f}(x) \approx c_0 + \sum_{i=1}^{n} c_i x_i + \sum_{i=1}^{n} \sum_{j \geq i}^{n} c_{ij} x_i x_j \qquad \text{Eq. 5-15}$$

and the form of the cubic polynomial model is:

$$\hat{f}(x) \approx c_0 + \sum_{i=1}^{n} c_i x_i + \sum_{i=1}^{n} \sum_{j \geq i}^{n} c_{ij} x_i x_j + \sum_{i=1}^{n} \sum_{j \geq i}^{n} \sum_{k \geq j}^{n} c_{ijk} x_i x_j x_k \qquad \text{Eq. 5-16}$$

In all of the polynomial models, $\hat{f}(x)$ is the response of the polynomial model; the $x_i. x_j. x_k$ terms are the components of the n-dimensional design parameter values; the c_0 , c_i , c_{ij} , c_{ijk} terms are the polynomial coefficients, and n is the number of design parameters. The number of coefficients, n_c, depends on the order of the polynomial model and the number of design parameters. For the linear polynomial:

$$n_{c.linear} = n + 1 \qquad \text{Eq. 5-17}$$

for the quadratic polynomial:

$$n_{c.quad} = \frac{(n+1)(n+2)}{2} \qquad \text{Eq. 5-18}$$

and for the cubic polynomial:

$$n_{c.cubic} = \frac{(n^3 + 6n^2 + 11n + 6)}{6} \qquad \text{Eq. 5-19}$$

There must be at least n_c data samples to form a fully determined linear system and solve for the polynomial coefficients. In Dakota, a least-squares approach involving a singular value decomposition numerical method is applied to solve the linear system.

Artificial Neural Network surrogate model

The Artificial Neural Network surrogate in Dakota employs a stochastic layered perceptron artificial neural network [49].

The method is designed to have a lower training cost than traditional neural networks. This is a useful feature for surrogate-based optimization and optimization under uncertainty, where new surrogates are constructed many times during the optimization process (i.e., one surrogate for each response function, and new surrogates for each optimization iteration).

The neural network is a non-parametric surface fitting method. Thus, along with kriging (Gaussian Process) and MARS, it can be used to model data trends that have slope discontinuities as well as multiple maxima and minima. However, unlike kriging, the neural network surrogate is not guaranteed to exactly match the response values of the data points from which it was constructed.

This surrogate can be constructed from fewer than $n_{c.quad}$ data points, however, it is a good rule of thumb to use at least $n_{c.quad}$ data points when possible.

The form of the SLP ANN model is

$$\hat{f}(x) \approx \tanh\big(\tanh\big((xA_0 + \theta_0)A_1 + \theta_1\big)\big) \qquad\qquad \text{Eq. 5-20}$$

where x is the current point in n-dimensional parameter space and the terms $A_0.\theta_0.A_1.\theta_1$ are the matrices and vectors that correspond to the neuron weights and offset values in the ANN model. These terms are computed during the ANN training process and are analogous to the polynomial coefficients in a quadratic surface fit. A singular value decomposition method is used in the numerical methods that are employed to solve for the weights and offsets.

5.4.2 NSGA-II: Non-dominated Sorting Genetic Algorithm

NSGA-II is one of the most popular multi-objective optimization algorithms with three special characteristics, a fast non-dominated sorting approach, a fast crowded distance estimation procedure, and a simple crowded comparison operator. Generally, NSGA-II can be roughly detailed as the following steps. The principle of the NSGA-II algorithm is shown in Fig. 5-11, and its basic steps are as follows:
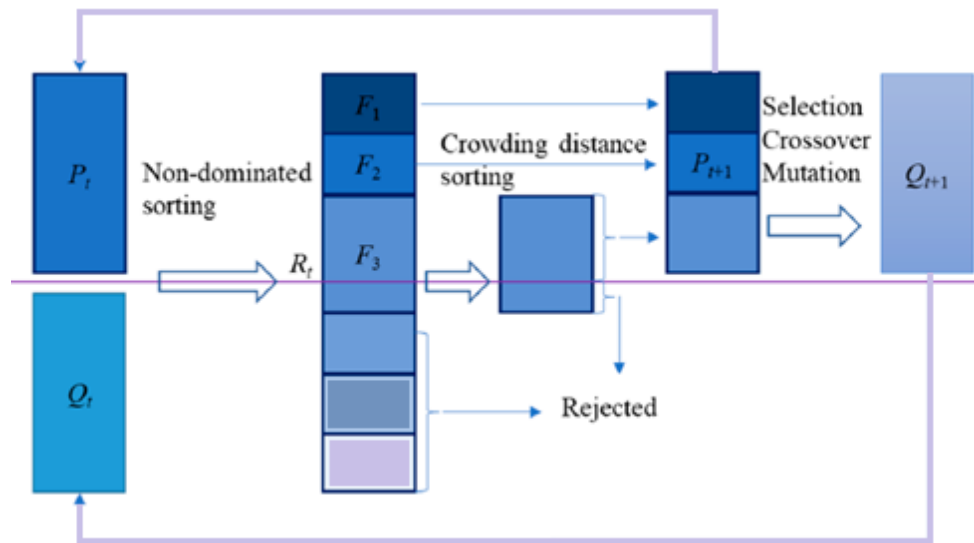
Fig. 5-11: Schematic diagram of NSGA-II algorithm [53]

Step 1: An initial population P_t of size, N is randomly generated at generation t = 0, and it is used to generate offspring population Q_t.

Step 2: A new population R_t with a size of 2N is obtained by merging P_t and Q_t. Then it is classified into several fronts (F_1, F_2, F_3, ...) based on non-dominated sorting. Meanwhile, the crowding distance of population individuals is calculated for each front.

Step 3: Select N suitable individuals from R_t according to non-dominated sort and crowding distance to form a new parent population P_{t+1}. In this step, the individuals with lower non-dominated ranks are first selected, and then the individuals with larger crowding distances are chosen.

Step 4: A new offspring population Q_{t+1} with a size of N is obtained from P_{t+1} by performing GA operators of selection, crossover, and mutation.

Step 5: The procedure from Step 2 is continued until the termination criterion is satisfied.

5.4.3   Weighted sum method

Before implementing the main optimization algorithm, it is a good practice to evaluate the performance of objective functions. The evaluation procedure is performed by connecting the results from the hydrostatic calculations in Python and the results from the hydrodynamic simulations performed in NEMOH. The geometries are then subjected to the constraints, whereas the geometries which not fulfill the performance constraints are eliminated. The weighted sum method is then applied to calculate the combined objective function. Lastly, the optimum geometry is selected subjectively from the Pareto Front. For more information, refer to [22].

To apply the weighted sum method, objective functions need to have the goal of obtaining the minimum value. Both objective functions are normalized with a value of 0 to 1. The combined objective function is formed by summing the weighted normalized objectives. This results in a single optimization objective as below:

$$minimize \; F(x) = \; w_1\overline{f_1(x)} + \; w_2\overline{f_2(x)} \qquad\qquad \text{Eq. 5-21}$$

where w_i is a weighting factor in the range [0; 1] that controls the weighting between the RMS nacelle acceleration and cost, with $\sum_{i=1}^{M} w_i = 1$. The bar indicates the normalized objectives.

To find the optimum geometries, 5 different weights are assigned between 0 and 1 for the combined objective function of the cost and RMS nacelle acceleration. Then Eq. 5-21 becomes:

$$minimize \; F(x) = \; w_1\overline{f_1(x)} + \; (1 - w_1)\overline{f_2(x)} \qquad\qquad \text{Eq. 5-22}$$

For $w_1 = [0, 0.25, 0.5, 0.75, 1]$

6. Results and discussions on optimization

6.1 Performance analysis

The RMS nacelle acceleration and the static platform pitch under a thrust load are shown for each point on the grid in Figures 6-1, 6-2, and 6-3. Only geometries that meet the performance requirements are shown. As expected, the RMS nacelle acceleration and static pitch angle decrease with increasing the submerged column height (hc) with the other variables being constant. Increasing (hc) causes a rise in GM, C_{55}, and the mass of the hull, which leads to a decrease in φ_{static}^{55} and a decrease in $RMS_{a_{nac}}$ according to Eq. 5-5, Eq. 2-61, and Eq. 5-2. In terms of performance constraints and objective functions, there are certain key results as follows:

It should be mentioned that while one variable changes, the rest of the variables remain fixed; however, the ballast mass is modified.

1. Increasing pontoon height (hp) by 16.5% (all other variables are kept constant) leads to:

- Decrease in $RMS_{a_{nac}}$ by 2.7% in EC5 and a 3.2% increase in $RMS_{a_{nac}}$ in EC2.
- Increase in cost of the platform by 2.7%.
- Increase in ballast mass by 17%.

2. Increasing side columns' submerged height (hc) by 9% (all other variables are kept constant) leads to:
- Decrease in $RMS_{a_{nac}}$ by 4.8% in EC5 and a 6.2% decrease in $RMS_{a_{nac}}$ in EC2.
- Increase in cost of the platform by 1.5%.

3. Increasing side columns' diameter (d) by 25% (all other variables are kept constant) leads to:

- Increase in $RMS_{a_{nac}}$ by 15.5% in EC5 and a 20% increase in $RMS_{a_{nac}}$ in EC2.
- Increase in cost of the platform by 16.3%.

4. Increasing column spacing (s) by 8.8 % (all other variables are kept constant) leads to:

- Increase in $RMS_{a_{nac}}$ by 8% in EC5 and a 9.8% increase in $RMS_{a_{nac}}$ in EC2.
- Increase in cost of the platform by 5.6%.

Considering the (hc) and (s) as the constant values, by increasing the d, the φ_{static}^{55} decrease. Based on the results, it can be interpreted that the most influential variable on the RMS nacelle acceleration is the column spacing. This is because a change in the column spacing has significant effects on the pitch RAO and consequently (according to the Eq. 5-2 and Eq. 5-3) on the $RMS_{a_{nac}}$. According to Fig. 6-1 and 6-2, a change in (hp) from 6m to 7m does not have significant effects on the RMS nacelle acceleration in different environmental conditions.

According to Fig. 6-3, the static pitch angle decreases significantly as (s) increases. The reason can be explained by the fact that by increasing (s), the GM indeed increases, and consequently the pitch stiffness, C_{55}, resulting in decreasing the static pitch angle. As we can see, there is a small variation in static pitch angle as the pontoon height changes from 6m to 7m.

Fig. 6-4 shows how the cost varies with the design variables for different pontoon heights (hp). The cost of the hull varies between 9.25 to 12.26 M€. The effects of the design variables on the cost are discussed in Sec. 6.2.
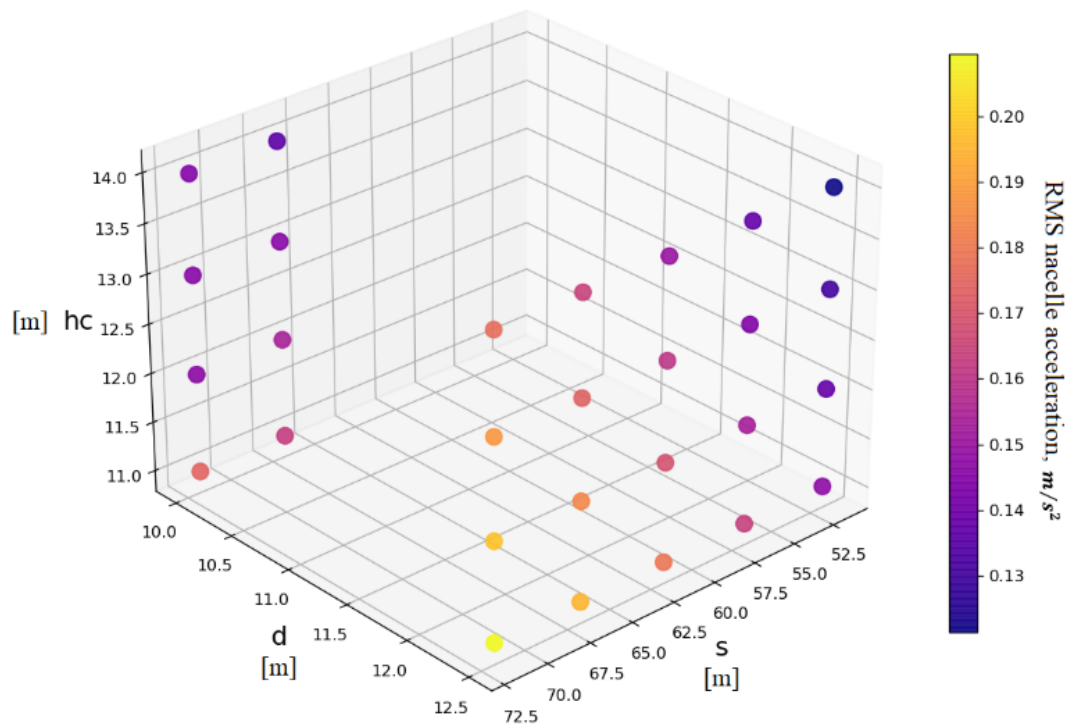
(a) for $hp = 6$m
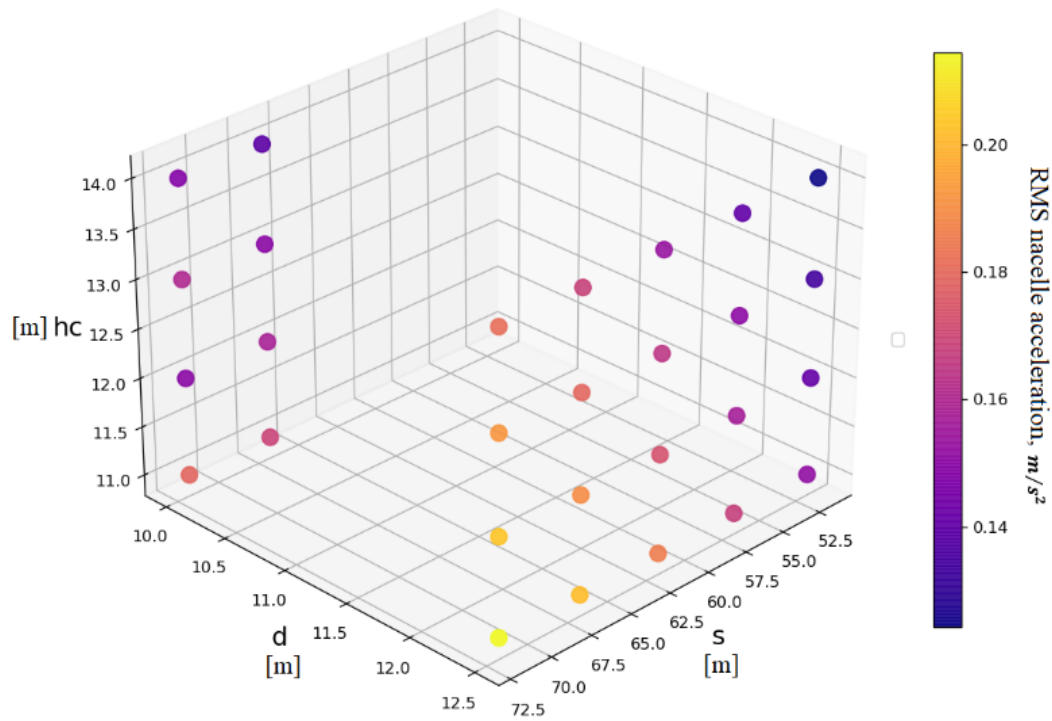
(b) for $hp = 7$m

Fig. 6-1: RMS nacelle acceleration versus design variables (EC2)
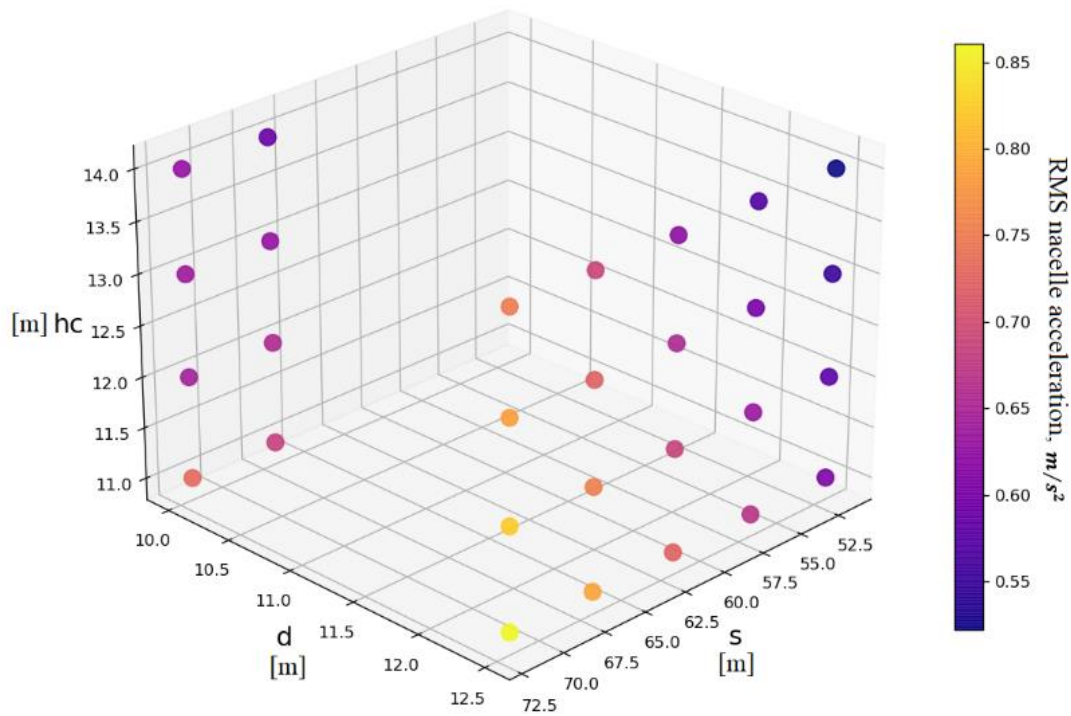
(a) for $hp = 6$m
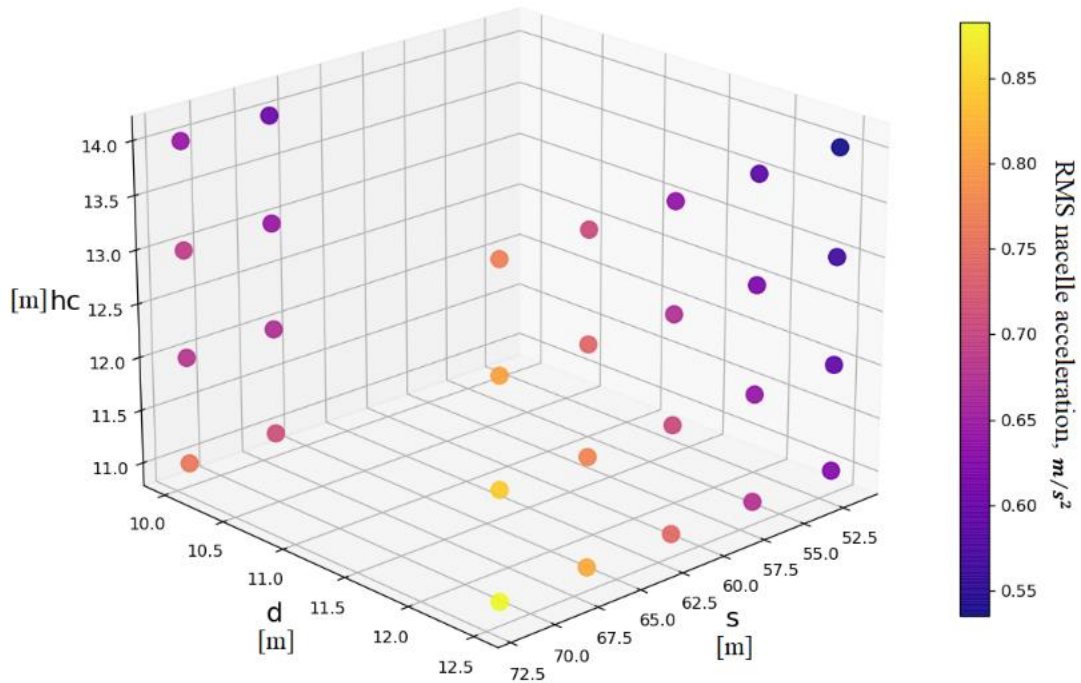
(b) for *hp* = 7m

Fig. 6-2: RMS nacelle acceleration versus design variables (EC5)
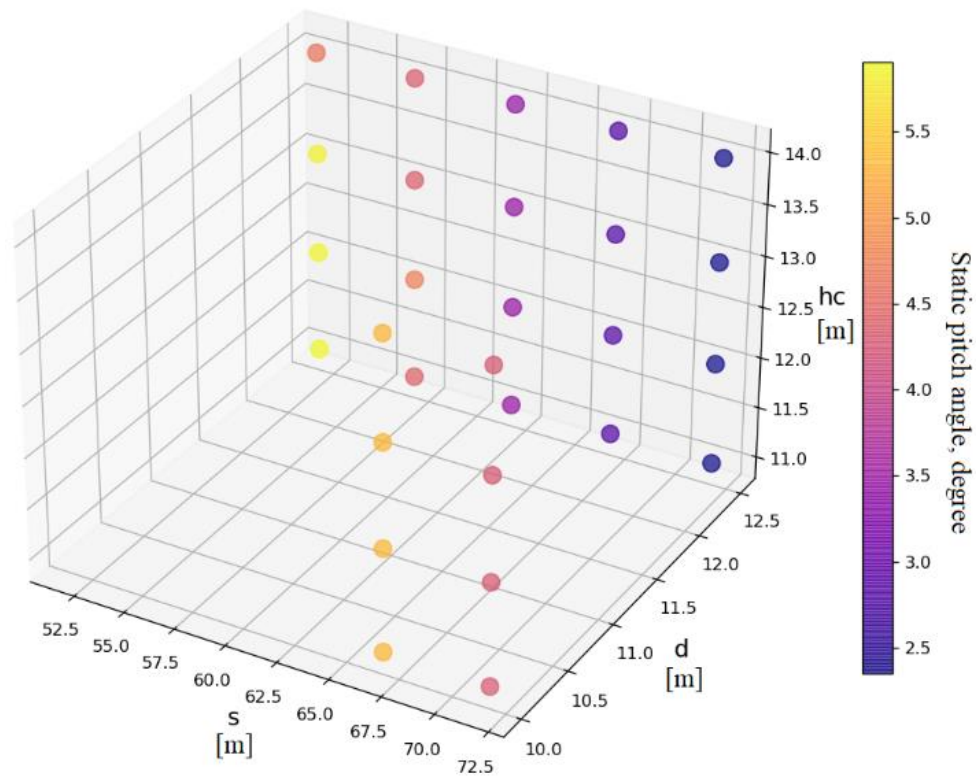
(a) for *hp* = 6m
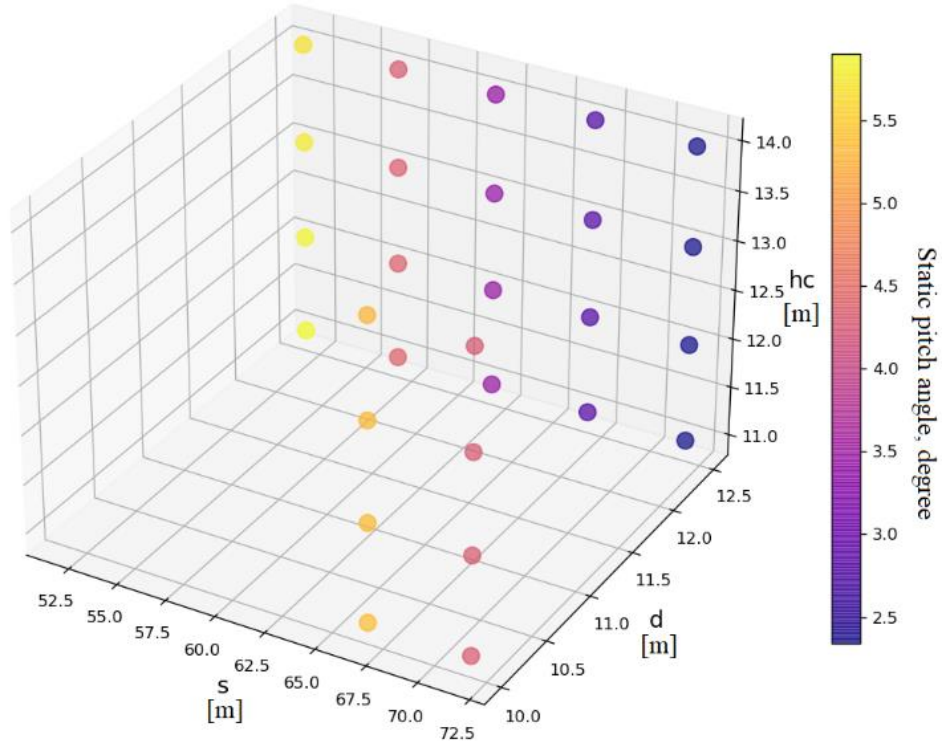
(b) for $hp = 7$m

Fig. 6-3: Static pitch angle versus design variables (at a wind speed of 11.4 m/s)
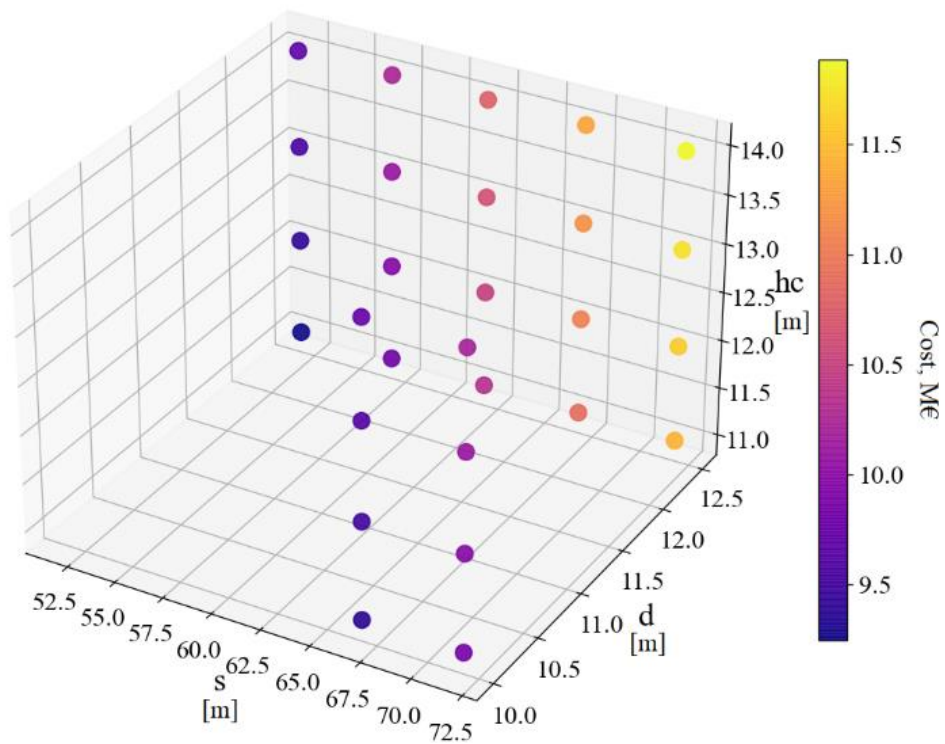
(a) for $hp = 6$m
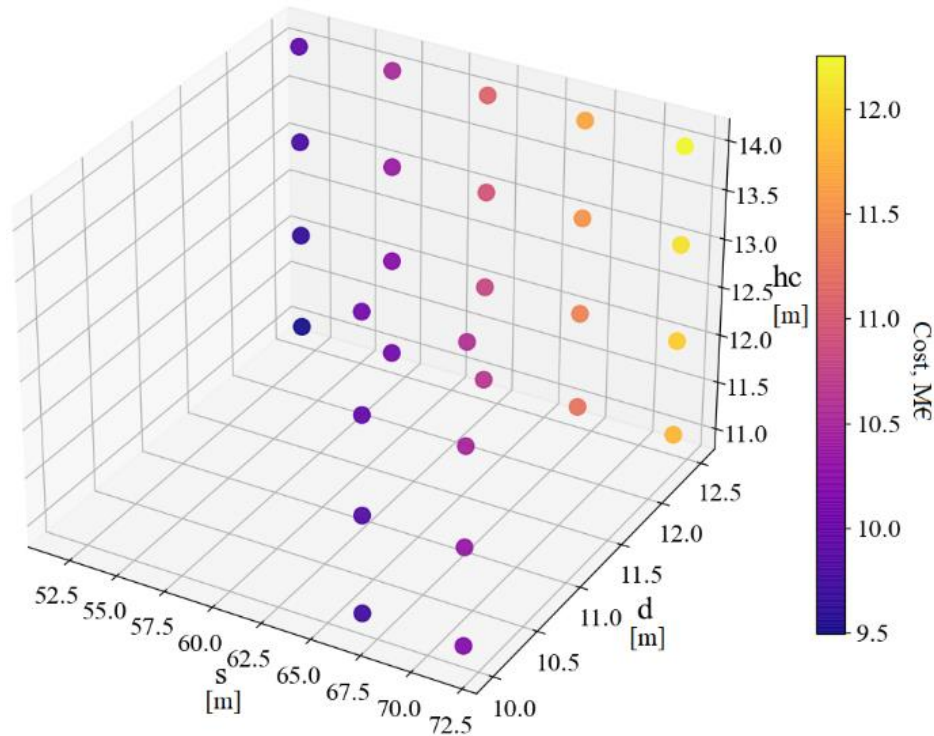
(b) for $hp = 7$m

Fig. 6-4: Cost versus design variables

6.2 Correlation matrix

Once all the necessary data (i.e. GM, cost, and RMS nacelle acceleration) for all geometries have been found, it is useful to investigate the correlation between them which allows us to have a global view of the more or less strong relationship between several variables. Table 6-1 shows the correlation matrix for variables in this study for different environmental conditions. As we can see, there is a strong positive correlation between the cost of the hull and its stability.

It has been found that the substructure becomes more stable as the dimensions and mass of the structure increase. The design variable that has the most influence on the cost is the column spacing (*s*). As we can see from Fig. 6-4, as the variable (*s*) changes, the pontoon steel volume changes considerably (box, half-cylinder, and triangle prism) which increases the cost of the hull significantly. The next influential variable on the hull cost is the column diameter (*d*). The reason is that as a variable (*d*) changes, all three columns change accordingly at the same time which increases the cost of the hull significantly.

There is a strong negative correlation between the RMS nacelle acceleration and the submerged column height. The RAO5 has a significant effect on the RMS nacelle acceleration (the hub height intensifies this effect).

It can be seen that there is a near-perfect negative correlation between the cost and φ_{static}^{55}. This can be explained by the fact that as the cost of the hull decreases (smaller hull) the static pitch angle increases, due to the decrease in submerged displaced volume and consequently C_{55}.

As we can see from correlation matrices, the only difference between these tables is related to the $RMS_{a_{nac}}$. The most significant change corresponds to the correlation between $RMS_{a_{nac}}$ and s. According to the sensitivity analysis performed in this thesis in Sec. 4.1, the column spacing, *s*, is the most influential variable on the hull's performance. Under the severe condition, EC5, changes in column spacing cause more significant changes in RMS nacelle acceleration than that under EC2.

Table 6-1: Correlation matrix for variables in the study under EC2 and EC5

	d	s	hc	hp	GM	φ_{static}^{55}	Cost	$RMS_{a_{nac}}$	Ballast mass
d	1								
s	0	1							
hc	0	0	1						
hp	0	0	0	1					
GM	0.2	0.7	0.03	-0.14	1				
$\boldsymbol{\varphi_{static}^{55}}$	-0.32	-0.65	-0.08	-0.04	-0.94	1			
Cost	0.42	0.54	0.2	0.2	0.85	-0.95	1		
$\mathbf{RMS}_{\mathbf{a_{nac}}}^{EC2}$	0.26	0.58	-0.49	0.1	0.76	-0.79	0.73	1	
$\mathbf{RMS}_{\mathbf{a_{nac}}}^{EC5}$	0.14	0.7	-0.44	0.1	0.81	-0.81	0.74	1	
Ballast mass	0.65	0.17	0.17	0.5	0.57	-0.75	0.88	0.58	1

6.3   Response surface regression under EC2

In this section, the regression equation is used to describe the relationship between the response (objective functions) and the inputs (design variables) in the work. The regression equation is an algebraic representation of the response surface.

6.3.1 $f_1(x)$ versus *d, s, hc, hp*

Regression Equation for objective function 1:

$$f_1(x) = 0.5674 + 0.13970 \text{ d} - 0.000373 \text{ s} + 0.02737 \text{ hc} - 0.00352 \text{ hp} - 0.000005 \text{ s}^2$$
$$+ 0.000116 \text{ hc}^2 + 0.005955 \text{ d*s} + 0.009389 \text{ d*hc} - 0.004633 \text{ d*hp}$$
$$+ 0.000012 \text{ s*hc} + 0.006032 \text{ s*hp} - 0.000093 \text{ hc*hp}$$

6.3.2 $f_2(x)$ versus *d, s, hc, hp*

Regression Equation for objective function 2:

$$f_2(x) = 0.469 - 0.0301 \, d - 0.00428 \, s - 0.0150 \, hc + 0.0048 \, hp - 0.000013 \, s^2$$
$$+ 0.000922 \, hc^2 + 0.000775 \, d*s - 0.000713 \, d*hc - 0.000108 \, d*hp$$
$$- 0.000110 \, s*hc + 0.000085 \, s*hp - 0.000338 \, hc*hp$$

The objective functions in CAESES software can be calculated using regression equations acquired from response surface regression analysis. This optimization analysis is discussed in the following section.

6.4 A sensitivity study on the objective functions under EC2

To perform optimization in this thesis, three different optimization approaches have been selected. The results of each approach are shown in a separate sub-section and the results are compared at the end.

6.4.1 Performance results based on the weighted sum method

According to the formulation of the weighted sum method mentioned in 4.2.1, the performance constraints for the 56 selected geometries in different environmental conditions are presented in Table 6-2. The combined objective function considers the cost and RMS nacelle acceleration of the semi-submersible structures, where all performance constraints are fulfilled. By evaluating the combined objective function, the geometries that minimize the objective function can be found.
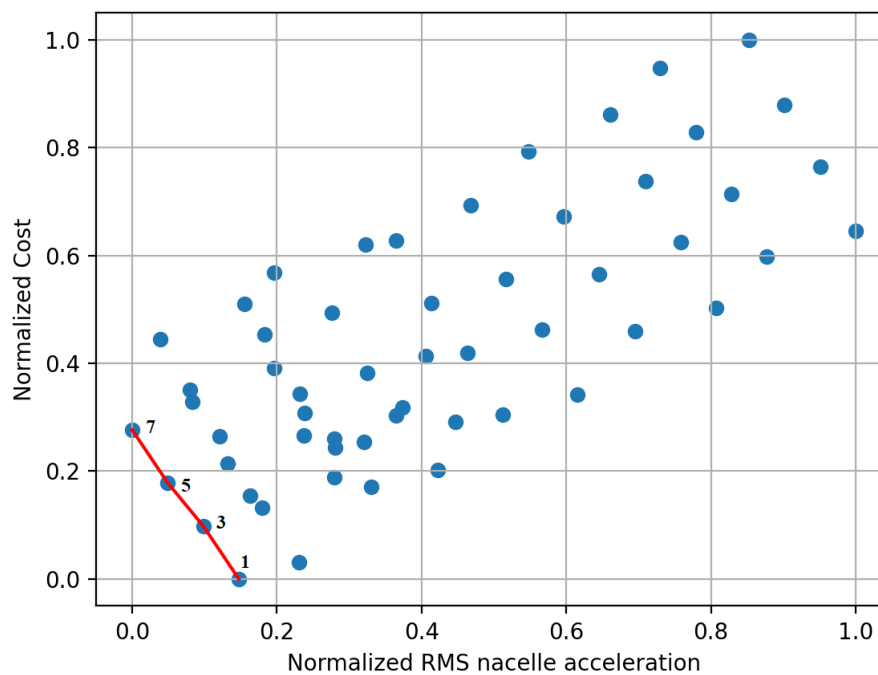
Fig. 6-5: Performance of different geometries under EC2 (red line represents the Pareto front) (weighted sum method)
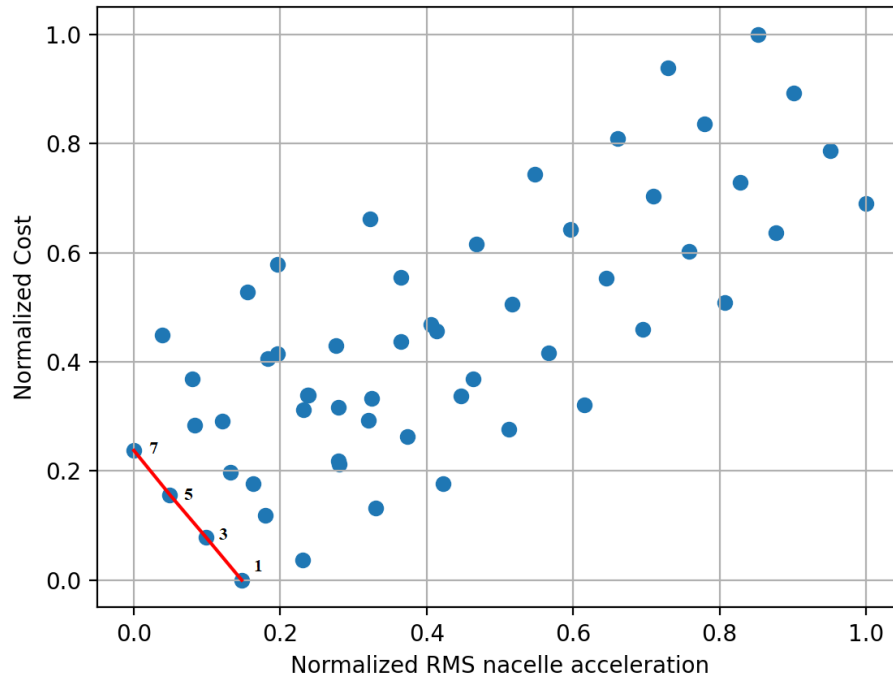
Fig. 6-6: Performance of different geometries under EC5 (red line represents the Pareto front) (weighted sum method)

As we can see from Fig. 6-5 and 6-6, the Pareto fronts in both environmental conditions are the same. Based on the weighted sum method, the environmental condition does not have any effect on the performance evaluation of the UMaine VolturnUS-S reference platform.

Table 6-2: Pareto front of optimal design points obtained from weighted sum method under EC2 and EC5 (non-normalized values)

index	[d, s, hc, hp] [m]	GM [m]	$RMS_{a_{nac}}(EC2)$ [g]	$RMS_{a_{nac}}(EC5)$ [g]	φ_{static}^{55} [degree]	steel weight [kg]
1	[12.5,51.75,11,6]	14.65	0.147	0.607	5.91	3698120
3	[12.5,51.75,12,6]	14.47	0.131	0.55	5.87	3757257
5	[12.5,51.75,13,6]	13.33	0.131	0.55	6.27	3816395
7	[12.5,51.75,14,6]	17.73	0.121	0.521	4.64	3875532

6.4.2 Performance results based on NSGA-II algorithm under EC2

The general settings for the NSGA-II optimization algorithm in the CAESES software are shown in Table 6-3.
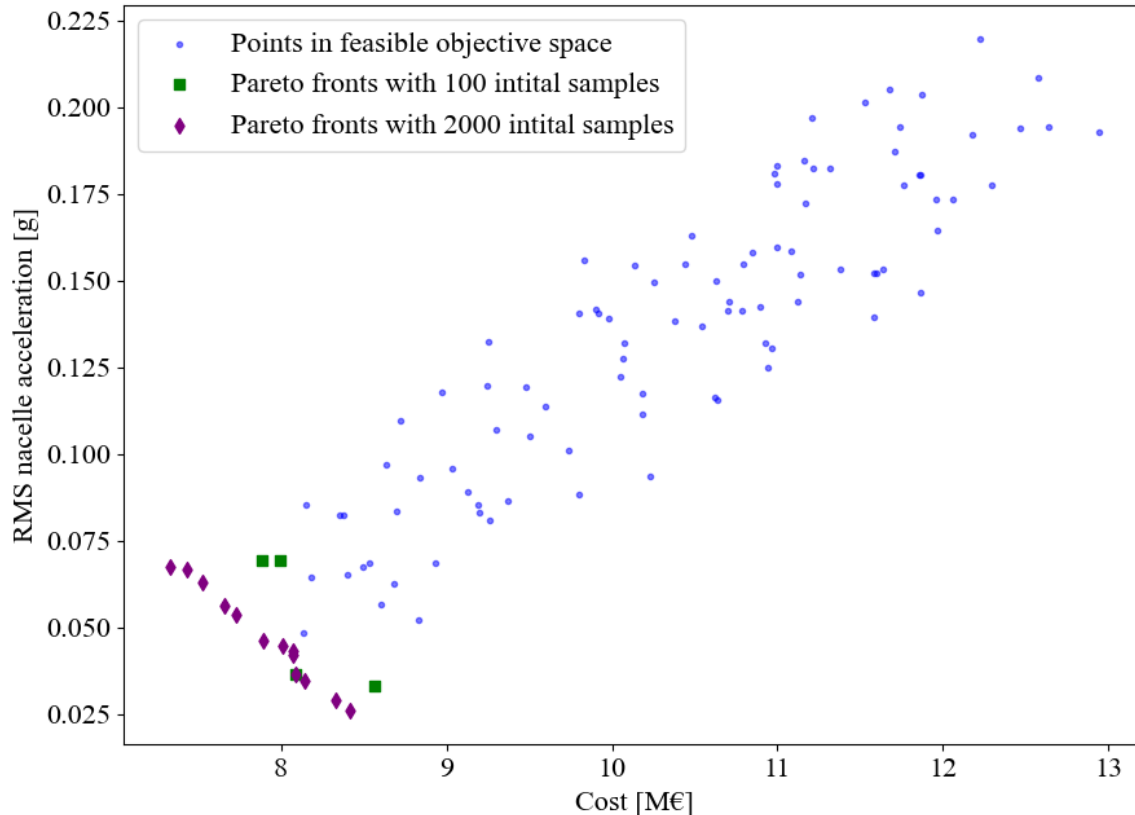
Fig. 6-7: Pareto front comparison with different initial samples for one generation

Before running the main optimization simulation, a sensitivity study is performed to investigate the effects of 'initial samples' and 'number of generations' on the Pareto front using NSGA-II. Fig. 6-7 and 6-8 show the results of this sensitivity study. As is shown in Fig. 6-7, the Pareto front is improved significantly as the number of initial samples increases. This can be explained by the fact that each iteration uses the previous results to improve the infeasible space and find the best geometry gradually. If we consider the Pareto front obtained when there are 2000 initial samples as a final one (purple rhombus), only one of the points of the Pareto front is correct when the initial samples are 100 (green rectangle).

The influence of the 'number of generations' factor on the Pareto front is shown in Fig. 6-8. As illustrated, the Pareto front becomes accurate as of the number of generations increases. For geometries with the RMS nacelle acceleration and cost of more than 0.06g and 7.5 M€ respectively, the optimal points in the Pareto front are more or less the same, however, there are more points once we increase the number of generations. According to this study, we may consider the number of generations and initial samples as critical factors in optimization settings.
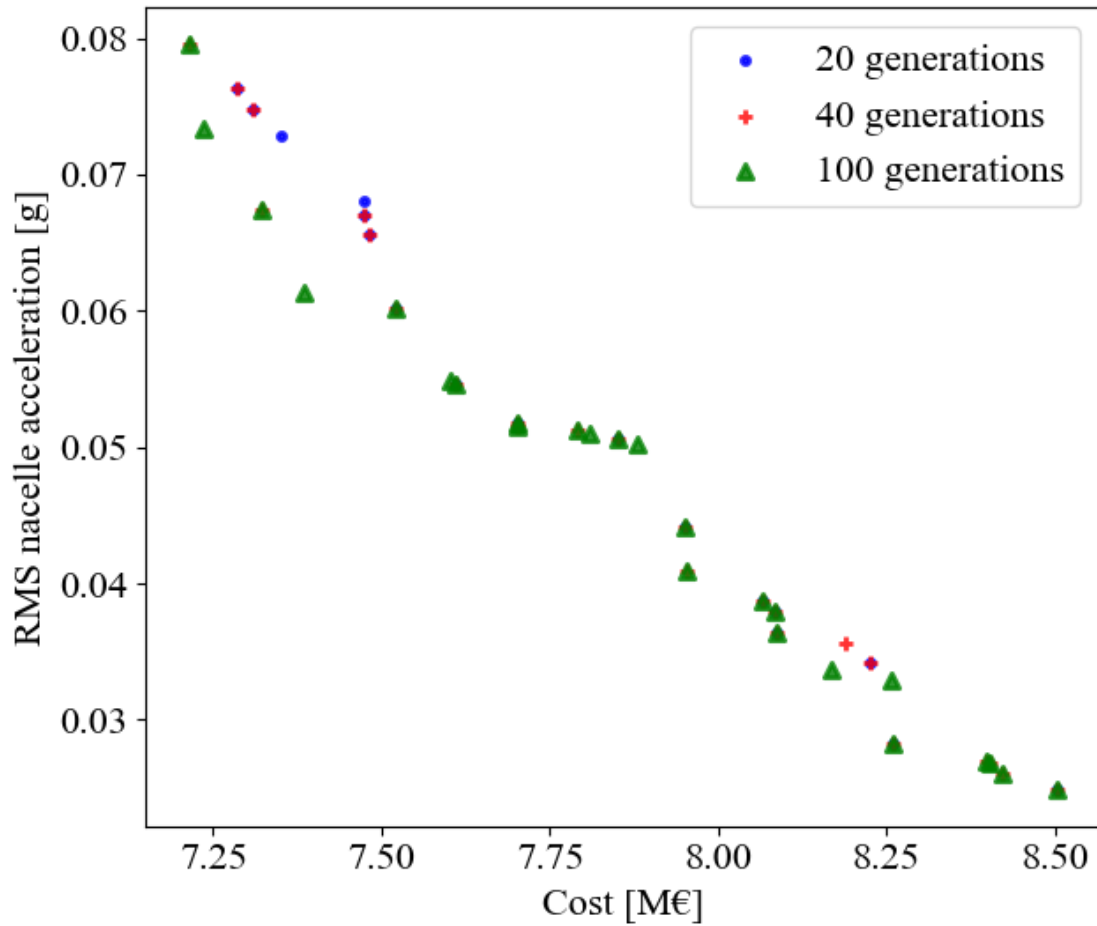
Fig. 6-8: Pareto front comparison with different numbers of generations for initial samples of 2000 (NSGA-II)

Table 6-3: General parameters in CAESES for NSGA-II

Setting	Value
Generations	100
Population size	100
Mutation probability	0.01
Crossover probability	0.9
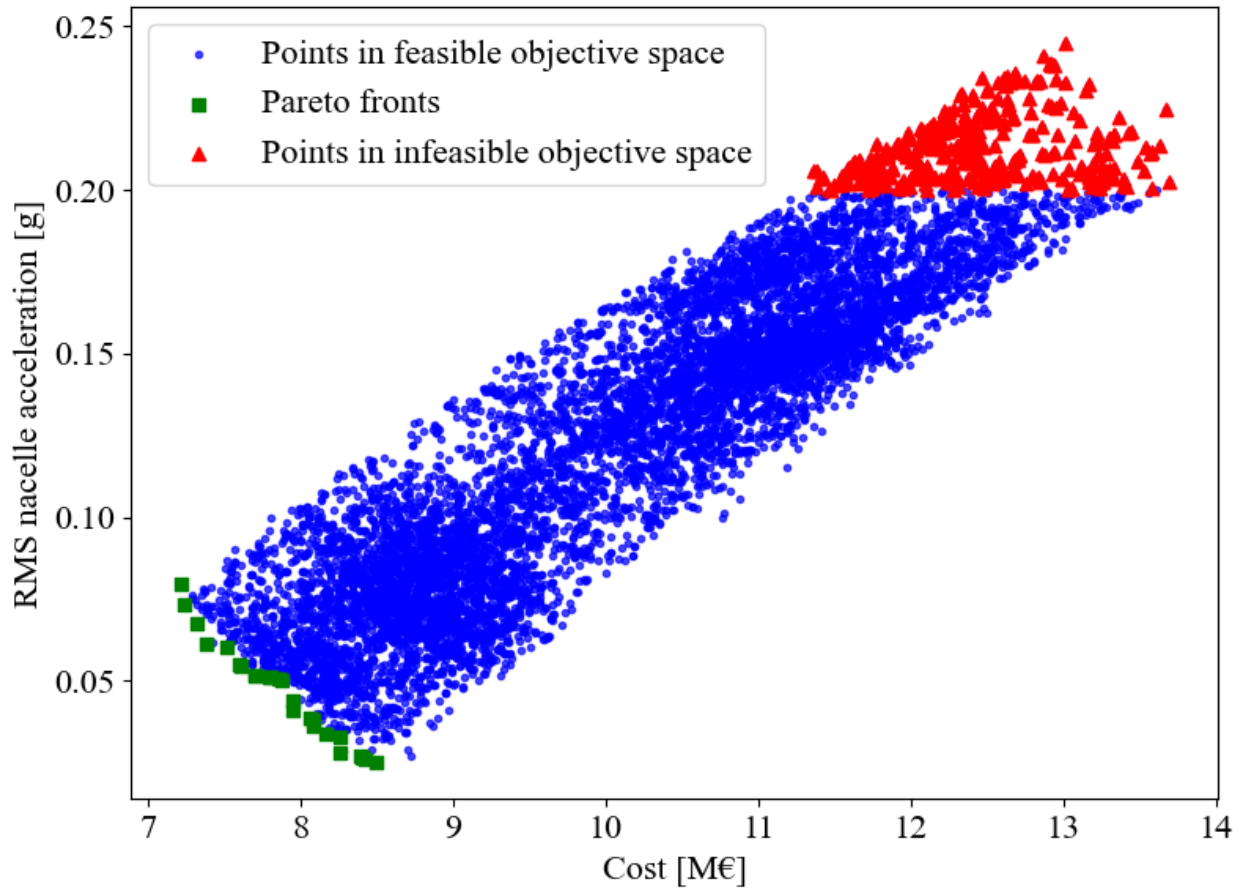
Fig. 6-9: Performance of different geometries using NSGA-II under EC2(100 generations)

Several simulations have been run to find the effects of the parameters of Table 6-3 on the Pareto front. The most influential item is the number of generations. Fig. 6-9 shows the Pareto front (green rectangles) obtained by the NSGA-II method. A total of 100 generations are performed in CEASES to analyze 9617 geometries. Red triangles show geometries that violate the performance constraint PC3.

The geometries in the Pareto front with their corresponding RMS nacelle acceleration and static pitch angle are shown in Table 6-4. The cost of the geometries in the Pareto front varies between 7 - 8 [M€] and the RMS nacelle acceleration between 0.028 - 0.066 [g]. This gives an overall overview of the future design of the semisubmersible platforms.

Fig. 6-10 shows a comparison of the critical variables (d) and (s) versus RMS nacelle acceleration for 2000 geometries.

Table 6-4: Pareto front of optimal design points obtained from NSGA-II under EC2

index	[d, s, hc, hp] [m]	$RMS_{a_{nac}}$ [g]	$Cost$ [M€]
1	[13.77,31.82,14.11, 6.15]	0.0364	8.085
2	[13.8,32.26,13.4, 6.42]	0.0419	8.07
3	[14.27,31.86,14.75, 6.16]	0.0257	8.415
4	[12.69,31.93,12.66, 7]	0.063	7.524
5	[12.72,31.8,12.05, 7.05]	0.0666	7.434
6	[13.8,31.95,12.52, 6.38]	0.0462	7.891
7	[13.07,32.15,13.24, 6.47]	0.0536	7.729
8	[14.1,31.9,13.53, 6.18]	0.0345	8.146
9	[14.04,32.56,12.8, 6.07]	0.0431	8.069
10	[12.67,32,11.95, 6.36]	0.0674	7.332
11	[14.15,31.79,14.44, 6.38]	0.0288	8.33
12	[13.64,32.52,13.5, 6.08]	0.0444	8.007
13	[13.11,31.83,12.6, 6.84]	0.0444	7.65
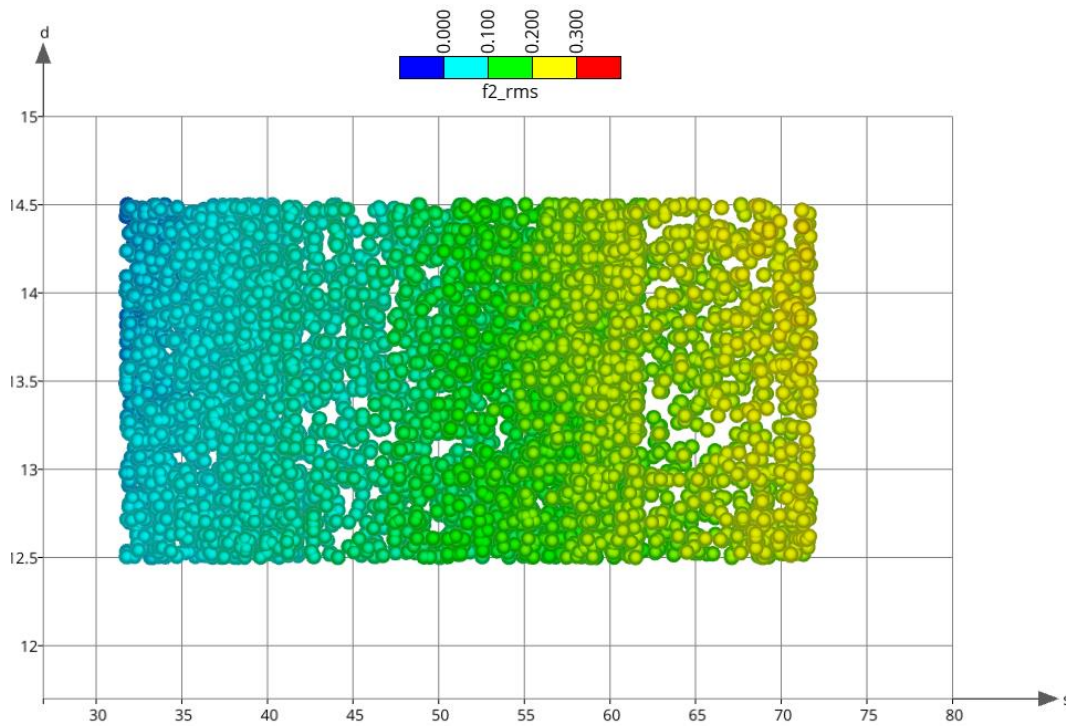
Fig. 6-10: Scatter diagram of a variation of RMS nacelle acceleration with two critical design variables (d) and (s)

The diagram can be used for a general overview of how the objective function values are spread for two design variables. In general, to have the RMS nacelle acceleration lower than 0.2g, we need to limit the column spacing (*s*) to less than 60m.

6.4.3 Performance results based on Global surface optimization under EC2

The general settings for global surface optimization methods (surrogate models) in the CAESES are shown in Table 6-5. The maximum number of optimal solutions to be considered after the optimization for this method is 30, however, based on the mathematical approximation model, this number can be different. Three approximation methods are used in global optimization algorithms and the results of each type are shown separately. Famous mathematical approaches for response surfaces are polynomial models, kriging (Gaussian process), radial basis functions, and neural networks.

Before performing the global optimization, design samples are created using Latin Hypercube Sampling in the Dakota Design Engine within CAESES. As we can see from Fig. 6-11, 2000 sample points based on input design variables are generated. In the next stage, Dakota generates a surrogate model based on the initial samples from the LHS method, runs a global optimization method on the surrogate model, and returns the Pareto front for each mathematical approximation method.
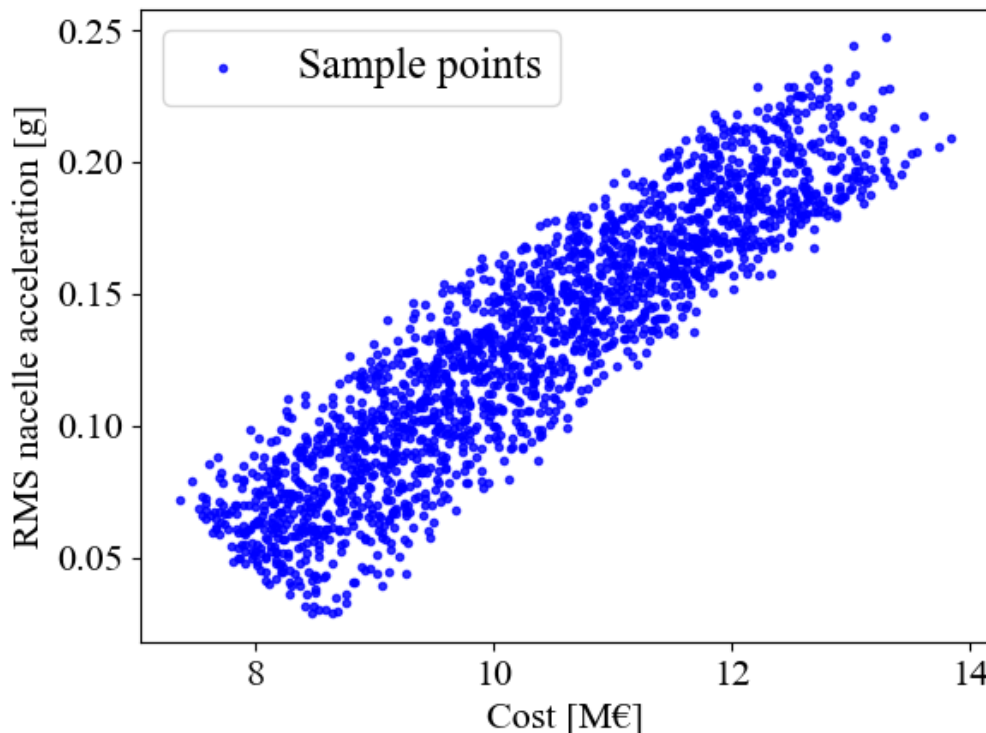
Fig. 6-11: Feasible design samples made by Latin Hypercube Sampling (LHS) under EC2
(initial samples: 2000)
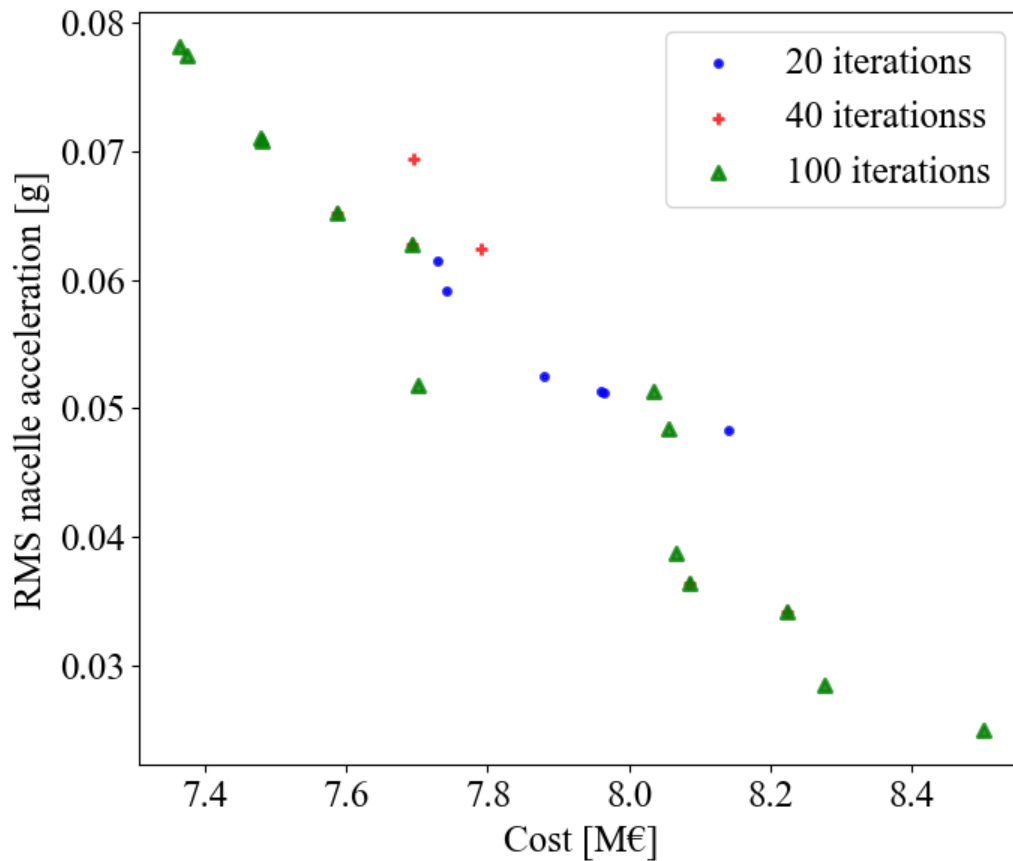
Fig. 6-12: Pareto front comparison with different numbers of iterations for initial samples of 2000 (Kriging model)

Fig. 6-13 (a-d) shows how the objective functions change with the variation of design variables. As can be seen in the Figures, most of the geometries in the Pareto front have a diameter between 12-13.5m, submerged column height of 11-13m, pontoon height of 6-7m, and column spacing of 30-35m.

Table 6-5: General settings in CAESES for Surrogate model

Setting	Value/Description	Remark
method	Global/Local optimization on response surface	Surrogate model global optimization
Iterations	100	The number of optimization runs on the response surface. In each iteration, a response surface is created and optimization is run on this model. One iteration means that the model is created only once and the optimization on this model is run only once.
Solutions considered	30	This is the maximum number of optimal solutions to be considered after each optimization on the response surface i.e. picked from the Pareto front.
Use result pool	yes	Existing designs from the resulting pool i.e. previous runs will be used for the generation of the initial response surface
Initial pollution size	2000	The number of designs in the initial population emulated in MOGA (Multi-objective Genetic Algorithm) procedure on the latest response surface.
Approximation type	Kriging/ Quadratic polynomial/Artificial Neural Network	
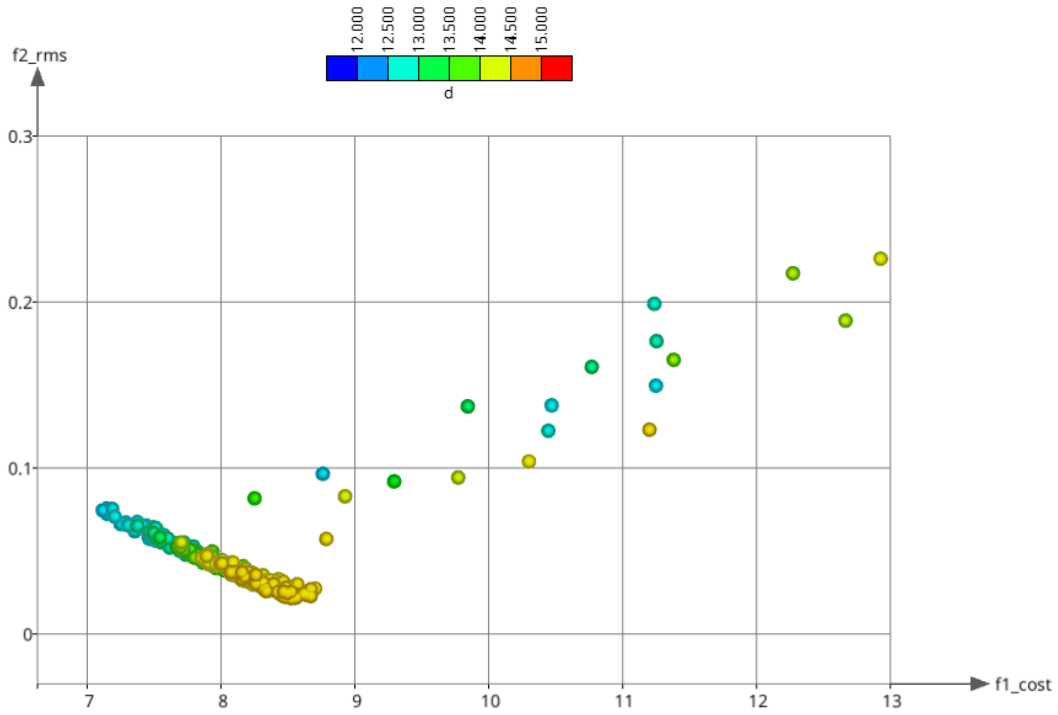
(a) vs. '*d*'
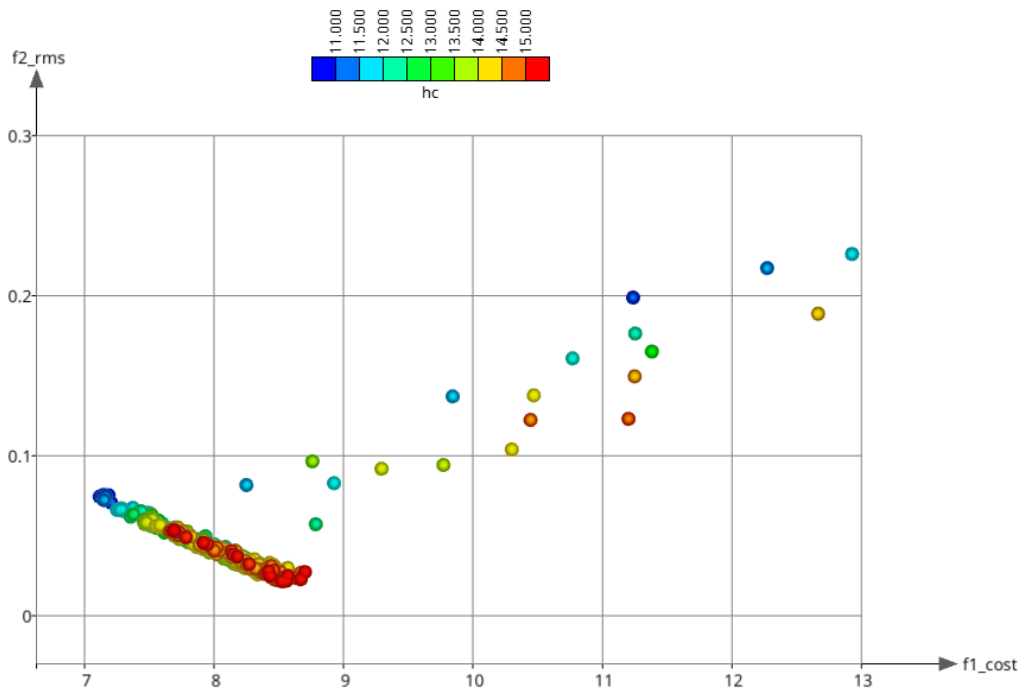
(b) vs. '*hc*'
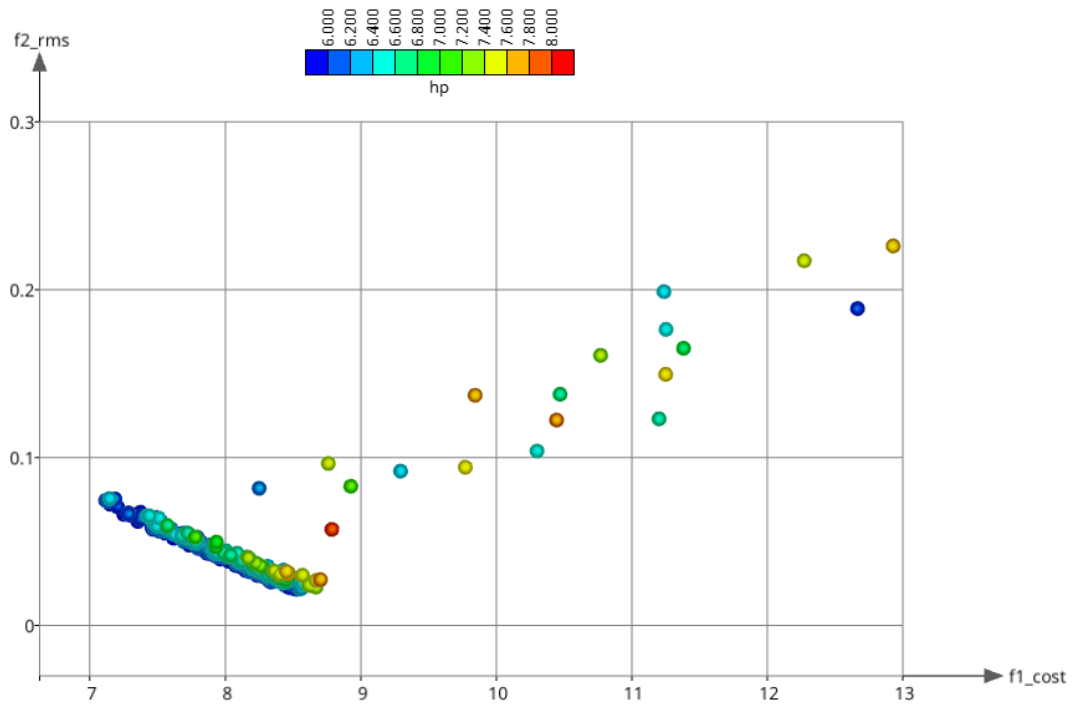
(c) vs. '*hp*'
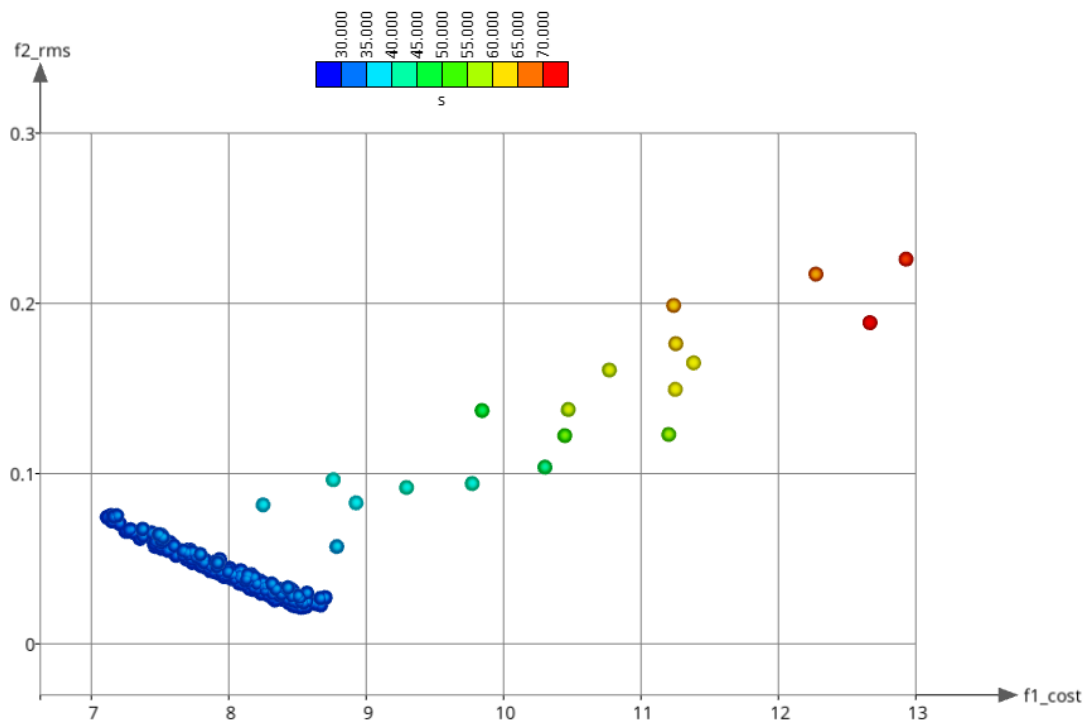
(d) vs. '*s*'

Fig. 6-13: Objective functions colored based on design variables' values under EC2
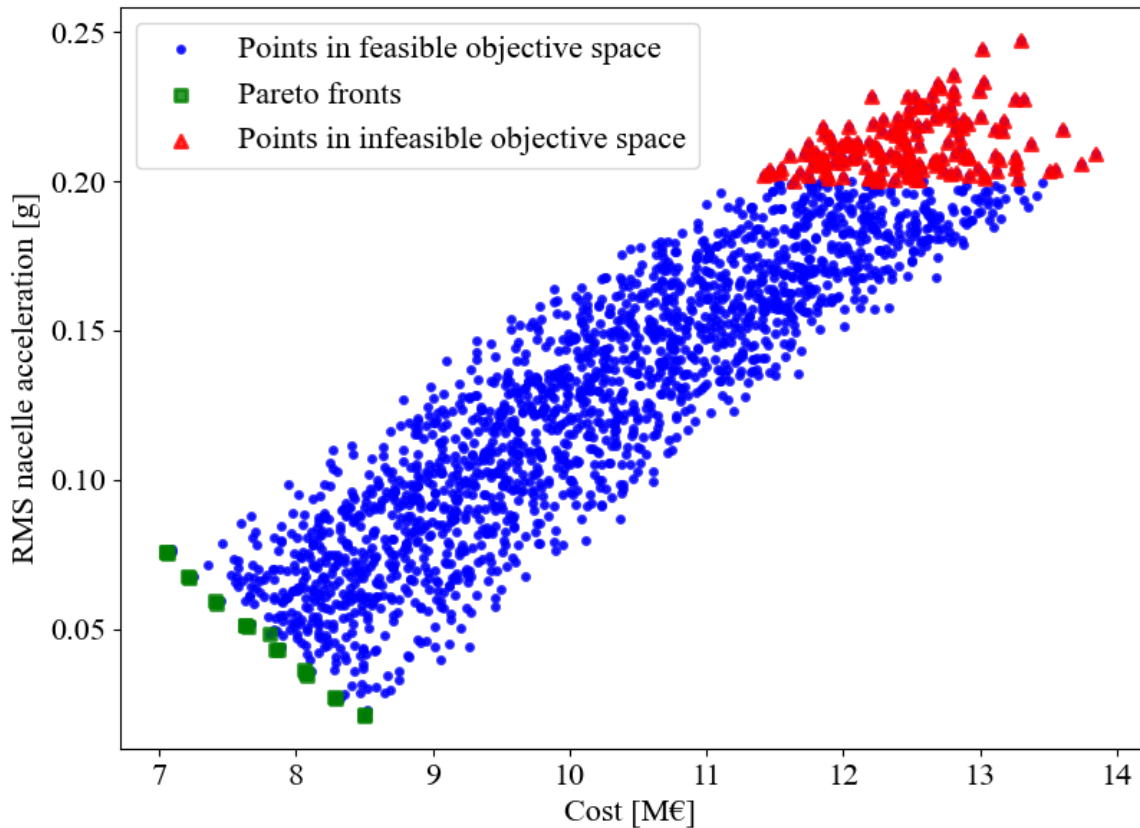
Fig. 6-14: Performance of different geometries using Kriging surrogate model under EC2

Figures 6-14, 6-15, and 6-16 show the Pareto front obtained from different surrogate models as it can be seen, Kriging is the fastest approximation type since it generates fewer points compared to other types. It can be seen that the distribution trend of optimal points in the Pareto front in all three surrogate models is the same. All optimal geometries (green rectangles) have a cost value between 7-8.6 M€ and RMS nacelle acceleration between 0.02-0.07 g. Tables 6-7, 6-8, and 6-9 show the optimum geometries in the Pareto front for different approximation types.
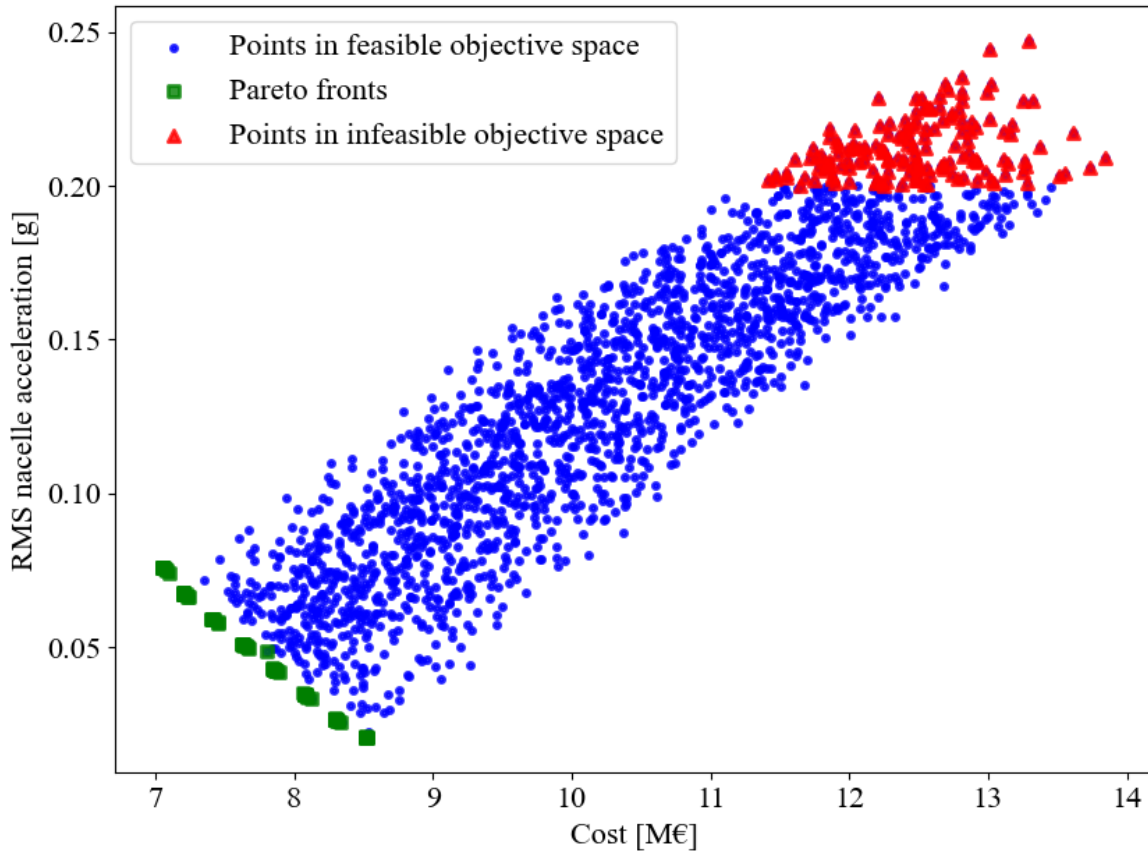
Fig. 6-15: Performance of different geometries using Quadratic polynomial surrogate model under EC2

Because Dakota settings describe design variables as continuous variables (rather than integers), any number can be chosen. The Dakota algorithm looks for the best options and displays the Pareto front.

To verify the accuracy and reliability of the surrogate models, randomly selected geometries from each model have been simulated with NEMOH and objective functions are estimated in Python. When compared to the NEMOH-Python interface, the differences between the findings of surrogate models and the NEMOH-Python interface can be considered an error. In this verification, the errors are found to be less than 1.09 percent. These small errors are neglected in this work. The results of this verification are shown in Table 6-6.
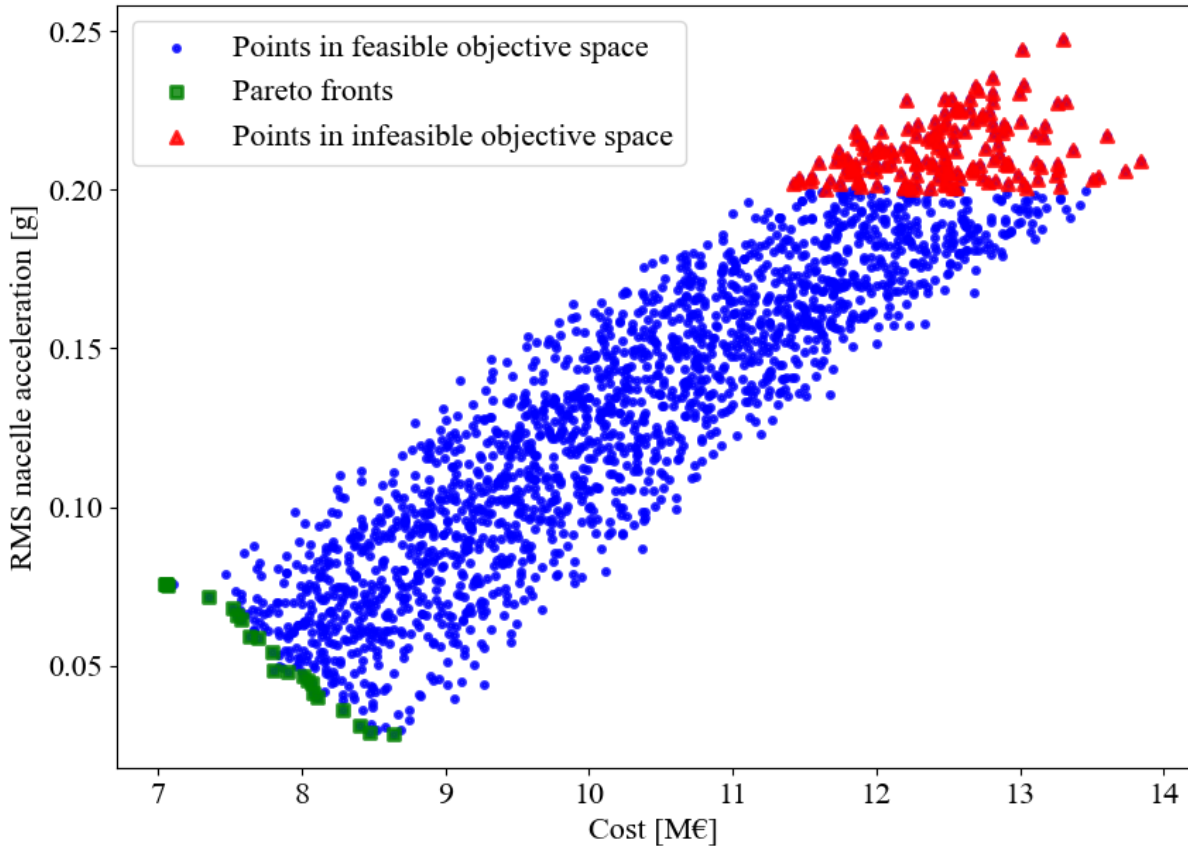
Fig. 6-16: Performance of different geometries using Artificial Neural Network surrogate model under EC2

Table 6-6: Surrogate model verification

Randomly selected geometry	Surrogate model		NEMOH		Absolute Maximum error
[d, s, hc, hp] [m]	$RMS_{a_{nac}}$ [g]	Cost [M€]	$RMS_{a_{nac}}$ [g]	Cost [M€]	%
[13.35, 32, 12.9, 6.03]	0.0499	7.7253	0.0494	7.68	1.01
[14.47, 31.87, 13.24, 6.21]	0.03	8.259	0.0302	8.256	0.66
[13.48, 31.76, 13.6, 6.06]	0.043	7.86	0.0426	7.82	0.93
[14.08, 32.21, 13.31, 6.06]	0.037	8.13	0.0358	8.1	1.09
[14.06, 31.8, 14.67, 6.29]	0.0294	8.32	0.0291	8.23	1.09
[13.55, 31.77, 13.55, 6.5]	0.0428	7.944	0.0426	7.9	0.55
[12.69, 32, 14.78, 6]	0.0522	7.725	0.0524	7.65	0.98
[12.82, 31.75, 14.92, 6.08]	0.049	7.78	0.0487	7.698	1.06
[14.14, 32.07, 14.07, 6.08]	0.031	8.26	0.0313	8.177	1.01

Table 6-7: Pareto front of optimal design points obtained from Kriging surrogate model under EC2

index	[d, s, hc, hp] [m]	$RMS_{a_{nac}}$ [g]	Cost [M€]
1	[13.46,31.87,14.76, 6.49]	0.0485	7.805
2	[13.72,32.43,14.65, 6]	0.0362	8.0638
3	[14.47, 32.08,14.97, 6]	0.0214	8.4971
4	[12.51, 31.84,14.59, 6]	0.0755	7.0644
5	[12.51, 31.84,14.59, 6]	0.0671	7.2157
6	[13.33, 31.86,14.27, 6]	0.0507	7.6487
7	[13.81, 31.92,12.76, 6]	0.0429	7.8754
8	[14.18, 31.92,13.83, 6]	0.0346	8.0845
9	[12.51, 31.8,12.55, 6]	0.0756	7.0565
10	[12.7, 31.93,13.38, 6]	0.0587	7.7561
11	[13.36, 31.75,12.89, 6]	0.0513	7.4171
12	[13.63, 31.86,13.91, 6]	0.0553	7.6339
13	[14.44, 31.8,12.55, 6]	0.043	7.8452
14	[14.47, 31.79,11.15, 6]	0.0267	8.2953
15	[12.5, 32.18,11.27, 6]	0.0211	8.5016
16	[12.51, 32.18,11.27, 6]	0.0757	7.2088
17	[12.83, 32.18,11.27, 6]	0.0675	7.4119
18	[13.32, 32.18,11.27, 6]	0.0593	7.6291
19	[14.28, 32.18,11.27, 6]	0.0352	8.0672
20	[14.33, 32.18,11.27, 6]	0.0272	8.2853

Table 6-8: Pareto front of optimal design points obtained from Quadratic polynomial surrogate model under EC2

index	[d, s, hc, hp] [m]	$RMS_{a_{nac}}$ [g]	Cost [M€]
1	[14.37,31.9,14.8, 6.17]	0.024	8.4779
2	[14.35,31.76,14.2, 6.24]	0.0263	8.3605
3	[14.43, 31.91,13.64, 6.53]	0.0291	8.3539
4	[14.22, 31.84,14.59, 6.28]	0.0273	8.3805
5	[14.34, 31.9,13.5, 6.22]	0.0309	8.252
6	[13.85, 31.87,13.27, 6.02]	0.0395	7.9762
7	[14.15, 31.87,13.27, 6.02]	0.0348	8.1051
8	[13.09, 31.81,14.13, 6.14]	0.0472	7.7958
9	[12.94, 31.83,14.35, 6.13]	0.0489	7.7633
10	[12.92, 31.75,13.7037, 6.16]	0.0514	7.6545
11	[12.54, 32.07,12.55, 6.03]	0.0646	7.3371
12	[13.63, 31.86,13.91, 6]	0.0553	7.6339
13	[14.44, 31.8,12.55, 6]	0.043	7.8452

Table 6-9: Pareto front of optimal design points obtained from Artificial Neural Network surrogate model under EC2

index	[d, s, hc, hp] [m]	$RMS_{a_{nac}}$ $[g]$	*Cost* [degree]
1	[14.04,32.22,14.91, 6.35]	0.031	8.4066
2	[14.42,32.34,12.72, 6.16]	0.0369	8.2064
3	[14.48, 32.29,11.99, 6.07]	0.0417	8.0896
4	[14.39, 32.04,12.47, 6.54]	0.0384	8.1613
5	[13.73, 31.85,13.19, 6.51]	0.0424	7.9557
6	[13.79, 32.34,12.72, 6.16]	0.0463	7.9361
7	[13.44, 32.07,11.99, 6.53]	0.0564	7.6905
8	[12.58, 31.90,13.32, 6.12]	0.0592	7.4611
9	[12.55, 31.89,12.63, 6.33]	0.0639	7.3697
10	[12.57, 31.75,12.01, 6.01]	0.0666	7.2332
11	[12.58, 31.78,11.4, 6.23]	0.0719	7.1774
12	[13.63, 31.86,13.91, 6]	0.0553	7.6339
13	[14.44, 31.8,12.55, 6]	0.043	7.8452
14	[14.47, 31.79,11.15, 6]	0.0267	8.2953
15	[12.5, 32.18,11.27, 6]	0.0211	8.5016
16	[12.51, 32.18,11.27, 6]	0.0757	7.2088
17	[12.83, 32.18,11.27, 6]	0.0675	7.4119
18	[13.32, 32.18,11.27, 6]	0.0593	7.6291

Fig. 6-17 shows a comparison of the Pareto front obtained from different surrogate models. As can be observed, all Pareto fronts have the same distribution point trend. Kriging surrogate model results are very close to the polynomial approximation model while the results of the NSGA-II (with Kriging model) and neural network model are approximately very close to each other for geometries with the cost of between 7.6-8 M€.
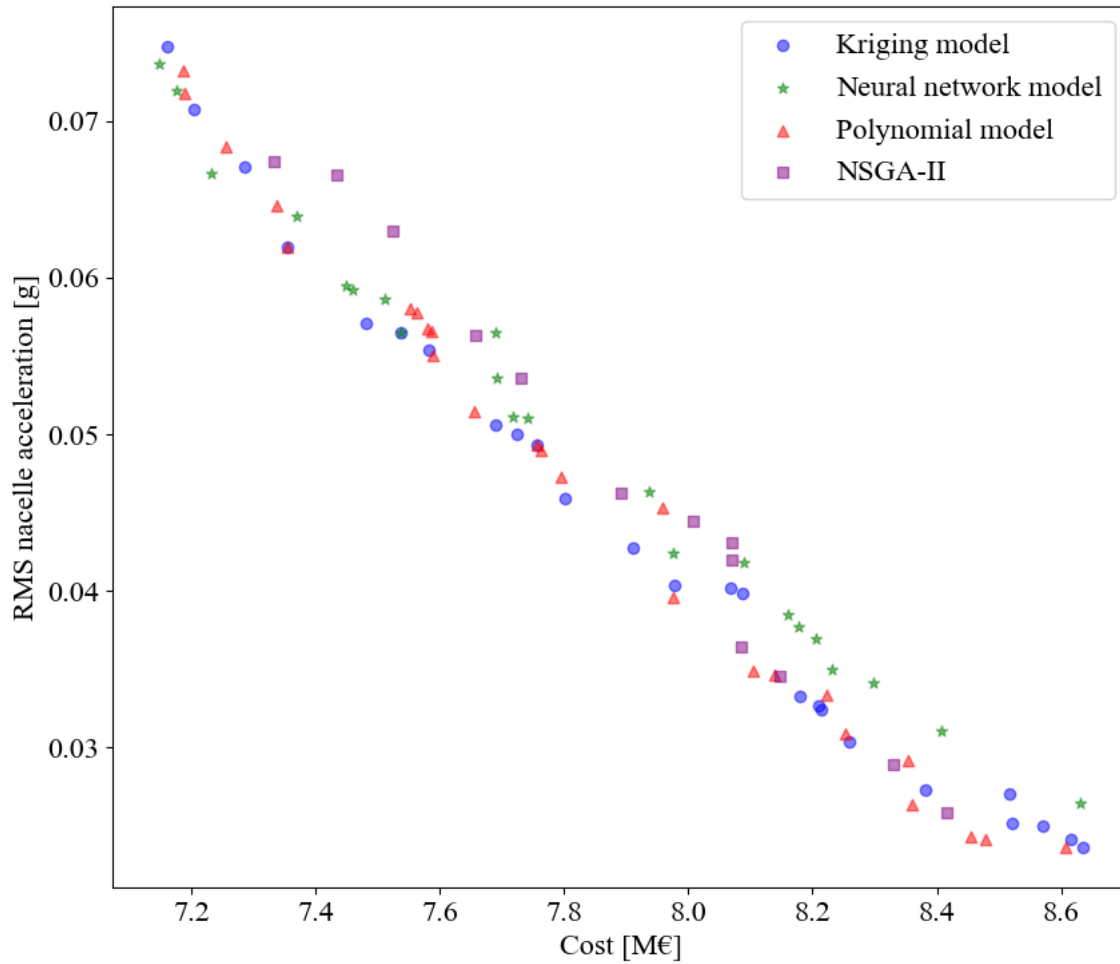
Fig. 6-17: Pareto front comparison for the different surrogate and optimization models (EC2)

Based on NSGA-II results, geometries with the cost of 7.3-7.7 M€ have higher values for the RMS nacelle acceleration compared to other models while geometries with the cost of 8.1-8.4 M€ have lower values.
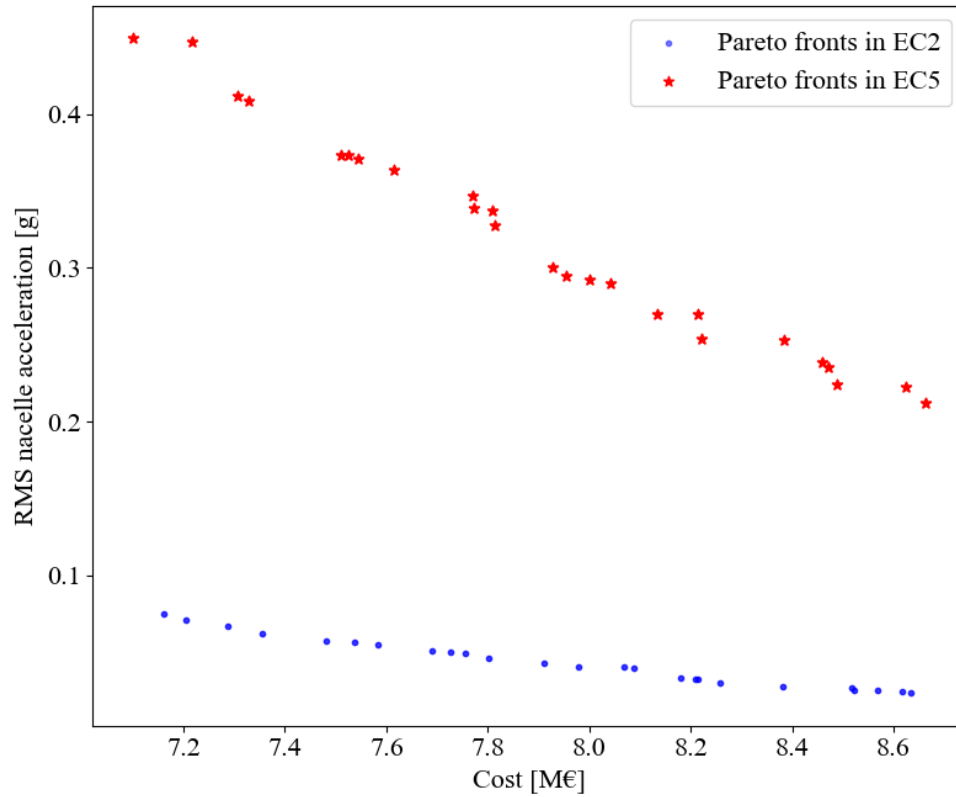
Fig. 6-18: Pareto front comparison for different environmental conditions (kriging model)
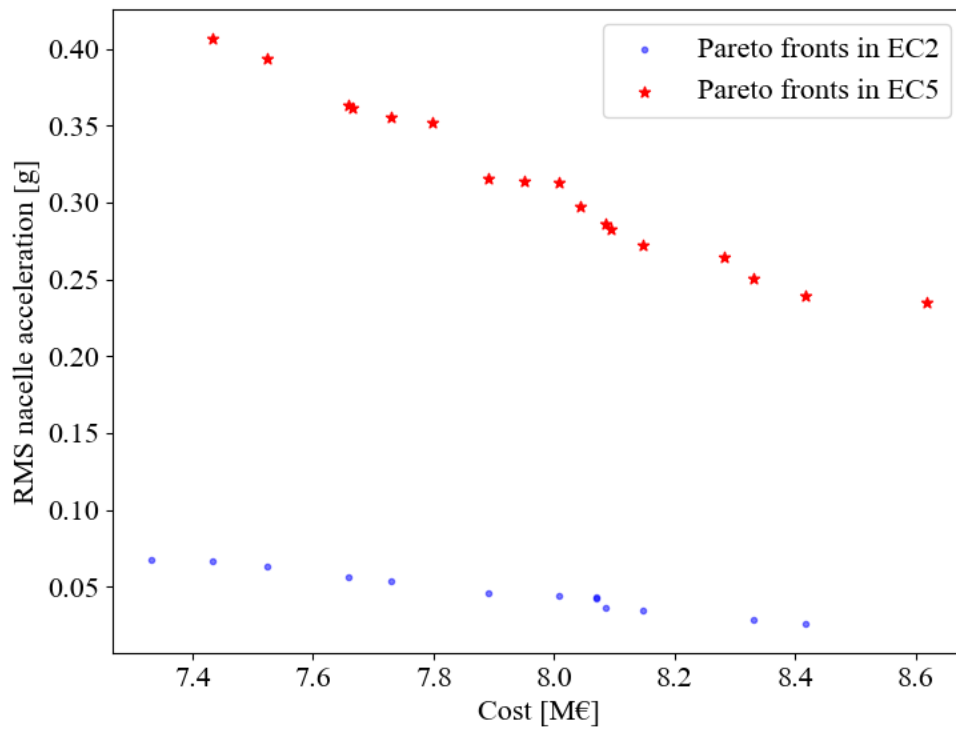
Fig. 6-19: Pareto front comparison for different environmental conditions
(NSGA-II with Kriging model)

A study is performed to investigate the influence of environmental conditions on the Pareto front for the Kriging surrogate model and NSGA-II. The results of this study are provided in Fig. 6-18 and 6-19.

As reflected in Fig. 6-18, the number of optimal geometries in the Pareto front for both environmental conditions of EC2 and EC5 are the same, however, the points in EC5 are more congested between the cost of 7.65-8.05 M€ in EC2.

Optimum geometries follow the same trend for the NSGA-II as is shown in Fig. 6-19, however, the number of geometries in the Pareto front is less than in the case of the Kriging model.

7. Conclusion and future work

7.1 Conclusion

In this thesis, a hydrodynamic optimization of the performance of semi-submersible floater for the FOWT is performed considering the first order hydrodynamic loads using open-source tools. The influence of geometrical variables on the hydrodynamic performance of the semisubmersible platform is investigated using a surrogate-based optimization method considering two objectives, namely the material cost of the hull and RMS nacelle acceleration. A comparative study is performed on the performance of geometries in two different environmental conditions. Three different optimization approaches namely the surrogate model, NSGA-II, and weighted sum have been selected. The results of each approach are presented and compared.

The optimum geometries have been shown based on the results. The main conclusions are summarized as follows:

- The submerged height of the semi-submersible floater has more effects on the response of the system in comparison with the pontoon height.
- The pitch and nacelle acceleration RAO can be reduced by using the pontoon and side columns for ballasting compared to using the pontoon alone.
- The diameter of the column has a considerable impact on the hull's cost.
- The RMS nacelle acceleration is reduced as the dimensions of the structure increase due to an increase in mass.
- The optimum geometries in the Pareto front depend on the environmental condition.
- Pareto fronts obtained from different approximation methods of surrogate models are approximately the same.
- The column spacing and pontoon height of the optimal geometries in the Pareto front are approximately consistent while the column diameter and the submerged column height have different values.
- Optimum geometries follow the same trend for different environmental conditions, however, the number of geometries in the Pareto fronts increases for EC5.

This study is expected to serve as a basis for the hydrodynamic optimization of the hull. Simplifications are made in the choice of design variables and linear methods are applied in the frequency domain hydrodynamic analysis.

Moreover, the results of the optimization show that with the given set of free variables of a semi-submersible platform it is possible to significantly reduce the response amplitude for the given site. However, this happens at the cost of increased expenditures for the material due to an increased structural mass.

Surrogate models used in this study have shown benefits including simplifying the object of study, reducing the computational burden for optimization, hastening parameter fitting and analysis, and allowing for sensitivity analysis to be performed. The results obtained from the surrogate models can give the wind industry professionals an overall overview of the optimization of the semi-submersible offshore wind turbine. What is the true Pareto front is likely something that will always be unknown. In some sense, one does not need optimization methods more accurate than the surrogates: One does not need a precise Pareto front but rather a Pareto neighborhood bordering the front. Having methods such as the Kriging, Polynomial, and Artificial Neural Network which estimate the optimal front is particularly appropriate for offshore floating structures design. The Pareto front of optimal design points obtained from optimization algorithms enables floating offshore wind turbine experts to balance conflicting design objectives according to specific trade-offs.

7.2   Recommendations for future work

The automated simulation and optimization procedure created and utilized in the thesis can be used as the foundation for future work using SALOME, NEMOH, Python, and CAESES. The recommendations for future work would be the following:

a) Implement the aerodynamic effect using an open-source program such as OpenFAST and analyze the coupled hydrodynamic and aerodynamic effects on the structure.

b) Increase the number of design variables (e.g. pontoon width and steel wall thickness) to explore more hull geometries.

c) Increase the number of constraints, for example, drift forces, suspension of mooring lines, dynamic pitch angle, and tower-based moment

d) Improving the sizing algorithms of structural elements to better reflect the dynamic loads they will face.

e) Improving the cost objective function by adding fabrication, installation, and maintenance costs as well as the cost of the mooring lines.

These changes would require a more iterative design evaluation approach, in which the results of the dynamics feed back into the sizing of the structure components until a well-sized design is converged upon.

References

[1]   DNV, Energy Transition Norway, 2021.

[2]   Jonkman, J., Butterfield, S., Musial, W., and Scott, G., "Definition of a 5- MW Reference Wind Turbine for Offshore System Development," National Renewable Energy Laboratory, Golden, CO, Technical Report No. NREL/TP- 500-38060,2009.

[3]   Beiter, P., Musial, W., et al., A Spatial-Economic Cost-Reduction Pathway Analysis for US Offshore Wind Energy Development from 2015–2030; Myhr A., Bjerkseter C., Ågotnes A. and Nygaard T. (2014), Levelised cost of energy for offshore floating wind turbines in a life cycle perspective; Seaplace analysis; Enzen analysis, EIT InnoEnergy, 2016.

[4]   Jonkman, J. M., and Musial, W., "Offshore Code Comparison Collaboration (OC3) for IEA Task 23 Offshore Wind Technology and Deployment," National Renewable Energy Laboratory, Golden, CO, Technical Report No. NREL/TP-5000-48191, 2010.

[5]   Vorpahl, F., Popko, W., and Kaufer, D., "Description of a Basic Model of the 'UpWind Reference Jacket' for Code Comparison in the OC4 Project Under IEA Wind Annex XXX," Fraunhofer Institute for Wind Energy and Energy System Technology, Bremerhaven, Germany, Technical Report, 2011.

[6]   Jonkman, J., Robertson, A., Popko, W., Vorpahl, F., Zuga, A., Kohlmeier, M., Larsen, T. J., Yde, A., Saeterto, K., Okstad, K. M., Nichols, J., Nygaard, T. A., Gao, Z., Manolas, D., Kim, K., Yu, Q., Shi, W., Park, H., Vasquez-Rojas, A., Dubois, J., Kaufer, D., Thomassen, P., de Ruiter, M. J., Peeringa, J. M., Zhiwen, H., and von Waaden, H., "Offshore Code Comparison Collaboration Continuation (OC4), Phase I-Results of Coupled Simulations of an Offshore Wind Turbine With Jacket Support Structure," The Twenty-Second International Offshore and Polar Engineering Conference, International Society of Offshore and Polar Engineers, Rhodes, Greece, June 17–22, Paper No. NREL/CP-5000- 54124, 2012.

[7]   Ryan, J.. "Farming the deep blue," Bord Iassaigh Mhara and Irish Marine Institue, Ireland, 2004.

[8]   Jaksic, V., O'Shea, R., Cahill, P., Murphy, J., Mandic. D. P., and Pakrashi, V., Dynamic response signatures of a scaled model platform for floating wind turbines in an ocean wave basin, the Royal Society, 2015.

[9]   Chandrasekaran, S., Design of Marine Risers with Functionally Graded Materials, ISBN: 9780128235614, 2021.

[10]   Stansberg, C.T., Current Effects on a Moored Floating Platform in a Sea State, OMAE2008-57621, 2008.

[11]   Luan, C., Design and Analysis for a Steel Braceless Semi-submersible Hull for Supporting a 5-MW Horizontal Axis Wind Turbine, PhD Theses. Norwegian University of Science and Technology, Trondheim, Norway, 2018.

[12]   Pegalajar-Jurado, A., State-of-the-art model for the LIFES50+ OO-Star Wind Floater Semi 10MW floating wind turbine, J. Phys.: Conf. Ser. 1104 012024, 2018.

[13] Zhou, S., Li, C., Xiao, Y., Lemmer, F., Yu, W., Cheng, P.W., optimization of the dynamic response of semi-submersibles: influence of the mooring system, IOWTC2019-7553, 2019

[14] Definition of the UMaine VolturnUS-S Reference Platform Developed for the IEA Wind 15-Megawatt Offshore Reference Wind Turbine, Technical Report, 2020.

[15] L. Xiong, L. Haining, J. Yang, and W. Zhao, "Motion responses of a moored barge in shallow water", Ocean Engineering, vol. 97, pp. 207-217, 2015.

[16] W. Journée, Johan M.J & Massie, Offshore Hydrodynamics. Delft: University of Technology, 2001.

[17] G. Clauss, F. Stempinski, M. Dudek, and M. Klein, "Water depth influence on wave-structure-interaction", Ocean Engineering, vol. 36, pp. 1396-1403, 2009.

[18] I. Bayati, S. Gueydon, and M. Belloli, "Study of the effect of water depth on potential flow solution of the OC4 semisubmersible floating offshore wind turbine", Energy Procedia, vol.80, pp. 168-176, 2015.

[19] Riggs H and Yim S, Structural dynamics Springer Handbook of Ocean Engineering Dhanak M and Xiros N 851-74, 2016.

[20] Gherbi A and Belgasmia M, Stochastic analysis basics and application of statistical linearization technique on a controlled system with nonlinear viscous dampers Handbook of Probabilistic Models Samui P, Bui D, Chakraborty S and Deo R 505-25, 2020.

[21] Morison, J. R., O'Brian, M. P., Johnson, J. W. and Schaaf, S. A.. "The force exerted by surface waves on piles," Journal of Petroleum Technology, Vol. 2, pp. 149-154, 1950.

[22] Milad H., Lin L., Filippos K., Zhiyu J., "Hydrodynamic performance evaluation of a semi-submersible floater using open-source tools', OMAE2022-78823, 2022.

[23] Definition of the UMaine VolturnUS-S Reference Platform Developed for the IEA Wind 15-Megawatt Offshore Reference Wind Turbine, Technical Report, 2020.

[24] Definition of the IEA Wind 15-Megawatt Offshore Reference Wind Turbine, Technical Report, 2020.

[25] K03 15MW semi-sub FOWT, www.orcina.com.

[26] Li, L., Gao, Z., and Moan, T., Joint Distribution of Environmental Condition at Five European Offshore Sites for Design of Combined Wind and Wave Energy Devices, J. Offshore Mech. Arct. Eng., vol. 137, no. 031901, doi: 10.1115/1.4029842, 2015.

[27] SALOME, Webpage. https://www.salome- platform.org/.

[28] NEMOH, Webpage. https://lheea.ec-nantes.fr/.

[29] http://www.python.org, Python 3.6.0, 2016.

[30] AQWA Reference Manual, ANSYS AQWA 2020 R1, ANSYS, Inc.

[31] H. J. D. K. Gans. "Manual for experiments of Numerical Methods in Ship Hydromechanics.", 2014.

[32] Abdel Ghani Aissaoui, Ahmed Tahour, Wind Turbines: Design, Control and Applications, 2016.

[33] Tracy, CC., Parametric design of floating wind turbines. MIT, M.Sc. thesis, 2007.

[34] Lemmer, F., Müller, K., Yu, W., Guzman, R.F., Kretschmer, M., Qualification of Innovative Floating Substructures for 10 MW Wind Turbines and Water Depths Greater than 50 m: Deliverable D4.3 Optimization Framework and Methodology for Optimized Floater Design, 2016.

[35] M.Akbari, P.Asadi,M.K.Besharati Givi, G.Khodabandehlouie, artificial neural network and optimization, Woodhead Publishing Series in Welding and Other Joining Technologies, Pages 543-599, 2014.

[36] K. Deb, Multi-Objective Optimization using Evolutionary Algorithms, John Wiley & Sons, Inc., 2001.

[37] Nyoman G., a review of multi-objective optimization: Methods and its applications, Cogent Engineering, Volume 5, 2018.

[38] Bulder, van H., Henderson, H., Pierik, S., Wignants, and Wolf, "Studie naar haalbaarheid van en randvoorwaarden voor drijvende offshore wind turbines," Tech. Rep., Dec. 2002.

[39] Henrik B. (ed), Jennifer R., Witold S., Frederik Z., Fangzhong M., Katherine D. (DTU), Evan G., Garrett B., Pietro B., Latha S. and Matt S. (NREL), Cost reduction and increase performance of floating WIND Technology, 2019.

[40] Matthew H., Brad B., and Curran C., Evolving Offshore Wind: A Genetic Algorithm-Based Support Structure Optimization Framework for Floating Wind Turbines, OCEANS'13 MTS/IEEE Bergen, Norway, 2013.

[41] Penalba, M., Kelly, T., and Ringwood, J.V., Using NEMOH for Modelling Wave Energy Converters: A Comparative Study with WAMIT. In: 12th European Wave and Tidal Energy Conference August, p. 10, 2017.

[42] DNVGL-ST-0119, Floating wind turbine structures, DNV GL AS, 2018.

[43] Wayman, E.N., Sclavounos, P.D., Butterfield, S., Jonkman, J., Musial, W., Coupled Dynamic Modeling of Floating Wind Turbine Systems, OTC-18287-MS, 2006.

[44] Hall, M., and A. Goupee. "Validation of a lumped-mass mooring line model with DeepCwind semisubmersible test data." Ocean Engineering, Vol. 104, pp. 590-603, 2015.

[45] Box, G. E., J. S. Hunter, et al., Statistics for experimenters: design, discovery and innovation, Wiley-Interscience, 2005.

[46] Kutner, M. H., C. J. Nachtsheim, et al., Applied linear statistical models, McGraw-Hill Irwin New York, 2005.

[47] Joaquim R. R. A. Martin, Andrew Ning, "Engineering Design Optimization", 2021.

[48] Apostolos Papanikolaou, Yan Xing-Kaeding, Johannes Strobel, Aphrodite Kanellopoulou, George Zaraphonitis and Edmund Tolo, Numerical and Experimental Optimization Study on a Fast, Zero Emission Catamaran, Marine Science and Engineering, 2020.

[49] Zhong-Hua H. and Ke-Shi Z., Surrogate-Based Optimization, Real-World Applications of Genetic Algorithms, Dr. Olympia Roeva (Ed.), ISBN: 978-953-51-0146-8, InTech, 2012.

[50] Friendship Systems AG, CAESES: CAE System Empowering Simulation Software. url: https://www.caeses.com/, 2022.

[51] Adams, B.M., Bohnhoff, W.J., Dalbey, K.R., Ebeida, M.S., Eddy, J.P., Eldred, M.S., Hooper, R.W., Hough, P.D., Hu, K.T., Jakeman, J.D., Khalil, M., Maupin, K.A., Monschke, J.A., Ridgway, E.M., Rushdi, A.A., Seidl, D.T., Stephens, J.A., Swiler, L.P., and Winokur, J.G., "Dakota, A Multilevel Parallel Object-Oriented Framework for Design Optimization, Parameter Estimation, Uncertainty Quantification, and Sensitivity Analysis: Version 6.15 User's Manual," Sandia Technical Report SAND2020-12495, 2021.

[52] Michael S. E., Anthony A. G., Bart G. van B. Waanders, Steven F. W., Jr., William E. H., and Mario P. Alleva, DAKOTA, A Multilevel Parallel Object-Oriented Framework for Design Optimization, Parameter Estimation, Uncertainty Quantification, and Sensitivity Analysis, Version 3.0 User's Manual, Sandia National Laboratories, 2002.

[53] Mohamed B., John T. H., Nathalie B., Rémi L., Joseph M., et al.. A Python surrogate modeling framework with derivatives. Advances in Engineering Software, Elsevier, 2019.

[54] F. Pedregosa, G. Varoquaux, A. Gramfort, V. Michel, B. Thirion, O. Grisel, M. Blondel, P. Rettenhofer, R. Weiss, V. Dubourg, J. Vanderplas, A. Passos, D. Cournapeau, M. Brucher, M. Perrot, and E. Duchesnay. Scikit-learn: Machine learning in Python. Journal of Machine Learning Research, 12:2825{2830, 2011.

[55] Gorissen D., Crombecq K., I. Couckuyt, T. Dhaene, and P. Demeester. A surrogate modeling and adaptive sampling toolbox for computer-based design. Journal of Machine Learning Research, 11:2051{2055, 2010.

[56] Rasmussen C. E. and Williams C. K. I.. Gaussian Processes for Machine Learning. Adaptive Computation and Machine Learning. MIT Press, Cambridge, MA, USA, 2006.

[57] Surrogate Modeling Toolbox (SMT: https://github.com/SMTorg/smt).

[58] Han, Z. -H., Zhang, K. -S., Song, W. -P., and Qiao, Z. -D., "Optimization of Active Flow Control over an Airfoil Using a Surrogate-Management Framework," Journal of Aircraft, Vol. 47, No. 2, pp. 603-612, 2010.

[59] Jones, D., Schonlau, M., Welch W., "Efficient Global Optimization of Expensive Black-Box Functions," Journal of Global Optimization, Vol. 13, pp. 455-492, 1998.

[60] Deb K., Pratap A., Agarwal S., and Meyarivan T.. A fast and elitist multiobjective genetic algorithm: NSGA-II. *Trans. Evol. Comp*, 6(2):182–197, 2002.

[61] Maoqing Z., Lei Wang, Zhihua Cui, Jiangshan Liu, Dong Du, and Weian Guo, Fast Non-dominated Sorting Genetic Algorithm II with Lévy Distribution for Network Topology Optimization, Mathematical Problems in Engineering, 2020.

[62] Bouhlel M. A. and Martins J. R. R. A.. Gradient-enhanced kriging for high-dimensional problems. Engineering with Computers, 1(35):157{173, 2019

[63] M. A. Bouhlel, N. Bartoli, J. Morlier, and A. Otsmane. An improved approach for estimating the hyperparameters of the kriging model for high-dimensional problems through the partial least squares method. Mathematical Problems in Engineering, 2016.

[64] Bouhlel M. A., Bartoli N., Otsmane A., and Morlier J.. Improving kriging surrogates of high-dimensional design models by partial least squares dimension reduction. Structural and Multidisciplinary Optimization, 53(5):935{952, 2016.

[65] Hwang J. T. and Martins J. R. R. A.. A fast-prediction surrogate model for large datasets. Aerospace Science and Technology, 75:74{87, 2018.

Results

This appendix in related to the continuation of the results shown in Chapter 5.
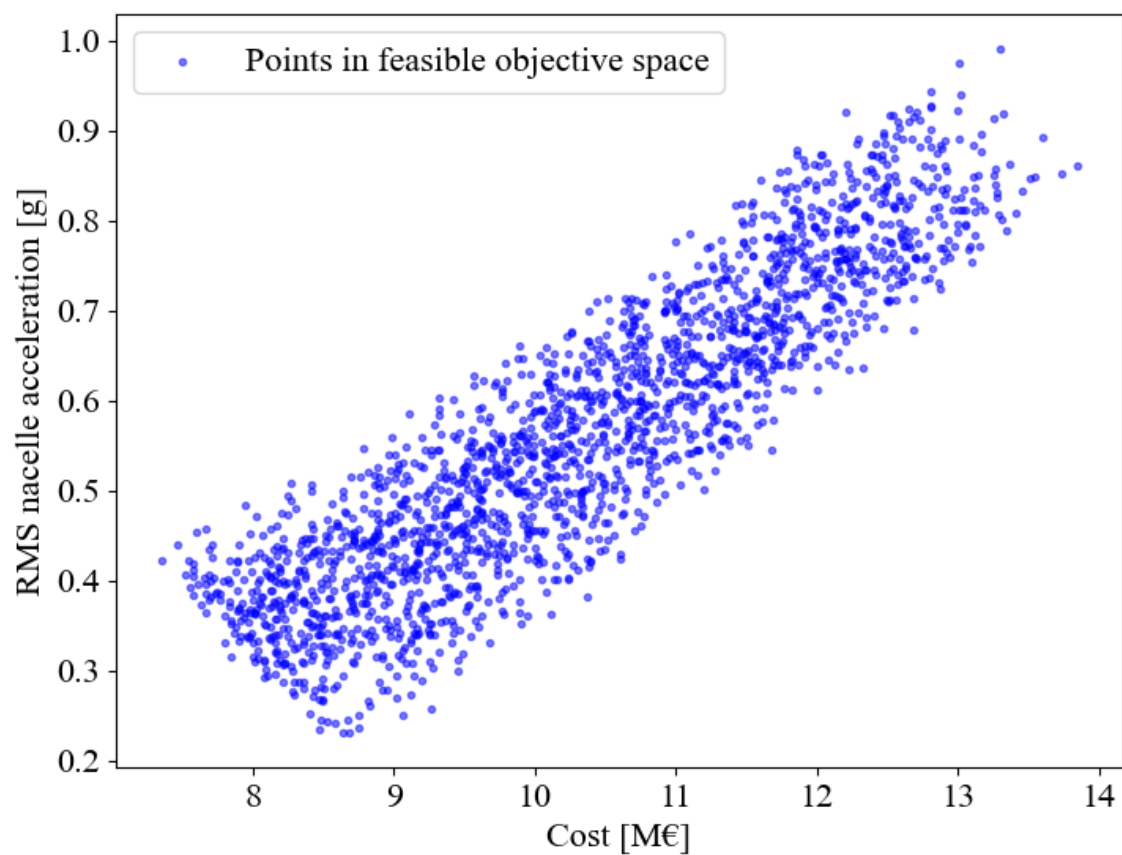
Response surface regression under EC5

Fig. A-1: LHS sampling under EC5

A.1. Response surface regression under EC5

$f_1(x)$ versus *d, s, hc, hp*

Regression Equation for objective function 1:

f1_cost = 0.5674 + 0.13970 d - 0.000373 s + 0.02737 hc - 0.00352 hp - 0.000005 s*s
+ 0.000116 hc^2 + 0.005955 d*s + 0.009389 d*hc - 0.004633 d*hp
+ 0.000012 s*hc + 0.006032 s*hp - 0.000093 hc*hp

$f_2(x)$ versus *d, s, hc, hp*

Regression Equation for objective function 2:

f2_rms = 2.802 - 0.1519 d - 0.04197 s - 0.0528 hc + 0.0256 hp
+ 0.000112 s*s + 0.00247 hc^2 + 0.003267 d*s - 0.00098 d*hc
- 0.00220 d*hp - 0.000342 s*hc + 0.000588 s*hp - 0.00141 hc*hp

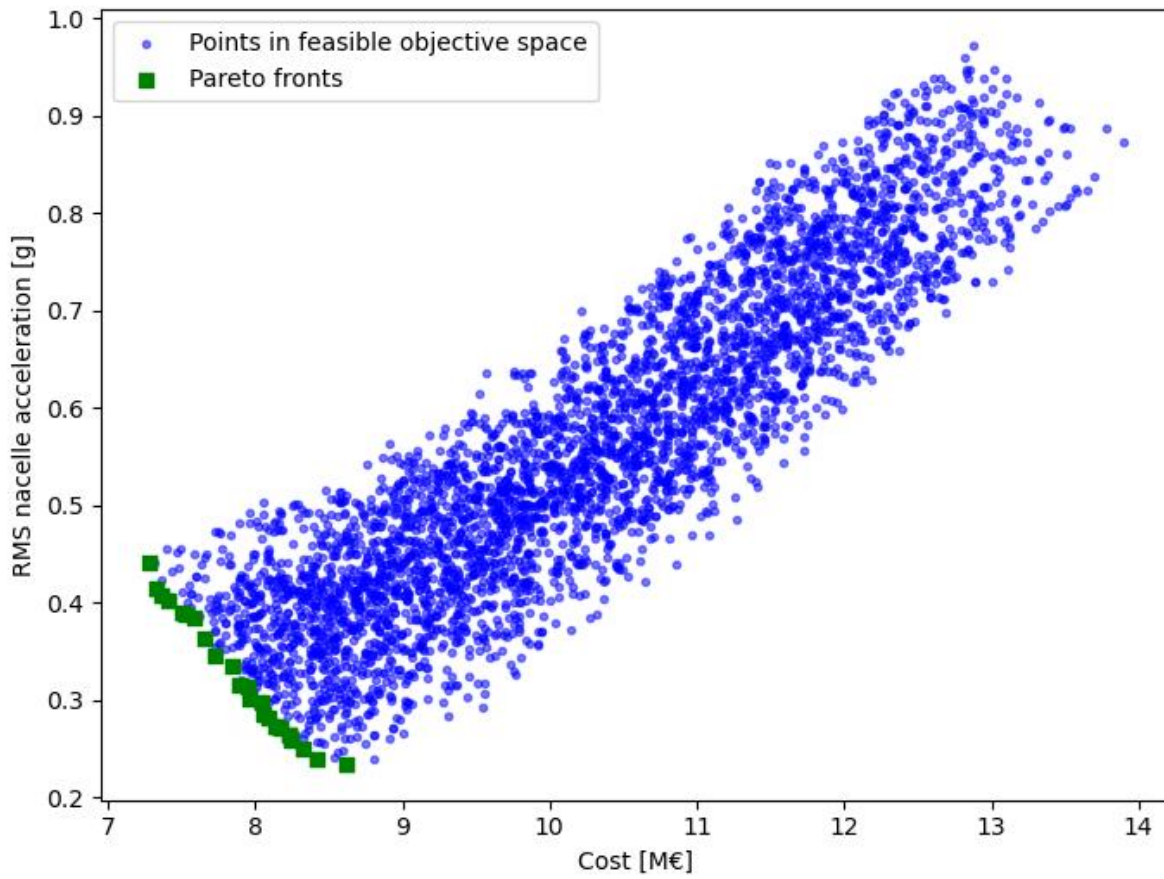# Performance results based on NSGA-II algorithm under EC5

Fig. A-2: Performance of different geometries using NSGA-II under EC5

Table A-1: Geometries in Pareto front using NSGA-II

index	[d, s, hc, hp] [m]	$\text{RMS}_{a_{nac}}$ $\left[\text{m/s}^2\right]$	φ^{55}_{static} [degree]
1	[13.46,31.87,14.76, 6.49]	0.211	7.805
2	[13.32,32.43,14.35, 6]	0.215	8.0638
3	[14.47, 32.08,14.97, 6]	0.32	8.4971
4	[12.51, 32.84,14.29, 6]	0.351	7.0644
5	[12.31, 31.84,13.59, 6]	0.274	7.2157
6	[13.33, 31.86,14.27, 6]	0.263	7.6487
7	[13.81, 32.92,12.76, 6]	0.321	7.8754
8	[14.18, 31.92,13.33, 6]	0.254	8.0845
9	[12.51, 31.8,12.55, 6.01]	0.374	7.0565
10	[12.7, 32.33,13.38, 6]	0.363	7.7561
11	[13.36, 31.75,12.89, 6.02]	0.296	7.4171
12	[13.63, 31.85,13.31, 6]	0.237	7.6339
13	[13.63, 31.75,14.51, 6]	0.336	8.833
14	[14.43, 31.35,13.21, 6]	0.246	7.6334
15	[13.63, 32.35,13.91, 6]	0.238	7.3821
16	[13.63, 31.35,12.92, 6]	0.335	7.6331
17	[14.13, 32.37,13.41, 6]	0.234	8.7892
18	[13.63, 31.25,13.11, 6.2]	0.223	8.6342

Theoretical and numerical aspects of the open-source NEMOH

This Appendix summarizes the theoretical and numerical aspects of the open-source BEM solver NEMOH [28]

NEMOH: open-source BEM code for calculation of hydrodynamic coefficients. BEM codes based on linear potential flow theory are still widely used for wave-structure interactions in numerical W2W models for WECs. BEM codes (WAMIT, Diodore, DIFFRACT, Hydrostar, Aquaplus, …) used for the computation of hydrodynamic coefficients are expensive (despite they were developed a long time ago). In Jan. 2014, ECN decided to release its BEM code in open source. NEMOH has been found very useful for many of its users but its full potential has not yet been realized because:

• Documentation is poor
• No verification and validation test cases

Free surface potential flow theory: assumptions

Inviscid fluid: $\nu = 0$
Incompressible and irrotational flow:

$\vec{\nabla} \cdot \vec{V} = 0$
$\vec{\nabla} \times \vec{V} = 0$
Velocity derives from a velocity potential:
$\vec{V} = \vec{\nabla}\Phi$
Pressure is obtained from Bernoulli formula:

$$p + \rho g z + \frac{1}{2} \left(\vec{\nabla}\Phi\right)^2 + \rho \frac{\partial \Phi}{\partial t} = Constant$$

Interest: flow is completely described by the velocity potential (scalar) Φ: 1 unknown Φ vs 4 unknowns (V_x, V_y, V_z and p)

NEMOH

$$\begin{cases} \Delta\Phi = 0 & M \in \Omega \\ \dfrac{\partial\Phi}{\partial n} = f(M) & M \in \overline{S_B} \\ \dfrac{\partial\Phi}{\partial n} = 0 & M \in S_{bottom} \\ \dfrac{\partial^2\Phi}{\partial t^2} + g\dfrac{\partial\Phi}{\partial n} = 0 & z = 0 \\ \sqrt{R}\left(\dfrac{\partial\Phi}{\partial n} - ik\right)(\Phi - \Phi_0) \to 0 & R \to \infty \end{cases}$$

> Linear BEM code (solves linear BVP)
> Use of the generalized mode approach
> Use of source distribution
> Wave part of the Green funtion is calculated using interpolation in a look-up table
> Outputs:
>   • 1st order hydrodynamic coefficients (added mass, radiation damping, excitation force)
>   • Far field coefficients (Kochin function)
>   • Free surface elevation, pressure field
>   • Removal of irregular frequencies (to be released soon)
>   • 2nd order coefficients (QTF) → see paper by Philippe et al.
> http://lheea.ec-nantes.fr/doku.php/emo/nemoh/start

NEMOH Mesh Folder

This folder contains 53 mesh files (.dat) obtained from SALOME-Python interface after hydrostatic analysis. These geometries are used in NEMOH-Python interface to calculate RAOs and objective functions.

s_51.75_d_12.5_cylH_11.0_ponH_6.0.dat
s_51.75_d_12.5_cylH_11.0_ponH_7.0.dat
s_51.75_d_12.5_cylH_12.0_ponH_6.0.dat
s_51.75_d_12.5_cylH_12.0_ponH_7.0.dat
s_51.75_d_12.5_cylH_13.0_ponH_6.0.dat
s_51.75_d_12.5_cylH_13.0_ponH_7.0.dat
s_51.75_d_12.5_cylH_14.0_ponH_6.0.dat
s_51.75_d_12.5_cylH_14.0_ponH_7.0.dat
s_56.75_d_12.5_cylH_11.0_ponH_6.0.dat
s_56.75_d_12.5_cylH_11.0_ponH_7.0.dat
s_56.75_d_12.5_cylH_12.0_ponH_6.0.dat
s_56.75_d_12.5_cylH_12.0_ponH_7.0.dat
s_56.75_d_12.5_cylH_13.0_ponH_6.0.dat
s_56.75_d_12.5_cylH_13.0_ponH_7.0.dat
s_56.75_d_12.5_cylH_14.0_ponH_6.0.dat
s_56.75_d_12.5_cylH_14.0_ponH_7.0.dat
s_61.75_d_12.5_cylH_11.0_ponH_6.0.dat
s_61.75_d_12.5_cylH_11.0_ponH_7.0.dat
s_61.75_d_12.5_cylH_12.0_ponH_6.0.dat
s_61.75_d_12.5_cylH_12.0_ponH_7.0.dat
s_61.75_d_12.5_cylH_13.0_ponH_6.0.dat
s_61.75_d_12.5_cylH_13.0_ponH_7.0.dat
s_61.75_d_12.5_cylH_14.0_ponH_6.0.dat
s_61.75_d_12.5_cylH_14.0_ponH_7.0.dat
s_66.75_d_10.0_cylH_11.0_ponH_6.0.dat
s_66.75_d_10.0_cylH_11.0_ponH_7.0.dat
s_66.75_d_10.0_cylH_12.0_ponH_6.0.dat
s_66.75_d_10.0_cylH_12.0_ponH_7.0.dat
s_66.75_d_10.0_cylH_13.0_ponH_6.0.dat
s_66.75_d_10.0_cylH_13.0_ponH_7.0.dat
s_66.75_d_10.0_cylH_14.0_ponH_6.0.dat
s_66.75_d_10.0_cylH_14.0_ponH_7.0.dat
s_66.75_d_12.5_cylH_11.0_ponH_6.0.dat
s_66.75_d_12.5_cylH_11.0_ponH_7.0.dat
s_66.75_d_12.5_cylH_12.0_ponH_6.0.dat
s_66.75_d_12.5_cylH_12.0_ponH_7.0.dat
s_66.75_d_12.5_cylH_13.0_ponH_6.0.dat
s_66.75_d_12.5_cylH_13.0_ponH_7.0.dat
s_66.75_d_12.5_cylH_14.0_ponH_6.0.dat
s_66.75_d_12.5_cylH_14.0_ponH_7.0.dat
s_71.75_d_10.0_cylH_11.0_ponH_6.0.dat

s_71.75_d_10.0_cylH_11.0_ponH_7.0.dat
s_71.75_d_10.0_cylH_12.0_ponH_6.0.dat
s_71.75_d_10.0_cylH_12.0_ponH_7.0.dat
s_71.75_d_10.0_cylH_13.0_ponH_6.0.dat
s_71.75_d_10.0_cylH_13.0_ponH_7.0.dat
s_71.75_d_10.0_cylH_14.0_ponH_6.0.dat
s_71.75_d_10.0_cylH_14.0_ponH_7.0.dat
s_71.75_d_12.5_cylH_11.0_ponH_6.0.dat
s_71.75_d_12.5_cylH_11.0_ponH_7.0.dat
s_71.75_d_12.5_cylH_12.0_ponH_6.0.dat
s_71.75_d_12.5_cylH_12.0_ponH_7.0.dat
s_71.75_d_12.5_cylH_13.0_ponH_6.0.dat
s_71.75_d_12.5_cylH_13.0_ponH_7.0.dat
s_71.75_d_12.5_cylH_14.0_ponH_6.0.dat
s_71.75_d_12.5_cylH_14.0_ponH_7.0.dat

NEMOH Working Folder

This folder shows the necessary files and folders in order to run properly, otherwise it will not run.

- Mesh
- Results
- .dat
- ID.dat
- input.txt
- LICENSE.txt
- Mesh.cal
- Mesh.exe
- Nemoh.cal
- nemohMesh.dat
- Normalvelocities.dat
- NOTICE.txt
- Original_Geom.hdf
- postProcessor.exe
- preProcessor.exe
- RAO.txt
- run.bat
- Solver.exe
- test.png
- test-sm.csv
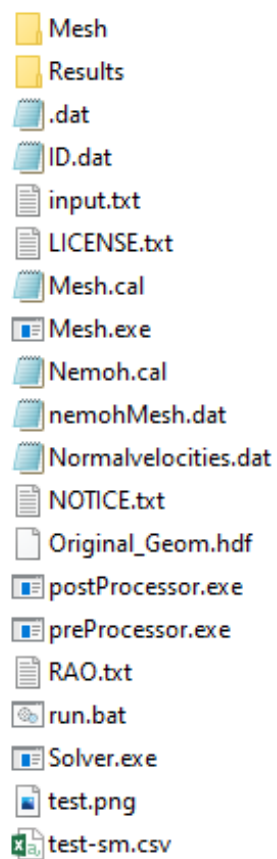
Sample DiffractionForce.tec File

This file shows a sample result obtained from NEMOH for diffraction force. Even columns show the amplitude and odd columns show the phase of the force.

```
VARIABLES="w (rad/s)"
"abs(F   1   1)" "angle(F   1   1)"
"abs(F   1   2)" "angle(F   1   2)"
"abs(F   1   3)" "angle(F   1   3)"
"abs(F   1   4)" "angle(F   1   4)"
"abs(F   1   5)" "angle(F   1   5)"
"abs(F   1   6)" "angle(F   1   6)"
Zone t="Diffraction force - beta =    0.000 deg",I=    81,F=POINT
  0.1000000E+00  0.2277004E+06 -0.1586757E+01  0.6050734E+02  0.2159781E+01  0.8720888E+05
  0.1175000E+00  0.2676837E+06 -0.1589481E+01  0.7349305E+02  0.2251992E+01  0.1205403E+06
  0.1350000E+00  0.3071907E+06 -0.1592324E+01  0.8776110E+02  0.2337633E+01  0.1573690E+06
  0.1525000E+00  0.3466459E+06 -0.1595168E+01  0.1030908E+03  0.2418701E+01  0.2012375E+06
  0.1700000E+00  0.3865285E+06 -0.1597945E+01  0.1198315E+03  0.2495203E+01  0.2471128E+06
  0.1875000E+00  0.4258774E+06 -0.1600846E+01  0.1374412E+03  0.2572485E+01  0.2986738E+06
  0.2050000E+00  0.4649174E+06 -0.1603831E+01  0.1568091E+03  0.2641162E+01  0.3556800E+06
  0.2225000E+00  0.5038005E+06 -0.1606866E+01  0.1772912E+03  0.2708037E+01  0.4126133E+06
  0.2400000E+00  0.5426766E+06 -0.1609926E+01  0.1988045E+03  0.2774083E+01  0.4765320E+06
  0.2575000E+00  0.5818826E+06 -0.1612961E+01  0.2220359E+03  0.2838452E+01  0.5448394E+06
  0.2750000E+00  0.6203591E+06 -0.1616193E+01  0.2459054E+03  0.2900059E+01  0.6110166E+06
  0.2925000E+00  0.6581697E+06 -0.1619577E+01  0.2712992E+03  0.2962056E+01  0.6805338E+06
  0.3100000E+00  0.6956582E+06 -0.1623014E+01  0.2975272E+03  0.3021927E+01  0.7605316E+06
  0.3275000E+00  0.7327199E+06 -0.1626624E+01  0.3250908E+03  0.3079762E+01  0.8305956E+06
  0.3450000E+00  0.7695200E+06 -0.1630454E+01  0.3531529E+03  0.3140069E+01  0.8970002E+06
  0.3625000E+00  0.8057247E+06 -0.1634293E+01  0.3832371E+03 -0.3078678E+01  0.9712794E+06
  0.3800000E+00  0.8403743E+06 -0.1638373E+01  0.4123183E+03 -0.3016917E+01  0.1051760E+07
  0.3975000E+00  0.8732489E+06 -0.1643036E+01  0.4419061E+03 -0.2956995E+01  0.1114919E+07
  0.4150000E+00  0.9046686E+06 -0.1648375E+01  0.4715512E+03 -0.2895695E+01  0.1166666E+07
  0.4325000E+00  0.9337304E+06 -0.1653963E+01  0.5025642E+03 -0.2829291E+01  0.1229505E+07
  0.4500000E+00  0.9596172E+06 -0.1660246E+01  0.5321868E+03 -0.2763740E+01  0.1293173E+07
  0.4675000E+00  0.9831876E+06 -0.1668103E+01  0.5625485E+03 -0.2697247E+01  0.1334455E+07
  0.4850000E+00  0.1003400E+07 -0.1677052E+01  0.5907038E+03 -0.2630835E+01  0.1355854E+07
  0.5025000E+00  0.1018801E+07 -0.1686967E+01  0.6192935E+03 -0.2560342E+01  0.1382759E+07
  0.5200000E+00  0.1029708E+07 -0.1699237E+01  0.6468508E+03 -0.2491374E+01  0.1410599E+07
  0.5375000E+00  0.1035865E+07 -0.1713873E+01  0.6697420E+03 -0.2425050E+01  0.1420910E+07
  0.5550000E+00  0.1037702E+07 -0.1731563E+01  0.6960816E+03 -0.2358214E+01  0.1404573E+07
  0.5725000E+00  0.1035217E+07 -0.1751659E+01  0.7179675E+03 -0.2287927E+01  0.1378188E+07
  0.5900000E+00  0.1027114E+07 -0.1774049E+01  0.7409057E+03 -0.2216163E+01  0.1358713E+07
  0.6075000E+00  0.1015068E+07 -0.1800701E+01  0.7633942E+03 -0.2147608E+01  0.1326375E+07
  0.6250000E+00  0.9990514E+06 -0.1832085E+01  0.7782726E+03 -0.2078564E+01  0.1286315E+07
  0.6425000E+00  0.9795082E+06 -0.1867308E+01  0.7911182E+03 -0.2015979E+01  0.1226385E+07
  0.6600000E+00  0.9558807E+06 -0.1906230E+01  0.8037236E+03 -0.1948058E+01  0.1160556E+07
  0.6775000E+00  0.9289234E+06 -0.1950434E+01  0.8189907E+03 -0.1876223E+01  0.1096017E+07
  0.6950000E+00  0.8984744E+06 -0.2002146E+01  0.8297733E+03 -0.1809420E+01  0.1030459E+07
  0.7125000E+00  0.8665788E+06 -0.2062717E+01  0.8327280E+03 -0.1746448E+01  0.9623377E+06
  0.7300000E+00  0.8345618E+06 -0.2133593E+01  0.8345417E+03 -0.1686887E+01  0.8913832E+06
  0.7475000E+00  0.8034680E+06 -0.2216144E+01  0.8326049E+03 -0.1625304E+01  0.8235847E+06
  0.7650000E+00  0.7756044E+06 -0.2312288E+01  0.8324631E+03 -0.1563067E+01  0.7600646E+06
  0.7825000E+00  0.7560289E+06 -0.2424250E+01  0.8333728E+03 -0.1494516E+01  0.7001252E+06
  0.8000000E+00  0.7500711E+06 -0.2548845E+01  0.8319241E+03 -0.1426902E+01  0.6446243E+06
  0.8175000E+00  0.7630502E+06 -0.2677748E+01  0.8239275E+03 -0.1361069E+01  0.5970412E+06
```

Sample RadiationCoefficients.tec File

This file shows a sample result obtained from NEMOH for added mass (even columns) and radiation damping (odd columns) coefficients.

```
VARIABLES="w (rad/s)"
"A  1  1" "B  1  1"
"A  1  2" "B  1  2"
"A  1  3" "B  1  3"
"A  1  4" "B  1  4"
"A  1  5" "B  1  5"
"A  1  6" "B  1  6"
Zone t="Motion of body    1 in DoF   1",I=    81,F=POINT
 0.1000000E+00  0.7821775E+07  0.1368915E+03 -0.1607938E+04  0.1379173E+00 -0.5196498E+04  0.3733560E+02  0.1525092E+06  0.3320079E+01
 0.1175000E+00  0.7821324E+07  0.2363899E+03 -0.1595912E+04  0.2380620E+00 -0.5307342E+04  0.4253578E+02  0.1532208E+06  0.6001877E+01
 0.1350000E+00  0.7825988E+07  0.3867425E+03 -0.1593967E+04  0.4099731E+00 -0.5322844E+04  0.4703219E+02  0.1522635E+06  0.1006591E+02
 0.1525000E+00  0.7837724E+07  0.6060238E+03 -0.1582149E+04  0.6431395E+00 -0.5475706E+04  0.4979143E+02  0.1537753E+06  0.1551254E+02
 0.1700000E+00  0.7843167E+07  0.9269997E+03 -0.1572912E+04  0.9785264E+00 -0.5518552E+04  0.5158838E+02  0.1531211E+06  0.2406184E+02
 0.1875000E+00  0.7847402E+07  0.1384145E+04 -0.1559913E+04  0.1515498E+01 -0.5640266E+04  0.5000737E+02  0.1539843E+06  0.3780360E+02
 0.2050000E+00  0.7859060E+07  0.2036815E+04 -0.1553874E+04  0.2280044E+01 -0.5752152E+04  0.4518013E+02  0.1546121E+06  0.5664781E+02
 0.2225000E+00  0.7875352E+07  0.2972864E+04 -0.1528333E+04  0.3417127E+01 -0.5818820E+04  0.3729229E+02  0.1543269E+06  0.8387965E+02
 0.2400000E+00  0.7883588E+07  0.4277888E+04 -0.1510439E+04  0.4978441E+01 -0.6014077E+04  0.2072538E+02  0.1560683E+06  0.1236503E+03
 0.2575000E+00  0.7894721E+07  0.6144228E+04 -0.1497326E+04  0.7325493E+01 -0.6076077E+04 -0.1661793E+01  0.1557966E+06  0.1823944E+03
 0.2750000E+00  0.7905434E+07  0.8727477E+04 -0.1467925E+04  0.1074519E+02 -0.6191691E+04 -0.3390869E+02  0.1564877E+06  0.2676190E+03
 0.2925000E+00  0.7930295E+07  0.1216699E+05 -0.1442809E+04  0.1549166E+02 -0.6381315E+04 -0.8222929E+02  0.1586901E+06  0.3860464E+03
 0.3100000E+00  0.7948304E+07  0.1699343E+05 -0.1414699E+04  0.2210783E+02 -0.6415882E+04 -0.1380030E+03  0.1578669E+06  0.5550789E+03
 0.3275000E+00  0.7959711E+07  0.2332927E+05 -0.1380453E+04  0.3119843E+02 -0.6533800E+04 -0.2148519E+03  0.1592245E+06  0.7882833E+03
 0.3450000E+00  0.7973102E+07  0.3141754E+05 -0.1358409E+04  0.4310878E+02 -0.6670322E+04 -0.3130832E+03  0.1617112E+06  0.1100196E+04
 0.3625000E+00  0.7990366E+07  0.4150944E+05 -0.1332452E+04  0.5954640E+02 -0.6597964E+04 -0.4129331E+03  0.1607938E+06  0.1510027E+04
 0.3800000E+00  0.8010737E+07  0.5383512E+05 -0.1287688E+04  0.8000769E+02 -0.6617515E+04 -0.5381340E+03  0.1623793E+06  0.2043303E+04
 0.3975000E+00  0.8021018E+07  0.6877772E+05 -0.1266543E+04  0.1044362E+03 -0.6675517E+04 -0.6880036E+03  0.1649608E+06  0.2717644E+04
 0.4150000E+00  0.8028484E+07  0.8626130E+05 -0.1255641E+04  0.1353370E+03 -0.6514805E+04 -0.8254997E+03  0.1644780E+06  0.3517696E+04
 0.4325000E+00  0.8032744E+07  0.1052225E+06 -0.1239681E+04  0.1719989E+03 -0.6320974E+04 -0.9681137E+03  0.1642708E+06  0.4491440E+04
 0.4500000E+00  0.8025628E+07  0.1276420E+06 -0.1227004E+04  0.2138697E+03 -0.6275791E+04 -0.1152020E+04  0.1669872E+06  0.5710654E+04
 0.4675000E+00  0.8019748E+07  0.1507231E+06 -0.1236762E+04  0.2628421E+03 -0.6045160E+04 -0.1311218E+04  0.1675960E+06  0.7079895E+04
 0.4850000E+00  0.8013170E+07  0.1740447E+06 -0.1252119E+04  0.3157668E+03 -0.5718094E+04 -0.1433786E+04  0.1657502E+06  0.8498318E+04
 0.5025000E+00  0.7994054E+07  0.2015019E+06 -0.1276753E+04  0.3740670E+03 -0.5436010E+04 -0.1574638E+04  0.1653068E+06  0.1021559E+05
 0.5200000E+00  0.7968019E+07  0.2262686E+06 -0.1326928E+04  0.4359538E+03 -0.5243665E+04 -0.1747464E+04  0.1669687E+06  0.1225252E+05
 0.5375000E+00  0.7938517E+07  0.2513441E+06 -0.1406122E+04  0.4963855E+03 -0.4897887E+04 -0.1861729E+04  0.1661256E+06  0.1416975E+05
 0.5550000E+00  0.7906646E+07  0.2743035E+06 -0.1489845E+04  0.5579922E+03 -0.4522988E+04 -0.1915765E+04  0.1626236E+06  0.1605229E+05
 0.5725000E+00  0.7870280E+07  0.2938788E+06 -0.1574541E+04  0.6193058E+03 -0.4138910E+04 -0.1946734E+04  0.1594332E+06  0.1791606E+05
 0.5900000E+00  0.7826681E+07  0.3142720E+06 -0.1676640E+04  0.6795667E+03 -0.3870858E+04 -0.2029296E+04  0.1586400E+06  0.2028129E+05
 0.6075000E+00  0.7786176E+07  0.3261131E+06 -0.1801984E+04  0.7269883E+03 -0.3612323E+04 -0.2096186E+04  0.1582072E+06  0.2279606E+05
 0.6250000E+00  0.7745006E+07  0.3354658E+06 -0.1949432E+04  0.7604417E+03 -0.3263826E+04 -0.2053249E+04  0.1543895E+06  0.2439254E+05
 0.6425000E+00  0.7710190E+07  0.3398712E+06 -0.2086779E+04  0.7838326E+03 -0.2991282E+04 -0.1961634E+04  0.1489214E+06  0.2539585E+05
 0.6600000E+00  0.7672173E+07  0.3416640E+06 -0.2217496E+04  0.8065089E+03 -0.2737148E+04 -0.1848693E+04  0.1442852E+06  0.2638156E+05
 0.6775000E+00  0.7643223E+07  0.3353303E+06 -0.2352395E+04  0.8171901E+03 -0.2542369E+04 -0.1801340E+04  0.1418329E+06  0.2834220E+05
 0.6950000E+00  0.7614300E+07  0.3241646E+06 -0.2494393E+04  0.8028251E+03 -0.2410277E+04 -0.1767212E+04  0.1405580E+06  0.3043156E+05
 0.7125000E+00  0.7599172E+07  0.3109584E+06 -0.2634945E+04  0.7625068E+03 -0.2276713E+04 -0.1625996E+04  0.1368708E+06  0.3115187E+05
 0.7300000E+00  0.7592367E+07  0.2954152E+06 -0.2759204E+04  0.7038636E+03 -0.2195903E+04 -0.1458165E+04  0.1319902E+06  0.3016397E+05
 0.7475000E+00  0.7595208E+07  0.2783738E+06 -0.2865055E+04  0.6364847E+03 -0.2135727E+04 -0.1268458E+04  0.1267111E+06  0.2820956E+05
 0.7650000E+00  0.7605582E+07  0.2620128E+06 -0.2957412E+04  0.5701578E+03 -0.2130949E+04 -0.1112837E+04  0.1230762E+06  0.2737891E+05
 0.7825000E+00  0.7626174E+07  0.2457512E+06 -0.3035433E+04  0.4818285E+03 -0.2129739E+04 -0.1019557E+04  0.1205469E+06  0.2760472E+05
 0.8000000E+00  0.7652624E+07  0.2334917E+06 -0.3090768E+04  0.3646519E+03 -0.2137262E+04 -0.9651233E+03  0.1189721E+06  0.2821056E+05
```

Sample FKForce.tec File

This file shows a sample result obtained from NEMOH for Froude-Krylov force. Even columns show the amplitude and odd columns show the phase of the force.

```
VARIABLES="w (rad/s)"
"abs(F   1   1)" "angle(F   1   1)"
"abs(F   1   2)" "angle(F   1   2)"
"abs(F   1   3)" "angle(F   1   3)"
"abs(F   1   4)" "angle(F   1   4)"
"abs(F   1   5)" "angle(F   1   5)"
"abs(F   1   6)" "angle(F   1   6)"
Zone t="FKforce - beta =    0.000",I=    81,F=POINT
  0.1000000E+00  0.2492631E+06 -0.1570821E+01  0.3046891E+00  0.3205117E-02  0.1163466E+07 -0.2842542E-04  0.8571307E+02  0.2761806E+01
  0.1175000E+00  0.2942245E+06 -0.1570820E+01  0.9479178E+00  0.3104496E+01  0.1125888E+07 -0.4865689E-04  0.8828780E+02  0.2677272E+01
  0.1350000E+00  0.3398962E+06 -0.1570836E+01  0.7793122E+00  0.3135327E+01  0.1082588E+07 -0.7871964E-04  0.1054998E+03  0.2693578E+01
  0.1525000E+00  0.3864279E+06 -0.1570866E+01  0.6884767E+00  0.3140883E+01  0.1033701E+07 -0.1222695E-03  0.1628756E+03  0.2803161E+01
  0.1700000E+00  0.4339847E+06 -0.1570897E+01  0.9005597E+00  0.3091147E+01  0.9794616E+06 -0.1848572E-03  0.1994859E+03  0.2848545E+01
  0.1875000E+00  0.4827435E+06 -0.1570940E+01  0.9209709E+00  0.4773441E-01  0.9201189E+06 -0.2740183E-03  0.2451273E+03  0.2881022E+01
  0.2050000E+00  0.5328856E+06 -0.1571002E+01  0.1753156E+00  0.7528973E+00  0.8560294E+06 -0.4012758E-03  0.2850527E+03  0.2871954E+01
  0.2225000E+00  0.5845864E+06 -0.1571085E+01  0.8676615E-01  0.1065611E+01  0.7875828E+06 -0.5837085E-03  0.3232545E+03  0.2898434E+01
  0.2400000E+00  0.6379876E+06 -0.1571203E+01  0.6399853E+00 -0.1597552E+00  0.7152811E+06 -0.8476843E-03  0.4137328E+03  0.2933928E+01
  0.2575000E+00  0.6931680E+06 -0.1571354E+01  0.3810337E+00 -0.2978394E+00  0.6397345E+06 -0.1234407E-02  0.4953752E+03  0.2945524E+01
  0.2750000E+00  0.7501048E+06 -0.1571560E+01  0.3078837E+00  0.2730453E+01  0.5616416E+06 -0.1810326E-02  0.5971969E+03  0.2964692E+01
  0.2925000E+00  0.8086212E+06 -0.1571844E+01  0.3928544E+00 -0.2719646E+01  0.4817540E+06 -0.2688576E-02  0.7205020E+03  0.2985238E+01
  0.3100000E+00  0.8683416E+06 -0.1572217E+01  0.5269840E+00  0.1892184E+00  0.4009278E+06 -0.4071288E-02  0.8934928E+03  0.3006748E+01
  0.3275000E+00  0.9286781E+06 -0.1572712E+01  0.6511746E+00  0.3068041E+01  0.3200128E+06 -0.6354014E-02  0.9981858E+03  0.3007577E+01
  0.3450000E+00  0.9888366E+06 -0.1573376E+01  0.6140303E+00  0.1468453E+00  0.2398361E+06 -0.1042708E-01  0.1171688E+04  0.3014205E+01
  0.3625000E+00  0.1047861E+07 -0.1574237E+01  0.2660860E+00 -0.2648397E+01  0.1611805E+06 -0.1882008E-01  0.1367976E+04  0.3025143E+01
  0.3800000E+00  0.1104710E+07 -0.1575355E+01  0.3168674E+00 -0.3087633E+01  0.8475391E+05 -0.4276120E-01  0.1608231E+04  0.3034996E+01
  0.3975000E+00  0.1158325E+07 -0.1576786E+01  0.4290281E+00  0.3050418E+01  0.1179863E+05 -0.3690805E+00  0.1828882E+04  0.3036515E+01
  0.4150000E+00  0.1207697E+07 -0.1578606E+01  0.5286102E+00 -0.1185118E+00  0.5953312E+05 -0.3058991E+01  0.2071036E+04  0.3044109E+01
  0.4325000E+00  0.1251906E+07 -0.1580905E+01  0.6869355E+00 -0.6248768E+00  0.1259673E+06 -0.3097435E+01  0.2357844E+04  0.3048274E+01
  0.4500000E+00  0.1290142E+07 -0.1583776E+01  0.3059658E+00  0.7153771E+00  0.1882073E+06 -0.3108821E+01  0.2628271E+04  0.3052229E+01
  0.4675000E+00  0.1321716E+07 -0.1587345E+01  0.3993138E+00 -0.2828349E+01  0.2458192E+06 -0.3114391E+01  0.2913254E+04  0.3052121E+01
  0.4850000E+00  0.1346048E+07 -0.1591761E+01  0.2192812E+00  0.2805758E+01  0.2984486E+06 -0.3117907E+01  0.3205441E+04  0.3057919E+01
  0.5025000E+00  0.1362689E+07 -0.1597196E+01  0.3034899E+00  0.3894694E+00  0.3457941E+06 -0.3120606E+01  0.3503839E+04  0.3057008E+01
  0.5200000E+00  0.1371302E+07 -0.1603860E+01  0.2652945E-01 -0.1681454E+01  0.3876057E+06 -0.3123041E+01  0.3794237E+04  0.3057355E+01
  0.5375000E+00  0.1371677E+07 -0.1612006E+01  0.3095781E+00 -0.2739704E+01  0.4236919E+06 -0.3125534E+01  0.4084986E+04  0.3058346E+01
  0.5550000E+00  0.1363730E+07 -0.1621944E+01  0.7968872E+00  0.2784812E+01  0.4539285E+06 -0.3128306E+01  0.4356356E+04  0.3056172E+01
  0.5725000E+00  0.1347520E+07 -0.1634045E+01  0.4920230E+00  0.1715319E+00  0.4782609E+06 -0.3131546E+01  0.4620357E+04  0.3055275E+01
  0.5900000E+00  0.1323250E+07 -0.1648762E+01  0.9467264E-01 -0.2772220E+01  0.4967040E+06 -0.3135428E+01  0.4878588E+04  0.3051887E+01
  0.6075000E+00  0.1291288E+07 -0.1666647E+01  0.3222151E+00  0.2463420E+01  0.5093601E+06 -0.3140131E+01  0.5097926E+04  0.3048482E+01
  0.6250000E+00  0.1252179E+07 -0.1688375E+01  0.3246586E+00  0.2536904E+01  0.5163901E+06  0.3137334E+01  0.5304598E+04  0.3044875E+01
  0.6425000E+00  0.1206662E+07 -0.1714763E+01  0.2034770E+00 -0.1511970E+01  0.5180347E+06  0.3130381E+01  0.5474534E+04  0.3040405E+01
  0.6600000E+00  0.1155698E+07 -0.1746805E+01  0.1620218E+00 -0.1158386E+01  0.5146015E+06  0.3121946E+01  0.5603284E+04  0.3033763E+01
  0.6775000E+00  0.1100490E+07 -0.1785685E+01  0.1670407E+00  0.2923558E+01  0.5064688E+06  0.3111746E+01  0.5707789E+04  0.3026330E+01
  0.6950000E+00  0.1042512E+07 -0.1832791E+01  0.2571133E+00  0.2782600E+01  0.4940708E+06  0.3099448E+01  0.5773763E+04  0.3017289E+01
  0.7125000E+00  0.9835364E+06 -0.1889678E+01  0.1455283E+00  0.1948810E+01  0.4778940E+06  0.3084666E+01  0.5806000E+04  0.3008553E+01
  0.7300000E+00  0.9256702E+06 -0.1957953E+01  0.1151443E+00 -0.2607718E+01  0.4584718E+06  0.3066949E+01  0.5792568E+04  0.2994576E+01
  0.7475000E+00  0.8713212E+06 -0.2039031E+01  0.5568333E-01 -0.2677945E+01  0.4363644E+06  0.3045772E+01  0.5738353E+04  0.2982493E+01
  0.7650000E+00  0.8231333E+06 -0.2133703E+01  0.1210829E+00  0.1481962E+01  0.4121796E+06  0.3020521E+01  0.5648912E+04  0.2966207E+01
  0.7825000E+00  0.7837941E+06 -0.2241510E+01  0.1149633E+00 -0.1776105E+01  0.3865264E+06  0.2990496E+01  0.5510047E+04  0.2948753E+01
  0.8000000E+00  0.7556889E+06 -0.2360109E+01  0.3824913E-01  0.2077275E+01  0.3600254E+06  0.2954902E+01  0.5344281E+04  0.2926669E+01
```

Sample Nemoh.cal File

This file controls the operation of NEMOH. The following is a sample file that can be used as a starting point for a single geometry.

```
|--- Environment ---------------------------------------------------------------------------------
1025.0                          ! RHO                ! KG/M**3        ! Fluid specific volume
9.81                            ! G                  ! M/S**2         ! Gravity
200.                            ! DEPTH              ! M              ! Water depth
0.      0.                      ! XEFF YEFF          ! M              ! Wave measurement point
--- Description of floating bodies --------------------------------------------------------------
1                               ! Number of bodies
--- Body 1 --------------------------------------------------------------------------------------
nemohMesh.dat   ! Name of mesh file
1809 1804  ! Number of points and number of panels
6                               ! Number of degrees of freedom
1 1. 0. 0. 0. 0. 0.             ! Surge
1 0. 1. 0. 0. 0. 0.             ! Sway
1 0. 0. 1. 0. 0. 0.             ! Heave
2 1. 0. 0. 0. 0. -2.2          ! Roll about CdG
2 0. 1. 0. 0. 0. -2.2          ! Pitch about CdG
2 0. 0. 1. 0. 0. -2.2          ! Yaw about CdG
6                               ! Number of resulting generalised forces
1 1. 0. 0. 0. 0. 0.             ! Force in x direction
1 0. 1. 0. 0. 0. 0.             ! Force in y direction
1 0. 0. 1. 0. 0. 0.             ! Force in z direction
2 1. 0. 0. 0. 0. -2.2          ! Moment force in x direction about CdG
2 0. 1. 0. 0. 0. -2.2          ! Moment force in y direction about CdG
2 0. 0. 1. 0. 0. -2.2          ! Moment force in z direction about CdG
0                               ! Number of lines of additional information
--- Load cases to be solved ---------------------------------------------------------------------
81      0.1     1.5             ! Number of wave frequencies, Min, and Max (rad/s)
1       0.      0.              ! Number of wave directions, Min and Max (degrees)
--- Post processing -----------------------------------------------------------------------------
0       0       0               ! IRF                             ! IRF calculation (0 for no calculation), time step and duration
0                               ! Show pressure
0       0.      0.              ! Kochin function                 ! Number of directions of calculation (0 for no calculations)
0       0       0       0       ! Free surface elevation          ! Number of points in x direction (0 for no calcutions) and y
```

Appended paper

Paper:

Hydrodynamic performance evaluation of a semi-submersible floater using open-source tools
Milad Hassani, Lin Li, Filippos Kalofotias, Zhiyu Jiang
Published in Proceedings of the ASME 2022 41st International
Conference on Ocean, Offshore and Arctic Engineering,
OMAE2022, June 5-10, 2022, Hamburg, Germany

OMAE2022-78823

HYDRODYNAMIC PERFORMANCE EVALUATION OF A SEMI-SUBMERSIBLE FLOATER USING OPEN-SOURCE TOOLS

Milad Hassani
Department of
Mechanical and
Structural Engineering
and Materials Science,
University of Stavanger,
Stavanger, Norway
m.hassani@stud.uis.no

Lin Li
Department of
Mechanical and
Structural Engineering
and Materials Science,
University of Stavanger,
Stavanger, Norway
lin.li@uis.no

Filippos Kalofotias
Vorticity Engineering
Bussum, Netherlands
filippos@vorticity.nl

Zhiyu Jiang
Department of
Engineering Sciences,
University of Agder
Grimstad, Norway
zhiyu.jiang@uia.no

ABSTRACT

Floating structures are viable alternatives for supporting wind turbines in deep water. Design of floating support structures is a challenging task, and a design evaluation requires considerations of costs and system performance.

An approach for evaluation of semi-submersible floaters has been developed in this paper. A braceless semi-submersible floater is selected and this floater is designed to support a 5-MW wind turbine in the North Sea. The evaluation framework consists of automatic modeling and numerical simulations in open-source tools. A Python-SALOME-NEMOH interface is used to obtain the hydrodynamic properties for geometries defined by various variables. The geometries are subjected to three performance constraints related to the static platform pitch, metacentric height, nacelle acceleration and wind loads in operating and parked conditions. Finally, the geometries are evaluated using two combined objective functions related to material cost and nacelle acceleration, and the Pareto Fronts are discussed. This work contributes to developing efficient design optimization methods for floating structures.

Keywords: Hydrodynamic response; open-source tool; floating wind turbine; semi-submersible; hull geometry

1. INTRODUCTION

Wind energy is an important source of natural renewable energy. In recent years, efforts have increased to create offshore wind farms to exploit this precious resource in many countries.

The USA, China and Norway are among countries with large potential for offshore wind turbine installations. To tap into high quality wind resources over deep waters, floating platforms for offshore wind turbines are being developed [1].

There are currently active projects in Denmark, Norway, Germany, Portugal, Spain, Sweden, and the United Kingdom [2, 3]. In the North Sea and Atlantic Ocean, two utility-scale offshore wind turbines are currently operating.

Semi-submersible floaters have many advantages compared to other alternatives. They are stable in harsh environments, have a large deck area, and are easy to construct and install [4, 5]. Semi-submersibles have natural frequencies that are inversely proportional to the platform's draft and length [5, 6]. Thus, the choice of geometric shapes is a key factor in the design of semi-submersibles. Existing semi-submersible wind turbine concepts generally use either three columns with the wind turbine on one side column or four columns with the wind turbine on the central column [7]. Figure 1 illustrates some innovative designs of semisubmersible wind turbines.

Design of offshore substructures is a complex process that considers the requirements of stability, tower inclination, and mooring loads, all of which are affected by wind, waves, and control actions [8]. For floating offshore wind turbines (FOWTs), it is desirable to eliminate the tower-top motions. FOWTs can be subjected to large platform motions which can decrease the structural design life or energy production. The oscillation of the tower top is a result of wind and wave-induced platform motions. Optimizing the shape of the substructure can

enhance the hydrodynamic properties and alleviate motion, thereby improving performance. Additionally, achieving cost reduction is also an important design consideration for FOWTs. The substructures' cost contributes significantly to the total cost of a FOWT [9]. Applying optimization techniques to hull shape designs has become an effective way to reduce the cost of FOWTs.

Use of open-source tools can lead to more control over the settings, more flexibility regarding the data manipulation and possible less man hours compared to many standard design processes from commercial software. In this work, NEMOH, SALOME and Python are the selected open-source tools.

FIGURE 1: INNOVATIVE CONCEPTS OF FOWT, 5-MW-CSC (LEFT), NAUTILUS (MIDDLE), OLAV OLSEN OO STAR (RIGHT), [7]

The focus of this paper is to provide a framework using open-source tools for performance evaluation, and a braceless semisubmersible floater is considered as a representative support structure for FOWTs. Frequency-domain analysis of the platform response is applied with pre-calculated hydrodynamic properties, and performances of different geometries are compared in terms of material cost and nacelle acceleration. The analysis using the proposed framework can be treated as a preliminary study before a full design optimization is achieved.

2. PARAMETERIZATION OF THE FLOATING SUPPORT STRUCTURE

2.1 Platform geometry

Luan et al. [7, 8] designed the 5-MW-CSC semi-submersible FOWT based on the OO-Star semi-submersible concept. The CSC semi-submersible floater is composed of three side columns and one central column; see Figures 1 and 2. The FOWT is symmetrical with the NREL 5 MW wind turbine mounted on the central column. Three columns are positioned around the turbine's centerline, and this configuration helps to achieve good hydrostatic performance. The added mass in heave, roll and pitch are mainly provided by the pontoons. There are no heave plates or braces. The box-shaped cross-section of the pontoons provide considerable viscous damping at the heave, roll and pitch resonant frequencies. The original dimensions of the hull in this study are shown in Table 1. An overview of the properties of the original design can be found in [7, 10]. The structural strength

and internal stiffness of the geometry are not considered in this work.

In this paper, the original 5-MW-CSC is applied as the baseline design. Different geometries are generated by changing the dimensions of the hull. The objective is to evaluate different performance constraints and to propose better hull geometries in terms of material cost of the hull and the acceleration of the turbine nacelle.

TABLE 1: MAIN CHARACTERISTICS OF 5-MW-CSC PLATFORM AT FULL SCALE [7, 10]

Parameter	Unit	Value
column diameter, d	m	6.5
column spacing, s	m	41
submerged column height, hc	m	24
Operating draft	m	30
Displaced volume	m³	10517
Floater steel mass	kg	1.686e6
COG (x,y,z)	(m,m,m)	(0,0,-18.9)
I_{xx} w.r.t COG	kg · m²	1.065e10
I_{yy} w.r.t COG	kg · m²	1.065e10
I_{zz} w.r.t COG	kg · m²	8.412e9

2.2 Design variables

In structural design optimization, it is useful to represent the structural geometry by a few parameters, which are defined as design variables. An example of a parametric study that considers a broad range of platform configurations can be found in [11].

There are many design variables that can be included in an optimization problem. In this work, we only consider three design variables. If a large number of variables is employed, linear or nonlinear constraints need to be applied to eliminate non-feasible designs. Therefore, prior to the evaluation of the hull, a sensitivity analysis was performed to verify the appropriate design variables and the variable range. Based on the sensitivity analysis performed in [12], the column spacing and draft are the main variables that are most correlated to the dynamic responses. Moreover, a sensitivity analysis is also carried out to determine the influence of the pontoon height and the submerged column height on the motion responses.

In this context, only the hull geometry will be varied, while the wind turbine remains unchanged. From the discussions above, this study considers a geometry with three design variables, namely the submerged height of the columns (hc), the diameter of the columns (d) and the spacing between the side columns (s); see Figure 2. The dependent variables changing with the design variables are the draft, pontoon width and ballast. In addition, constant pontoon height and constant steel thickness (3mm) are assumed for the pontoons and columns. The design variables are shown in Table 2.

TABLE 2: DESIGN VARIABLES

Design variables	Unit	Range of values
column diameter, d	m	[4.5, 5.5, 6.5, 7.5, 8.5]
column spacing, s	m	[36, 41, 46, 51]
submerged column height, hc	m	[20, 22, 24, 26, 28]

2.3 Mass and ballast of the support structure

A mass model is firstly constructed which calculates the mass characteristics of the FOWT structure with respect to the center of gravity (COG) of the system (point O) and the buoyancy of the floater, so the ballast requirement can be determined. With changing the variables stated in Table 2, the structural mass, the displaced water volume and resulting buoyancy change as well. The amount of ballast is set to be modifiable, in order to maintain the hub height and freeboard. The ballast mass is set according to the surplus buoyancy of the system – the remaining buoyancy force after subtracting wind turbine weight and platform structural weight.

(a) Side view

(b) Plan view
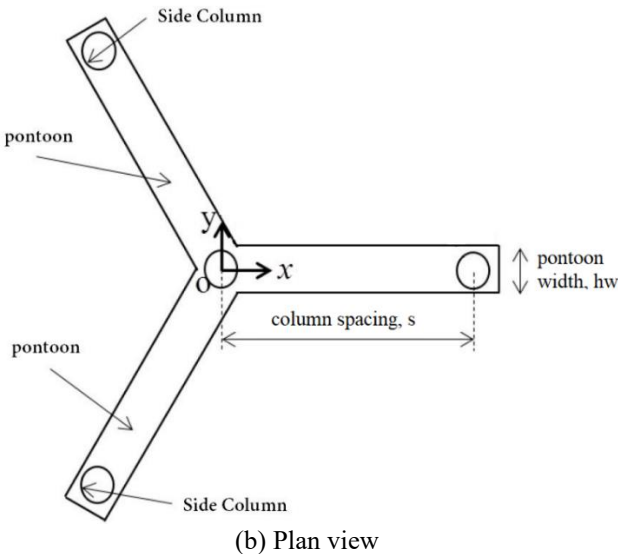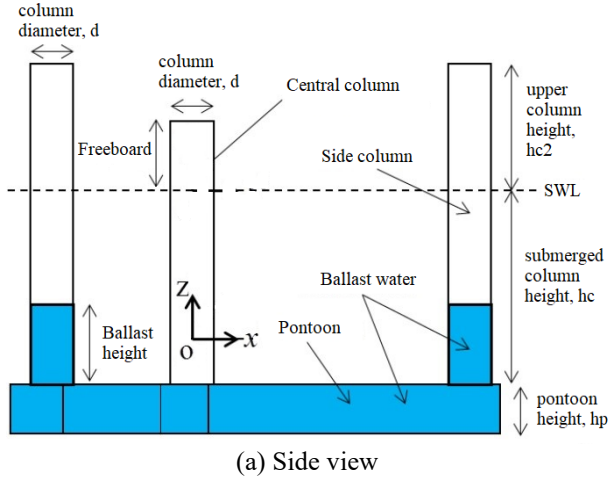
FIGURE 2: BRACELESS SEMISUBMERSIBLE [7]

In this study, for all geometries in the design space, the pontoon and side columns are considered for ballasting, see Figure 2. The effects of different ballasting scenarios on motion responses are discussed in Sec. 6.2.

The ballast density is assumed to be the same as sea water density, which is 1025 kg/m³.

3. MODELING METHODOLOGY

After parametrization of the support structure, the performance of the design needs to be evaluated. The evaluation of each geometry in the design space and calculation of its objective function values are handled in Python-SALOME-NEMOH interface.

3.1 Hydrodynamics of the semi-submersible FOWT

NEMOH [13] is an open source Boundary Element Method (BEM) solver. The BEM, also known as panel method employs Green's functions to transform a flow problem into a problem of source distribution on the body surface. Based on this, the radiated velocity potentials are solved to determine the wave excitation forces, the added mass and radiation damping terms. In this study, the water depth and wave direction are assumed to be 100m and zero-degree respectively. The geometry and mesh for each design are generated in SALOME, which is also an open-source software that provides a generic pre- and post-processing platform for numerical simulation. Before NEMOH is called, the surface of each geometry is built and discretized in SALOME [14]. The exported meshes from SALOME in Python to be used in NEMOH. The NEMOH input files are updated for each geometry in Python.

3.2 Viscous damping

The results from NEMOH based on linear wave theory does not take into account viscous forces, the hydrodynamic results calculated from computer programs that only use linear wave theory fail to produce accurate vessel responses [15]. The viscous damping from flow separation is the dominant damping contribution for semi-submersibles. It is usually well modelled through the Morison equation, if the drag coefficients are calibrated well [16]. Often, in frequency-domain analysis, the viscous damping force is linearized by as the multiplication of an equivalent linear damping coefficient, B^{vi}, and the velocity in the corresponding degree of freedom. See below:

$$F_{vis} = B^{vi} * \dot{x} \qquad (1)$$

For Morison type of drag forces, the equivalent damping coefficient is proportional to the root-mean-square (RMS) of the corresponding velocity depending on the sea states. In this study, the viscous damping in pitch for each geometry was considered, the RMS pitch velocity can be obtained at different sea states based on:

$$RMS_{\dot{x}_{55}} = \sqrt{\int_0^\infty \omega^2 \, S_{x_{55}}(\omega) \, d\omega} \qquad (2)$$

where,

$S_{x_{55}}(\omega)$ is the is the spectral density of the pitch motion for corresponding sea states.

The equivalent damping coefficients for different geometry and sea states are obtained by an interactive approach. First, a reference damping coefficient to consider the viscous effects is calculated for the baseline geometry by tuning the RAOs and verifying with the previous research (see Figure 8). This initial damping coefficient corresponds to the initial RMS velocity of the baseline geometry. Then, for different geometries at given sea states, a new RMS velocity can be calculated using the same initial damping coefficient. Thus, the equivalent damping is updated to correspond to this new RMS velocity. This process continues until the RMS velocity converges. Figure 3 shows a flowchart of how the viscous damping is estimated in this study.
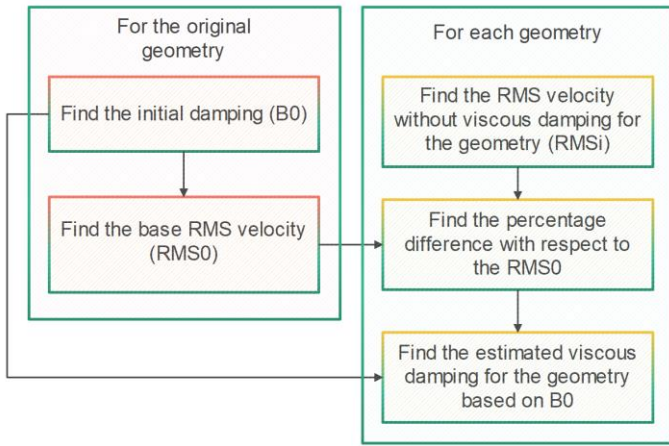
FIGURE 3: FLOWCHART OF THE VISCOUS DAMPING ESTIMATION

3.3 Response Amplitude Operator

Response Amplitude Operators (RAOs) are the core of all sea keeping assessment. It shows the variation of the floater's response with the frequency. Using B^{vi} for the viscous damping terms, the RAO can be written as:

$$RAO(\omega) = \frac{\hat{F}(\omega)}{\{-\omega^2 \cdot (M + A(\omega)) + i\omega \cdot (B(\omega) + B^{vi}) + C\}} \quad (3)$$

where,

M – is a matrix of the structure's mass and inertia around the COG of the system

A – is a matrix of hydrodynamic added mass

B – is a matrix of radiation damping

$\hat{F}$ – is a complex amplitude of the wave excitation force acting on the structure per unit wave amplitude

C - is a platform stiffness matrix

4. EVALUATION FRAMEWORK

The evaluation procedure is performed by connecting the results from the hydrostatic calculations in Python and the results from the hydrodynamic simulations performed in NEMOH. The geometries are then subjected to the constraints, whereas the geometries which not fulfil the performance constraints are eliminated. The weighted sum method is then applied to calculate the combined objective function. Lastly the optimum geometry is selected subjectively from the Pareto Fronts. Figure 4 shows the flowchart of the evaluation framework.

4.1 Objective functions

The first objective function is the material cost of the hull, and the goal is to minimize the steel weight. Hence, $minimize$ $f_1(\text{x})$.

$$f_1(x) = m_{steel} c_{steel} \quad (4)$$

where x is a design variable vector, m is the mass and c is the cost for each type of material of the concept considered. The cost in this study is a floating platform cost only. Because of the inexpensive materials that can be used as ballast, the cost of the ballast is not considered.

For a floating wind turbine, large platform motions can potentially reduce turbine lifetime or energy production. To account for this, the minimization of platform motions that cause problematic turbine loadings is used as another optimization objective. In this study, the acceleration of the nacelle is considered. The high fore-aft nacelle motion may create extra loads on the wind turbine, causes fatigue in the drivetrain, and decreases the lifetime of the system [17]. In order to formulate the second objective function $f_2(x)$, the linearity of the simplified dynamic system was exploited to define the nacelle acceleration RAO at each sea state condition. The metric for the platform motions that affect the wind turbine is the root-mean-square (RMS) of the fore-aft nacelle acceleration [7], calculated as:

$$f_2(x) = RMS_{a_{nac}} = \sqrt{\int_0^\infty |RAO_{a_{nac}}(\omega)|^2 S(\omega)\, d\omega} \quad (5)$$

where,

- $S(\omega)$ (JONSWAP) is the is the spectral density of the waves at prescribed sea states (Hs and Tp)
- $RAO_{a_{nac}}(\omega)$ is the fore-aft nacelle acceleration response amplitude operator.

$$RAO_{a_{nac}}(\omega) = -\omega^2(RAO_1 + h_{nacelle}\, RAO_5) \quad (6)$$

The numerical subscripts denote the platform degrees of freedom (DOFs) – 1 being surge and 5 being pitch – and $h_{nacelle}$ is the distance from the CoG of the system to the nacelle.

In order to apply the weighted sum method, objective functions need to have the goal of obtaining the minimum value. Both objective functions are normalized with a value of 0 to 1. The combined objective function is formed by summing the weighted normalized objectives. This results in a single optimization objective as below:

$$minimize\ F(x) = w_1\overline{f_1(x)} + w_2\overline{f_2(x)} \quad (7)$$

where w_i is a weighting factor in the range [0; 1] that controls the weighting between the RMS nacelle acceleration and cost, with $\sum_{i=1}^{M} w_i = 1$. The bar indicates the normalized objectives.
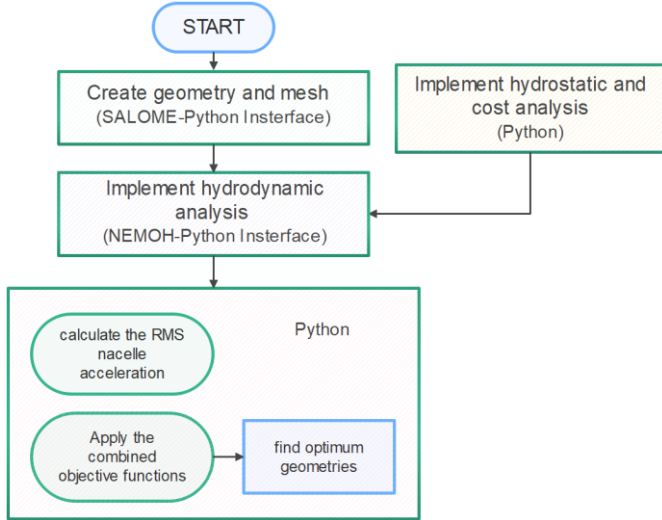

FIGURE 4: FLOWCHART OF AN EVALUATION FRAMEWORK

4.2 Performance constraints

The following performance constraints are applied in this work to ensure the candidate designs are feasible.

PC1) Initial metacentric height (GM$_0$):
The floater must have a GM equal to or greater than zero in order to maintain intact hydrostatic stability. Metacentric height greater than 1 m is chosen in this study for the semi-submersible based on DNVGL-ST-0119 Standard [18]. This GM is for the wind turbine in the operating phase.

$$GM_0 > 1 \qquad (8)$$

PC2) RMS nacelle acceleration ($RMS_{a_{nac}}$):
The nacelle acceleration performance constraint is selected based on Ref. [11]. The common operational limit for the maximum allowable nacelle acceleration is 0.2g to 0.3g, where $g = 9.81 \frac{m}{s^2}$ is the gravitational acceleration. The tolerated acceleration highly depends on the specific turbine. As it is applied by Hall et al. [19], the standard deviation of the nacelle acceleration is selected as the second performance constraint used in the present research.

$$RMS_{a_{nac}} < 0.2g \qquad (9)$$

PC3) Static pitch angle due to the mean wind thrust (φ_{static}^{55}):
An important aspect to consider for preliminary design is the effect of the wind that acts on the turbine, causing the inclination of the tower and a decrease in energy productivity. The system should be stable within the standard threshold value of the heel angle and also must maintain an acceptable steady-state heel angle (less than 10 degree) in maximum static wind loading

conditions beyond which the wind turbine loses substantial efficiency [10, 20].

The maximum static wind thrust was taken as 800,000 N, which is the steady state thrust at the rated wind speed of 11.4 m/s and acts on the wind turbine hub [21]. The necessary restoring coefficient should be higher than the restoring coefficient needed to limit the pitch to 10 degrees, as shown here:

$$C_{55lim} > \frac{F_{thrust}\, h_{nacelle}}{\varphi_{static}^{55}} \qquad (10)$$

where, F_{thrust} is the static wind thrust at rated wind speed and $h_{nacelle}$ is the hub height measured from COG of the system. φ_{static}^{55} should be less than $10°$. For floating offshore wind turbines, this is a commonly used restriction [11, 21, 22, 23]. In order to satisfy this constraint, the geometry must have more pitch restoring coefficient than C_{55lim}. A sufficient restoring coefficient can be achieved by adjusting the dimensions of the substructure, and by adding more ballast. The hub height has been adjusted for each geometry with respect to the COG of the system.

4.3 Environmental conditions

To study the dynamic response of the floater, suitable environmental conditions must be applied. Joint data for wind and waves from the North Sea is chosen for this analysis [24]. The environmental data is based on hourly samples from a hindcast model for years 2001 and 2010. Table 3 identifies the environmental conditions in this study. The U_w at the hub height (90 m) ranges from the cut-in wind speed (3 m/s) to the extreme wind speed at the reference site. The rated wind speed (11.4 m/s) is also included in the analysis. The corresponding H_s for each U_w is chosen as the most probable value from the conditional distribution of H_s given U_w, while the T_p values are the most probable values from the conditional distribution of T_p given both U_w and H_s [24].

Table 3: ENVIRONMENTAL CONDITIONS

EC	Mean wind speed (m/s)	H_s (m)	T_p (s)
1	3	1.46	10.91
2	11.4	2.59	10.18
3	24	6.14	11.22
4	25	6.51	11.34
5	31.2	15.6	14.5

EC1 is a mild condition and the cut-in wind speed is considered. EC2 is situated at the rated wind speed.
EC3 and EC4 have above-rated wind speeds. The maximum thrusts are less than that for EC2. U_w in EC4 corresponds to the cut-off wind speed. The wave spectrum for this spans a much larger frequency range than compared to the previous ECs.

EC5 is the extreme case, where the wind speed corresponds to 50 year return period. The rotor is parked in this condition.

5. VERIFICATION OF RESULTS

In order to have reasonable results at the end of the optimization approach, it is important to perform sensitivity studies on the mesh size and verify the RAOs.

5.1 Convergence study on the mesh size

The accuracy of the hydrodynamic analysis using the panel method depends on the mesh size. Considering that the highest wave frequency involved in the calculations is 1.5 rad/s and using a required length of $\frac{\lambda}{8}$ [23], the geometries are meshed with a maximum element size of 2 m. Additionally, the mesh sensitivity analysis was also considered. The mesh sensitivity results and a mesh model generated in SALOME are shown in Figure 5 and 6 respectively.

Table 4: MESH SENSITIVITY ANALYSIS
(HULL GEOMETRY $d = 6.5$m, $s = 41$m, $hp = 24$m)

Mesh scenario	Number of the panels	Panel length [m]
Mesh 1	1096	2.6
Mesh 2	1456	2.25
Mesh 3	1804	2
Mesh 4	2144	1.8
Mesh 5	2621	1.6

Five mesh scenarios are evaluated. Each scenario corresponds to a specific panel length, as indicated in Table 4.

(a) A55

(b) B55
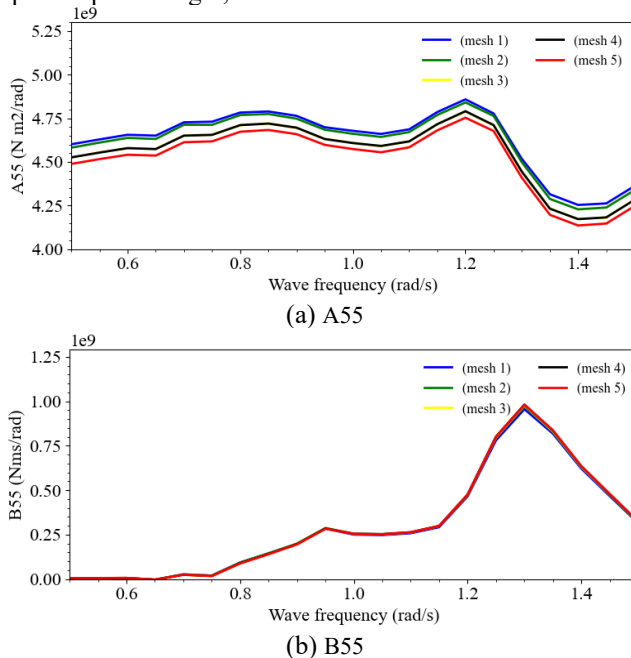
FIGURE 5: INFLUENCE OF THE MESH ON HYDRODYNAMIC COEFFICIENTS

As it can be directly deduced from the Figure 5 (a, b), there are only minor differences between the NEMOH results for the last three different mesh refinements. If the mesh scenario MS5 produces the most accurate results, then the differences produced by the Mesh 4 and Mesh 3 mesh scenarios, with respect to the Mesh 5, can be considered as errors. The maximum error values obtained from the analyzed NEMOH results are found to be less than 1.6%.
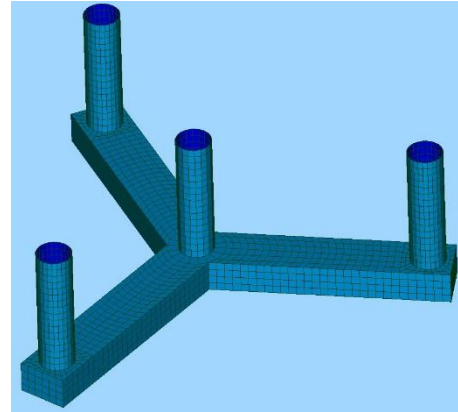
FIGURE 6: MESH MODEL IN SALOME (Mesh 3)

5.2 Verification of motion RAOs

Once the panel length has been verified and the most important hydrodynamic coefficients have been validated, it is necessary to determine if the equations of motion are solved in a correct manner. In order to accomplish this, an investigation is performed to find RAO data of the geometry similar to the one analyzed in the present work. The geometry in the present research is the same as that in [7, 10]. Figure 8 presents a comparison of the pitch RAO from the present study (with and without viscous damping) with that from previous research. As we can see, the pitch RAO value reaches at its maximum at 0.205 rad/s and 0.6425 rad/s. Then, it reduces gradually as the wave frequency increases. As expected, the peak of the pitch RAO at its natural frequency reduces significantly with the addition of the viscous damping. As the viscous damping increases, the peak response decreases. There is a good agreement in the Pitch RAO with the previous work after adding viscous damping (See Figure 8).

6. RESULTS AND DISCUSSION

100 semisubmersible geometries in the design space (see Table 2) have been simulated using the proposed methodology and the properties of each geometry such as the mass, ballast and the meshes are updated accordingly in the hydrodynamic analysis.

6.1 Sensitivity analysis on design variables

As we discussed in Sec. 2.2, before applying any evaluation methodology to a given system, the effects of design variables on the hull should be understood in order to allow adequate

6

interpretation of the evaluation results. The design variables for the sensitivity study are *hc* and *hp*.
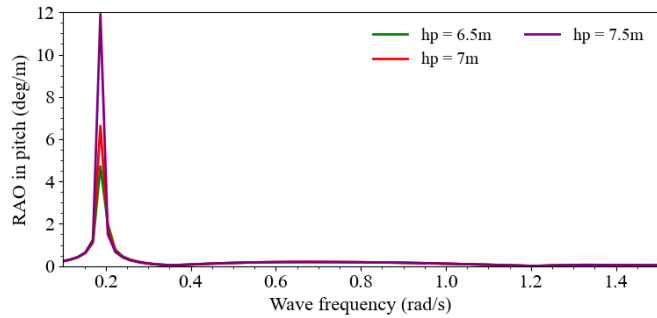
(a) Pontoon height as a design variable for *hc* = 24m

(b) Submerged column height as a design variable for *hp* = 6m

FIGURE 7: PITCH RAO (*d* = 6.5m, *s* = 41m)

When subplots (a) and (b) of Figure 7 are compared, as *hp* changes by 7.7%, the pitch RAO magnitude increases by almost 63%. Pitch RAO, on the other hand, increases by 125% as *hc* increases by 8.3%.

Based on the pitch RAO results using different values for selected design variables, it is found that the submerged column height (*hc*) has more influence on the motion response.

6.2 Hydrostatic and ballast analysis

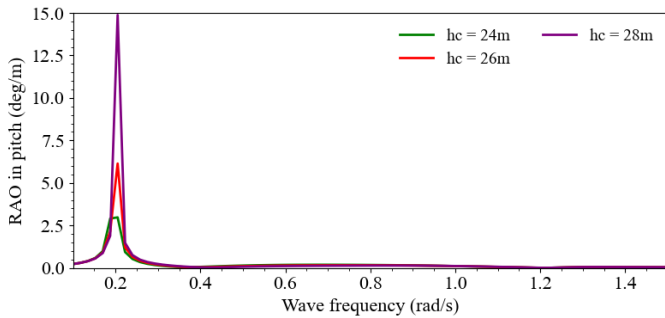The location of the ballast water inside the floater for a specific geometry influences the COG and the mass matrix of the structure, and thus will influence both the hydrostatic performance as well as the nacelle acceleration. The ballast water can be located in the pontoon or in the side columns. Compared to the ballast in the pontoon, the ballast in the side columns will give higher COG, lower nacelle acceleration RAO and higher GM. Two different ballasting scenarios are considered for the original geometry. In both scenarios the draft of the hull is the same, while mass and stiffness matrices refer to the COG are different. The required ballast height in the side columns for the second scenario is 10m which increases the metacentric height by 20% compared to scenario one.

It can be seen from the Figures 9 and 10, by considering the pontoon and side columns for ballasting, the pitch and nacelle acceleration RAO have been decreased significantly at low frequencies. Therefore, due to the high amplitude pitch response which leads to high RMS nacelle acceleration in the case of

pontoon only, in this study both pontoon and side columns are considered for ballasting. The comparison between different ballasting scenarios is shown in Figures 9 and 10. It can be observed that increasing the total mass of the structure in Equation (2) and (5), decreases the response of the structure and also the nacelle acceleration. Figure 11 shows how the metacentric height changes with respect to the design variables of the hull.
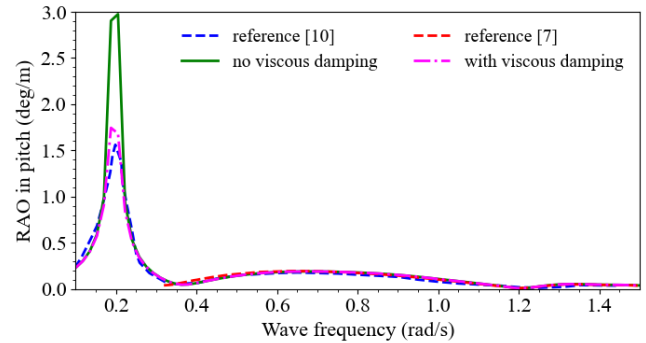
FIGURE 8: PITCH RAO COMPARISON WITH THE PREVIOUS RESEARCH
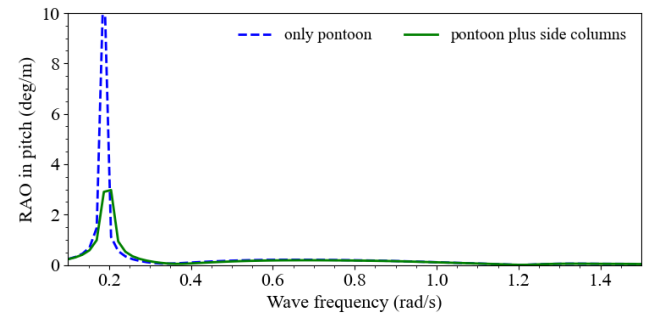
FIGURE 9: PITCH RAO USING DIFFERENT BALLASTING SCENARIOS (HULL GEOMETRY *d* = 6.5M, *s* = 41M AND *hc* = 24M)
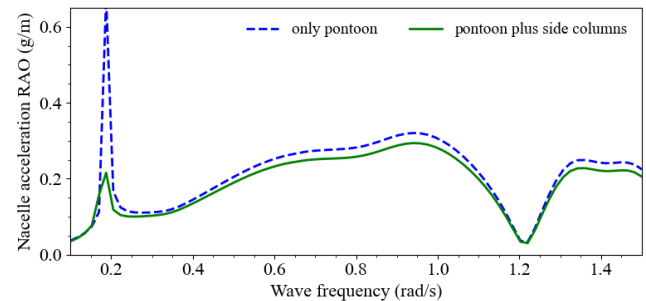
FIGURE 10: NACELLE ACCELERATION RAO WITH DIFFERENT BALLASTING
(HULL GEOMETRY *d* = 6.5M, *s* = 41M AND *hc* = 24M, EC2)

Based on the hydrostatic analysis, most of the structures with column dimeter *d* less than 5.5m are not stable and could not pass the GM constraint PC1. The reason is that these structures are very small for supporting the NREL 5MW. The column diameter has significant effects on the stability. By

keeping the s and hc as constant values, GM increases with the increasing d.

FIGURE 11: GM VERSUS DESIGN VARIABLES

6.3 Performance analysis

In Figures 12 and 13, the RMS nacelle acceleration and the static platform pitch under a thrust load are presented for each point on the grid. Only geometries which fulfill the performance constraints are shown. As expected, the RMS nacelle acceleration and the static pitch decrease with increasing the submerged column height hc while the other v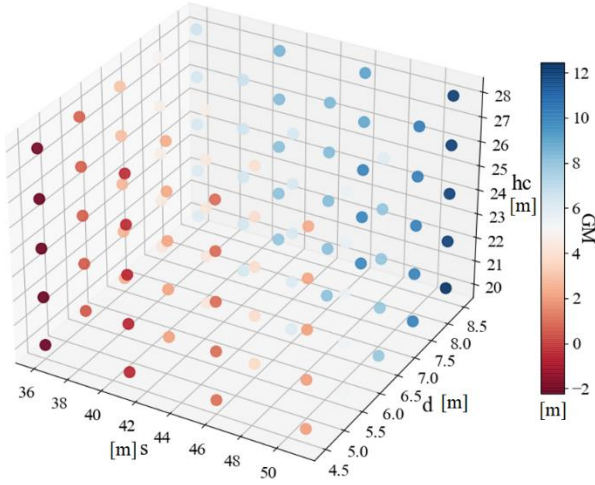ariables being constant. Increasing hc results in increase in GM, C_{55} and the mass of the hull, in which according to Equation (10), leads to decrease in $\varphi_{\text{static}}^{55}$ and based on Equation 3 and 5 leads to decrease in $RMS_{a_{nac}}$.

Considering the hc and s as the constant values, increasing the d, decreases the $\varphi_{\text{static}}^{55}$. The column dimeter is found having insignificant effects on the $RMS_{a_{nac}}$.

According to the Figure 13, the static pitch angle decreases significantly as s increases. The reason can be explained by the fact that by increasing s, the GM increases and consequently C_{55} results in decreasing the static pitch angle. It is observed that 12% increase in s results in 34% decrease in static pitch angle.

6.4 Correlation matrix

Once all the necessary data (i.e. GM, cost and RMS nacelle acceleration) for all geometries have been found, it is useful to investigate the correlation between them which allows us to have a global view of the more or less strong relationship between several variables. Table 5 shows the correlation matrix for variables in this study. As we can see, there is a strong positive correlation between the cost of the hull and its stability.

It has been found that the substructure becomes more stable as the dimensions and mass of the structure increase. The design variable that has the most influence on the cost is the column diameter d. The reason is as a variable d changes, all four columns change accordingly at the same time which increase the cost of the hull significantly. There is a strong negative

correlation between the RMS nacelle acceleration and the submerged column height. The RAO5 has a significant effect on the RMS nacelle acceleration (the hub height intensifies this effect). This is discussed in Sec. 6.6.

Table 5: CORRELATION MATRIX FOR VARIABLES IN THE STUDY

	d	hc	s	GM	Cost	**RMS**
d	1					
hc	0	1				
s	0	0	1			
GM	0.68	0.1	0.43	1		
Cost	0.8	0.24	0.2	0.96	1	
RMS	-0.01	-0.87	0.48	0.24	0.02	1
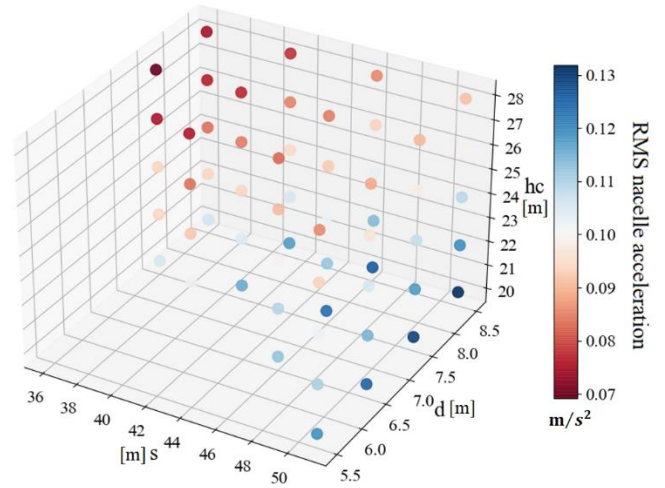
FIGURE 12: RMS NACELLE ACCELERATION VERSUS VARIABLES (EC2)
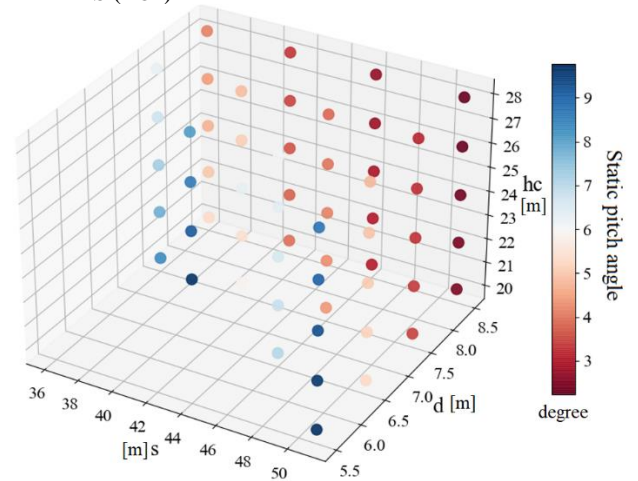
FIGURE 13: STATIC PITCH ANGLE VERSUS DESIGN VARIABLES (AT A WIND SPEED OF 11.4 M/S)

8

6.5 Sensitivity study on the objective functions

To find the optimum geometries, 9 different weights are assigned between 0 and 1 for the combined objective function of the cost and RMS nacelle acceleration. Then Equation (7) becomes:

$$minimize\ F(x) = w_1\overline{f_1(x)} + (1 - w_1)\overline{f_2(x)} \quad (11)$$

For $w_1 = [0, 0.125, 0.25, 0.375, 0.5, 0.625, 0.75, 0.875, 1]$

The performance constraints for the selected optimum geometries in different environmental conditions are presented in Table 6 and 7 respectively. Due to the limited space, only results for EC2 and EC5 are shown. The combined objective function considers the cost and RMS nacelle acceleration of the semi-submersible structures, where all performance constraints are fulfilled. By evaluating the combined objective function, the geometries that minimize the objective function can be found.

Table 6: PERFORMANCE CONSTRAINTS FOR THE OPTIMUM GEOMETRIES FOR EC2 (NON-NORMALIZED VALUES)

index	[d, cs, hc] [m]	GM [m]	$RMS_{a_{nac}}$ $[m/s^2]$	φ_{static}^{55} [degree]	steel weight [kg]
9	[5.5,51,20]	5.35	0.12	9.76	1692500
8	[5.5,51,22]	5.4	0.11	9.64	1724900
7	[6.5,41,22]	5.06	0.1	9.7	1739200
6	[5.5,51,24]	5.56	0.1	9.34	1757300
5	[6.5,41,24]	5.31	0.09	9.16	1777500
4	[6.5,41,26]	5.59	0.08	8.63	1815800
3	[6.5,41,28]	5.9	0.07	8.11	1854100
2	[7.5,36,26]	6.35	0.07	6.77	1931000
1	[7.5,36,28]	6.75	0.06	6.29	1975200

**Table 7:** PERFORMANCE CONSTRAINTS FOR THE OPTIMUM GEOMETRIES FOR EC5 (NON-NORMALIZED VALUES)

index	[d, cs, hc] [m]	GM [m]	$RMS_{a_{nac}}$ $[m/s^2]$	φ_{static}^{55} [degree]	steel weight [kg]
9	[5.5,51,20]	5.35	0.54	9.76	1692500
8	[5.5,51,22]	5.4	0.51	9.64	1724900
7	[6.5,41,22]	5.06	0.45	9.7	1739200
5	[6.5,41,24]	5.31	0.41	9.16	1777500
4	[6.5,41,26]	5.59	0.37	8.63	1815800
3	[6.5,41,28]	5.9	0.34	8.11	1854100

Table 6 and 7 must be interpreted together with Figures 14 and 15, which show the performance of different geometries for different environmental conditions. The red line represents the Pareto Front, which is a set of Pareto efficient solutions obtained by a Python algorithm using the scikit-learn library. Each index in the figure refers to the specific geometry of the design space. The indices in Table 6 and 7 are ordered based on Equation (11) and weight factor.

Although the platform RAOs in EC2 and EC5 are similar, with slight variations due to viscous damping, the motion and acceleration responses are different because of difference in the input wave spectra. This leads to different optimum geometries in the two environmental conditions.

For EC5, six optimum geometries are found since both $w_1 = 0.625$ and 0.75 correspond to index 7 and both $w_1 = 0$, 0.125 and 0.25 correspond to index 3 (see Table 6). The optimum geometry with $w_1 = 0$, is indicated with index 9 in EC2 and EC5 as shown in Figures 14 and 15. This geometry has the cheapest cost but the highest RMS nacelle acceleration. On the other hand, geometries with index 1 in EC2 and index 3 in EC5 have the highest cost with the lowest RMS nacelle acceleration. This observation is reasonable, as the two objectives are conflicting with each other.
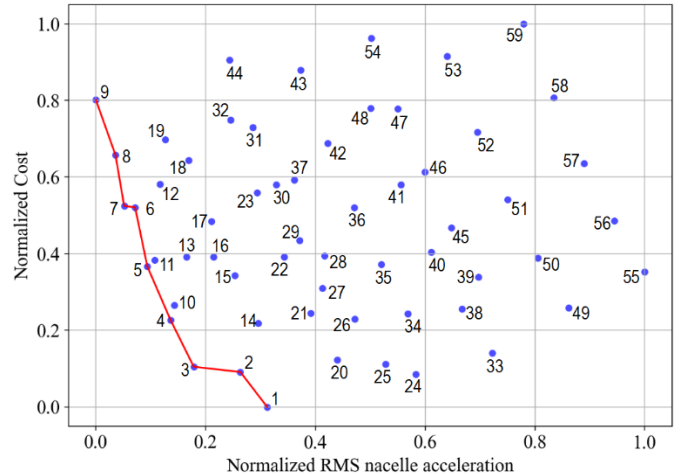
FIGURE 14: PERFORMANCE OF DIFFERENT GEOMETRIES UNDER EC2 (RED LINE REPRESENTS THE PARETO FRONTS)
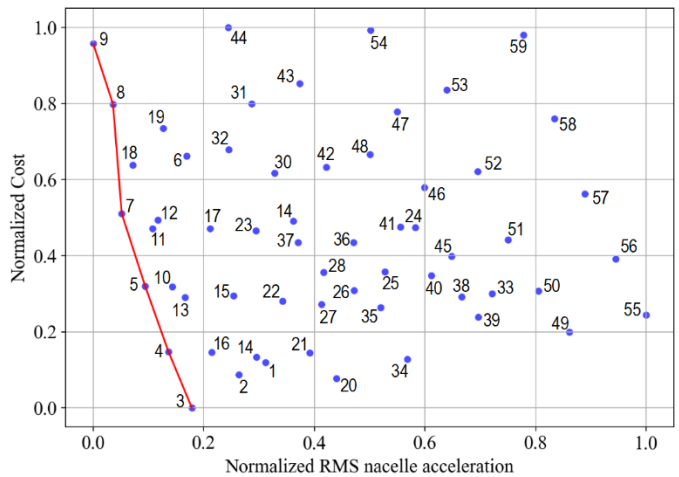
FIGURE 15: PERFORMANCE OF DIFFERENT GEOMETRIES UNDER EC5 (RED LINE REPRESENTS THE PARETO FRONTS)

9 © 2022 by ASME

Comparing Figures 14 and 15, we observe that approximately 67% of the optimum geometries remain in the Pareto Front when the environmental condition changes from EC2 to EC5. In Figure 15, geometries with indices 1, 2 and 6 are not in the vicinity of the Pareto Front, meaning that these solutions do not satisfy Equation (11). The reason is because in EC5, the RMS nacelle acceleration for these geometries is increased significantly and the F(x) in Equation (11) are not minimum. Consequently, these geometries do not lie on the Pareto Front.

As we can see from the Table 6 and 7, increasing the dimensions of the structure decreases the RMS nacelle acceleration. The natural frequency of the structure can become lower than the peak frequency of the wave as the mass of the structure increases. Therefore, the nacelle acceleration is reduced. As we have already discussed in Sec. 6.4, the pitch motion response of the structure changes due to the change in mass matrix as the variables are modified, and RAO5 has the greatest influence on the RMS nacelle acceleration.

Based on the results, the geometries which give the best tradeoff between objective functions for the cost and RMS nacelle acceleration are indicated with indices 4, 5 and 7. These three optima remain on the Pareto Front in these two environmental conditions. For selection of the final optimum design, we must consider a full set of environmental conditions and other realistic design constraints, e.g., fatigue litmit. This aspect is not pursued further in this study.

7. CONCLUSION

In this paper, evaluation of the performance of semi-submersible floaters for the FOWT is performed considering the first order hydrodynamic loads using open- source tools. The influence of geometrical variables on the hydrodynamic performance of the semisubmersible platform is investigated using a weighted sum optimization approach.

The hydrodynamic performance of the semi-submersible platform is investigated by considering two objectives, namely the material cost of the hull and RMS nacelle acceleration. A comparative study is performed for the performance of geometries in two different environmental conditions. The optimum geometry has been chosen based on the results. The main conclusions are summarized as follows:

- The submerged height of the semi-submersible floater has more effects on the response of the system than the pontoon height does.
- The pitch and nacelle acceleration RAO can be reduced by ballasting the pontoon and side columns instead of by ballasting the pontoon alone.
- The diameter of the column has a considerable impact on the hull's cost.
- The RMS nacelle acceleration is reduced as the dimensions of the structure increase due to increase in mass.
- The optimum geometries on the Pareto Front depend on the environmental condition.

This study serves as a basis for hydrodynamic evaluation of the hull. Simplifications are made in the choice of design variables and linear methods are applied in the frequency domain hydrodynamic analysis.

Future work can be considered by implementing more design variables, e.g. pontoon width, pontoon height and length, to explore more hull geometries, and more realistic constraint and cost model can be established. Moreover, an optimization algorithm should be implemented based on the proposed framework.

REFERENCES

[1] Beaudry-Losique, J., a *national offshore wind strategy: creating an offshore wind energy industry in the United States. US Department of Energy, Office of Energy Efficiency and Renewable Energy, Wind & Water Power Program; US Department of the Interior, Bureau of Ocean Energy Management, Regulation, and Enforcement,* 2011

[2] Godø, S. N., *Dynamic response of floating wind turbines. Department of Marine Technology, Norwegian University of Science and Technology, Trondheim, Norway,* 2013

[3] Andrus, C., *Floating foundation for offshore wind turbines.* Ship Offshore *3, 58–59,* 2011

[4] Jaksic, V., O'Shea, R., Cahill, P., Murphy, J., Mandic. D. P., and Pakrashi, V., *Dynamic response signatures of a scaled model platform for floating wind turbines in an ocean wave basin, the Royal Society,* 2015

[5] Chandrasekaran, S., *Design of Marine Risers with Functionally Graded Materials, ISBN: 9780128235614,* 2021

[6] Stansberg, C.T., *Current Effects on a Moored Floating Platform in a Sea State, OMAE2008-57621,* 2008

[7] Luan, C., *Design and Analysis for a Steel Braceless Semi-submersible Hull for Supporting a 5-MW Horizontal Axis Wind Turbine, PhD Theses. Norwegian University of Science and Technology, Tr*ondheim, Norway, 2018

[8] Pegalajar-Jurado, A., *State-of-the-art model for the LIFES50+ OO-Star Wind Floater Semi 10MW floating wind turbine, J. Phys.: Conf. Ser. 1104 012024,* 2018.

[9] Zhou, S., Li, C., Xiao, Y., Lemmer, F., Yu, W., Cheng, P.W., *optimization of the dynamic response of semi-submersibles: influence of the mooring system, IOWTC2019-7553,* 2019

[10] Zhang, L., W. Shi, M. Karimirad, C. Michailides, Z. Jiang*., Second-order hydrodynamic effects on the response of three semisubmersible floating offshore wind turbines, Ocean Engineering 107371,* 2020

[11] Tracy, CC.,*Parametric design of floating wind turbines. MIT, M.Sc. thesis,* 2007

[12] Lemmer, F., Müller, K., Yu, W., Guzman, R.F., Kretschmer, M., *Qualification of Innovative Floating Substructures for 10 MW Wind Turbines and Water Depths Greater than 50 m: Deliverable D4.3*

Optimization Framework and Methodology for Optimized Floater Design, 2016

[13] NEMOH, *Webpage. https://lheea.ec-nantes.fr/*

[14] SALOME, *Webpage. https://www.salome-platform.org/*

[15] Journée, W., Johan, M.J., Massie. *Offshore Hydrodynamics. Delft: University of Technology*, 2001

[16] Morison, J.R., *The Force Distribution Exerted by Surface Waves on Piles. Institute of Engineering Research, Wave Research Laboratory, Tech. rep.* 1953

[17] Penalba, M., Kelly, T., and Ringwood, J.V., *Using NEMOH for Modelling Wave Energy Converters: A Comparative Study with WAMIT. In: 12th European Wave and Tidal Energy Conference August, p. 10,* 2017

[18] DNVGL-ST-0119, *Floating wind turbine structures,* 2018

[19] Hall, M., Buckham, B., and Crawford, C., *Hydrodynamics-based floating wind turbine support platform optimization: A basis function approach. In: Renewable Energy 66,* 2014

[20] Sclavounos, P., Tracy, C., *Floating Offshore Wind Turbines: Responses in a Seastate Pareto Optimal Designs and Economic Assessment, OMAE2008-57056,* 2008

[21] Wayman, E.N., Sclavounos, P.D., Butterfield, S., Jonkman, J., Musial, W., *Coupled Dynamic Modeling of Floating Wind Turbine Systems, OTC-18287-MS,* 2006

[22] Bulder, v. H., Huijsmans, H., Snijders, P., *Studie naar haalbaarheid van en randvoorwaarden voor drijvende offshore wwindturbines*, Tech. Rep., Dec. 2002.

[23] Hall, M., Buckham, B., Crawford, C., *Evolving Offshore Wind: A Genetic Algorithm-Based Support Structure Optimization Framework for Floating Wind Turbines, OCEANS'13 MTS/IEEE Bergen, Norway,* 2013

[24] Li, L., Gao, Z., and Moan, T., *Joint Distribution of Environmental Condition at Five European Offshore Sites for Design of Combined Wind and Wave Energy Devices, J. Offshore Mech. Arct. Eng., vol. 137, no. 031901, doi: 10.1115/1.4029842,* 2015

[25] Gans, H.J.D.K., *Manual for experiments of Numerical Methods in Ship Hydromechanics,* 2014

[26] Chen, J., Li, C., *Design Optimization and Coupled Dynamics Analysis of an Offshore Wind Turbine with a Single Swivel Connected Tether, Energies 13(14):3526,* 2020

[27] Leimeister, M., Kolios, A., Collu, M., *Critical review of floating support structures for offshore wind farm deployment, Journal of Physics: Conference Series 1104 012007,* 2018

[28] Wind Europe. *Floating Offshore Wind Vision Statement. p. 16. url: https://windeurope.org/about-wind/reports/floating-vision-statement,* 2017

[29] Hong, L., Möller, B., *Offshore wind energy potential in China: under technical, spatial and economic constraints. Energy 36 (7), 4482–4491,* 2011

[30] Luan, C., Gao, Z., Moan, T. *Design and analysis of a braceless steel 5-MW semisubmersible wind turbine. In: ASME 2016 35th International Conference on Ocean, Offshore and Arctic Engineering. American Society of Mechanical Engineers Digital Collection, OMAE2016-54848,* 2016

[31] Odijie, A.C., Wang, F., Ye, J., *A Review of Floating Semisubmersible Hull Systems: Column Stabilized Unit, Ocean Engineering, Ocean Engineering, 144. pp. 191-202. ISSN 0029-8018,* 2017